Molecular Simulation of Deep Eutectic Solvents

Seyed Salehi, H.

DOI
10.4233/uuid:a802da95-9c59-41a3-ab87-9ad2d7d4b25f

Publication date
2022

Document Version
Final published version

Citation (APA)
Seyed Salehi, H. (2022). *Molecular Simulation of Deep Eutectic Solvents*. [Dissertation (TU Delft), Delft University of Technology]. https://doi.org/10.4233/uuid:a802da95-9c59-41a3-ab87-9ad2d7d4b25f

Hirad S. Salehi

Molecular Simulation of Deep Eutectic Solvents

Delft University of Technology

Molecular Simulation of Deep Eutectic Solvents

Proefschrift

ter verkrijging van de graad van doctor
aan de Technische Universiteit Delft,
op gezag van de Rector Magnificus, Prof.dr.ir. T.H.J.J. van der Hagen,
voorzitter van het College voor Promoties,
in het openbaar te verdedigen op
maandag 30 mei 2022 om 12:30 uur

door

Hirad SEYED SALEHI
Master of Science in Mechanical Engineering,
Technische Universiteit Delft, Nederland
geboren te Teheran, Iran

Dit proefschrift is goedgekeurd door de promotoren.

Samenstelling promotiecommissie bestaat uit:

Rector Magnificus,	voorzitter
Prof.dr.ir. T.J.H. Vlugt	Technische Universiteit Delft, promotor
Dr. O.A. Moultos	Technische Universiteit Delft, copromotor

Onafhankelijke leden:

Prof.dr. L. Lin	National Taiwan University, Taiwan & Ohio State University, USA
Prof.dr. E.A. Pidko	Technische Universiteit Delft
Prof.dr.ir. B. Schuur	Universiteit Twente
Prof.dr.ir. R. Tuinier	Technische Universiteit Eindhoven
Prof.dr.ir. W. de Jong	Technische Universiteit Delft

This work was sponsored by NWO Domain Science for the use of supercomputer facilities. Thijs J.H. Vlugt acknowledges NWO-CW (Chemical Sciences) for a VICI grant.

Keywords: Deep eutectic solvents, Monte Carlo simulations, Molecular Dynamics, thermodynamics, transport properties, phase equilibrium

Printed by: Ridderprint B.V.

Cover design by Hirad Seyed Salehi

ISBN: 978-94-6366-501-8

An electronic version of this dissertation is available at
http://repository.tudelft.nl/

"It's called chemistry, I have it with everybody!"
Jeff Winger, *Community*

Contents

1 Introduction **1**
- 1.1 Deep eutectic solvents 1
- 1.2 Molecular simulation of DESs 4
- 1.3 Outline of this thesis 9

2 Hildebrand and Hansen solubility parameters of deep eutectic solvents **15**
- 2.1 Introduction 16
- 2.2 Computational details 20
- 2.3 Results and discussion 24
  - 2.3.1 Solubility parameters from vaporization energies . . 24
  - 2.3.2 Vaporization of individual components 29
  - 2.3.3 Correlations with other DES properties 32
- 2.4 Conclusions 34

3 Solubilities of CO_2, H_2S, CH_4, CO, H_2, and N_2 in deep eutectic solvents **37**
- 3.1 Introduction 38
- 3.2 Computational details 39
- 3.3 Results and discussion 45
  - 3.3.1 Densities and radial distribution functions 45
  - 3.3.2 Solubilities 49
- 3.4 Conclusions 59

4 Vapor pressures and vapor phase compositions of deep eutectic solvents **61**
- 4.1 Introduction 62
- 4.2 Computational details 64
- 4.3 Results and discussion 72
  - 4.3.1 Partial pressures and vapor phase compositions . . . 72

4.3.2 Vapor pressures and enthalpies of vaporization . . . 77
4.3.3 Effect of liquid composition on DES properties . . . 80
4.4 Conclusions . . . 89

5 Thermodynamic, transport, and structural properties of hydrophobic deep eutectic solvents 91
5.1 Introduction . . . 92
5.2 Computational details . . . 93
5.3 Results and discussion . . . 96
5.3.1 Thermodynamic and transport properties . . . 96
5.3.2 Liquid structure . . . 110
5.4 Conclusions . . . 118

6 Interfacial properties of hydrophobic deep eutectic solvents with water 119
6.1 Introduction . . . 120
6.2 Computational details . . . 121
6.3 Results and discussion . . . 126
6.3.1 Force field validation . . . 126
6.3.2 Density profiles and interfacial tensions . . . 126
6.3.3 Hydrogen bond analysis . . . 137
6.4 Conclusions . . . 144

Conclusions 147

Appendix 151

References 199

Summary 239

Samenvatting 245

Curriculum vitae 251

List of publications 253

Acknowledgments 255

Chapter 1

Introduction

1.1 Deep eutectic solvents

For many years, room temperature ionic liquids (ILs), i.e., salts with melting points lower than 100°C, have been acknowledged as superior solvents compared to volatile organic compounds (VOCs), due to properties such as tunable solubilities, very low vapor pressures, and non-flammability [1–3]. In 2003, Abbott et al. [4] found that a mixture of choline chloride and urea (both solids at room temperature) exhibits a eutectic melting point significantly lower than the melting points of the individual components, thus forming a liquid phase at room temperature. This mixture was referred to as a 'deep eutectic solvent' (DES) [4]. Ever since, a growing number of DESs have been synthesized from various precursors. DESs share many favorable thermo-physical properties with ILs, such as high solvation with respect to many solutes, low vapor pressures, wide temperature range for liquidity, tunability, and low melting points [5–14]. Unlike ILs, DESs are typically easy and cost-effective to prepare (with no further purification requirements), biodegradable, and non-toxic [6, 10, 15, 16]. DESs may contain both charged (ions) and charge-neutral components, resulting in an even wider variety of possible DES structures [6, 11] compared to ILs (which are only composed of ions). Due to their properties, DESs have been regarded as 'greener' alternatives to ILs and VOCs, and have received tremendous attention from researchers in recent years. DESs have been considered for a wide array of applications, such as gas capture and separation (e.g., CO_2), metal electrodeposition, catalysis, drug solubilization, biomass processing, battery systems, and liquid-liquid extraction processes (e.g., glycerol from biodiesel) [6, 10, 11, 13, 17, 18].

Several classes of DESs have been reported in literature based on the chemical nature of the precursors that are used. Smith et al. [6] categorized DESs into mixtures composed of: (I) salts and metal halides, (II) salts and metal halide hydrates, (III) organic salts and hydrogen bond donors, and (IV) metal halides and hydrogen bond donors. Several DESs based on natural and charge-neutral compounds have also been investigated in literature [12, 17]. Recently, a new class of DESs based on phenolic hydrogen bond donating groups was introduced by Abranches et al. [19]. The most commonly studied DESs to date are of type III, in which a hydrogen bond donor (HBD) is mixed with a salt composed of a cation and an anion (such as choline chloride), as hydrogen bond acceptor (HBA).

For many years, DESs reported in literature were of hydrophilic nature until van Osch et al. [20] introduced a new class of hydrophobic DESs in 2015. These DESs are often mixtures of HBA and HBD components, which are charge-neutral or charged (salts) hydrophobic molecules, with hydrophobic functional groups (e.g., long alkyl chains). Hydrophobic DESs have received much attention as water-immiscible solvents with many potential applications ranging from carbon capture to water purification, and extraction of metabolites from plants [11, 21]. DESs based on tetraalkylammonium halides and fatty acids (e.g., decanoic acid), for instance, have been considered for a large number of applications, such as CO_2 capture [5, 22, 23], extraction of fatty acids [20], antibiotics [24], sugar-derived molecules [25, 26], and metal ions [27–30] from aqueous solutions, and extraction of pigments from different beverages [31]. It has been shown by van Osch et al. [20] that the degree of hydrophobicity (e.g., the cation chain length) of these DESs determines the extent to which the DES components leach into the water phase, adversely affecting the extraction process of solutes from aqueous solutions.

A schematic representation of a typical solid-liquid phase diagram for (deep) eutectic mixtures is shown in Fig. 1.1, where the eutectic point is denoted by 'E'. It is important to note that the molar ratio in which the DES components (e.g., HBA and HBD) are mixed (not necessarily the eutectic molar ratio, i.e., x_{E} in Fig. 1.1) plays a crucial role in determining the melting point and other physico-chemical properties of DESs [10]. DESs are often characterized by a large melting point depression of the mixture compared to the melting points of the pure component (as observed in Fig. 1.1), and an extensive hydrogen bonding network between the various components [4, 6, 7]. The precise definition of a DES is, however, debated [14, 21, 32]. For instance, it has been suggested that a considerable difference between the eutectic point of the mixture and the ideal solution eutectic

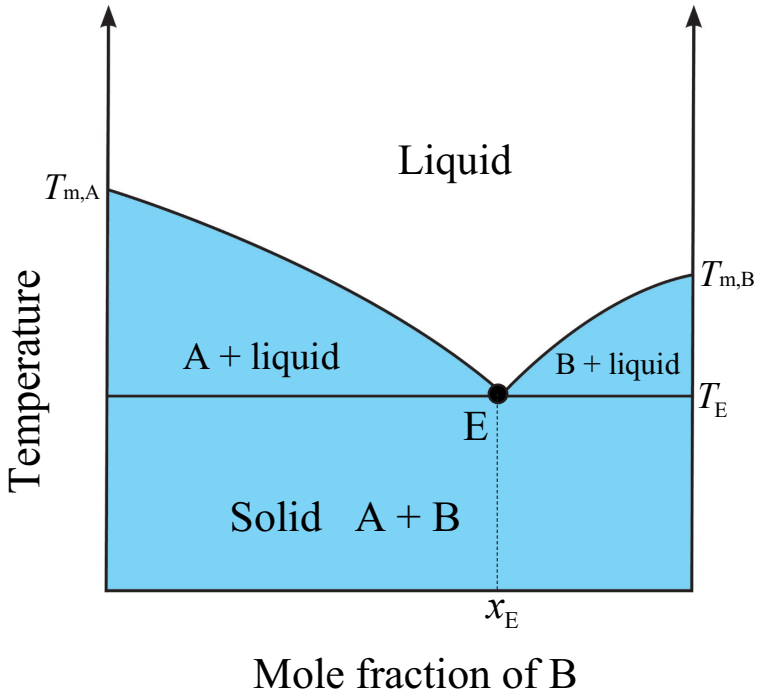

Figure 1.1: A schematic solid-liquid phase equilibrium diagram for a binary (deep) eutectic mixture (composed of components A and B), in terms of temperature as a function of the mole fraction of component B, at constant pressure. The eutectic point of the mixture, and the melting points of pure A and pure B components are denoted by 'E', $T_{m,A}$, $T_{m,B}$, respectively. The blue areas indicate the regions where solid phases (A or B) are formed. As an example, for choline chloride-urea DES, the values of $T_{m,ChCl}$ ('ChCl' denotes choline chloride), $T_{m,urea}$, T_E, and $x_{E,urea}$ at 1 atm are 302°C, 133°C, 12°C, and 0.67, respectively [4].

point (and not the melting points of the individual components) is necessary for the definition of a DES [14, 32]. The necessity of hydrogen bonds for the formation of DESs has also been questioned [14, 32]. Based on these alternative definitions, many of the reported DESs are classified as simple eutectic mixtures rather than 'deep' eutectic solvents [32]. Therefore, the solid-liquid phase equilibrium of a mixture must be well-characterized before it can be labeled as a 'DES'.

1.2 Molecular simulation of DESs

The optimal design of a solvent (e.g., DES) for a specific chemical process requires accurate knowledge of the thermo-physical properties and phase equilibria of the solvent and its mixtures with other compounds. Additionally, the relationship between these properties and the chemical structure of the solvent needs to be investigated. To measure various thermodynamic and structural properties of neat DESs and mixtures of DESs with other molecules, experiments have been performed by several research groups [33–48]. DESs are a relatively new class of solvents, and have a wide window of possible structures due to the very large number of potential precursor compounds and mixing molar ratios. Therefore, experimental data are still lacking for many properties of the reported DESs, e.g., for phase equilibria of DES/water mixtures. Additionally, many DESs have relatively large viscosities (particularly at low temperatures) [13, 37] and high hygroscopicities (tendency to absorb water) [49], which can adversely affect the experimental measurements, and in some cases, may lead to inconsistent results [50–53]. To understand and establish structure/property relationships, and predict the thermodynamic and phase equilibrium properties of DESs at various conditions, e.g., when measurements are unavailable, contradictory, dangerous, difficult to perform, expensive, or when the DES has not yet been synthesized, thermodynamic modeling is often performed. A variety of methods have been used, including (but not limited to) the use of equations of state (EoS), particularly based on statistical associating fluid theory (SAFT) [54, 55], excess Gibbs energy (ΔG^{ex}) models, and molecular simulations. Details on the various thermodynamic modeling methods used for studying DESs can be found in Refs. [42, 56–68].

Molecular simulation is a powerful modeling tool to study properties of materials, as it provides relationships between the macroscopic properties and atomic/molecular-level interactions, dynamics, and structure, based on the principles of statistical thermodynamics [69, 70]. The knowledge of these relationships can be used to design novel materials with optimal thermo-physical properties [58, 71–75]. Molecular simulation can also be used as an alternative to experiments for obtaining properties of materials, when experiments are challenging or impossible due to extreme conditions (e.g., very high/low pressures or temperatures) [69, 70]. For DESs and ILs, due the wide variety of possible structures, molecular simulations can be particularly useful for predicting the properties of the different structures, instead of costly and time-consuming experiments, and finding potential candidates for specific applications [58, 76–79].

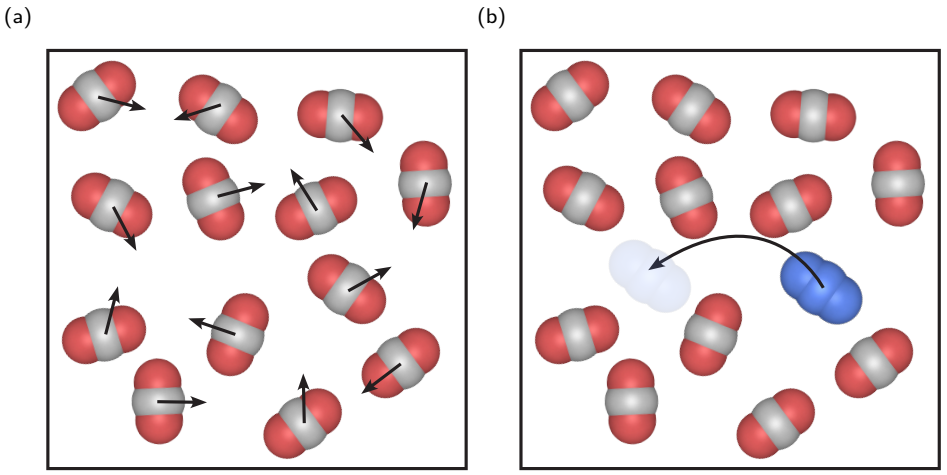

Figure 1.2: Schematic representations of (a) Molecular Dynamics (MD) and (b) Monte Carlo simulations for CO_2. In MD simulations, atoms/molecules move collectively according to the resultant inter-atomic forces, based on Newton's equations of motion. In MC simulation, trial moves are performed (e.g., translation or reinsertion) for randomly selected molecules (shown in blue in (b)) or groups of molecules. These trial moves are accepted or rejected based on the detailed balance condition [69]. Collective trial moves can also be performed in MC simulations, e.g., see Refs. [80, 81].

The two main classical molecular simulation techniques, namely Molecular Dynamics (MD) and Monte Carlo (MC) simulations [69, 70], are based on inter-atomic interaction potentials (i.e., 'force fields') defined for the studied material. These force fields determine the non-bonded (e.g., dispersion and electrostatic) and bonded (e.g., bond-stretching, bond-bending, dihedrals, and improper dihedrals) interactions of each system as a function of the positions of all atoms in the system. The interaction parameters of classical force fields are often obtained from fitting the force fields to experimental data, or from quantum mechanical calculations [70].

Schematic representations of MD and MC simulations are shown in Fig. 1.2. In classical MD simulations, all atoms/molecules in the simulation box are displaced as a function of time according to the resultant forces/torques based on Newton's equations of motion. This method is deterministic in nature, and yields trajectories in phase-space, over which time averages of various thermodynamic and transport properties can be computed. In MC simulations, an ensemble of system states is generated based on random (probabilistic) trial moves. These trial moves attempt to make random changes to the configuration of the system (resulting in new system states), for instance by translation, rotation, or reinsertion of a

randomly selected molecule, or by changing the volume of the simulation box. These trial moves are accepted or rejected based on the energies of the old and new configurations, according to the detailed balance condition (using the so-called 'acceptance rules') [69]. This ensures that the sampling of configuration space is performed according to the statistical weight of each state. The ensemble average of various thermodynamic and structural properties can then be computed from MC simulations. MD simulations are often carried out in closed ensembles (i.e., with a fixed number of molecules), whereas MC simulations offer a variety of open ensembles (in which the numbers of molecules change), such as the Gibbs ensemble [69, 82, 83], the grand canonical ensemble [69, 84–86], and the osmotic ensemble [87, 88]. In an open ensemble, the fluctuation of the number of molecules is sampled using trial moves that attempt to insert/delete molecules [69, 89]. These molecule insertions/deletions are often inefficient (i.e., low acceptance probabilities) for systems with strong/specific intermolecular interactions, high densities, or large molecules [89–91]. To improve the efficiency of insertion/deletion trial moves, a variety of advanced techniques (and combinations thereof) are used in MC simulations, such as the configurational-bias Monte Carlo (CBMC) [92–95], the continuous fractional component Monte Carlo (CFCMC) [91, 96–100], and the recoil growth (RG) scheme [101, 102]. It is important to note that unlike in MD simulations, the time dimension is not defined in MC simulations, and thus, MC simulations are not suitable for computing transport properties (which are time dependent) [69]. Using powerful supercomputers, it is now possible to perform molecular simulations for millions of atoms and for simulation times in the order of miliseconds [70]. In principle, quantum mechanical computational methods (based on solving Schrödinger's equations), such as density functional theory (DFT) [103], provide more accurate interaction energies compared to classical force fields. However, these methods are computationally intensive, and therefore, cannot be used for length- or timescales typically achieved in force field-based molecular simulations. For a more detailed description of MD and MC methods, the reader is referred to Refs. [69, 70, 104–107]. Several software packages are also available for MD (e.g., GROMACS [108, 109], LAMMPS [110], NAMD [111]) and MC simulations (e.g., Brick-CFCMC [81, 112], Cassandra [113, 114], GOMC [115], RASPA [116], and Towhee [117]).

In recent years, MD simulations have been used to compute densities [59, 61, 68, 77, 118–128], heat capacities [59, 61, 68, 121], isothermal compressibilities [118, 126], surface tensions [59, 118, 126], diffusion coefficients [59, 61, 68, 77, 118, 119, 121, 124, 126, 128–132], ionic conductivities [77, 127,

128], thermal conductivities [133], viscosities [59, 118, 123, 126–130], and the liquid structures [43, 59, 61, 68, 77, 119–125, 127–130, 132, 134–139] of neat DESs and mixtures of DESs with other compounds. It is still, however, challenging to compute properties of DESs accurately and efficiently from molecular simulations [56, 58, 62]. This is due to the fact that DES mixtures are composed of a wide range of different chemical structures (with hydrophilic and hydrophobic domains), and the intermolecular interactions within DESs are often very complex, consisting of considerable contributions from van der Waals, dipole-dipole, and hydrogen bonding interactions [6, 13, 18]. This leads to an extensive heterogeneity of DESs at the nanoscale [18, 75, 122, 140–142] (similar to ILs [143, 144]), the effect of which on the thermodynamic and transport properties is challenging to study. Such intricate structures and interactions complicate the development of force fields that are accurate for the computation of a wide array of properties, and at the same time, are transferable between various DES systems. Due to the strong intermolecular interactions of DESs (and thus high viscosities), the equilibration of these systems, especially at low temperatures, is often a slow and tedious process [56], and may require special techniques to improve (e.g., a compression decompression scheme [61, 68] or annealing [145, 146]). Because of these strong intermolecular interactions and a high liquid (number) density, it is also difficult to efficiently insert (or delete) molecules into (or from) DES mixtures when using MC simulations in open ensembles [147]. This may be the reason for the very limited number of available MC simulation studies for DES-containing systems [52, 147, 148].

Although numerous experimental and modeling studies are now available in the literature, large knowledge gaps still exist regarding the structure and intermolecular interactions of DESs, and the influence of the structure and interactions on thermo-physical properties. In this thesis, these structure/property relationships are studied for a variety of key thermodynamic and phase equilibrium properties, and for relevant DES mixtures, using MD and MC simulations. The DESs studied in the various chapters of this thesis are summarized in Table 1.1. It is important to note that DESs 1-8 of Table 1.1 are composed of ionic HBA components, i.e., a cation and the chloride anion, while DESs 9 and 10 only consist of charge-neutral molecules. The molecular structures of the components (except for the chloride anion) of all the DESs are shown in Figs. A1 to A12 of the Appendix. In this thesis, the performance of the current methods and force field parameters for the computation of various properties of these DESs is evaluated, and if possible, enhanced. The main challenges with respect to the molecular simulations of DESs are discussed, and recommendations are provided for

Table 1.1: HBA and HBD components, abbreviations, HBA:HBD molar ratios used in the simulations (unless stated otherwise), and average molar masses (corresponding to the listed molar ratios) for the DESs in this thesis. The molar mass of each DES was obtained by using the relation $M = \sum x_i M_i$, where x_i is the mole fraction of each DES component i (HBD or HBA), and M_i is the molar mass of component i.

#	HBA	HBD	abbreviation	HBA:HBD	$M/[\mathrm{g\,mol^{-1}}]$
1	choline chloride	urea	ChClU	1:2	86.57
2	choline chloride	ethylene glycol	ChClEg	1:2	87.91
3	choline chloride	glycerol	ChClG	1:2	107.93
4	choline chloride	malonic acid	ChClMa	1:1	121.84
5	choline chloride	oxalic acid	ChClOa	1:1	114.83
6	tetrabutylammonium chloride	decanoic acid	TBAC-dec	1:2	207.48
7	tetraheptylammonium chloride	decanoic acid	THAC-dec	1:2	263.59
8	tetraoctylammonium chloride	decanoic acid	TOAC-dec	1:2	282.29
9	DL-menthol	decanoic acid	Men-dec	2:1	161.60
10	thymol	decanoic acid	Thy-dec	1:2	164.92

further improvements. Although the prediction of the melting point and thus the solid-liquid phase equilibrium of DESs from molecular simulations can be of great practical interest, these calculations are often challenging for such complex molecules [149–151], and were therefore not considered here.

1.3 Outline of this thesis

This thesis focuses on providing a computational framework for studying a wide variety of thermodynamic, structural, and transport properties of DESs, as well as presenting new, insightful information on the intermolecular interactions of DESs and the influence of these interactions on the macroscopic properties. Chapters 2, 3, and 4 are devoted to the computation of the solubility parameters, gas solubilities (absorption loading and Henry coefficients), enthalpies of vaporization, vapor pressures, and vapor phase compositions of hydrophilic choline-chloride based DESs. In chapters 5 and 6, the thermodynamic, transport, and structural properties of decanoic acid-based hydrophobic DESs and the interfacial properties of these DESs with water are investigated. Detailed descriptions of all chapters are presented in the rest of this section.

In chapter 2, the solubility parameters of choline chloride-based DESs with different HBD components are computed from MD simulations. The solubility parameter is a thermodynamic property that estimates the polarity (strength of intermolecular interactions) of a molecule, and thus the mutual miscibility of materials. Two types of solubility parameters were obtained for the DESs based on the computation of the enthalpies of vaporization: the Hildebrand [152] and the Hansen [153] solubility parameters. The Hildebrand solubility parameter lumps all intermolecular interactions into a single quantity, while the Hansen solubility parameter contains separate contributions from dispersion, polar, and hydrogen bonding interactions. For choline chloride-urea, two force fields were considered, namely OPLS [154] and the General Amber Force Field (GAFF) [155], while for the other DESs, only the OPLS force field was used. Only slight differences were observed between the computed solubility parameters of choline chloride-urea from the two force fields. The computed solubility parameters indicated a high polarity for the DESs. Unlike for pure compounds, the solubility parameter is not thermodynamically well-defined for mixtures. Therefore, to be able to compute the solubility parameters of DESs, a pseudo-pure compound approach was taken. Each DES was assumed to be a pure compound consisting of DES clusters, which were composed of

the HBD and HBA components with the same molar ratio as in the DES liquid phase. This approach provides an estimation for the overall polarity and solubility parameter of each DES. However, it assumes the clusters to be the vaporizing entities of the DESs. To evaluate this assumption, enthalpies of vaporization (and corresponding solubility parameters) were also computed for each of the components of the DES mixtures (HBD and HBA). Based on the computed vaporization enthalpies, it was found that the vapor phase of the DESs is likely dominated by the HBD component (the more volatile component). The effect of temperature was found to be negligible on the computed Hildebrand solubility parameters. The computed vaporization energies and cohesive energy densities were correlated with the activation energies of viscosity and the Gordon parameters [156] of the DESs, respectively.

In chapter 3, the solubilities of CO_2, CH_4, H_2S, CO, N_2, and H_2 were computed in choline chloride-urea and choline chloride-ethylene glycol DESs, from MC simulations. Experimental data are scarce, and in some cases contradictory, for the solubilities of these gases in DESs, particularly for the more insoluble gases [52, 53, 157]. Therefore, MC simulations can serve as an alternative method to estimate the solubilities, and possibly resolve the inconsistencies between the experimental data. As explained in Section 1.2, for DES systems, the equilibration and molecule insertions/deletions are challenging in MC simulations in open ensembles, due to the strong intermolecular interactions. Therefore, the state-of-the-art CFCMC method[91, 96–100] was used, which is based on an efficient, gradual insertion/deletion of molecules. The method also entails additional trial moves, such as reinsertions and identity changes of molecules, that can facilitate the equilibration of the system. The excess chemical potentials at infinite dilution, and thereby the Henry coefficients of the solute gases were directly computed from the CFCMC method. The Henry coefficient results were corroborated by computing the isothermal absorption loading of CO_2 in choline chloride-ethylene glycol from simulation in the osmotic ensemble. For both DESs, the order of the computed gas solubilities at 328 K was the following: $H_2S > CO_2 > CH_4 > H_2 > CO > N_2$, in agreement with experimental data. The Henry coefficients of these gases in both DESs were highly underestimated from the simulations, compared to experimental data. The influence of the force field parameters and the charge scaling factor on the computed Henry coefficients was found to be significant.

In chapter 4, the excess Gibbs energies, and thereby the vapor pressures and vapor phase compositions of choline chloride-urea and choline chloride-ethylene glycol DESs were computed from MC simulations. The

computation of the excess Gibbs energy (excess chemical potential) from the observed probability distribution of the interaction scaling parameter, as performed in chapter 3, becomes increasingly challenging for larger molecules with stronger interactions (e.g., DES components). Therefore, thermodynamic integration was used in chapter 4 as an alternative method for the computation of excess Gibbs energies. The vapor phases of the DESs were assumed to be composed of isolated HBA (choline chloride) and HBD components. The computed vapor pressures and enthalpies of vaporization were mostly in agreement with experimental data. According to the computed vapor phase compositions, small amounts of the HBA component (ca. 9% mole fraction-based) are found in the vapor phase of choline chloride-urea, whereas the vapor phase of choline chloride-ethylene glycol is essentially completely composed of the HBD component. These findings corroborate the results from chapter 2 on the vapor phase composition of DESs. The influence of the liquid phase composition (i.e., the mole fraction of the HBD) on the computed properties was investigated. The enthalpies of vaporization, and the partial pressures of choline chloride (in both DESs) and urea were not considerably influenced by the liquid phase composition, whereas the partial pressure of ethylene glycol increased with an increase in the liquid phase mole fraction of ethylene glycol in the DES. The activity coefficients of ethylene glycol in choline chloride-ethylene glycol were computed using a modified version of Raoult's law. Due to the fact that pure urea and pure choline chloride are solid at the studied temperatures, it was not possible to compute the activity coefficients of these components. The calculated activity coefficients of ethylene glycol showed a highly non-ideal behavior with negative deviations from Raoult's law.

In sharp contrast to hydrophilic DESs, only few studies exist in literature that investigate the structural and thermodynamic properties of hydrophobic DESs at the nanoscale [132, 139, 158]. Therefore, theoretical knowledge on the intermolecular interactions and the influence of these interaction on the properties of hydrophobic DESs is largely lacking. In chapter 5, thermodynamic, transport, and structural properties of hydrophobic DESs composed of tetraalkylammonium chloride and decanoic acid were computed for a wide temperature range from MD simulations. The computed properties included densities, shear viscosities, finite size-corrected self-diffusivities, ionic conductivities, radial distribution functions (RDFs), and hydrogen bond populations. The considered DESs are highly viscous at lower temperatures [20], which makes the precise computation of transport properties challenging and time-consuming. Therefore, very long simulations (up to 650 ns) and elevated temperatures were required for these computations.

The influence of the ionic charge scaling factor on the computed densities and viscosities was also examined. Based on the best agreement of the simulation results with experimental data, a charge scaling factor of 0.6 was used in the production runs for all DESs. The effect of the cation alkyl chain length on the computed thermodynamic properties and liquid structure was studied by using different chain lengths (4, 7, or 8 carbon atoms) for the tetraalkylammonium cation. The computed densities and transport properties were in agreement with experimental data, particularly for the DESs with smaller alkyl chain lengths. It was found that while the liquid structures and hydrogen bond networks of the studied DESs are not considerably affected by the cation alkyl chain length, the motion of the molecules is increasingly hampered at larger alkyl chain lengths, resulting in higher viscosities and smaller diffusion coefficients.

Although hydrophobic DESs have been proposed for a wide range of liquid-liquid extraction processes of solutes from water, very little is known about the extent of the hydrophobicity of these DESs, and the interfacial properties of DES/water biphasic systems. In chapter 6, the interfacial properties of DESs based on decanoic acid and various HBAs (tetrabutylammonium chloride, DL-menthol, and thymol) with water were computed at different temperatures from MD simulations. Large system sizes were used (up to 40000 atoms) to capture the interfaces of these DESs with water. The computed properties included interfacial tensions, density profiles of various mixture components, hydrogen bond number densities, and mutual DES/water solubilities (from the obtained density profiles). Different charge scaling factors were used for the tetrabutylammonium chloride-decanoic acid and thymol-decanoic acid DESs. It was found that a charge scaling factor of 0.6 underestimates the amount of leaching of the salt from tetrabutylammonium chloride-decanoic acid into water, while a charge scaling factor of 0.8 results in a larger extent of leaching, which is in better agreement with experimental observations. This effect was partly associated with the stronger chloride-water hydrogen bonds at the larger charge scaling factor. For the thymol-decanoic acid/water mixture, the use of different charge scaling factors affected the decanoic acid-water hydrogen bonds, and consequently the DES/water interfacial tensions. Considering charge scaling factors of 0.7 and 1 for the HBA and HBD components of thymol-decanoic acid, the computed interfacial tensions of the DESs were in the following order: tetrabutylammonium chloride-decanoic acid $<$ thymol-decanoic acid $<$ DL-menthol-decanoic acid, which is in agreement with experimental observations. All computed properties were insensitive to temperature. A preferential alignment of the oxygen atoms of decanoic acid towards the

aqueous phase (for maximized hydrogen bonding) was observed at the interfaces of all DES/water systems.

Chapter 2

Hildebrand and Hansen solubility parameters of deep eutectic solvents

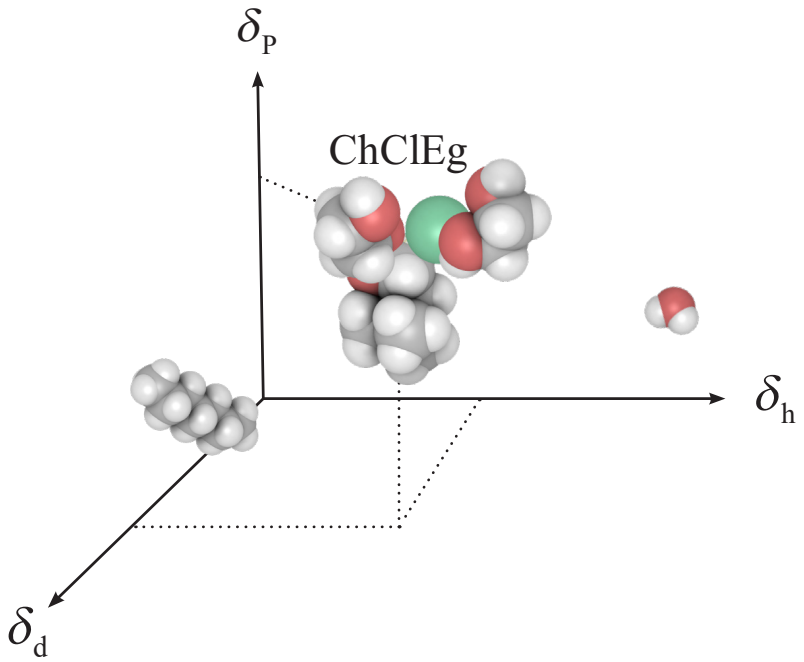

This chapter is based on the following paper: H.S. Salehi, M. Ramdin, O.A. Moultos, T.J.H. Vlugt, Computing solubility parameters of deep eutectic solvents from Molecular Dynamics simulations, *Fluid Phase Equilibria*, **2019**, 497, 10-18.

2.1 Introduction

As mentioned in chapter 1, DESs have been considered in a wide range of applications (e.g., gas capture and liquid-liquid extraction) as potential solvents [10, 13]. It is therefore crucial to be able to predict the solvation of DESs with respect to other compounds. The polarity of a solvent, such as a DES, is a key property that determines the overall ability of the solvent to dissolve various solutes. This is often discussed in the context of the 'like-dissolves-like' rule of thumb [159–162], i.e., compounds with similar polarities are miscible, while compounds with different polarities are completely or partially immiscible. The quantification of polarity is, however, not straightforward, and a variety of physical parameters have been used to achieve this [160]. One of the key parameters used to quantify the polarity of compounds is the solubility parameter, first introduced in 1936 by Hildebrand [152]. The Hildebrand solubility parameter, δ_{H}, is defined as the square root of the cohesive energy density:

$$\delta_{\mathrm{H}} = \sqrt{\frac{\Delta E^{\mathrm{vap}}}{V_{\mathrm{m}}}} \tag{2.1}$$

where ΔE^{vap} is the energy of vaporization (e.g., in $\mathrm{J\,mol^{-1}}$), and V_{m} is the molar volume (e.g., in $\mathrm{m^3\,mol^{-1}}$) of the solvent.

The enthalpy of vaporization (ΔH^{vap}) of a compound can be computed from the vapor pressure data, by linear regression using the Clausius-Clapeyron relation [163]:

$$\ln\left(\frac{P^{\mathrm{v}}}{[\mathrm{Pa}]}\right) = -\frac{\Delta H^{\mathrm{vap}}}{RT} + C \tag{2.2}$$

where P^{v} is the vapor pressure, T is the absolute temperature, R is the universal gas constant, C is a constant, and the enthalpy of vaporization has been assumed to be temperature independent. Assuming the vapor phase is an ideal gas, the vaporization energy can be computed as $\Delta E^{\mathrm{vap}} = \Delta H^{\mathrm{vap}} - RT$, which can be used in Eq. 2.1.

Although Equation 2.1 is simple to use, a complication may arise for non-volatile solvents, such as ILs, DESs, and polymers, due to the lack or scarcity of experimental vapor pressure data needed to obtain values for ΔE^{vap}. To overcome this limitation, the Hildebrand solubility parameter has been correlated with other physical quantities like the surface tension, intrinsic viscosity, dielectric constant, melting point, the activation energy of viscosity, and infinite dilution activity coefficients [164–177]. For instance,

the solubility parameter of a compound is correlated with the surface tension (with air), γ, according to [174]:

$$\delta_{\mathrm{H}}^2 = k\gamma V_{\mathrm{m}}^{-1/3} \tag{2.3}$$

in which V_m is the molar volume of the solvent and k is a constant that depends on the coordination numbers of molecules [174, 178]. Kilaru et al. [165] used Eq. 2.3 to estimate the solubility parameters of ILs. The intrinsic viscosity, η^{int}, is related to the solubility parameter through the Mangaraj equation [179]:

$$\eta^{\mathrm{int}} = \eta_{\mathrm{max}}^{\mathrm{int}} \exp\left[-A(\delta_{\mathrm{H}}^{\mathrm{solv}} - \delta_{\mathrm{H}}^{\mathrm{sol}})\right] \tag{2.4}$$

where A is a fitting parameter, and $\delta_{\mathrm{H}}^{\mathrm{solv}}$ and $\delta_{\mathrm{H}}^{\mathrm{sol}}$ are the solubility parameters of the solvent and the solute, respectively. The intrinsic viscosity exhibits a maximum ($\eta_{\mathrm{max}}^{\mathrm{int}}$) at a point where the interaction between the solute and the solvent is the strongest. The intrinsic viscosity method has been used to predict the solubility parameters of ILs and polymers [167, 170, 179]. Moganty and Baltus [169] correlated the activation energy of viscosity ($E_{\mathrm{a}}^{\mathrm{vis}}$) with the solubility parameter of ILs as:

$$\delta_{\mathrm{H}} = \sqrt{\frac{cE_{\mathrm{a}}^{\mathrm{vis}}}{V_{\mathrm{m}}}} \tag{2.5}$$

in which c is a constant. The value of c largely depends on the shape and size of the molecule under consideration. For instance, c is set to 4 for non-spherical molecules, and to 3 for small spherical molecules [156, 180]. The activation energy of viscosity appears explicitly in the Arrhenius-type equation which is often used to model the temperature dependence of viscosity, η, as:

$$\eta = A \exp\left[\frac{E_{\mathrm{a}}^{\mathrm{vis}}}{RT}\right] \tag{2.6}$$

where A is a constant, R is the universal gas constant, and T is the absolute temperature. Some substances (e.g., molten salts with glass transition [181]), however, exhibit a non-Arrhenius behavior, particularly at lower temperature. For many ILs and DESs, the Vogel-Fulcher-Tammann (VFT)

equation has been used to describe the temperature dependence of viscosity more accurately than the Arrhenius model [45, 181–185]:

$$\eta = A \exp\left[\frac{B}{T - T_0}\right] \tag{2.7}$$

in which A, B and T_0 are constants, and T is the absolute temperature. The temperature dependent activation energies of viscosity, $E_a^{vis}(T)$, from the VFT equation are then computed as [186]:

$$E_a^{vis}(T) = BR\left[\frac{T}{T - T_0}\right]^2 \tag{2.8}$$

where T is the absolute temperature, R is the universal gas constant, and B and T_0 are the constants in Eq. 2.7, obtained from regression.

The Hildebrand solubility parameter can only be used for non-polar and weakly polar compounds without specific interactions like hydrogen bonding [187]. This is due to the fact that the cohesive energy density of a mixture of polar compounds can no longer be accurately estimated using the geometric mean of the cohesive energy densities of the individual components [187]. In 1967, Hansen extended the work of Hildebrand, and introduced a solubility parameter which accounts for contributions from various interactions [153]:

$$\delta_t^2 = \delta_d^2 + \delta_p^2 + \delta_h^2 \tag{2.9}$$

where δ_d, δ_p, and δ_h, are the contributions from dispersion (van der Waals) interactions, polar (dipole-dipole) interactions, and hydrogen bonding, respectively, and δ_t denotes the total Hansen solubility parameter. The dispersion contribution is expected to be significant for non-polar solvents, whereas the polar component is larger for molecules with larger dipole moments. The hydrogen bonding term is used when hydrogen bonds exist between molecules in the system. In that case, dipole-dipole and dispersion forces are not sufficient to describe the overall polarity of molecules. The miscibility of two (polar or non-polar) compounds is quantified by computing the differences of the corresponding Hansen components (distances in the 3-dimensional 'Hansen space') of the compounds. Compounds with similar values for the components of the Hansen solubility parameter (small distances in Hansen space) are more likely to be miscible, while with dissimilar values of the Hansen components (large distances in Hansen space),

the two compounds are less likely to be mutually soluble [188, 189]. Therefore, the knowledge of these solubility parameters can be useful for selecting solvents for certain applications. It is important to note that it is experimentally challenging to measure the polarity or (Hansen) solubility parameters, especially for non-volatile solvents. The ability of solvents to dissolve solutes is often experimentally measured by means of solvatochromic parameters, which are correlated with the hypsochromic (blue) or bathochromic (red) shift of the UV-vis spectra of certain probe molecules (dyes) as a function of the solvent polarity [190, 191]. The two most commonly used polarity scales are the Reichardt's dye scale (E_{T} parameter) [192, 193] and the Kamlet-Taft scale (π^*, α, and β parameters) [194–196]. The Kamlet-Taft equation relies on a linear solvation energy relationship given by [39]:

$$X = X_0 + s(\pi^* + d\delta^*) + a\alpha + b\beta \tag{2.10}$$

where X is a certain property of the solute (e.g., solubility, equilibrium constant, reaction rate, etc.) in a given solvent, X_0 is the same property in a reference state, π^* is the dipolarity/polarizability of the solvent, δ^* is a polarizability correction term, α and β are measures for the hydrogen bond donating and hydrogen bond accepting capabilities of the solvent, and a, b, d, and s are constants. Experimental measurements of E_{T} or Kamlet-Taft parameters are time-consuming, and proper probe molecules should be very carefully chosen to avoid solubility and stability problems [34, 197].

Due to the large number of possible DESs and limited experimental polarity data, it is not straightforward to select the best candidates for a specific application. In screening studies, it is often sufficient to have a rough estimate of the polarity of a solvent. Hence, molecular simulation can be a powerful tool to investigate the polarity of a solvent by the computation of the dispersion, polar, and hydrogen bonding contributions to the solubility parameter. MD simulations have indeed been used to compute the solubility parameters of ILs, organic solvents, pharmaceuticals, and polymers [188, 198–203]. Here, MD simulations were performed to compute the Hildebrand and Hansen solubility parameters of ChClU, ChClG, ChClEg, ChClMa, and ChClOa DESs (listed in Table 1.1). In Section 2.2, simulations details and computational methods are outlined. In Section 2.3, the MD simulation results are presented, and compared with available experimental data and/or correlations. Finally, in Section 2.4, conclusions are provided regarding the estimation of the solubility parameters of non-volatile solvent mixtures, such as DESs.

2.2 Computational details

The force field parameters developed by Doherty and Acevedo [59], based on the OPLS force field [154], were used for all DESs. For comparison, the General Amber Force Field (GAFF) [155] parameters, reported by Perkins et al. [61, 121], were also used for ChClU. Both force fields are all-atom and non-polarizable, and include non-bonded Lennard-Jones (LJ) and electrostatic interactions, as well as bonded interactions, i.e., bond-stretching, bond-bending, torsions, and improper torsions. The 1-4 intramolecular interaction energies were scaled according to the GAFF [155, 204] (0.5 for LJ interactions and 0.833 for electrostatic interactions) and OPLS (0.5 for both the LJ and electrostatic interactions) force fields. To take the effective polarization into account, the ionic charges were scaled by 0.8 [59, 61]. The charge scaling approach is often used in the simulations of ILs and DESs, as it yields a better agreement between the simulation results and experimental data [59, 61, 145]. The intramolecular exclusion terms between the hydrogen and oxygen atoms of the hydroxyl groups in ethylene glycol, glycerol, oxalic acid and malonic acid were not considered in the simulations. It was found from test simulations that the omission of these interactions has negligible effects on the density (below 1 % relative difference) and the RDFs of the corresponding DESs, compared to the computed densities and RDFs in the original publications [59, 61]. These interactions are not expected to affect the computed solubility parameters, as the average non-bonded intramolecular energies cancel out in Eq. 2.1. To prevent atomic overlaps, the LJ parameters $\epsilon = 0.001\,\mathrm{kcal\,mol^{-1}}$ and $\sigma = 0.1\,\text{Å}$ were set for unprotected hydrogen atoms in the hydroxyl groups of the DES [205]. The force field parameters of all the molecules are provided in Tables A1 to A16 and A21 to A36 of the Appendix. The molecular structures of the components (except for the chloride anion) of all DESs are shown in Figs. A1 to A6 of the Appendix. The particle-particle particle-mesh (PPPM) method, with a relative error of 10^{-5}, was used to compute the long-range electrostatic energies. Cutoff radii of 12 Å and 40 Å were used in the condensed and gas phase simulations, respectively, for both LJ and short-range electrostatic energies. The LJ potential was truncated and shifted at the cutoff radius, and in the liquid phase simulations, analytic tail corrections [70] were used. The Lorentz-Berthelot (arithmetic) and Jorgensen (geometric) mixing rules [70] were used to compute the LJ interactions of non-identical atom types for the GAFF and OPLS force fields, respectively.

The solubility parameters of the DESs were computed using Eq. 2.1. It is important to note that Eq. 2.1 can be straightforwardly used for

pure compounds, whereas it is not well-defined for mixtures (e.g., DESs). This is due to the fact that the mixture components may have different vaporization energies (particularly in non-ideal mixtures, such as DESs), and thus, it is not clear which vaporization energy must be used in Eq. 2.1 (i.e., the average vaporization energy or the vaporization energies of specific components). Therefore, the solubility parameters of mixtures are often determined from solubility measurements [206], correlations with other physical properties of the mixture [171, 173], or mixing rules [187, 207]. If the dissolution of a solute in the solvent mixture (i.e., the polarity of the solvent) is largely determined by intermolecular interactions with specific components of the mixture (e.g., through hydrogen bonding), it may be more appropriate to consider the vaporization energy (and the corresponding solubility parameter) of that component. However, this information may not be available a priori. Therefore, the average vaporization energy of the mixture components may be used as an alternative to determine the polarity (i.e., the solubility parameter) of a solvent mixture. Here, the solubility parameters of the DESs were computed based on a pseudo-pure compound approach, where each DES was assumed to be a pure compound composed of 'DES clusters'. For each DES with an HBA:HBD molar ratio of n_1/n_2, a DES cluster was defined to be composed of n_1 HBA molecules and n_2 HBD molecules (i.e., the smallest unit of the pseudo-pure DES). The assumption of DESs as pseudo-pure compounds has been extensively used in perturbed-chain SAFT (PC-SAFT) modeling studies [22, 26, 60, 129, 208, 209]. The pseudo-pure compound approach clearly allows for the use of Eq. 2.1, where DES clusters are assumed to be the vaporizing entities. The computed solubility parameter of each DES would then represent an average intermolecular energy per unit of volume (the interaction of a cluster with its surrounding), and may be used for a rough estimation of the solubilities of different compounds in DESs.

Assuming total vaporization of the liquid phase, the molar energy of vaporization of each DES, ΔE^{vap}, was computed from the MD simulations according to:

$$\Delta E^{\text{vap}} = N_{\text{A}} \frac{\left\langle \sum_{i=1}^{N} E_i^{\text{v}} - E^{\text{l}} \right\rangle}{N} \tag{2.11}$$

where N_{A} is the Avogadro's number, the brackets $\langle ... \rangle$ denote an ensemble average, N is the total number of molecules of the vaporizing entity (i.e., DES clusters) in the liquid (condensed) phase, the summation runs over all molecules i of the vaporizing entity in the gas phase, E_i^{v} is the energy of an individual entity in the vapor phase (assuming ideal gas phase), and

E^{l} is the total energy of the condensed phase. For each DES, liquid phase simulations were performed in the isobaric-isothermal (NPT) ensemble at various temperatures (298 K to 358 K) and 1 atm, using three independent runs with different randomly generated initial configurations. Depending on the DES and temperature, equilibration times of 50 ns to 300 ns were used. After reaching equilibrium, production runs of up to 100 ns were performed to compute the various energy components for each system. 50 HBA ion pairs were used in the simulations, and the number of the HBD molecules was adjusted according to the HBA:HBD molar ratio of each DES (Table 1.1). The average energies of the ideal gas phase were obtained by performing simulations in the canonical (NVT) ensemble for a single isolated DES cluster, at the same temperature as in the corresponding liquid phase simulation, and multiplying the resulting energies by the number of clusters in the liquid phase (according to the summation in Eq. 2.11). From the final configuration of each liquid phase simulation, three DES clusters were randomly selected as initial configurations for the gas phase simulations, and the results were subsequently averaged over all the independent runs. In all gas phase simulations, the box size was set to 200 Å to ensure that the interactions between the cluster and its periodic images are negligible. The gas phase DES clusters were equilibrated for 0.5 ns, and the average energies were computed from production runs of 1 ns. The velocity Verlet algorithm [69, 210, 211] was used to integrate Newton's equations of motion. A timestep of 1 fs was used in the condensed phase simulations. For the gas phase simulations, the timestep size was reduced to 0.1 fs to avoid the disintegration of the clusters. Therefore, during the gas phase simulations, the DES components stayed close to each other, keeping the clusters intact. The Nosé-Hoover thermostat and barostat [69] were used to impose the temperature and pressure. All simulations were performed with the LAMMPS software [110] (version 16 Feb. 2016), and initial configurations for the liquid phase simulations were generated using PACKMOL [212].

The currently available force fields for DESs, including those used here, do not have an explicit hydrogen bond term, which means that the polar and hydrogen bond contributions to the Hansen solubility parameter cannot be obtained separately. Therefore, the polar and hydrogen bond contributions were combined into a single electrostatic term, δ_{e}, as [201, 213, 214]:

$$\delta_{\mathrm{e}} = \sqrt{\delta_{\mathrm{p}}^2 + \delta_{\mathrm{h}}^2} \tag{2.12}$$

The Hansen solubility parameters were calculated from the average potential energies of the condensed phase simulations and the energies of individual molecules in the gas phase, according to [188]:

$$\delta_k^2 = \left(\frac{\left\langle \sum_{i=1}^{N} E_i^{k,\mathrm{v}} - E_i^{k,\mathrm{l}} \right\rangle}{\langle V^{\mathrm{l}} \rangle} \right) \tag{2.13}$$

where k are the components of the Hansen solubility parameter and potential energy (k = d for dispersion, and k = (p + h) = e for electrostatic), the brackets $\langle ... \rangle$ denote an ensemble average, the summation runs over all molecules i of the vaporizing entity in the gas phase, N is the total number of molecules of the vaporizing entity in the liquid phase, and V^{l} is the volume of the liquid phase simulation box. Unlike the Hildebrand solubility parameter, the total Hansen solubility parameter does not account for the bonded interactions, and only contains contributions from non-bonded dispersion and electrostatic interactions. Therefore, it is expected that the computed values of these two quantities will slightly differ [188]. The Hansen solubility parameters were computed from the same condensed phase and ideal gas simulations as for computing the Hildebrand solubility parameters, where in addition to the total potential energy of the system, the contributions from the electrostatic and dispersion forces were also obtained (Eq. 2.13).

It is important to note that little is known about the composition and configuration (e.g., neutral molecules, ion pairs, DES clusters) of the vapor phases of hydrophilic DESs, including those studied in this chapter. Recently, Dietz et al. [42] measured the vapor pressures of six hydrophobic DESs, as well as the partial pressures of the individual components of these DESs. From the experimental results, it was found that the vapor phase of the studied hydrophobic DESs was largely dominated by the most volatile component (either the HBD or the HBA). Dietz et al. [42] reported larger vapor pressures for the studied DESs compared to the vapor pressures of most ILs. This was associated with the ability of the DES components to separately evaporate from the mixture, whereas the vaporization in ionic liquids only occurs for ion pairs. Here, to represent the average intermolecular interactions of the DESs, the solubility parameters were computed for DES clusters, i.e., assuming that DES clusters are the vaporizing entities. The validity of this assumption was evaluated by computing the vaporization energies of the individual HBD and HBA components of each DES, and comparing the computed values to those of DES clusters. It has

been shown in several studies that the vapor phase of ILs mainly consists of charge neutral ion pairs with one cation and one anion (and no larger clusters) [156, 215–219]. Therefore, the HBA component of each DES in the vapor phase simulations was assumed to consist of an isolated ion pair. The vapor pressure and vapor phase composition of DESs as a function of temperature and liquid phase composition are studied further in chapter 4 of this thesis.

To compute the energy of vaporization for each DES component i (e.g., the HBD), the energy of the liquid phase was obtained before, i.e., $E^{\mathrm{l}}(N_i)$ (N_i denotes the number of the molecules of component i), and after removing one molecule, i.e., $E^{\mathrm{l}}(N_i - 1)$, of this component from the liquid mixture. The energy of a single molecule of each component (the HBD or the HBA) in the vapor phase (ideal gas) was also computed ($E^{\mathrm{v}}(1)$). The molar energy of vaporization was then computed using the following equation:

$$\Delta E^{\mathrm{vap}} = N_{\mathrm{A}} \left\langle E^{\mathrm{l}}(N_i - 1) + E^{\mathrm{v}}(1) - E^{\mathrm{l}}(N_i) \right\rangle \tag{2.14}$$

Based on this energy of vaporization, the Hildebrand solubility parameter was also computed from Eq. 2.1 for each component of the DESs. Two kinds of heat of vaporization are typically defined for mixtures: integral and differential [220]. The integral heat of vaporization corresponds to the total vaporization of the liquid phase, expressed per mole of the mixture. The differential heat of vaporization corresponds to the vaporization of one mole of the mixture from such amount of liquid that the composition of the liquid phase is not changed. Therefore, the vaporization energy of DES clusters, computed from Eq. 2.11, is related to the integral heat of vaporization. The vaporization energy computed from Eq. 2.14 does not describe either of the two heats of vaporization, as it assumes partial vaporization of the mixture, while the liquid phase composition changes.

2.3 Results and discussion

2.3.1 Solubility parameters from vaporization energies

The (experimental) energies and enthalpies of vaporization of the DESs were calculated by fitting Eq. 2.2 to the experimental vapor pressure data by Shahbaz et al. [51], and Ravula et al. [50], which were measured at elevated temperatures (45 −95 °C and 40 −160 °C, respectively) using thermogravimetric analysis (TGA). The vaporization enthalpies obtained from the experimental data were assumed to be independent of temperature, and

thus accurate for lower temperatures. A minimum value of the correlation coefficient (R^2) of 0.9831 from the regression of the vapor pressure data indicated that for all the DESs, the vapor pressure-temperature relationship can be well described by Eq. 2.2. The Clausius-Clapeyron equation (Eq. 2.2) is derived on the basis of the equality of chemical potentials of the vaporizing entity in liquid and vapor phases, when temperature and pressure are changed. This equation is frequently used for modeling vapor-liquid phase equilibria of pure compounds, although it can also be applied to mixtures [221]. The enthalpy of vaporization computed from this equation, applied to mixtures, is an average of vaporization enthalpies of the mixture components according to the vapor phase composition. The vapor phase compositions of the DESs studied here have not yet been measured. Therefore, the experimental vaporization enthalpies obtained from Eq. 2.2 can provide useful insight into the vapor phase compositions of the DESs, when compared with the simulation results. In chapter 4, the vapor phase compositions of ChClU and ChClEg will be rigorously computed from MC simulations and thermodynamic integration.

The enthalpies of vaporization and Hildebrand solubility parameters, as well as the total Hansen solubility parameters, and the individual contributions to the Hansen solubility parameters, computed from the MD simulations, are presented in Table 2.1 for all DESs at 298 K. The vaporization enthalpies from the experimental vapor pressure data are also listed in the table. No experimental data were found for the vapor pressures or enthalpies of vaporization of neat ChClMa and ChClOa. The computed enthalpies of vaporization from MD are based on the vaporization of DES clusters, and thus have the units of kJ per mole of DES cluster. However, in literature, molar masses and molar volumes of DESs are often implicitly reported based on '1 mole of DES', with an HBA:HBD molar ratio of n_1/n_2, defined by:

$$1\ [\text{mol DES}] = \frac{n_1}{n_1+n_2}[\text{mol HBA}] + \frac{n_2}{n_1+n_2}[\text{mol HBD}] \tag{2.15}$$

With this definition, 1 mole of DES cluster (composed of n_1 moles of the HBA and n_2 moles of the HBD) needs to be considered as:

$$1\ [\text{mol DES cluster}] = (n_1+n_2)\,[\text{mol DES}] \tag{2.16}$$

To allow for comparison with experimental molar volumes in literature, the computed molar volumes in Table 2.1 are reported in units of cm^3

Table 2.1: Computed molar volumes, enthalpies of vaporization, and solubility parameters of DESs at 298 K and 1 atm from MD simulations. The Hildebrand solubility parameters, as well as the total Hansen solubility parameters and the various contributions (dispersion and electrostatic) to the Hansen solubility parameters are listed. The computed molar volumes and enthalpies of vaporization from MD are in units of cm^3 per mole of DES and kJ per mole of DES cluster, respectively. The enthalpies of vaporization obtained from the experimental vapor pressure data by [51] (denoted by 'exp1'), and [50] (denoted by 'exp2') are also listed.

DES	force field	$V_\mathrm{m}/[\mathrm{cm}^3\,\mathrm{mol}^{-1}]$	$\delta_\mathrm{d}/[\mathrm{MPa}^{1/2}]$	$\delta_\mathrm{e}/[\mathrm{MPa}^{1/2}]$	$\delta_\mathrm{t}/[\mathrm{MPa}^{1/2}]$	$\delta_\mathrm{H}/[\mathrm{MPa}^{1/2}]$	$\Delta H^\mathrm{vap}_\mathrm{sim}/[\mathrm{kJ\,mol}^{-1}]$	$\Delta H^\mathrm{vap}_\mathrm{exp1}/[\mathrm{kJ\,mol}^{-1}]$	$\Delta H^\mathrm{vap}_\mathrm{exp2}/[\mathrm{kJ\,mol}^{-1}]$
ChClU	GAFF	71.1	18.5	24.9	31.1	30.5	201	46.9	79.0
ChClU	OPLS	75.2	21.8	23.1	31.8	31.6	228	46.9	79.0
ChClG	OPLS	90.8	24.9	19.3	31.5	31.0	265	67.7	70.9
ChClEg	OPLS	78.2	21.8	19.2	29.1	29.3	204	-	55.8
ChClMa	OPLS	99.0	26.4	24.3	35.9	35.6	253	-	-
ChClOa	OPLS	92.5	22.3	25.9	34.2	33.4	217	-	-

per moles of DES. It can be observed that the enthalpies of vaporization obtained from the experimental vapor pressure data of ChClU, ChClG, and ChClEg are considerably lower than the ones computed from MD simulations. This may be caused by a different experimental vapor phase composition of the DESs, compared to the one assumed in the MD simulations, where only DES clusters are present in the vapor phase. It can be observed that for ChClG, the enthalpy of vaporization from the experimental data by Ravula et al. [50] is comparable to the one from the data by Shahbaz et al. [51] for ChClG, while it is much larger in the case of ChClU. The computed enthalpies of vaporization from MD are larger than the enthalpies of vaporization found in literature for many ILs [156, 170, 176, 222–224].

The large values of the computed Hildebrand and Hansen solubility parameters suggest a highly polar nature for the studied DESs. The computed solubility parameters are larger than the ones reported for most ILs [156, 167, 169, 170, 172, 175, 223], indicating a larger polarity of the DESs compared to ILs (assuming DES clusters as the vaporizing entities). The differences between the computed total Hansen solubility parameters and the Hildebrand solubility parameters fall within the uncertainty ranges, i.e., standard deviations (0.27-0.57 $MPa^{1/2}$). The observed slight differences between the average values of these quantities are expected due to the exclusion of bonded interactions in the Hansen solubility parameter formulation [188]. The effects of dipole-dipole interactions and hydrogen bonding are lumped into the electrostatic component of the Hansen solubility parameter, as the force field used in this chapter do not have separate hydrogen bonding terms. While ChClU and ChClOa exhibit a larger contribution of electrostatic forces to the total Hansen solubility parameter, compared to dispersion forces, the other considered DESs show the opposite. For ChClU, both the OPLS and GAFF force fields result in a larger electrostatics component of the Hansen solubility parameter, compared to the dispersion component. This comparison implies a higher importance of dipole-dipole/hydrogen bonding interactions in ChClU and ChClOa, needed to be overcome for vaporization, compared to the other DESs. Nevertheless, for all DESs, both the computed electrostatic and dispersion components of the Hansen solubility parameter are considerable. This indicates the complicated nature of the intermolecular interactions in these solvents, which consist of large contributions from both the dispersion and electrostatic (hydrogen bonding and dipole-dipole) forces. The two force fields used for ChClU resulted in only slight differences in the computed Hildebrand and total Hansen solubility parameters. Since the HBA is the same for

all the DESs, the differences in the computed solubility parameters can be attributed to the influence of the HBDs on the intermolecular interactions of the DES clusters. Considering the Hildebrand solubility parameter, it can be observed that the DESs containing HBDs with carboxylic acid functional groups (ChClMa and ChClOa) show the highest polarity, followed by ChClU (with an amide group), and ChClG and ChClEg (with hydroxyl groups). The electrostatic contribution to the Hansen solubility parameter indicates a stronger dipolarity/hydrogen bonding for ChClOa, ChClMa and ChClU, compared to ChClG and ChClEg with alcohol-based HBDs.

Pandey et al. [34] investigated the polarity of DESs using absorbance and fluorescence solvatochromic probes, and indeed found high polarities for ChClU, ChClEg, ChClG, and ChClMa (all with molar ratios of 1:2), compared to several common molecular solvents and ILs. Nevertheless, the relative polarities of these DESs with respect to each other was strongly dependent on the solvatochromic probe used in the experiments. Therefore, it is not possible to make a definitive comparison between the polarities obtained in the aforementioned work and the solubility parameters computed here. In another study, Pandey and Pandey [225] computed the Kamlet-Taft parameters of ChClU, ChClG, and ChClEg. The polarizability/dipolarity parameters (π^*) of the DESs were in the following order: ChClU > ChClG > ChClEg, in agreement with the relative magnitudes of the Hildebrand solubility parameters and the electrostatic components of the Hansen solubility parameter computed here (Table 2.1). Florindo et al. [226] also investigated the polarity of hydrophobic and hydrophilic DESs, using the betaine dye 33 response and Kamlet-Taft parameters. The polarizability/dipolarity of choline chloride-based DESs was shown to be very high compared to common organic solvents and ILs. The values of π^* for these DESs were in the following order: ChClU > ChClG > ChClMa > ChClEg.

Moganty and Baltus [169] showed that the solubility parameters of many ILs are insensitive to temperature. In other studies, only a slight decrease in the solubility parameters of ILs with temperature has been reported [169, 170, 172, 223]. To investigate the influence of temperature, the Hildebrand solubility parameters of the DESs were computed at different temperatures from MD simulations. The temperature dependence of the solubility parameters is shown in Fig. 2.1. It can be observed that within the error bars (i.e., standard deviations), the computed solubility parameters do not change as a function of temperature. Nevertheless, the average solubility parameters of ChClU, ChClG and ChClEg may suggest a slightly decrease with an increase in temperature. This decrease in the average solubility parameters was caused by an increase in the molar volumes of the DESs,

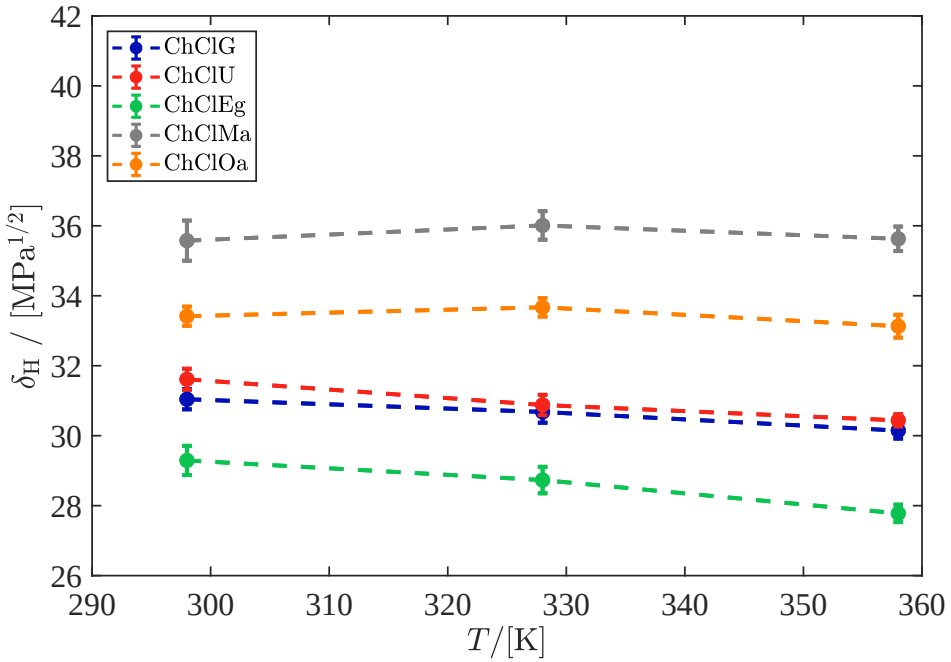

Figure 2.1: Computed Hildebrand solubility parameters of DESs, as a function of temperature (at 1 atm) from MD simulations, based on the vaporization of DES clusters.

accompanied by a slight decrease in the energies of vaporization. A similar insensitivity towards temperature was observed for the total Hansen solubility parameters, and the electrostatic and dispersion parts of the Hansen solubility parameters (not shown here). Consistently, it has been found that the solubilities of several compounds in DESs are not very sensitive to temperature [25, 26]. In the study by Pandey and Pandey [225], the Kamlet-Taft dipolarity/polarizability (π^*) and hydrogen bond basicity (β) parameters of choline chloride-based DESs were shown to negligibly change with temperature. The molar electronic transition energy of betaine dye (E_T) and the hydrogen bond acidity parameter (α), however, decreased with an increase in temperature. The responses of ANS and Prodan probes, contrary to the response of pyrene, indicated a weak temperature dependence of the polarities of the DESs, in agreement with the results in Fig. 2.1.

2.3.2 Vaporization of individual components

In the calculations of the Hildebrand and Hansen solubility parameters, the vaporizing entities of the DESs were considered to be clusters composed of the HBD and HBA molecules. However, it is likely that the gas phase is

not entirely composed of DES clusters. The vapor pressure and enthalpy of vaporization of a DES are strongly affected by the strength of intermolecular interactions within the liquid mixture. The component that is less 'bound' to the system, can more easily escape into the vapor phase during the evaporation process. It is important to investigate which components of the DESs have lower vaporization enthalpies, and thus dominate the vapor phase. Therefore, the vaporization enthalpies of the HBD and HBA components in ChClU, ChClG, and ChClEg were computed using Eq. 2.14, and are listed in Table 2.2, along with those of DES clusters computed previously. The listed enthalpies of vaporization have the units of kJ per number of moles of the vaporizing entity. It can be observed that for all DESs, the computed average enthalpies of vaporization of the HBD components are considerably smaller than those of the HBA components and DES clusters. This indicates that it is more likely for HBD molecules to escape from the condensed phase into the vapor phase. Therefore, the vapor phases of the DESs are likely dominated by the HBD molecules. It can be observed that the computed vaporization enthalpies of the HBDs are closer to the experimental vaporization enthalpies obtained using the Clausius-Clapeyron equation (Table 2.1). This further indicates the vaporization of the HBD molecules prior to other components.

The results in Table 2.2 are consistent with the observations by Dietz et al. [42], where the more volatile components dominated the vapor phases (with vapor phase mole fractions of 0.85 to 1.00) of the studied hydrophobic DESs. It is interesting that while the vaporization enthalpies of the HBD components are lower than those of most ILs, the computed vaporization enthalpies of the HBA components (i.e., choline chloride salt) have a similar magnitude to the vaporization enthalpies of ILs reported in literature [156, 170, 176, 222, 223]. It can be observed that the OPLS and GAFF force fields result in different average vaporization enthalpies for the HBD (urea) component of ChClU, despite an overlap of the uncertainty ranges (ca. $12\,\mathrm{kJ\,mol^{-1}}$ and $15\,\mathrm{kJ\,mol^{-1}}$, respectively). By comparing the two values with the experimental enthalpies, and based on the assumption of vaporization of the HBD component from the mixture, the OPLS force field leads to a more accurate value for the vaporization enthalpy of ChClU. The computed vaporization enthalpies of the HBD components glycerol and ethylene glycol (in ChClG and ChClEg, respectively) are comparable to the experimental vaporization enthalpies of these compounds in pure form ($81\,\mathrm{kJ\,mol^{-1}}$ and ca. $58\,\mathrm{kJ\,mol^{-1}}$ for glycerol [227] and ethylene glycol [228], respectively). This indicates a similar magnitude for the intermolecular

Table 2.2: Computed enthalpies of vaporization and Hildebrand solubility parameters from MD simulations at 298 K and 1 atm, based on various vaporizing entities, i.e., the HBD, HBA, and DES clusters. The solubility parameters are computed based on the molar volume of the vaporizing species in the liquid phase of each DES.

DES	force field	$\Delta H^{\mathrm{vap}}_{\mathrm{HBD}}/[\mathrm{kJ\,mol^{-1}}]$	$\Delta H^{\mathrm{vap}}_{\mathrm{HBA}}/[\mathrm{kJ\,mol^{-1}}]$	$\Delta H^{\mathrm{vap}}_{\mathrm{cluster}}/[\mathrm{kJ\,mol^{-1}}]$	$\delta_{\mathrm{H}}^{\mathrm{HBD}}/[\mathrm{MPa}^{1/2}]$	$\delta_{\mathrm{H}}^{\mathrm{HBA}}/[\mathrm{MPa}^{1/2}]$	$\delta_{\mathrm{H}}^{\mathrm{cluster}}/[\mathrm{MPa}^{1/2}]$
ChClU	GAFF	107	153	201	31.2	26.6	30.5
ChClU	OPLS	82	165	228	26.5	26.8	31.6
ChClG	OPLS	100	148	265	26.8	23.1	31.0
ChClEg	OPLS	73	175	204	24.5	27.1	29.3

interactions of these molecules in pure form to those in the DES mixtures (ideal behavior).

The computed Hildebrand solubility parameters are also listed in Table 2.2 based the vaporization of the various components. It can be observed that the computed solubility parameters based on the vaporization of the HBD and HBA components are generally smaller than those based on the vaporization of DES clusters. The computed solubility parameters for the vaporization of both the HBD and HBA components are similar to the solubility parameters of ILs [156, 167, 169, 170, 172, 175, 223]. The relative magnitudes of the computed solubility parameters of the DESs depend on the considered vaporizing species. For instance, the vaporization of the HBD component of ChClG results in a larger solubility parameter compared to ChCEg, while based on the vaporization of the HBA component, ChClEg has a larger solubility parameter compared to ChClG. At this point, no clear relationship can be established between the computed solubility parameters based on the vaporization of the various components ($\delta_{\mathrm{H}}^{\mathrm{HBD}}$, $\delta_{\mathrm{H}}^{\mathrm{HBA}}$, and $\delta_{\mathrm{H}}^{\mathrm{cluster}}$). It would be interesting to investigate whether such relationship can provide useful information about the non-ideality of the mixtures.

2.3.3 Correlations with other DES properties

Following the approach of Moganty and Baltus [169] for ILs, to obtain the proportionality constant in Eq. 2.5 for DESs, the energies of vaporization (using the OPLS force field) are plotted in Fig. 2.2 as a function of the activation energies of viscosity. In this figure, the vaporization energies of the DES clusters and HBD components from the MD simulations, as well as the vaporization energies obtained from the experimental vapor pressure data are used. The activation energies of viscosity were taken from experimental studies [33, 36, 42, 45, 181, 185, 226, 229–232]. In those studies, both the VFT and Arrhenius modeling approaches have been used to obtain the activation energies of viscosity. Although a perfect correlation between the two quantities is not observed in Fig. 2.2, the data are concentrated within specific regions of the plot. The vaporization energies of the DES clusters are scattered around the line $y = 4.41\,x$. Thus, the value of the constant in Eq. 2.5 is obtained as 4.41 for DES clusters, which is close to the values reported in literature for ILs (ca. 4.3 [169]). The experimental vaporization energies and the vaporization energies of the HBDs from MD, show smaller proportionality constants, i.e., 1.48 and 1.69, respectively. To construct a more precise correlation between the two quantities in Fig. 2.2, a larger number of experimental and simulation data is required.

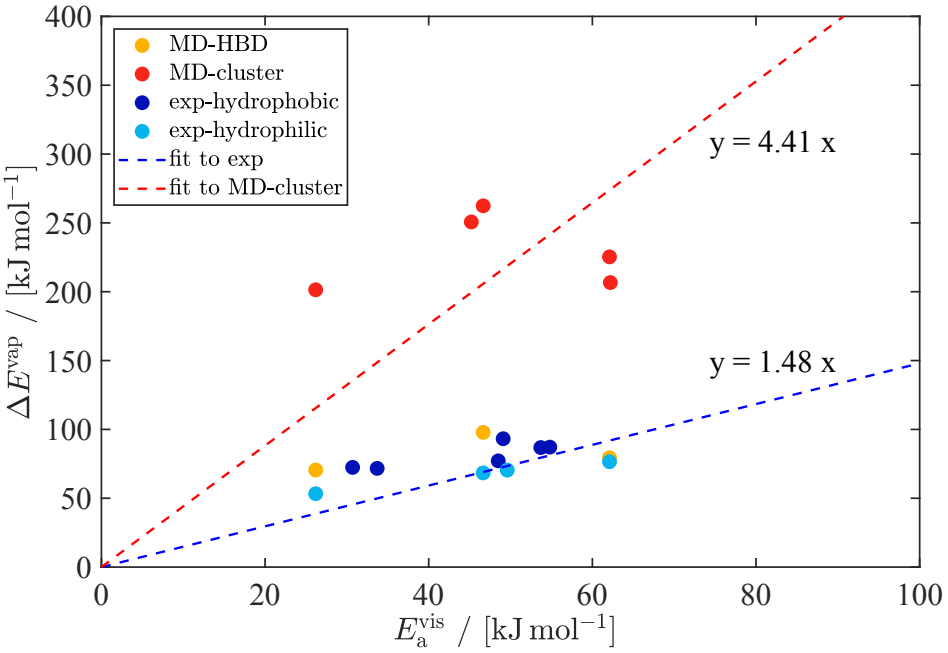

Figure 2.2: Vaporization energies of DES clusters (red circles) and HBD components (orange circles) from MD simulations at 298 K and 1 atm, and experimental vaporization energies [42, 50, 51] (light blue for hydrophilic, and dark blue for hydrophobic DESs), as a function of the experimental activation energies of viscosity of the DESs. The linear fits to the vaporization energies of DES clusters from MD, and the experimental vaporization energies, are denoted by the red and blue dashed lines, respectively.

The Hildebrand solubility parameters of the DESs were correlated with the surface tensions using Eq. 2.3. However, instead of the molar volume, V_{m}, the molecular volume, $V_{\mathrm{mol}} = V_{\mathrm{m}}/N_{\mathrm{A}}$ (N_{A} is the Avogadro's number), was used. The parameter $\gamma V_{\mathrm{mol}}^{-1/3}$ (γ is the surface tension with air) is referred to as the Gordon parameter (G) [156]. Experimental densities [33, 35, 36, 45, 181, 229–231, 233–239] and surface tensions [6, 33, 37, 232, 240] from literature were used to determine the Gordon parameters of the DESs. No surface tension data were found from literature for ChClOa. The computed cohesive energy densities (the squares of the Hildebrand solubility parameters) from MD are shown in Fig. 2.3 as a function of the experimental Gordon parameters of the DESs, for the vaporization of DES clusters and HBDs. The cohesive energy densities and Gordon parameters were both computed based on 1 mole of the vaporizing component. It can be observed that the cohesive energy densities computed for the vaporization of both the HBD components and DES clusters are highly correlated with the Gordon

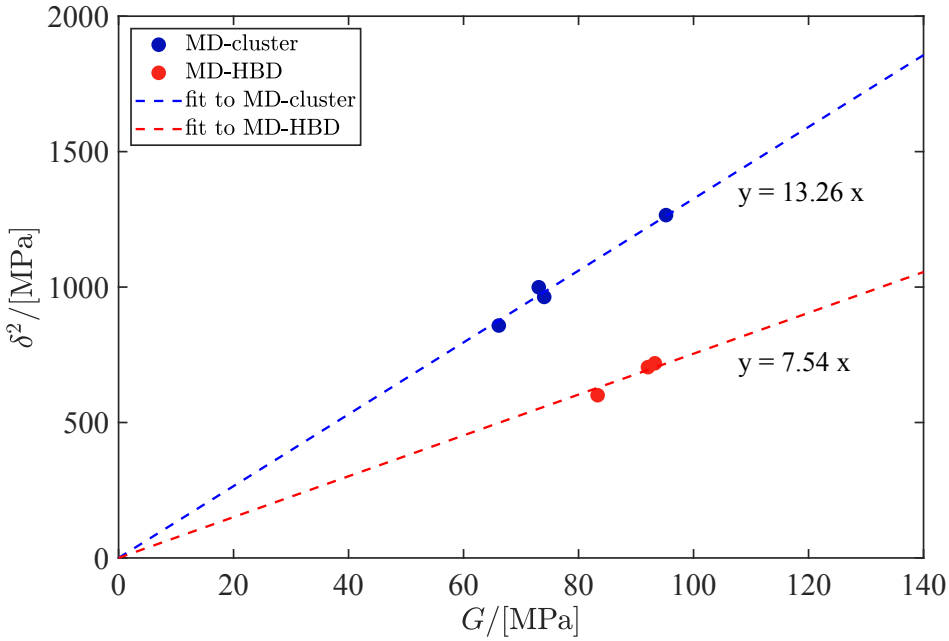

Figure 2.3: Computed cohesive energy densities (the squares of the solubility parameters) from MD simulations at 298 K and 1 atm, as a function of the experimental Gordon parameter ($\gamma V_{\mathrm{mol}}^{-1/3}$) for various DESs. The symbols denote the computed data, and the dashed lines represent the linear fits to the data. The data points based on the vaporization of DES clusters and HBD components are shown with blue and red colors, respectively.

parameters (R^2 values of 0.87 and 0.98, respectively). The linear regression of the data for the vaporization of DES clusters leads to a value of 13.26 for the constant parameter in Eq. 2.3, which is comparable to the values reported for ILs in literature (ca. 11 [156]). This parameter is computed as 7.54 for the vaporization of the HBD components. Similar to the correlation in Fig. 2.2, a larger number of data is required to establish more precise correlations between the solubility parameters and the Gordon parameters of DESs.

2.4 Conclusions

The Hildebrand and Hansen (dispersion and electrostatic components) solubility parameters were computed for five DESs from MD simulations, considering the HBD, HBA or DES clusters as the vaporizing entities. Relatively large solubility parameters were obtained, indicating that the studied DESs are polar solvents. The larger electrostatic components of the Hansen

solubility parameter suggested a stronger dipolarity/hydrogen bonding for the carboxylic acid-containing DESs. The relative importance of the electrostatic and dispersion components were different for different DESs. For ChClU and ChClOa, the electrostatic contribution was larger, while for the other DESs, the dispersion component played a more important role. The computed solubility parameters were relatively insensitive to temperature. The enthalpies of vaporization of the various DES components, i.e., HBD, HBA, and DES clusters, were computed. For comparison, experimental enthalpies of vaporization were obtained by fitting the vapor pressure data from literature to the Clausius-Clapeyron relation. The smaller vaporization enthalpies of the HBD components (also closer to experimental enthalpies) strongly suggested that the HBD molecules are more likely to vaporize prior to the other species from the mixture. The GAFF and OPLS force fields resulted in slightly different average vaporization enthalpies and solubility parameters. The computed solubility parameters of the DESs based on the vaporization of DES clusters were larger than those of common ILs reported in literature, whereas the solubility parameters computed based on the vaporization of the HBD or HBA components were comparable to those of ILs. The vaporization energies of DES clusters and the HBD components were correlated with the experimental activation energies of viscosity of the DESs. The correlation indicated ratios $\Delta E^{\mathrm{vap}}/E_{\mathrm{a}}^{\mathrm{vis}}$ of 4.41 and 1.69 between the two quantities, for the vaporization of DES clusters and HBDs, respectively. The former value is close to the value reported in literature for ILs (ca. 4.3). The correlation between the cohesive energy density of the DESs and the experimental Gordon parameter suggested ratios of 13.26 and 7.54 between the two parameters, for the vaporization of DES clusters and HBDs, respectively. The former value is close to the one reported in literature for ILs (ca. 11). To establish more precise correlations, more experimental and simulation data are necessary. The results of this chapter show how powerful MD simulations are for computing and predicting the enthalpies of vaporization and solubility parameters of non-volatile compounds, such as DESs, when experimental data are lacking. The estimations provided here for the solubility parameters can be used in screening studies that are based on polarities of DESs.

Chapter 3

Solubilities of CO_2, H_2S, CH_4, CO, H_2, and N_2 in deep eutectic solvents

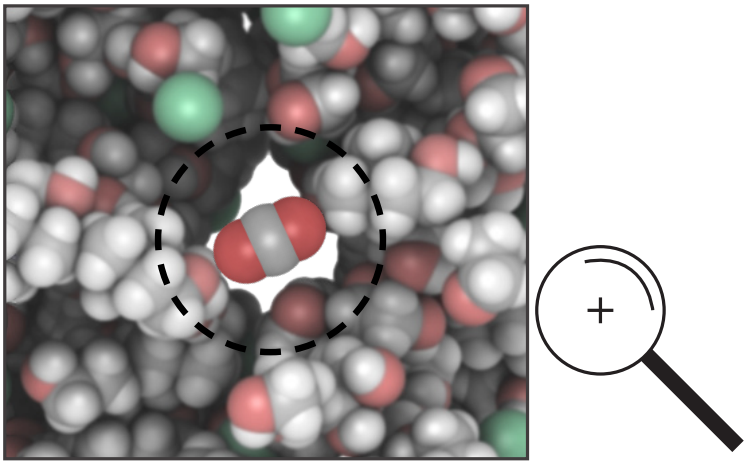

This chapter is based on the following paper: H.S. Salehi, R. Hens, O.A. Moultos, T.J.H. Vlugt, Computation of gas solubilities in choline chloride urea and choline chloride ethylene glycol deep eutectic solvents using Monte Carlo simulations, *Journal of Molecular Liquids*, **2020**, 316, 113729.

3.1 Introduction

The solubility parameters computed in chapter 2 can provide rough estimates for the solubilities of various compounds in DESs, and can therefore be used in screening studies. For the design or selection of an optimal solvent for a specific application, such as carbon capture, however, the precise knowledge of the solubilities (e.g., the Henry coefficient or absorption loading) is crucial. The solubility measurement data for DESs in literature are mostly limited to CO_2 and SO_2, while very limited data are available for sparingly soluble gases, such as CH_4 and CO. Furthermore, the reported experimental solubilities from different sources are in some cases inconsistent. For instance, the mole fraction-based Henry coefficient of CO_2 in ChClU has been reported as ca. 57 MPa (5 MPa molality-based) at 328 K by Mirza et al. [53], while several other studies have published values in a range of 16 MPa to 20 MPa [40, 52, 157, 241]. This inconsistency may be due to differences in the experimental methods and conditions used by the various research groups. Notably, a variety of pressure ranges were used for these solubility measurements, e.g., 8.5 bar to 125 bar [241], 6 bar to 45 bar [157], 0.1 bar to 2 bar [52], 3 bar to 60 bar [40], and 0.4 bar to 1.5 bar [53]. It is possible that in some of the high pressure measurements of the absorption isotherm, the Henry regime was not reached. Furthermore, the water content of the DES varies between experimental studies. The presence of water in DESs may affect the intermolecular interactions and physical properties of DESs [29, 45, 181, 230, 242, 243]. Studies have suggested that the water content of a DES may behave as an antisolvent, and adversely influence the CO_2 solubility [233, 244]. Another example of the inconsistent solubilities in literature is the Henry coefficient of CH_4 in ChClU at 328 K, for which Liu et al. [52] reported a mole fraction-based value of 231 MPa (extrapolated value), while Xie et al. [157] obtained a value of 47 MPa. It is also possible that rather than differences in the measured solubilities, the inconsistency lies in the reporting of the data, e.g., by assuming different units and definitions, without clearly stating these assumptions. Due to the limited availability of experimental solubility data in literature for DESs, and the inconsistencies of the available data, molecular simulation may be considered as an alternative for these experiments.

MC simulations have been used as a reliable means for computing the solubility of solute molecules in a variety of solvents, including ILs [79, 245–251]. For instance, Ramdin et al. [245] used the CFCMC method to compute the solubilities of pre-combustion gases (CO_2, CO, N_2, CH_4, and H_2S) in the IL [bmim][Tf_2N], and suggested that the IL is suitable for

pre-combustion carbon capture, provided that the syngas is desulfurized prior to the capture process. Liu et al. [52] performed MC simulations for mixtures of ChClU with various solutes (H_2S, CO_2, and CH_4), and computed RDFs between atomic sites, in order to better comprehend the absorption mechanism of these solutes. However, the authors did not use MC simulations to directly calculate the phase equilibrium (solubility) of the solutes in the DES. In sharp contrast to MC simulations, several studies are available in literature that have used EoS and excess Gibbs energy modeling approaches to compute solubilities in DESs [22, 53, 60, 63–65, 157, 252–257]. Recently, Jahanbakhsh-Bonab [258] computed the solubilities and selectivities of various gases (CO_2, CH_4, C_2H_6, and H_2S) in the choline chloride-phenyl propionic acid DES (as a potential candidate for natural gas sweetening) by direct MD simulation of the vapor-liquid interface. The limited use of MC simulations for DESs is likely because of the strong intermolecular interactions, including hydrogen bonding, that result in a high viscosity of most common DESs, and may cause slow equilibration, difficult molecule insertions, and inefficient sampling of the phase-space.

In this chapter, MC simulations were performed to compute the solubilities of CO_2, H_2S, CH_4, CO, H_2, and N_2 molecules in ChClU and ChClEg with HBA:HBD molar ratios of 1:2, as well as the densities and RDFs of the neat (without the solutes) DESs. The CFCMC method [91] was used to enhance the equilibration and molecule insertions, and directly compute the excess chemical potential at infinite dilution, and thus the Henry coefficients of the gases in the DESs. Section 3.2 is devoted to the description of the simulations details, consisting of the force field parameters used for the various molecules, as well as the computational methods to obtain the densities and the Henry coefficients. In Section 3.3, the simulation results are discussed, and compared with the limited experimental data from literature. Finally, in Section 3.4, conclusions are provided regarding the MC simulations of DESs for solubility computations.

3.2 Computational details

The GAFF force field parameters [61, 121, 155], were used for ChClU and ChClEg. The force field parameters consisted of bonded interactions (bond-bending and torsion), and LJ and electrostatic non-bonded energies. The ionic (partial) charges were scaled by 0.8 and 0.9 for ChClU and ChClEg, respectively, to take effective polarization into account [61, 121]. The 1-4 intramolecular interaction energies were scaled by 0.5 and 0.833 for the LJ and electrostatics interactions [155, 204], respectively. To examine

the effect of force field on the computed solubilities, the OPLS force field [59, 154] was also used for ChClEg. This force field also comprised the aforementioned non-bonded and bonded terms. For the OPLS model, the ionic charges were scaled by 0.8 [59], and the 1-4 LJ and electrostatic intramolecular energies were scaled by 0.5 [154]. Using both force fields, the LJ parameters $\epsilon = 0.001\,\mathrm{kcal\,mol^{-1}}$ and $\sigma = 0.1\,\text{Å}$ were set for the unprotected hydrogen atoms of hydroxyl groups, in order to prevent atomic overlaps [205]. All bond lengths were kept fixed at the equilibrium distances during the simulations. The improper torsion potentials were not taken into account. MD test simulations showed that this had little effect on the density of ChClU using the GAFF force field, i.e., the density at 328 K was computed as $1.199\,\mathrm{kg\,m^{-3}}$ and $1.217\,\mathrm{kg\,m^{-3}}$, with and without the improper torsions, respectively (relative difference of ca. 1.5%). All solute molecules were modeled as rigid objects. The Transferable Potentials for Phase Equilibria (TraPPE) force field parameters were used for CO_2, CH_4 (united atom), N_2, and H_2S [259–261]. The two-site force field by Cracknell [262] was used for H_2, and the three-site model by Martín-Calvo et al. [263] was used for CO. The force field parameters of all the molecules are provided in Tables A1 to A12, A17 to A24, and A57 of the Appendix. The molecular structures of all solute gases (except for methane) and the components (except for the chloride anion) of all DESs are shown in Figs. A1 to A3 and A13 to A17 of the Appendix. Long-range electrostatic interactions were computed with the Ewald summation method [69, 264]. The Ewald parameters were set based on a relative precision of 10^{-6}. A cutoff radius of 10 Å was used for both LJ and short-range electrostatic interactions. For ChClU, the LJ potential was shifted at the cutoff radius, and no analytic tail corrections [70] were used, whereas for ChClEg, analytic tail corrections were used, but the LJ potential was not shifted. These choices regarding the shifting of the LJ potential and the use of analytic tail corrections were made to obtain a closer agreement between the computed densities of the DESs and the experimental densities reported in literature [36, 181, 235, 265]. To accurately compute the solubilities, however, analytic tail corrections were used for the solute molecules in both DESs, accounting for the long-range solvent-solute LJ interactions. The Lorentz-Berthelot and Jorgensen mixing rules [70] were applied to calculate the LJ interactions of non-identical atom types for the GAFF and OPLS models, respectively.

The densities of ChClU and ChClEg, as well as solubilities, i.e., Henry coefficients, of the gas molecules in these DESs were calculated from MC simulations in the *NPT* ensemble. The densities were computed at 1 bar and various temperatures (308 K-338 K). RDFs were computed for vari-

ous atom pairs of the DESs from the same simulations as for the density computation. The solubilities were calculated from a separate set of simulations at a temperature of 328 K and a hydrostatic pressure of 1 bar, in the *NPT* ensemble. 50 HBA and 100 HBD molecules were used for both DESs, corresponding to the HBA:HBD eutectic molar ratio of 1:2. Initial configurations were generated at a lower density, and the simulation box was compressed to the equilibrium density at the specified pressure and temperature. The equilibrium box size in these simulations was typically around 27 Å. After equilibration, average properties were computed from production runs. For each data point of the computed density, 10 independent simulations were run, each for 10^6 equilibration and 10^6 production cycles. The solubility simulations comprised 20 independent runs, for which up to 4×10^6 equilibration and 12×10^6 production cycles were used. For the calculation of solubilities, block averaging was performed, where the results of the production runs were divided into 4-7 blocks, depending on the system. For each block, the average Henry coefficient was computed from the 20 independent runs. The overall mean and standard deviation were then computed for these block averages. During each MC cycle, trial moves were performed with fixed probabilities to thermalize the system. The number of trial moves per MC cycle was set equal to the total number of molecules in the system. These trial moves included translations and rotations of the molecules, volume changes of the simulation box, and changes of the internal configurations of the molecules. The internal configurations of the molecules were altered using random changes in bond angles and dihedral angles. The maximum displacements of all the thermalization trial moves were adjusted to allow for 50% acceptance probabilities.

All simulations were carried out using the open-source MC code, Brick-CFCMC [81, 91, 112], which is developed in our group for phase and reaction equilibria, and is particularly optimized for high-density liquid phase simulations with difficult equilibration, as in the case of ILs and DESs. Brick-CFCMC applies a modified version of the CFCMC method [96–98] by Poursaeidesfahani et al. [91, 99, 100] for molecule insertions, that enables a direct computation of the excess chemical potentials (and Henry coefficients) of various molecules in the system. The CFCMC method was not used in the simulations performed for the computation of the densities and RDFs, and was only applied in the solubility simulations. In the CFCMC method, one or more extra molecules, referred to as 'fractional' molecules, are introduced to the system. All other molecules are referred to as 'whole' molecules. The interactions of a fractional molecule with other molecules are scaled by a coupling parameter, λ, which can have a value in the range $[0, 1]$; a value

of 0 means that the fractional molecule has no interactions with other molecules (ideal gas molecule) and a value of 1 indicates that the fractional molecule is fully interacting (whole molecule). The value of λ is changed in the course of the simulation by $\Delta\lambda$, essentially inflating or deflating the fractional molecule. The value of $\Delta\lambda$ is taken randomly from a uniform distribution in the range $[-\Delta\lambda_{\max}, \Delta\lambda_{\max}]$, where $\Delta\lambda_{\max}$ is fixed (here at 0.2) during the simulation. Two additional trial moves were performed in the simulations, next to thermalization and λ-change trial moves: (1) The fractional molecule was reinserted at a random position in the box, without changing the value of λ. (2) An identity change trial move was performed, where the fractional molecule was turned into a whole molecule and a randomly selected whole molecule of the same type was changed to a fractional molecule with the same previous value of λ.

The observed probability distribution of λ is generally non-uniform due to the free energy barriers encountered when the value of λ changes. Therefore, a biasing weight function, $W(\lambda)$, is constructed to overcome these free energy barriers and sample the λ-space with equal probability. The Boltzmann average of any observable A is then computed using [99]:

$$\langle A \rangle = \frac{\langle A \exp[-W(\lambda)] \rangle_{\text{biased}}}{\langle \exp[-W(\lambda)] \rangle_{\text{biased}}} \tag{3.1}$$

The Wang-Landau algorithm [266, 267] was used in the equilibration runs to construct an initial biasing weight function. The iterative scheme [98] was applied in between the consecutive production runs to further modify the weight function, and yield a more uniform observed probability distribution of λ. 1000 bins were used to obtain a histogram of the values of λ, and thus the probability of occurrence of each value. Two fractional molecules were used in each solubility simulation, i.e., one of the HBD and one of the solute gas. The fractional molecule of the HBD was used to enhance the equilibration of the system (by λ-change and identity change trial moves), while the fractional molecule of the solute was used to compute the solubility of the solute in the DES.

To increase the interactions of a fractional molecule from $\lambda = 0$ to $\lambda = 1$, first, the LJ interactions were linearly switched on until $\lambda = \lambda_{\text{switch}}$ (where λ_{switch} was set to 0.8), by using the scaling parameter λ_{LJ}. In this range of λ, the electrostatic interactions of the fractional molecule were switched off. In the range $\lambda = \lambda_{\text{switch}}$ to $\lambda = 1$, the electrostatic interactions were linearly switched on by using the scaling parameter λ_{el}, while the LJ interactions remained fully switched on. A similar procedure was used to reduce the

interactions of the fractional molecule from $\lambda = 1$ to $\lambda = 0$, where the electrostatic interactions were linearly scaled in the range $[\lambda_{\text{switch}}, 1]$ (while $\lambda_{\text{LJ}} = 0$), and the LJ interactions were linearly scaled in the range $[0, \lambda_{\text{switch}}]$ (while $\lambda_{\text{el}} = 1$). A similar but slightly different scaling scheme is used in chapter 4 of this thesis, see also Section 4.2. The intermolecular LJ energy, U_{LJ}, between interaction sites i and j was scaled according to a soft-core interaction potential [268, 269]:

$$U_{\text{LJ}}(r_{ij}) = 4\epsilon_{ij}\lambda_{\text{LJ}}\left[\left(\frac{1}{\alpha(1-\lambda_{\text{LJ}})^b + (r_{ij}/\sigma_{ij})^c}\right)^{12/c} - \left(\frac{1}{\alpha(1-\lambda_{\text{LJ}})^b + (r_{ij}/\sigma_{ij})^c}\right)^{6/c}\right] \tag{3.2}$$

where r_{ij} is the distance between i and j, σ_{ij} and ϵ_{ij} are the LJ parameters, and α, b and c are constants. The values of these constants are often set to $\alpha = 0.5$, $b = 2$, and $c = 6$ in CFCMC simulations [97, 99, 270, 271]. Here, the values for these parameters were set to $\alpha = 0.0025$, $b = 1$, and $c = 48$. This set of values has been shown to minimize the statistical variance of the derivative of the total energy with respect to λ, resulting in a more efficient sampling of λ-space [269, 272]. To scale the electrostatic interactions, each of the (partial) charges in the fractional molecules was multiplied by λ_{el}, and in the real-space and exclusion terms, the parameter r_{ij} was replaced by $r_{ij} + A(1 - \lambda_{\text{el}})$ (where A was set to 0.01 Å) to avoid singularities at small distances r_{ij} [81, 270]. The exact functional forms for the scaling of the electrostatic interactions, as well as the LJ tail corrections are provided in the Supporting Information of Ref. [81]. Only the intermolecular LJ and electrostatic interactions were scaled in the simulations, and no intramolecular interactions (bond-bending, torsion, LJ, and electrostatic energies) were scaled.

The molality-based Henry coefficient of solute i, $K^{\text{m}}_{\text{H},i}$, is defined as [257, 273, 274]:

$$K^{\text{m}}_{\text{H},i} = \lim_{f_i \to 0} \frac{f_i}{m_i/m_0} \tag{3.3}$$

in which f_i is the fugacity of the solute molecule in the gas phase, m_i is the molality of the solute in the solution (in $\text{mol}\,\text{kg}^{-1}$), and m_0 is set to $1\,\text{mol}\,\text{kg}^{-1}$. The unit of the Henry coefficient in Eq. 3.3 is therefore the same as the unit for fugacity, e.g., MPa. A large Henry coefficient indicates a low solubility of the solute. The fugacity of solute i is the product of its

fugacity coefficient, ϕ_i, and the total pressure, P. At low pressures, such as the pressure used in the solubility simulations (1 bar), $\phi_i \to 1$. Therefore, f_i of the solute can be replaced by its partial pressure, P_i, in Eq. 3.3. Due to the small vapor pressure of DESs, the vapor phase may be assumed to contain only the solute gas molecules. P_i is thus equal to the total pressure (P), imposed in the simulations. The Henry coefficient of solute i, defined in Eq. 3.3, can be computed as a function of its excess chemical potential at infinite dilution, $\mu_i^{\text{ex},\infty}$, as [69, 275]:

$$K_{\text{H},i}^{\text{m}} = m_0 RT\rho \exp\left[\frac{\mu_i^{\text{ex},\infty}}{k_{\text{B}}T}\right] \tag{3.4}$$

where R is the universal gas constant (in $\text{J}\,\text{mol}^{-1}\text{K}^{-1}$), T the temperature (in K), and ρ is the mass density of the DES (in $\text{kg}\,\text{m}^{-3}$). The resulting Henry coefficient is thus in units of Pa. It is also possible to define the Henry coefficient in terms of the mole fraction, where m_i/m_0 is replaced by the mole fraction of solute i, x_i, in Eq. 3.3, and the right-hand side of Eq. 3.4 is divided by the molar mass of the DES (in $\text{kg}\,\text{mol}^{-1}$). To compute the Henry coefficient from Eq. 3.4, the excess chemical potential of each solute i was obtained at infinite dilution from the unbiased (Boltzmann sampled) probability distribution of λ of the fractional molecule of the solute, when λ approaches 0 ($p_i(\lambda \to 0)$) and 1 ($p_i(\lambda \to 1)$) [91, 99]:

$$\mu_i^{\text{ex},\infty} = -k_{\text{B}}T \ln \frac{\langle p_i(\lambda \to 1)\rangle}{\langle p_i(\lambda \to 0)\rangle} \tag{3.5}$$

where $k_{\text{B}}T$ is the Boltzmann constant, and the brackets $\langle ...\rangle$ denote an ensemble average. Alternatively, thermodynamic integration can be used to compute the excess chemical potential (excess Gibbs energy), see Eq. 4.2.

To verify the Henry coefficient calculations, the molality-based absorption isotherm of CO_2 in ChClEg (using the GAFF model) was computed at 328 K from CFCMC simulations in the expanded osmotic ensemble [79, 96, 245, 276]. In the osmotic ensemble, the system is considered in equilibrium with an ideal gas reservoir. The temperature and hydrostatic pressure (of the system and the reservoir), as well as the chemical potential of the solute in the reservoir and one extensive variable of the system, here the number of DES molecules, are kept fixed. The number of solute gas molecules in the liquid mixture and the volume of the system are changed to ensure phase equilibrium between the system and the reservoir. A pressure range of 0.1 bar to 10 bar was used to compute the CO_2 loading. The reservoir

was assumed to be entirely composed of the solute gas (with a mole fraction of 1), as DESs have negligible vapor pressure. The chemical potential of the solute at each pressure was specified in terms of its fugacity coefficient, which was determined from the NIST REFPROP [277] software, based on the Peng-Robinson EoS [278]. A fractional molecule (osmotic fractional molecule) of the solute gas was used for molecule insertions in (and deletions from) the mixture. An additional fractional molecule (*NPT* fractional molecule) of the solute gas was used in the system to allow for the identity change trial move and thus enhanced sampling. The identity change and reinsertion trial moves performed in the osmotic ensemble were similar to the *NPT* ensemble trial moves, described earlier in this section. The λ-change trial moves in the osmotic ensemble were performed in the same way as in the *NPT* ensemble for when $0 < \lambda < 1$. However, if after a λ-change trial move the value of λ of the osmotic fractional molecule became larger than 1, the fractional molecule was transformed into a whole molecule, and a new osmotic fractional molecule was inserted at a random position in the simulation box, with a scaling parameter of $\lambda - 1$ [96]. Similarly, if the value of λ dropped below 0, the osmotic fractional molecule was deleted from the simulation box, and a randomly selected whole molecule was turned into an osmotic fractional molecule with a value of $\lambda + 1$ for the scaling parameter [96]. In the latter case, if no whole molecules were present in the simulation box, the trial move was rejected.

3.3 Results and discussion

3.3.1 Densities and radial distribution functions

The densities of ChClEg and ChClU were computed at various temperatures without the use of the CFCMC method. The resulting densities are shown in Fig. 5.2 as a function of temperature for the two DESs. The results are compared with the densities obtained from MD simulations by Perkins et al. [61, 121] with the same force fields, as well as with experimental data [36, 181, 235, 265]. It can be observed that the computed densities from MC slightly deviate from the MD results by Perkins et al. [61, 121]. For ChClEg, the densities from the MC simulations are slightly larger than the values by Perkins et al. [121], and for ChClU, the densities from the MC simulations are slightly smaller [61]. As bond-stretching and improper torsion are not yet implemented in Brick-CFCMC [81, 91, 112], these potentials were not considered in the MC simulations. The exclusion of these energies, combined with the differences in the use of tail corrections and

shifting of the LJ potential, and dissimilar cutoff radii and system sizes may be the cause of such density differences between the MC simulations and the MD results of Perkins et al. [61, 121]. Nonetheless, excellent agreement between the MC simulation results and experimental data is observed for the densities of both DESs. Several other studies have reported very similar experimental densities for these DESs [233, 234, 279]. This indicates that the densities of DESs can be accurately computed using MC simulations, even when more advanced techniques such as CFCMC are not used.

RDFs were computed for various atom pairs in both DESs, using the GAFF force field parameters (Fig. 3.2). The results agree with the RDFs reported in literature from MD simulations with the same force field [61, 121, 128]. For instance, in both the MC simulations performed here and the MD simulations of Perkins et al. [121], the interaction of the hydroxyl hydrogen of choline with the chloride anion ($HO_{choline}$-Cl) in ChClEg, shows a first RDFs peak at ca. 2.3 Å with an intensity of ca. 11. Therefore, MC simulations are able to reproduce the liquid structure of the DESs without the need to use the CFCMC technique. Considering the relatively high viscosities of these DESs at the simulation temperature of 328 K (24 cP for ChClEg, and 95 cP for ChClU [37]), this is an important finding. However, it is expected for such computations to be more challenging at lower temperatures where the viscosities are significantly higher [35, 181, 185]. The computed RDFs of ChClU from the MC simulations are in agreement with the model fitted experimental data (neutron diffraction) of Hammond et al. [280]. For instance, two RDF peaks are obtained from the MC simulations for the interaction of the oxygen of urea with chloride (O_{urea}-Cl), at 4.5 Å with an intensity of 1.5 Å, and at 5.2 Å with an intensity of 2.2 Å. Hammond et al. [280] reported comparable peak intensities, although the position of the first peak was reported slightly lower (ca. 3.8 Å), compared to the MC simulations. Several other computational studies are available that report RDFs for ChClU and ChClEg, based on MD and DFT simulations [118, 134, 136, 137]. Differences can be observed to various extents between the RDFs computed here and the RDFs reported in literature, due to the dissimilarity of the modeling methods and/or parameters (e.g., force fields). For instance, for ChClU, the computed RDFs from the MC simulations are in agreement with the MD results of Kumari et al. [137], using the CHARMM36 force field [281, 282], except for some differences in the first peak intensities. For instance, the computed values of the first RDF peaks, from the MC simulations, for the interactions of the nitrogen of urea with chloride (N_{urea}-Cl), the hydrogen of urea with chloride (H_{urea}-Cl), and the hydroxyl hydrogen of choline with chloride

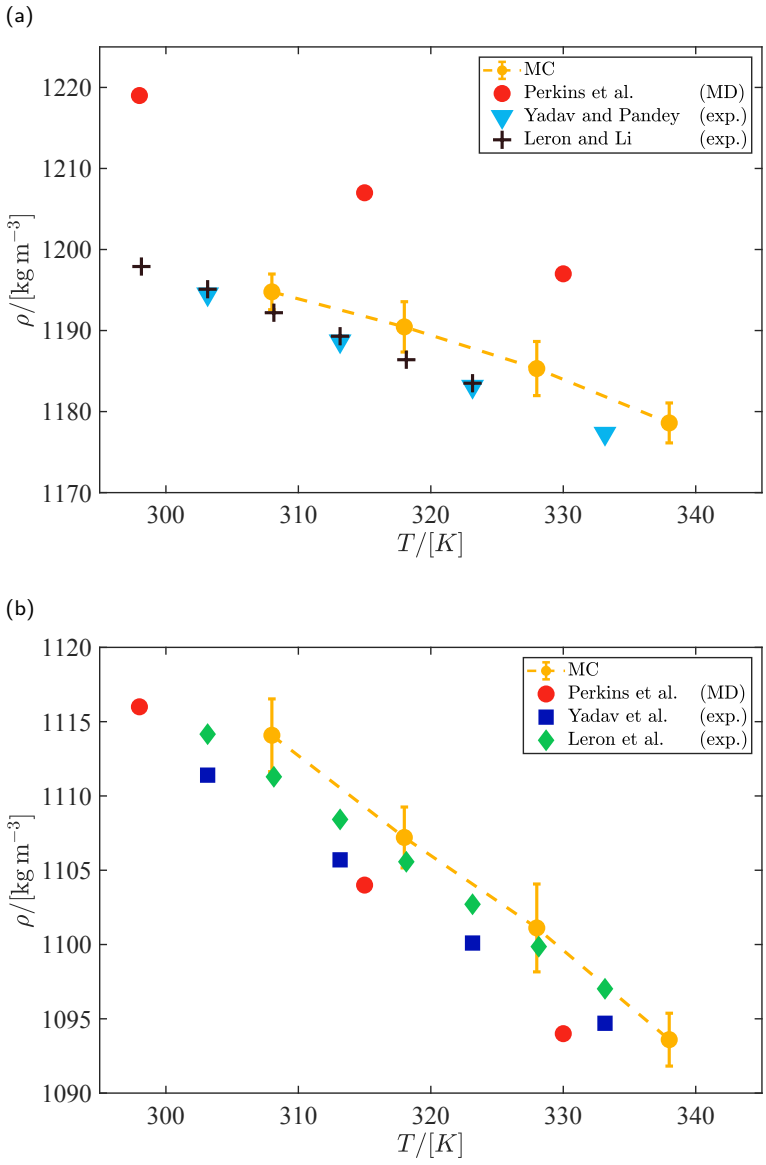

Figure 3.1: Computed densities of (a) ChClU and (b) ChClEg, at various temperatures and 1 bar from MC simulations (orange circles and dashed line), compared to the MD results by Perkins et al. [61, 121] (red circles), and experimental data by Yadav and Pandey [181] (blue triangles), Leron and Li [235] (black pluses), Yadav et al. [36] (blue squares), and Leron et al. [265] (green diamonds). The small differences between the computed densities from MC and the MD simulation results of Perkins et al. [61, 121] may be due to the exclusion of improper torsion and bond-stretching energies from the MC simulations, and/or the differences in the use of tail corrections, shifting of the LJ potential, cutoff radius, and system size.

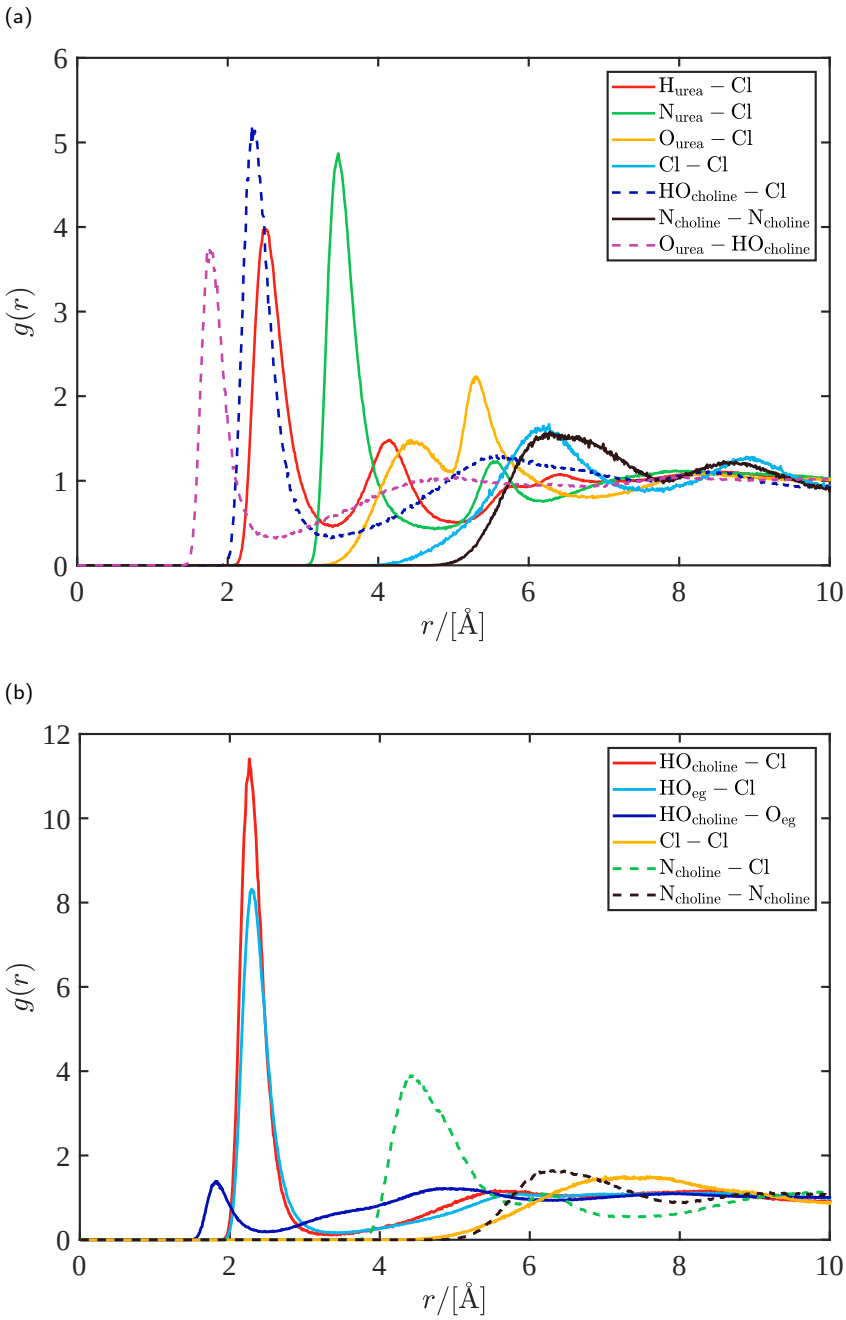

Figure 3.2: Computed RDFs for various atom pairs in (a) ChClU and (b) ChClEg, from MC simulations at 328 K and 1 bar. The notations 'HO' and 'eg' are used for hydroxyl hydrogen and ethylene glycol, respectively.

($HO_{choline}$-Cl) are ca. 4.9, 4, and 5.2, respectively, whereas Kumari et al. [137] reported these values as ca. 6.8, 6, and 11. The peak positions and the intensities of the other peaks (higher solvation shells) are, however, in agreement between the MC simulations and the results of Kumari et al. [137]. Differences between the RDFs are more pronounced when comparing the MC simulation results with the MD results by Sun et al. [136], where force field parameters based on OPLS/Amber [283] and an ionic charge scaling factor of 0.9 were used. For ChClEg, the computed RDFs from the MC simulations, in most cases, differ in the intensity of the first peak from the RDFs reported by Ferreira et al. [118], using MD simulations with force field parameters based on OPLS [154, 284, 285], and an ionic charge scaling factor of 0.8. For instance, the first peak intensity of the RDF of the interaction of the hydroxyl hydrogen of ethylene glycol with chloride (HO_{eg}-Cl) was computed as 11.4 from the MC simulations, while Ferreira et al. [118] reported a value of ca. 7. It is noteworthy that in the aforementioned studies, the ionic charge scaling factors were adjusted to obtain the best agreement between the simulation results and experimental data. Therefore, depending on the accuracy of the force field, different scaling factors were used by different authors. The differences between the RDFs from the various studies highlight the fact that an accurate modeling of the liquid structure of DESs using MC/MD simulations significantly depends on the use of optimal force field parameters.

3.3.2 Solubilities

The Henry coefficients of CO_2, H_2S, CH_4, CO, H_2, and N_2 in ChClU and ChClEg DESs were computed using the CFCMC method in the *NPT* ensemble. The equilibration of each mixture was verified by monitoring the changes in density and total energy. The liquid structures of the systems were investigated by computing RDFs. The obtained RDFs were in agreement with the RDFs computed from the simulations in which CFCMC was used (Fig. 3.2). This means that the presence of the additional fractional molecules of the HBD and solutes did not change the liquid structures of the DESs. This is consistent with the observations by Rahbari et al. [271] that the presence of a small number of fractional molecules, i.e., up to ca. 1% of the total number of molecules, does not change the thermodynamic properties. The average observed probability distribution of λ was investigated for the solute fractional molecules at the end of each production run as a measure of λ-space sampling. As shown in Fig. 3.3a, observed probability distributions of λ were flat for all the solutes in both DESs ($p^{obs} \to 1$ for the whole range of λ), indicating that the sampling of λ-space was sufficient. As

explained in Section 3.2, to obtain flat probability distributions for λ (and reduce the uncertainties in the computed Henry coefficients), long equilibration and production runs (several million MC cycles) were required, owing to the high viscosities and densities of the DESs. The obtained weight functions of all the solute fractional molecules in ChClU, averaged over all independent runs, are shown in Fig. 3.3b. The difference in the weight function between $\lambda = 0$ and $\lambda = 1$ represents the free energy change of dissolution of the solute. By examining the weight functions of the different solutes in ChClU, in Fig. 3.3b, it becomes apparent that CO_2 and H_2S are much more soluble than CH_4, CO, H_2, and N_2. The free energy barriers shown in Fig. 3.3b are encountered when the interactions of the fractional molecule of the solute with its surrounding molecules are gradually scaled by λ, i.e., the molecule is gradually inserted (or deleted). The free energy barrier of insertion/deletion depends on the λ-scaling pathway, which can be modified by, for instance, setting different values for the constants α, b, and c in Eq. 3.2. The LJ interactions are observed to impose a larger free energy barrier for the insertion/deletion of CO_2 and H_2S compared to the electrostatic interactions. The models used for CH_4 and H_2 have no partial charges and thus have flat weight functions in the electrostatic scaling range (0.8 to 1). For these molecules, the free energy change of dissolution is entirely due to the LJ interactions with the DES. Although the models for CO and N_2 include partial charges, the contribution of the electrostatic interactions to the free energy change of dissolution is much smaller than that of the LJ interactions. Similar observed probability distributions of λ, and weight functions were obtained for the dissolution of the gases in ChClEg (not shown here).

The computed molality-based Henry coefficients from the CFCMC simulations are listed in Table 3.1 for both DESs. For ChClEg, the obtained values using both the GAFF and OPLS force fields are provided in the table. Except for CO_2, experimental data are very scarce for the solubilities of the studied gases in ChClU. No experimental data have been reported for the solubilities of theses gases (except for CO_2) in ChClEg. Some of the experimental data found in literature are also listed in Table 3.1. In case the reported Henry coefficients were on a mole fraction basis, a conversion to molality-based values was performed, using the molar masses of the DESs (listed in Table 1.1). It can be observed that the computed Henry coefficient of CO_2 in ChClU from CFCMC (6 MPa) is larger than the experimental data by Xie et al. [157], and Liu et al. [52] by a factor of 4. Leron et al. [40], and Li et al. [241] have also reported Henry coefficients ranging from 1.4 MPa to 1.7 MPa (molality-based) for the dissolution of CO_2 in ChClU.

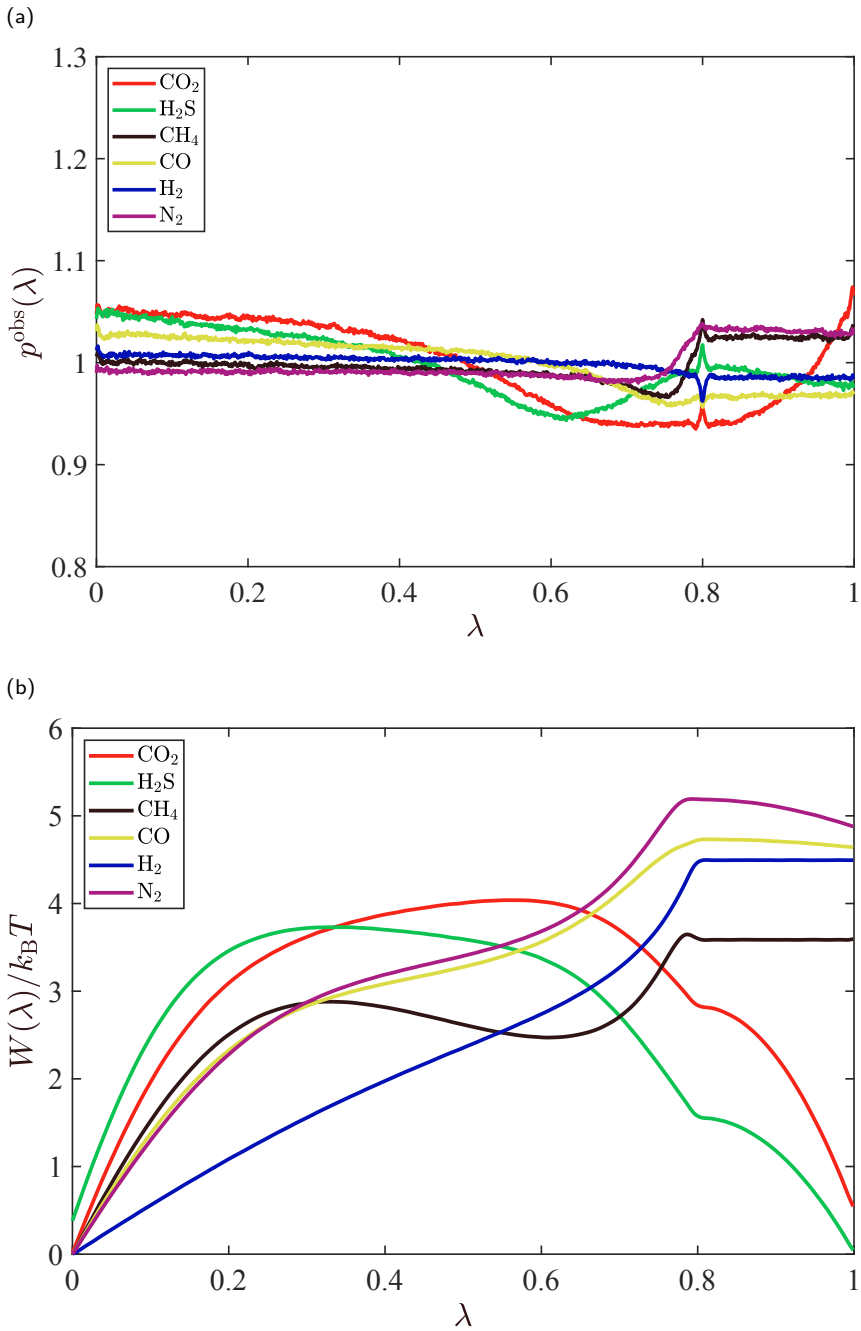

Figure 3.3: (a) Observed probability distributions of λ of the fractional molecules of various gases in ChClU at 328 K and 1 bar (averaged over all independent runs). (b) The corresponding weight functions used to make the observed probability distributions of λ flat.

However, as shown in Table 3.1, the Henry coefficient by Mirza et al. [53] is much larger than the other experimental data, and is closer to the computed value from CFCMC. As discussed in Section 3.1, such inconsistencies may be due to the different pressure ranges used for the solubility measurements. Furthermore, the water content of the DES used by Mirza et al. [53] (wt.% 2.4) is higher than in the other studies, which could be the reason for the larger reported Henry coefficient. However, for ChClU with a similar water content (wt.% 1.9), Xie et al. [233] reported the Henry coefficient of CO_2 as 1.75 MPa (molality-based). The authors also showed that upon an increase in the moisture content of ChClU from wt.% 1.9 to wt.% 9.1, the Henry coefficient increased to 1.93 MPa, which is still lower that the value reported by Mirza et al. [53]. This contradiction, in addition to the scarcity of data for the other gases, makes the comparison between the simulation results and experimental data difficult. The computed Henry coefficients of the other gases are significantly larger than the experimental data (up to a factor of 88 for N_2). As can be observed in Table 3.1, the reported experimental Henry coefficients of CH_4 differ by a factor of 5. This is an indication that more experiments are required to confirm the solubilities of such insoluble gases in ChClU. Nonetheless, it can be observed that the relative order of the Henry coefficients of the various solutes agrees reasonably well with the experimental data. The computed solubilities from CFCMC are in the order $H_2S > CO_2 > CH_4 > H_2 > CO > N_2$, whereas experimental data indicate the solubilities as $H_2S > CO_2 > CH_4 > N_2 > H_2 > CO$ at the same temperature, differing only in the relative solubility of N_2. It is important to note that the relative magnitudes of the Henry coefficients of the gases are consistent with the observations regarding the computed weight functions (Fig. 3.3b), as a representation of the free energy change of dissolution. Using the GAFF force field parameters, the computed Henry coefficient of CO_2 in ChClEg is equal (within the uncertainties) to the Henry coefficient in ChClU. The Henry coefficient of CO_2 in ChClEg is nonetheless in better agreement with the experimental data. It can be observed that the average Henry coefficients obtained using the OPLS parameters are, for all the gases except H_2S, larger than the values computed using the GAFF parameters. The difference between the computed Henry coefficient of CO_2 in ChClEg and the reported experimental data is thus larger when the OPLS parameters are used, implying better suitability of the GAFF force field for these computations. For H_2S, the GAFF and OPLS force fields result in comparable Henry coefficients, although the average Henry coefficient is slightly larger when the GAFF force field is used. The differences in the computed Henry coefficients obtained using the OPLS and GAFF force

Table 3.1: Computed average Henry coefficients (molality-based) at 328 K for various gases in ChClU and ChClEg from CFCMC simulations in the *NPT* ensemble, using the GAFF [61, 121] and OPLS [59] (only for ChClEg) force fields. Experimental data available from literature [52, 53, 157, 257] (also at 328 K) are listed for comparison. The values in parentheses are the standard deviations to the precision of the last significant digit.

		K_H^m/[MPa]					
		CO_2	H_2S	CH_4	CO	H_2	N_2
ChClU	CFCMC-GAFF	6.1 (4)	2.7 (2)	134.0 (133)	392.0 (393)	300.0 (92)	456.2 (295)
	Xie et al. [157]	1.4	-	4.1	6.8	5.8	5.1
	Liu et al. [52]	1.5 [a]	0.5 [a]	20.1 [a]	-	-	-
	Mirza et al. [53]	5.0 [b]	-	-	-	-	-
ChClEg	CFCMC-GAFF	6.0 (2)	2.0 (2)	101.8 (52)	313.8 (209)	256.3 (73)	373.2 (281)
	CFCMC-OPLS	6.6 (4)	1.8 (1)	141.6 (37)	576.3 (418)	432.1 (177)	661.9 (510)
	Leron and Li [257]	4.7 [a]	-	-	-	-	-
	Mirza et al. [53]	3.8 [b]	-	-	-	-	-

[a] Interpolated values.
[b] Values extracted from figures.

fields are larger for the more insoluble gases. To draw final conclusions on which force field predicts the solubilities more accurately, experimental data are required for the solubilities of these gases in ChClEg. The computed solubilities in ChClEg, using both the GAFF and OPLS force fields, have the same relative order as in ChClU, with H_2S as the most soluble gas, and N_2 as the least soluble gas. The computed Henry coefficients for ChClEg are generally smaller than those for ChClU, when the GAFF force field is used for both DESs, suggesting that ChClEg is a better solvent for the studied gases. When the OPLS force field is used for ChClEg, however, the computed Henry coefficients are mostly larger than for ChClU (except for H_2S), indicating ChClU as a superior solvent. Nevertheless, the comparison is more coherent when the same force field (e.g., GAFF) is used for both DESs.

To verify the computations of the Henry coefficients in the *NPT* ensemble, simulations were carried out in the osmotic ensemble to compute the solubility of CO_2 in ChClEg, using the GAFF force field for the DES. Thereby, the absorption isotherm of CO_2 was computed at 328 K as a function of the hydrostatic pressure. The resulting isotherm is presented in terms of the dimensionless molality (m/m_0) in Fig. 3.4. As can be observed in the figure, the solubility of CO_2 increases almost linearly when the pressure is elevated. The inverse of the slope of the isotherm at infinite dilution ($m/m_0 \to 0$) provides the Henry coefficient. The Henry coefficient was obtained by a linear fit to the low-pressure part of the isotherm (i.e., first five points). The fitting (with R^2=0.999) resulted in a Henry coefficient of 5.5 MPa, which is in agreement with the value obtained from the *NPT* ensemble simulations. The lines corresponding to the Henry coefficients, obtained from both the *NPT* ensemble and the osmotic ensemble simulations, are presented in Fig. 3.4. The difference between the two lines is small when $m/m_0 \to 0$, and increases when the pressure/molality increases. This is due to the fact that the Henry coefficient from the *NPT* simulations was obtained at infinite dilution, in accordance with the definition in Eq. 3.3. Experimental solubility data by Leron and Li [257], and Mirza et al. [53] are also presented in Fig. 3.4. The experimental data indicate a higher solubility and a lower Henry coefficient (as inferred from the inverse of the slope of the isotherm) of CO_2 in ChClEg, compared to the computed values from the osmotic ensemble simulations. This is consistent with the results obtained from the *NPT* simulations (Table 3.1). The solubility data of CO_2 in a commonly studied IL, i.e., [bmim][Tf_2N] [286], are also shown in Fig. 3.4 for comparison. It can be observed that the experimental solubility of CO_2

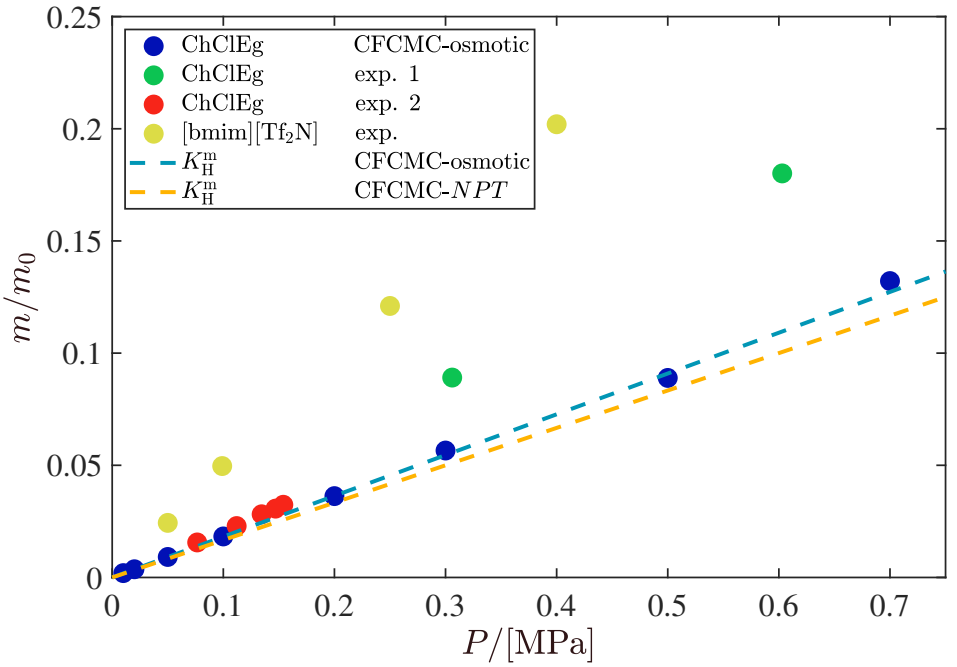

Figure 3.4: Computed absorption isotherm of CO_2 in ChClEg in terms of the non-dimensional molality, m/m_0 (m_0 is set to 1 mol kg^{-1}), from the osmotic ensemble CFCMC simulations (blue circles). The error bars are smaller that the symbols, and are therefore not shown. The blue and orange dashed lines correspond to the Henry coefficients obtained from the simulations in the osmotic and *NPT* ensembles, respectively. Experimental data for CO_2 absorption in ChClEg by Leron and Li [257] (green circles), denoted as 'exp. 1', and Mirza et al. [53] (red circles), denoted as 'exp. 2', and in the ionic liquid [bmim][Tf_2N] by Anthony et al. [286] (yellow circles) are shown for comparison.

in [bmim][Tf_2N] is larger than the experimental solubility in ChClEg. This is qualitatively consistent with the simulation results.

Overall, there is a considerable difference between the computed Henry coefficients of the gases in the DESs (for ChClU in particular) and the experimental data from literature. Aside from the uncertainties in the experimental data, it is possible that the force field parameters of the DESs, although yielding accurate thermodynamic properties for the neat DESs [59, 61, 121, 128] (with no solutes), are not optimal in combination with the models used for the solute gases. A particularly influential parameter in the force fields of ILs and DESs is the ionic charge scaling factor, f_q, which may significantly affect the computation of thermo-physical and structural properties [61, 68, 142, 287]. A smaller scaling factor (farther from 1) leads to weaker ionic interactions. Weaker ionic interactions result in a

lower density of the IL/DES and thus larger free volume, required for the dissolution of solutes. Therefore, it is expected that reducing the ionic charge scaling factor increases the solubilities of gases (decreases the Henry coefficients). Conversely, a larger scaling factor (closer to 1) increases the strength of ionic interactions, and therefore yields higher densities and lower gas solubilities. The value of the scaling factor depends on the specific force field used in the simulations, and is often tuned to obtain a better agreement of the simulation results with experimental data [59, 61, 287, 288]. It is thus possible that the scaling factors used for the DESs are too large (and the cohesive interactions too strong) to allow for the dissolution of solutes.

To investigate the influence of the ionic charge scaling factor, the Henry coefficients of CO_2, H_2S, and CH_4 in ChClU and ChClEg were computed at 328 K in the *NPT* ensemble, using the GAFF force field for the DESs and smaller charge scaling factors. The charge scaling factor was reduced from 0.8 to 0.7 for ChClU, and from 0.9 to 0.8 for ChClEg. The results are presented in Fig. 3.5, where the Henry coefficients with the original charge scaling factors are also shown for comparison. It can be observed that, as expected, the reduction of the ionic charge scaling factor results in a decrease in the Henry coefficients of all the solute molecules (increased solubilities). The Henry coefficients for ChClU with the charge scaling factor of 0.7 are obtained as 4.1 MPa, 1.7 MPa, and 40.8 MPa (molality-based) for CO_2, H_2S, and CH_4, respectively. The Henry coefficients of these gases in ChClEg are calculated as 3.8 MPa, 1.4 MPa, and 60.1 MPa, using the charge scaling factor of 0.8. For ChClEg with a charge scaling factor of 0.8, the Henry coefficient of CO_2 is in agreement with the experimental value by Mirza et al. [53], but it is smaller than the value by Leron et al. [265] (Table 3.1). Therefore, the improvement in the accuracy of the computed Henry coefficient, using the smaller charge scaling factor, depends on the considered experimental data (similarly for ChClU). The charge scaling factor of 0.7 for ChClU results in enhanced agreement between the simulation results and the experimental data by Xie et al. [233], and Liu et al. [52] (Table 3.1). Nevertheless, the differences between the computed Henry coefficients and the experimental data are still considerable for ChClU. As discussed, smaller charge scaling factors result in lower densities, and may therefore compromise the accuracy of the computed densities. Here, the reduced charge scaling factors resulted in densities of 1160 $\mathrm{kg\,m^{-3}}$ and 1070 $\mathrm{kg\,m^{-3}}$ for ChClU and ChClEg, respectively, which are lower than the computed densities using larger scaling factors (Fig. 5.2). The relative differences between the computed densities using different ionic charge scaling factors are therefore 2.1% and 2.8% for ChClU and ChClEg, respectively.

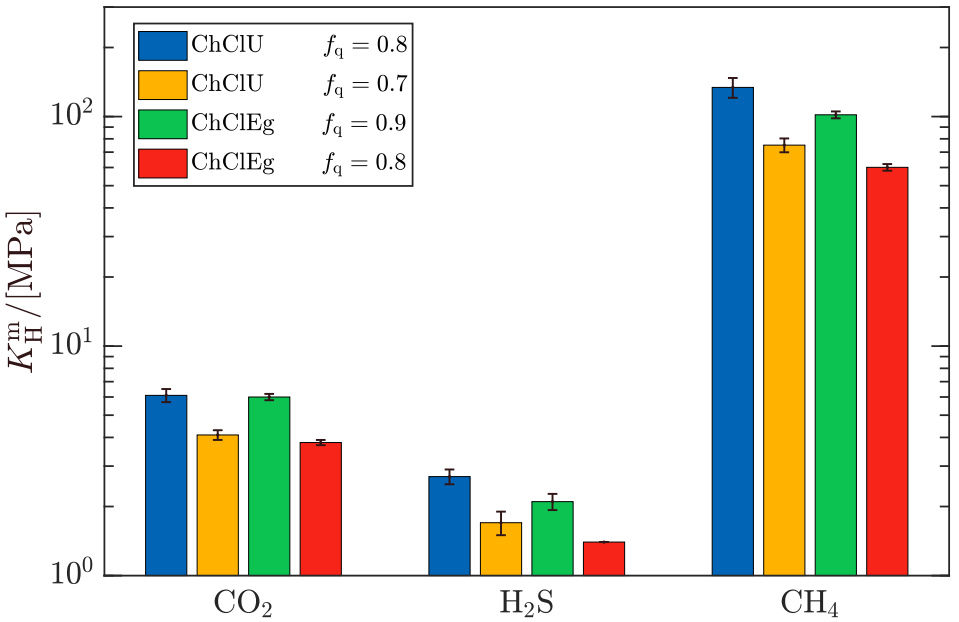

Figure 3.5: Comparison of the computed Henry coefficients (molality-based) of CO_2, H_2S, and CH_4 in ChClU and ChClEg, using the GAFF force field parameters with different ionic charge scaling factors (f_q) for the DESs.

Moreover, the smaller charge scaling factors lead to an underestimation of experimental densities by 1.7% and 2.5%. Nevertheless, such density differences between simulation results and experimental data are not significant, and are also observed in the MD simulations by Perkins et al. [61], and Doherty and Acevedo [59], using the GAFF and OPLS force fields, respectively. It should further be studied how these reduced charge scaling factors affect the liquid structure and other thermodynamic/transport properties (e.g., viscosity and diffusion coefficients) of the DESs. A closer agreement between the computed Henry coefficients for ChClU and the experimental data by Xie et al. [233], and Liu et al. [52], however, will require even smaller ionic charge scaling factors. This will in turn result in less accurate calculations of the density and possibly other DES properties.

It has been suggested that charge scaling models can poorly predict the phase behavior of IL mixtures [287, 289]. Cui et al. [290] investigated the effect of charge scaling on solvation properties of ILs with respect to various solutes, and concluded that such models underestimate solute-solvent interactions and thus the free energies of solvation, compared to experimental data. However, the authors stated that the differences are more pronounced in the case of more polar solutes (e.g., ammonia), whereas

solute-solvent interactions are well reproduced by such models for non-polar solutes (e.g., CO_2) with dominant dispersion interactions. The authors further suggested that for the solvation of polar solutes, explicit polarization of the models is necessary for an accurate description of the interactions. It is also possible that the properties of mixtures of DESs with other molecules are more accurately computed by using a polarizable force field, compared to the simple charge scaling method. It has been shown by García et al. [120] that the charge derivation scheme has a substantial influence on the computed structural and thermodynamic properties of the choline chloride-levulinic acid DES. Additionally, charge assignment can be carried out for either isolated ions/molecules or DES clusters. García et al. [120] argued that decisions regarding the charge assignment method should be made with great caution in order to result in an accurate modeling of DESs. Therefore, other charge derivation schemes, for instance based on mixture properties, could improve the accuracy of solubility computations. Recently, Schauperl et al. [291] developed a new version of the restrained electrostatic potential (RESP) method [292], RESP2, in which partial atomic charges are obtained based on a combination of gas phase and aqueous phase charges. In contrast, the original RESP method [292], by which Perkins et al. [61, 121] derived the charges of DESs (the charges used here), only performs gas phase quantum mechanical computations. It is therefore interesting to see if new force field models developed based on mixture parameters, such as RESP2 [291], could lead to more accurate solubility computations.

As previously discussed, according to Fig. 3.3b, the LJ interactions of the solutes with ChClU show a large contribution to the free energy change of dissolution (particularly for the more insoluble gases). Therefore, modification of the solute-solvent LJ interactions may improve the results of the solubility computations. To that end, one may consider using different mixing rules or modifying the currently used mixing rules in order to adjust the strength of interactions between specific atoms of the solute and the DES [293–295]. Here, force field parameters were used as proposed in the original publications, and no further re-parameterization of the charges and LJ parameters was performed. Although such re-parameterization may result in more accurate values for some of the Henry coefficients, there is no guarantee that the obtained parameters are transferable to other DES systems.

3.4 Conclusions

The Henry coefficients of various gases in ChClEg and ChClU were computed using CFCMC simulations in the *NPT* ensemble. The GAFF force field parameters were used for both DESs, in addition to the OPLS parameters for ChClEg. The results were corroborated by additional computations of the absorption isotherm for CO_2 in ChClEg (in the osmotic ensemble). The densities and RDFs of the DESs were computed using MC simulations without applying the CFCMC method. It was observed that the MC simulations could accurately reproduce the densities and RDFs of the DESs. The computed solubilities of the gases were, however, considerably lower (higher Henry coefficients) than the experimental data reported in literature. The OPLS force field resulted in larger Henry coefficients of the gases in ChClEg (except for H_2S), compared to the GAFF force field, suggesting that the GAFF force field may be more suitable for the solubility computations. The order of solubilities for both ChClU and ChClEg (using both force fields) at 328 K was obtained as $H_2S > CO_2 > CH_4 > H_2 > CO > N_2$, which is in reasonable agreement with experimental measurements reported in literature. It was shown that using smaller ionic charge scaling factors leads to lower densities and higher gas solubilities (smaller Henry coefficients). Nevertheless, the scarcity and contradiction of experimental data raise uncertainty over the precise solubilities and the accuracy of the predictions from the simulations. It is possible that the combination of the force field parameters of the DESs and those of the solute molecules is not suitable for the solubility computations. The use of force fields with explicit polarization terms, alternative charge derivation schemes, and adjusting the solute-solvent LJ interactions were proposed as possible ways to improve the predictions of the simulations.

Chapter 4

Vapor pressures and vapor phase compositions of deep eutectic solvents

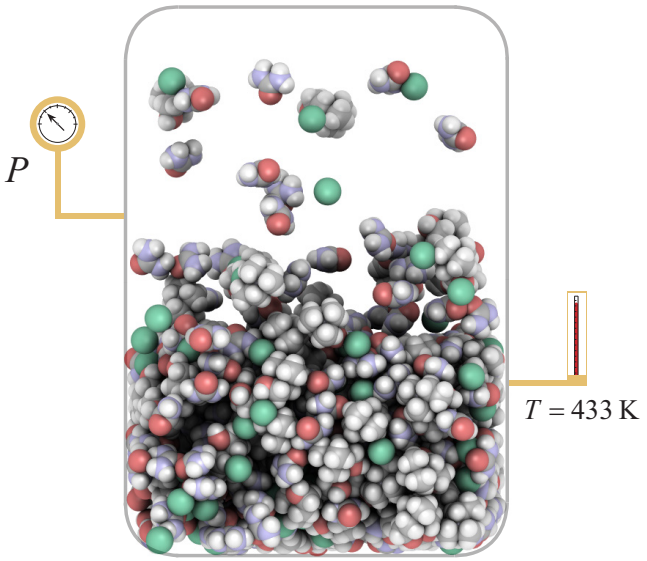

This chapter is based on the following paper: H.S. Salehi, H.M. Polat, F. de Meyer, C. Houriez, C. Coquelet, T.J.H. Vlugt, O.A. Moultos, Vapor pressures and compositions of choline chloride urea and choline chloride ethylene glycol deep eutectic solvents from molecular simulation, *Journal of Chemical Physics*, **2021**, 155, 114504.

4.1 Introduction

DESs and ILs are often regarded as superior solvents compared to VOCs (e.g., toluene), due to a negligible vapor pressure at room temperature [6–8, 12]. Such a low vapor pressure would potentially limit the emission and loss of a DES into the atmosphere, and may facilitate the separation of solutes from DESs by distillation [42]. Despite the widespread acknowledgment of the low vapor pressures of DESs, very few studies are available in literature, reporting measurements of the vapor pressures of these solvents [26, 42, 50, 51, 296–299]. Wu et al. [298] measured, for the first time, the vapor pressures of aqueous solutions of choline chloride-based DESs, with DES mole fractions ranging from 0.035 to 0.45. Shahbaz et al. [51] measured the vapor pressures of neat DESs, composed of a variety of HBA and HBD components, using the TGA method. The authors found that the vapor pressures of the DESs based on urea are lower than those of the DESs based on glycerol (with the same HBA component). Moreover, the measured vapor pressures of glycerol-based DESs were lower than the vapor pressure of pure glycerol, indicating stronger intermolecular interactions within the DESs. It was further concluded that the vapor pressures of DESs are higher than those of commonly studied ILs. Ravula et al. [50] measured the vapor pressures of several DESs (along with some ILs and molecular solvents) in a wide range of temperatures, using the TGA method. While the authors found a reasonable agreement between the vapor pressure data of choline chloride glycerol with those by Shahbaz et al. [51], the obtained vapor pressures of choline chloride urea were higher than those reported by Shahbaz et al. [51] by an order of magnitude.

As DESs are mixtures, the DES components can, in principle, vaporize separately from the liquid phase into the vapor phase, thereby changing the composition of the liquid phase. The first characterization of the vapor phase composition of DESs was performed by Dietz et al. [42], where the authors measured the partial pressures of the components of several hydrophobic DESs, using headspace gas chromatography-mass spectrometry (HS-GC-MS). The vapor pressure and composition were shown to be dominated by the most volatile component of the DESs. The obtained vapor pressures indicated a lower volatility of the hydrophobic DESs compared to common organic solvents, and a higher volatility compared to common ILs. The authors also showed that the HS-GC-MS method is more reliable than TGA for the determination of the vapor pressures of DESs. HS-GC-MS has been used in a few other publications to determine the vapor pressures and compositions of DESs [26, 296, 299]. Lima et al. [296] measured partial

pressures of sulfolane-based DESs at various concentrations of the HBD component (sulfolane). It was shown that the vapor phases of these DESs are dominated by sulfolane as the more volatile component. Consistently, an increase in the salt concentration (decrease in the sulfolane concentration) resulted in lower vapor pressures.

The small magnitude of vapor pressure and the hygroscopicity of DESs are factors that make precise measurements of the vapor pressures and vapor phase compositions of these materials challenging [50, 51]. This is reflected by the scarcity of such data, and the disparities between the few available experimental vapor pressure data from different sources [50, 51]. Therefore, computational and modeling tools can play an important role in the prediction and understanding of the vapor-liquid equilibrium of DESs, particularly in cases where experimental data are unavailable, scarce, or inconsistent. Nevertheless, very few modeling studies are available in the literature that report computations of the vapor phase properties of DESs, or establish a relationship between these properties and the liquid structure of DESs. The PC-SAFT equation of state [55] and the conductor-like screening model for real solvents (COSMO-RS) [300] have been used in a few studies to model vapor pressures of DESs [26, 42, 296, 299, 301]. MD simulations have been performed to compute the solubility parameters and enthalpies of vaporization of choline chloride-based DESs [118, 127, 302]. The partial pressures and vapor phase compositions of these DESs are not available in literature. In chapter 2, it was concluded, based on the computed vaporization enthalpies from MD, that the HBD component (the most volatile component) likely dominates the vapor phase of choline chloride-based DESs. However, no precise vapor phase composition was provided in chapter 2. It is interesting to note that in the studies by Rai and Maginn [303, 304], vapor pressures, enthalpies of vaporization, normal boiling points, and critical properties were computed for imidazolium-based ILs, using MC simulations in the Gibbs ensemble. This method has the ability to directly calculate several vapor-liquid equilibrium properties, and provide the vapor phase configuration of molecules (e.g., isolated molecules/ions, ion pairs, or clusters) and the vapor phase composition (in the case of mixtures). However, these simulations can only be carried out for sufficiently high temperatures and thus high vapor pressures (ca. 15 kPa-300 kPa in the study by Rai and Maginn [303]), where an adequate number of molecules is transferred to the gas phase at a reasonable system size.

In this chapter, MC simulations were performed in combination with thermodynamic integration to compute the excess Gibbs energies and thereby, the vapor pressures of ChClEg and ChClU. From the computed

partial pressures, vapor phase compositions were obtained for each DES. Enthalpies of vaporization were calculated from the obtained vapor pressures using the Clausius-Clapeyron relation. The activity coefficients of ethylene glycol in ChClEg were computed to quantify the non-ideality of the mixture. To investigate the influence of the liquid phase composition on the computed properties, three different HBA:HBD molar ratios, i.e., 1:1.5, 1:2 (the eutectic ratio of both DESs), and 1:3, were considered in the simulations of each DES. In Section 4.2, the simulation details and computational methods are discussed. In Section 4.3, the simulation results are discussed, and when possible, compared with experimental data from literature. Finally, in Section 4.4, conclusions are provided regarding the computation of vapor pressures and vapor compositions of DESs from MC simulations.

4.2 Computational details

The all-atom non-polarizable GAFF force field [155] was used to model both ChClEg and ChClU. Bonded interactions, including bond-bending and torsion, and non-bonded interactions, consisting of LJ and electrostatic potentials, were used to account for the intra- and intermolecular interactions. All bond lengths were kept fixed at equilibrium lengths, and improper torsions were not taken into account. It was shown in chapter 3 that bond rigidity and the exclusion of improper torsions do not have a considerable influence on the accuracy of the computed densities and liquid structures of ChClEg and ChClU. All partial charges were taken from the studies by Perkins et al. [61, 121], in which the charges were derived at the HF/6-31G* level of theory using the RESP method [292, 305]. The charges of ions (choline and chloride) were scaled by 0.9 and 0.8 in ChClEg and ChClU, respectively, to enhance the agreement between the simulation results and experimental data [61, 121]. To prevent atomic overlaps, the LJ parameters $\epsilon = 0.001\,\mathrm{kcal\,mol^{-1}}$ and $\sigma = 0.1\,\text{Å}$ were used for unprotected hydroxyl hydrogen atoms [205]. Scaling factors of 0.5 and 0.833 were used for the 1-4 intramolecular LJ and electrostatic energies, respectively [155, 204]. The force field parameters of all the molecules are provided in Tables A1 to A4, A9 to A12, and A17 to A20 of the Appendix. The molecular structures of the components (except for the chloride anion) of both DESs are shown in Figs. A1 to A3 of the Appendix. The Ewald summation method, with a relative precision of 10^{-6}, was used to calculate the long-range electrostatic energies [69, 264]. The LJ and short-range electrostatic potentials were truncated at a cutoff radius of 10 Å. Analytic

tail corrections were used to account for the long-range contributions of the LJ energies [70]. The Lorentz-Berthelot mixing rules were used to calculate the LJ interactions between non-identical atom types [70]. It is important to note that in chapter 3, the force field parameters of ChClU and ChClEg (with molar ratios of 1:2) were validated with experimental data and MD simulation results.

All simulations were performed using the open-source Brick-CFCMC software, [81, 91, 112] which applies the CFCMC method [91, 96–100] for molecule insertions, as discussed in chapter 3. To compute the average liquid phase densities and excess Gibbs energies, simulations were performed in the *NPT* ensemble at a pressure of 1 bar and different temperatures. The simulations of ChClU were carried out at 393 K and 433 K. For ChClEg, the simulations were performed at 353 K and 393 K. For each DES, three sets of simulations were performed at different HBA:HBD molar ratios, i.e., 1:1.5, 1:2 (eutectic ratio), and 1:3. Each molar ratio corresponds to a certain mole fraction of the HBD component (urea or ethylene glycol) in the mixture, defined as:

$$x_{\mathrm{HBD}} = \frac{N_{\mathrm{HBD}}}{N_{\mathrm{HBD}} + N_{\mathrm{ChCl}}} \tag{4.1}$$

where N_{HBD} and N_{ChCl} are the number of molecules of the HBD component (urea or ethylene glycol), and the number of choline chloride ion pairs (half of the total number of ions of the HBA), respectively. Therefore, the HBA:HBD molar ratios ($N_{\mathrm{HBA}}/N_{\mathrm{HBD}}$) of 1:1.5, 1:2, and 1:3 correspond to the HBD mole fractions of 0.6, 0.67, and 0.75. The mole fraction of choline chloride in the DESs can be calculated as $x_{\mathrm{ChCl}} = 1 - x_{\mathrm{HBD}}$. The numbers of molecules and mole fractions of the DES components used in the simulations, as well as the average liquid phase box sizes after equilibration at 393 K and 1 atm, are listed in Table 4.1 for ChClU and ChClEg at different liquid compositions.

For each combination of temperature and molar ratio, two separate sets of simulations were carried out, i.e., one containing an additional fractional molecule of the HBD, and one containing an additional fractional 'group' [112] of the HBA, as vaporizing entities. The fractional group of the HBA consisted of a single fractional molecule/ion of chloride and a single fractional molecule/ion of choline. The grouping of the choline and chloride ions into a single HBA component was carried out in accordance with experimental and computational studies of ILs, in which the vapor phase has been shown to mostly consist of isolated ion pairs (i.e., one cation and one

Table 4.1: The numbers of molecules N_i of each DES component i used in the liquid phase simulations, at different HBA:HBD molar ratios. The DES components are: choline cation, chloride anion, and urea or ethylene glycol HBD component. The mole fractions of choline chloride (HBA component) and the HBD component (urea or ethylene glycol) are also listed. For all systems, the average liquid phase box sizes (L) after equilibration at 393 K and 1 atm are also listed.

DES	molar ratio	N_{cation}	N_{anion}	N_{HBD}	x_{HBD}	x_{ChCl}	$L/[\text{Å}]$
ChClU	1:1.5	60	60	90	0.60	0.40	27.3
	1:2	50	50	100	0.67	0.33	26.5
	1:3	40	40	120	0.75	0.25	26.1
ChClEg	1:1.5	60	60	90	0.60	0.40	28.1
	1:2	50	50	100	0.67	0.33	27.5
	1:3	40	40	120	0.75	0.25	27.4

anion), rather than single ions or large clusters [156, 215–219, 303, 306, 307]. Thermodynamic integration was used to compute the excess Gibbs energy of each DES component (HBA or HBD) in the NPT ensemble, $\Delta G^{\text{ex}}_{NPT}$, according to [69]:

$$\Delta G^{\text{ex}}_{NPT} = \Delta A^{\text{ex}}_{NVT} = \int_0^1 \left\langle \frac{\partial U}{\partial \lambda} \right\rangle \mathrm{d}\lambda \tag{4.2}$$

where $\Delta A^{\text{ex}}_{NVT}$ is the excess Helmholtz energy of that component, computed in the NVT ensemble, λ is the scaling parameter of the fractional molecule/group of the DES component, U is the potential energy of the system, and the brackets $\langle ... \rangle$ denote an ensemble average. We used 50 values of λ, evenly distributed in the range (0,1), to compute the integral in Eq. 4.2. For each value of λ, a separate simulation was carried out (λ was fixed during each simulation), from which the ensemble average in Eq. 4.2 was computed. In Brick-CFCMC, the values of $\partial U/\partial \lambda$ are automatically computed for all non-bonded interactions, including the Ewald summation [81]. To enhance the accuracy of the integration in Eq. 4.2, a cubic spline was fit to $\langle \partial U/\partial \lambda \rangle$ as a function of λ.

It is important to note that in principle, the excess Gibbs energy (the excess chemical potential) of a fractional molecule can also be computed from the probability distribution of λ in a single simulation (Eq. 3.5), where a random walk is carried out in λ-space. This method was successfully employed in chapter 3 to compute the solubilities of gases in DESs. Although this method is accurate and reliable for small fractional molecules with relatively weak interactions, e.g., CO_2, the sampling of λ-space becomes increasingly

challenging and inefficient when the size and the strength of interaction of the fractional molecule become larger (e.g., DES components), resulting in large uncertainties in the computed excess Gibbs energies. Therefore, thermodynamic integration was used in this chapter as an alternative method to compute the excess Gibbs energies of DES components.

All liquid phase simulations were started from well-equilibrated initial configurations (in terms of the density and total energy) at the respective temperature. 3×10^5 additional equilibration MC cycles, and 4×10^5 production MC cycles were used for each value of λ. Each MC cycle consisted of various trial moves (as many as the number of molecules), selected with fixed probabilities, to thermalize the system. These trial moves included translations, rotations, volume changes, changes of the internal configuration of molecules (angles and dihedrals), reinsertions of the fractional molecule at a random position in the box, and exchanges of the identity of the fractional molecule with a randomly selected whole molecule. No trial moves that attempt to change λ were performed, as the value of λ was fixed in each simulation. For each data point, 3-5 independent runs were carried out, from which the mean and standard deviation were calculated. Similar to the methodology used in chapter 3, two separate parameters, i.e., λ_{LJ} and λ_{el}, were used to independently scale the LJ and electrostatic interactions of the fractional molecules/groups. This scaling was performed using the following scheme: between $\lambda = 0.0$ and $\lambda = 0.5$, the LJ interactions were scaled using λ_{LJ}, while the electrostatic interactions remained fully switched-off ($\lambda_{\mathrm{el}} = 0.0$), and between $\lambda = 0.5$ and $\lambda = 1.0$, the electrostatic interactions were scaled using λ_{el}, while the LJ interactions remained fully switched-on ($\lambda_{\mathrm{LJ}} = 1$). With the linear scaling scheme described in chapter 3, λ_{el} and λ_{LJ} as a function of the overall scaling parameter λ would not be differentiable at $\lambda_{\mathrm{switch}}$ (here 0.5). To overcome this issue, and to prevent atomic overlaps for fractional molecules, the following continuous and differentiable functions (for $\lambda \in (0, 1)$) were used in this chapter for the scaling of λ_{LJ} and λ_{el} with λ [81]:

$$\lambda_{\mathrm{LJ}} = \begin{cases} \frac{20}{9}\lambda & 0.0 < \lambda < 0.4, \\ 1 - \frac{100}{9}(\lambda - \frac{1}{2})^2 & 0.4 \leq \lambda < 0.5, \\ 1.0 & 0.5 \leq \lambda < 1.0, \end{cases} \tag{4.3}$$

and

$$\lambda_{\mathrm{el}} = \begin{cases} 0.0 & 0.0 < \lambda < 0.5, \\ \frac{100}{9}(\lambda - \frac{1}{2})^2 & 0.5 \leq \lambda < 0.6, \\ \frac{-11}{9} + \frac{20}{9}\lambda & 0.6 \leq \lambda < 1.0. \end{cases} \tag{4.4}$$

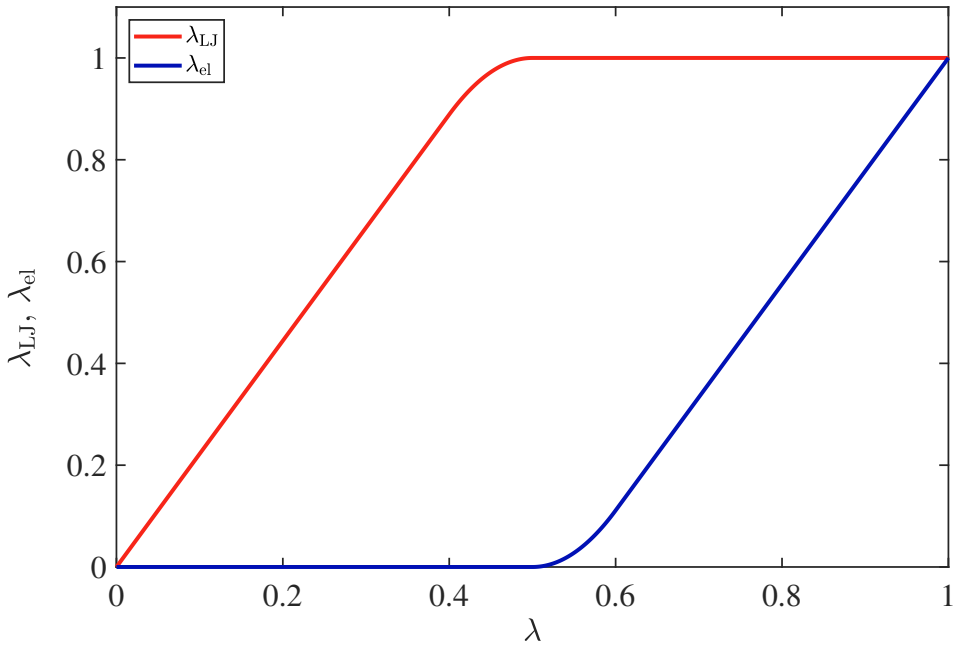

Figure 4.1: The LJ and electrostatic scaling parameters (λ_{LJ} and λ_{el}, respectively) as a function of the overall scaling parameter (λ) of the fractional molecule/group. The expressions for λ_{LJ} and λ_{el} as functions of λ are provided in Eqs. 4.3 and 4.4 [81].

The functions in Eqs. 4.3 and 4.4 are also depicted in Fig. 4.1. Using this scaling scheme, by definition, $\partial U/\partial\lambda = 0$ at $\lambda = 0.5$. The same functions and parameters as described in chapter 3 were used here for the scaling of the LJ (Eq. 3.2) and electrostatic interactions with λ_{LJ} and λ_{el}.

The vapor phase of the DESs was assumed to be an ideal gas composed of isolated, non-interacting molecules of the HBD component (urea or ethylene glycol), and isolated, non-interacting choline chloride (HBA component) ion pairs. Due to the low vapor pressures of the DESs [50, 51], the ideal gas approximation of the vapor phase is reasonable. The assumption of choline chloride existing in the vapor phase as isolated ion pairs, has also been used in the simulations of ILs [306, 308] and other salts, e.g., NaCl [309], and is consistent with experimental observations of the vapor phase of ILs [156, 215, 219], as discussed earlier. Test simulations were carried out in the gas phase at various box sizes to examine whether dimer formation was favorable for the HBD molecules. No considerable dimer formation was found in the simulations, reinforcing the assumption that the HBD molecules exist as monomers in the gas phase.

The vapor pressures of the DESs, P^{v}, was defined as:

$$P^{\mathrm{v}} = P_{\mathrm{HBD}} + P_{\mathrm{ChCl}} \tag{4.5}$$

in which P_{HBD} and P_{ChCl} are the partial pressures of the HBD and choline chloride (HBA) components, respectively. In a few publications, the vapor pressure of a DES (P^{v}) is referred to as the 'total vapor pressure' [26, 42, 296, 299]. The vapor phase mole fraction of each component i (HBD or HBA) can be computed as $y_i = P_i/P^{\mathrm{v}}$.

The vapor phase chemical potential of the HBD component can be computed according to [309]:

$$\mu^{\mathrm{v}}_{\mathrm{HBD}}(T, P^{\mathrm{v}}) = \Delta_{\mathrm{f}} G^0_{\mathrm{HBD}} + RT \ln \frac{P_{\mathrm{HBD}}}{P^0} \tag{4.6}$$

where $P^0 = 1\,\mathrm{bar}$ is the reference state pressure, $\Delta_{\mathrm{f}} G^0_{\mathrm{HBD}}$ is the Gibbs energy of formation of the HBD at P^0, T is the absolute temperature, k_{B} is the Boltzmann constant, and P_{HBD} is the partial pressure of the HBD.

The liquid phase chemical potential of the HBD can be computed as [309]:

$$\begin{aligned}\mu^{\mathrm{l}}_{\mathrm{HBD}}(T, P^{\mathrm{v}}) =& \Delta_{\mathrm{f}} G^0_{\mathrm{HBD}} + RT \ln \frac{N_{\mathrm{HBD}} k_{\mathrm{B}} T}{P^0 V} + \Delta G^{\mathrm{ex,l}}_{\mathrm{HBD}} \\ &+ \overline{V}_{\mathrm{HBD}}(P^{\mathrm{v}} - P^0)\end{aligned} \tag{4.7}$$

in which N_{HBD} is the number of the HBD molecules in the DES liquid phase, $\Delta G^{\mathrm{ex,l}}_{\mathrm{HBD}}$ is the liquid phase excess Gibbs energy of the HBD, computed from the simulations using thermodynamic integration (Eq. 4.2), V is the liquid phase volume of the DES, and $\overline{V}_{\mathrm{HBD}}$ is the partial molar volume of the HBD in the liquid phase. Assuming that the excess volume of the liquid phase is negligible [77], the partial molar volume of the HBD can be approximated by V/N_{HBD}, in which V is the liquid phase volume of the DES. This approximation is supported by the MD simulation results of Celebi et al. [77] for ChClU. Although neglected here for simplicity, the excess volume can in principle be computed from the Kirkwood-Buff integrals [310]. Considering the low vapor pressures of the DESs compared to the value of the reference state pressure P^0 (1 bar), P^{v} can be neglected in the last term of Eq. 4.7. The value of the last term of Eq. 4.7 is often very small compared to the other terms, and is therefore neglected (such as in the derivation by Dawass et al. [272]). For instance, in the simulations of ChClEg (with a molar ratio of 1:2, at 353 K) performed here, the value

of this term was computed as ca. $-0.02\,\mathrm{kJ\,mol^{-1}}$, which is considerably smaller than the computed liquid phase excess Gibbs energy ($\Delta G^{\mathrm{ex,l}}_{\mathrm{HBD}}$) of ethylene glycol, i.e., ca. $28.08\,\mathrm{kJ\,mol^{-1}}$. Although the last term of Eq. 4.7 was not neglected in the computations of this chapter, the aforementioned approximations were carried out for simplification. Considering the small value of this term, these approximations would have negligible influence on the final result.

Using the equality of the liquid and vapor phase chemical potentials (Eqs. 4.6 and 4.7), the partial pressure of the HBD component was computed from the simulations according to:

$$P_{\mathrm{HBD}} = \frac{N_{\mathrm{HBD}} k_{\mathrm{B}} T}{V} \exp\left[\frac{\Delta G^{\mathrm{ex,l}}_{\mathrm{HBD}} - \frac{V}{N_{\mathrm{HBD}}} P^0}{RT}\right] \tag{4.8}$$

It can be observed that in deriving Eq. 4.8, the term $\Delta_{\mathrm{f}} G^0_{\mathrm{HBD}}$ (in Eqs. 4.6 and 4.7) was cancelled out. Therefore, the value of this term was not required in the calculations. As mentioned earlier, in the derivation of the final expression for P_{HBD}, the value of P^{v} on the right hand side of Eq. 4.7 was neglected due to the low vapor pressures of DESs. However, without this approximation, one would need to iteratively solve for the value of P_{HBD} when equating Eqs. 4.6 and 4.7.

The vapor phase chemical potential of choline chloride can be computed according to [309]:

$$\mu^{\mathrm{v}}_{\mathrm{ChCl}}(T, P^{\mathrm{v}}) = \Delta_{\mathrm{f}} G^0_{\mathrm{Ch}} + \Delta_{\mathrm{f}} G^0_{\mathrm{Cl}} + \Delta G^{\mathrm{ex,v}}_{\mathrm{ChCl}} + 2RT \ln \frac{P_{\mathrm{ChCl}}}{P^0} \tag{4.9}$$

where $\Delta_{\mathrm{f}} G^0_{\mathrm{Ch}}$ and $\Delta_{\mathrm{f}} G^0_{\mathrm{Cl}}$ are the Gibbs energies of formation of choline and chloride ions at the reference state pressure $P^0 = 1\,\mathrm{bar}$, $\Delta G^{\mathrm{ex,v}}_{\mathrm{ChCl}}$ is the excess Gibbs energy of choline chloride in the vapor phase (accounting for the interaction between choline and chloride in each isolated ion pair), and P_{ChCl} is the partial pressure of choline chloride. The factor 2 on the right hand side of Eq. 4.9 originates from the fact that a single choline chloride molecule is composed of 2 ions. The vapor phase excess Gibbs energy of choline chloride was computed from gas phase simulations in the NVT enemble using a single fractional group of choline chloride (i.e., one fractional molecule/ion of choline, and one fractional molecule/ion of chloride), according to [309]:

$$\Delta G^{\mathrm{ex,v}}_{\mathrm{ChCl}} = \Delta A^{\mathrm{ex}}_{NV^*T} - RT - RT \ln \frac{V^* P^0}{k_{\mathrm{B}} T} \tag{4.10}$$

where V^* is the volume of the gas phase simulation box, and $\Delta A^{\text{ex}}_{NV^*T}$ is the excess Helmholtz energy of choline chloride at the (fixed) gas phase simulation volume (V^*), computed from thermodynamic integration (Eq. 4.2). The last term in Eq. 4.10 is a volume correction term to $\Delta G^{\text{ex,v}}_{\text{ChCl}}$, from volume V^* to the reference state volume $V^0 = k_{\text{B}}T/P^0$. To correct for the finite size effects, the value of $\Delta G^{\text{ex,v}}_{\text{ChCl}}$ was computed at different simulation volumes V^* from Eq. 4.10, and the results were linearly extrapolated to infinite volume ($V^* \to \infty$) by plotting the values of $\Delta G^{\text{ex,v}}_{\text{ChCl}}$ as a function of the inverse of the size of the simulation box [309, 311].

The liquid phase chemical potential of choline chloride can be computed as [309]:

$$\begin{aligned}\mu^{\text{l}}_{\text{ChCl}}(T, P^{\text{v}}) =& \Delta_{\text{f}}G^0_{\text{Ch}} + \Delta_{\text{f}}G^0_{\text{Cl}} + 2RT \ln \frac{N_{\text{ChCl}} k_{\text{B}} T}{P^0 V} \\ &+ \Delta G^{\text{ex,l}}_{\text{ChCl}} + \overline{V}_{\text{ChCl}}(P^{\text{v}} - P^0)\end{aligned} \tag{4.11}$$

in which N_{ChCl} is the number of choline chloride ion pairs (half of the total number of ions), $\Delta G^{\text{ex,l}}_{\text{ChCl}}$ is the excess Gibbs energy of choline chloride in the liquid phase (from Eq. 4.2), V is the volume of the simulation box of the DES liquid phase, and $\overline{V}_{\text{ChCl}}$ is the partial molar volume of choline chloride in the liquid phase. The factor 2 in the third term of the right hand side of Eq. 4.11 is due to the fact that a single choline chloride molecule consists of 2 ions. Similar to the derivation for the HBD component (Eq. 4.7), P^{v} can be neglected in Eq. 4.11, and $\overline{V}_{\text{ChCl}}$ can be approximated by V/N_{ChCl}.

By equating Eqs. 4.9 and 4.11, the partial pressure of choline chloride in the DESs was computed as:

$$P_{\text{ChCl}} = \frac{N_{\text{ChCl}} k_{\text{B}} T}{V} \exp\left[\frac{\Delta G^{\text{ex,l}}_{\text{ChCl}} - \Delta G^{\text{ex,v}}_{\text{ChCl}} - \frac{V}{N_{\text{ChCl}}} P^0}{2RT}\right] \tag{4.12}$$

in which $\Delta G^{\text{ex,v}}_{\text{ChCl}}$ is the extrapolated value of the vapor phase excess Gibbs energy to infinite volume. Similar to the derivation for the HBD component, by equating Eqs. 4.9 and 4.11, the terms $\Delta_{\text{f}}G^0_{\text{Ch}}$ and $\Delta_{\text{f}}G^0_{\text{Cl}}$ were cancelled out. As for the HBD component, the value of P_{ChCl} would need to be calculated iteratively, if one does not neglect the value of P^{v} on the right hand side of Eq. 4.11.

To investigate the non-ideality of the ChClEg mixture, the activity coefficient of ethylene glycol, γ_{eg}, was computed according to the modified Raoult's law [312]:

$$\gamma_{\mathrm{eg}} = \frac{P_{\mathrm{eg}}}{x_{\mathrm{eg}} P_{\mathrm{eg}}^{\mathrm{sat}}} \tag{4.13}$$

where P_{eg} is the computed partial pressure of ethylene glycol in the vapor phase of ChClEg (from Eq. 4.8), x_{eg} is the mole fraction of ethylene glycol in the liquid phase of ChClEg (Eq. 4.1), and $P_{\mathrm{eg}}^{\mathrm{sat}}$ is the saturated vapor pressure of pure ethylene glycol. To obtain $P_{\mathrm{eg}}^{\mathrm{sat}}$, liquid phase simulations were carried out for pure ethylene glycol, and the excess Gibbs energy was computed at 353 K and 1 bar (in the NPT ensemble) from thermodynamic integration, according to Eq. 4.2. The value of $P_{\mathrm{eg}}^{\mathrm{sat}}$ was then calculated using Eq. 4.8, assuming an ideal gas phase of isolated molecules. The same force field parameters were used for pure ethylene glycol as in the simulations of ChClEg. The activity coefficient calculations were not performed for choline chloride, due to the fact that pure choline chloride is a solid (with a melting point of ca. 575 K) at the simulated temperatures. Urea has an experimental melting point of ca. 406 K, which is lower than the simulated temperature of 433 K. However, test MC simulations of pure urea (using the same force field parameters as in ChClU) showed a glassy state at 433 K, with limited changes in the configuration of the system. A density of ca. 1400 kg m^{-3} was obtained for urea at 433 K and 1 bar, which is considerably larger than the experimental value of ca. 1335 kg m^{-3} at room temperature and pressure (solid state). Thus, the force field parameters used in this chapter are likely unsuitable for simulations of pure urea. The activity coefficient was therefore not calculated here for urea in ChClU mixtures.

4.3 Results and discussion

4.3.1 Partial pressures and vapor phase compositions

To compute the excess Gibbs energies of the HBA and HBD components, the function $\langle \partial U/\partial \lambda \rangle$ was integrated according to Eq. 4.2. The obtained values of $\langle \partial U/\partial \lambda \rangle$ (averaged over all independent runs), as a function of λ, are presented in Fig. 4.2 for the HBD (urea or ethylene glycol) and choline chloride components of ChClU (at 393 K) ChClEg (at 353 K). A similar figure was obtained for choline chloride in the vapor phase simulations (Fig. A19 of the Appendix). For choline chloride in the vapor phase, the excess Gibbs

energy ($\Delta G^{\mathrm{ex,v}}_{\mathrm{ChCl}}$) was computed using Eq. 4.10. To correct for the finite size effects, the obtained data for $\Delta G^{\mathrm{ex,v}}_{\mathrm{ChCl}}$ were linearly extrapolated to infinite volume, as a function of the inverse of the box size [309, 311]. The vapor phase excess Gibbs energies of choline chloride ($\Delta G^{\mathrm{ex,v}}_{\mathrm{ChCl}}$) in ChClEg and ChClU, as a function of the inverse of the box size, are presented in Fig. 4.3 for box sizes of 35 Å, 50 Å, 75 Å, and 100 Å. It can be observed in Fig. 4.3 that for both DESs, the values of $\Delta G^{\mathrm{ex,v}}_{\mathrm{ChCl}}$ show a linear dependence (within the error bars) on the inverse of the box size.

The computed values for the excess Gibbs energies, partial pressures, and vapor phase mole fractions are listed in Table 4.2 for both components of ChClU and ChClEg, at a molar ratio of 1:2 (eutectic ratio) and various temperatures. It can be observed that for both ChClU and ChClEg, the liquid phase excess Gibbs energies of choline chloride ($\Delta G^{\mathrm{ex,l}}_{\mathrm{ChCl}}$) are significantly larger than those of the HBD components ($\Delta G^{\mathrm{ex,l}}_{\mathrm{HBD}}$), indicating a larger magnitude for the intermolecular interactions of choline chloride in the mixtures. Although partially compensated by $\Delta G^{\mathrm{ex,v}}_{\mathrm{ChCl}}$, the larger excess Gibbs energies of choline chloride compared to those of the HBD molecules in the DES mixtures, resulted in considerably smaller partial pressures for choline chloride (Table 4.2). Additionally, the larger number of HBD molecules in each DES mixture, compared to that of choline chloride, contributes to the larger partial pressure of the HBD component. As can be observed in Table 4.2, the liquid phase excess Gibbs energy of urea in ChClU is larger than that of ethylene glycol in ChClEg, resulting in a considerably larger vapor pressure of ethylene glycol (by two orders of magnitude) compared to urea. This is consistent with the fact that ethylene glycol in pure form is much more volatile than pure urea [313, 314]. The absolute values of the liquid and vapor phase excess Gibbs energies of choline chloride in ChClEg are larger than in ChClU. The differences in the values of $\Delta G^{\mathrm{ex,v}}_{\mathrm{ChCl}}$, and to some extent the values of $\Delta G^{\mathrm{ex,l}}_{\mathrm{ChCl}}$, between ChClEg and ChClU are due to the larger values of ionic charges used for choline chloride in ChClEg (+/- 0.9) compared to those in ChClU (+/- 0.8). The absolute value of the 'net' excess Gibbs energy of choline chloride ($\Delta G^{\mathrm{ex,l}}_{\mathrm{ChCl}} - \Delta G^{\mathrm{ex,v}}_{\mathrm{ChCl}}$) is also larger in ChClEg than in ChClU, resulting in a much smaller partial pressure for choline chloride in ChClEg.

As can be observed in Table 4.2, the values of the partial pressures of the HBD and HBA components are closer to each other in ChClU compared to ChClEg. As a result, the vapor phase of ChClU is composed of finite amounts of both urea (ca. 91% at 353 K) and choline chloride (ca. 9% at 353 K), while the vapor phase of ChClEg is entirely composed of ethylene glycol. As expected, an increase in temperature yields smaller excess Gibbs

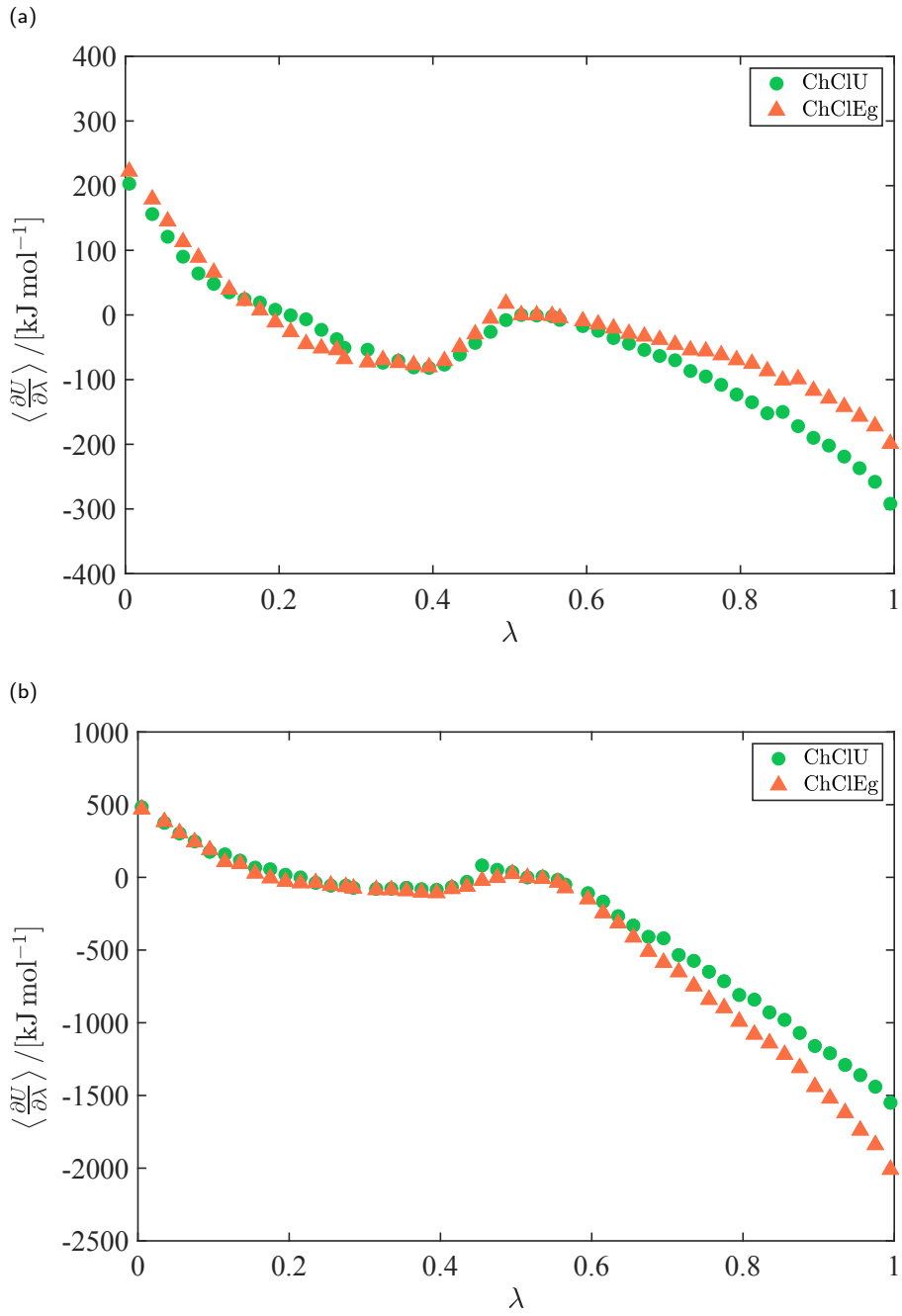

Figure 4.2: Ensemble averages of the derivative of the total energy with respect to λ, as a function of λ, for (a) the HBD (urea or ethylene glycol), and (b) choline chloride in ChClU (at 393 K) and ChClEg (at 353 K), from the liquid phase simulations.

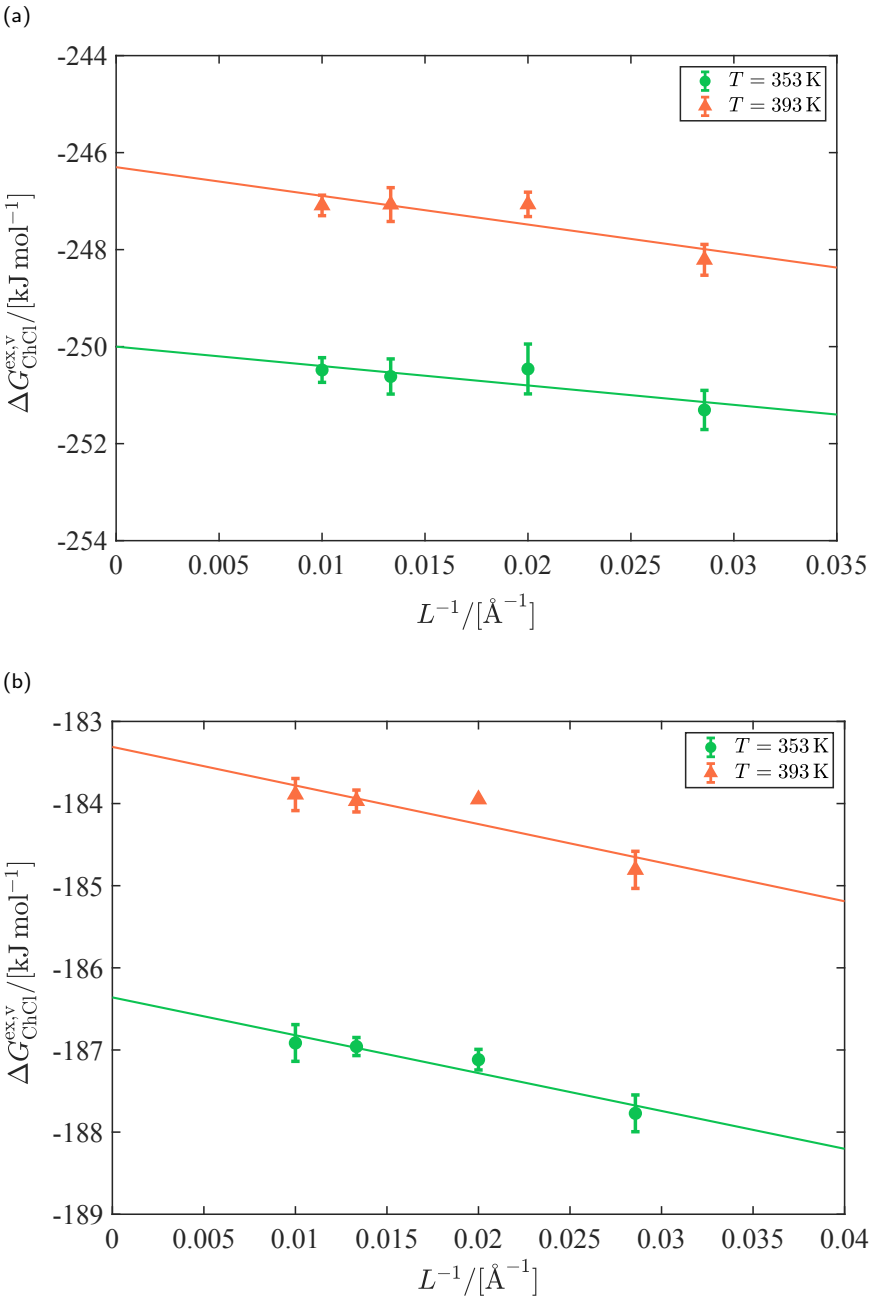

Figure 4.3: Computed vapor phase excess Gibbs energies of choline chloride in (a) ChClEg, and (b) ChClU, as a function of the inverse of the box size, at different temperatures. The solid lines depict the linear fits used for the extrapolation of $\Delta G^{\mathrm{ex,v}}_{\mathrm{ChCl}}$ to infinite volume.

Table 4.2: Computed liquid phase excess Gibbs energies, vapor phase excess Gibbs energies (only for choline chloride as these values are zero by definition for the HBD components), partial pressures, and vapor phase mole fractions for the HBD component, i.e., urea or ethylene glycol, and choline chloride (HBA component) in ChClU and ChClEg, at various temperatures, from MC simulations. The values in parentheses are the standard deviations to the precision of the last significant digit.

DES	T/[K]	$\Delta G^{\mathrm{ex,l}}_{\mathrm{HBD}}$/[kJ mol^{-1}]	$\Delta G^{\mathrm{ex,l}}_{\mathrm{ChCl}}$/[kJ mol^{-1}]	$\Delta G^{\mathrm{ex,v}}_{\mathrm{ChCl}}$/[kJ mol^{-1}]	P_{HBD}/[Pa]	P_{ChCl}/[Pa]	y_{HBD}	y_{ChCl}
ChClU	393	-51.2(10)	-299.6(33)	-186.4(2)	4.8(14)	$4.8(20) \times 10^{-1}$	0.91(7)	0.09(7)
	433	-47.4(4)	-291.1(28)	-183.5(2)	$6.0(6) \times 10^{1}$	5.3(20)	0.92(6)	0.08(6)
ChClEg	353	-30.3(5)	-398.3(28)	-250.1(4)	$7.9(13) \times 10^{2}$	$1.4(6) \times 10^{-4}$	1.00(0)	0.00(0)
	393	-27.6(5)	-385.7(3)	-246.5(3)	$5.6(8) \times 10^{3}$	$7.1(3) \times 10^{-3}$	1.00(0)	0.00(0)

energies and larger partial pressures for both the HBA and HBD components of ChClU and ChClEg. The computed vapor phase compositions are, however, not significantly affected by temperature (Table 4.2). It is important to note that as no experimental data are available in literature for the partial pressures and vapor phase compositions of ChClEg and ChClU, no comparisons can be made between the simulation results and experimental measurements. The computed values for the partial pressures and vapor compositions of the DESs, thus, serve as the first estimates for these parameters. It is important to note, however, that vapor phase compositions and partial pressures have been measured and reported in literature for a few other (mostly hydrophobic) DESs [26, 42, 296, 299]. For instance, the measurements of Dietz et al. [42] indicate the vapor phase mole fractions of the more volatile components of the considered hydrophobic DESs to lie in the range of 0.85 to 1.00 This is in agreement with the results obtained in this chapter, where the vapor phases of ChClEg and ChClU are shown to be dominated by the more volatile component (HBD), although to different extents (Table 4.2).

4.3.2 Vapor pressures and enthalpies of vaporization

The vapor pressure of each DES mixture was obtained by summing the computed partial pressures of the HBA and HBD components (Eq. 4.5). The enthalpies of vaporization, ΔH^{vap}, were calculated by correlating the vapor pressures with temperature, using the Clausius-Clapeyron equation (Eq. 2.2) [163]. Alternatively, excess enthalpies, and thus enthalpies of vaporization, can be computed from Kirkwood-Buff integrals [315], or from thermodynamic integration of the covariance of the enthalpy and $\partial U/\partial\lambda$ [316]. These methods are not considered further here.

The calculated vapor pressures and enthalpies of vaporization of ChClU and ChClEg (both with molar ratios of 1:2) are listed in Table 4.3. The experimental data by Ravula et al. [50], and Shahbaz et al. [51] (denoted by 'exp1' and 'exp2' in Table 4.3, respectively) are also listed for comparison. The experimental values for the vapor pressures of the DESs at higher temperatures (433 K for ChClU, and 393 K for ChClEg) were obtained by extrapolation of the data, using Eq. 2.2. The experimental data sets were well described by Eq. 2.2, with correlation coefficients of $R^2 > 0.995$. The quality of the regression could not be evaluated for the simulation results, as the vapor pressures were only computed at two temperatures.

As also shown in Table 2.1, there is a clear disparity between the two sets of experimental data by Ravula et al. [50], and Shahbaz et al. [51] for ChClU. It can observed in Table 4.3 that the data by Ravula et al.

Table 4.3: Computed vapor pressures and enthalpies of vaporization of ChClU and ChClEg at various temperatures, from MC simulations, compared with the experimental data by Ravula et al. [50] (exp1), and Shahbaz et al. [51] (exp2). The values in parentheses are the standard deviations to the precision of the last significant digit.

DES	T/[K]	$P^{\mathrm{v}}_{\mathrm{MC}}$/[Pa]	$P^{\mathrm{v}}_{\mathrm{exp1}}$/[Pa]	$P^{\mathrm{v}}_{\mathrm{exp2}}$/[Pa]	$\Delta H^{\mathrm{vap}}_{\mathrm{MC}}$/[kJ mol^{-1}]	$\Delta H^{\mathrm{vap}}_{\mathrm{exp1}}$/[kJ mol^{-1}]	$\Delta H^{\mathrm{vap}}_{\mathrm{exp2}}$/[kJ mol^{-1}]
ChClU	393	5.3(15)	2.9×10^1	2.9	89.3(100)	79.0	46.9
	433	$6.6(6) \times 10^1$	2.8×10^2 [a]	1.1×10^1 [a]			
ChClEg	353	$7.9(13) \times 10^2$	9.5×10^1	-	56.6(60)	55.8	-
	393	$5.6(8) \times 10^3$	7.2×10^2 [a]	-			

[a] Extrapolated values

[50] indicate considerably larger values for the vapor pressure and enthalpy of vaporization of ChClU, compared to the data by Shahbaz et al. [51]. These discrepancies may be related to the difficulty of measuring such low pressures and/or the use of the TGA method, which has been questioned in other studies of DESs [42]. As a result of these inconsistencies, it is difficult to make precise comparisons between the simulation results and the experimental data. As can be observed in Table 4.3, the computed vapor pressure of ChClU at 393 K from the simulations lies between the experimental data, but closer to the value by Shahbaz et al. [51]. Similarly, at 433 K, the computed vapor pressure of ChClU lies between the extrapolated experimental values. It can be observed that the computed enthalpy of vaporization of ChClU is in agreement with the value by Ravula et al. [50], while it is considerably larger than the value reported by Shahbaz et al. [51]. For ChClEg, at both temperatures, the computed vapor pressures are significantly larger than the (extrapolated) experimental values by Ravula et al. [50], possibly due to an overestimation of the volatility of ethylene glycol in ChClEg from the simulations (Table 4.2). The computed and experimental enthalpies of vaporization of ChClEg are, however, in excellent agreement. As can be observed in Table 4.3, at 393 K, the computed vapor pressure of ChClEg is considerably larger than that of ChClU (consistent with the experimental data), due the larger partial pressure of ethylene glycol compared to that of urea (Table 4.2). The computed and experimental vapor pressures of both DESs are much larger than the vapor pressures of commonly studied ILs [50, 317], e.g., 0.93 Pa for [bmim][BF_4] at 503 K [50].

In chapter 2, the enthalpies of vaporization of the HBA and HBD components of several choline chloride-based DESs were computed from average potential energies in separate liquid and gas phase MD simulations. From those simulations, the enthalpy of vaporization of urea in ChClU (with the same GAFF force field parameters as used here), and the enthalpy of vaporization of ethylene glycol in ChClEg (using OPLS force field) were obtained as 107 kJ mol^{-1} and 73 kJ mol^{-1}, respectively (Table 2.2). These values are in agreement with the enthalpies of vaporization of ChClU and ChClEg obtained in this chapter (Table 4.3). Such agreement is likely due to the fact that the vapor phase of these DESs is dominated by the HBD component (urea or ethylene glycol), as supported by the results in Table 4.2. The method of computation of the enthalpies of vaporization based on average liquid and gas phase potential energies (as used in chapter 2), has also been employed in other studies to compute the vaporization enthalpies/energies of DESs [118, 127] and ILs [284, 306, 308, 318]. Although this is a simple and computationally cheap method for obtaining

the enthalpy of vaporization, it does not provide the vapor pressure and vapor phase composition (in case of mixtures), as does the method used in this chapter. Moreover, for mixtures (e.g., DESs), only the vaporization enthalpies of different components, such as HBA, HBD, or clusters, can be obtained, and the enthalpy of vaporization of the mixture cannot be computed. Neither of these methods, however, provide the configuration of the molecules in the gas phase (e.g., isolated molecules/ions, ion pairs, dimers, or clusters), and this configuration must therefore be assumed in the simulations. As mentioned in Section 4.1, the use of MC simulations in the Gibbs ensemble (performed by Rai and Maginn [303, 304] for ILs) directly provides the gas phase configuration of molecules. However, for such low vapor pressures as obtained in this chapter, a very large system size would be necessary for such simulations, which would result in a higher computational cost to achieve the same level of precision. The system sizes considered here are relatively small, saving additional computational costs.

4.3.3 Effect of liquid composition on DES properties

The densities of the DESs with different mole fractions of the HBD (or HBA:HBD molar ratios) were computed directly from the liquid phase simulations in the *NPT* ensemble. The results are presented in Fig. 4.4, for ChClEg at 353 K, and ChClU at 393 K. It can be observed in Fig. 4.4 that the density of ChClU increases significantly by increasing the mole fraction of the HBD (urea). This is consistent with the findings of Celebi et al. [77] from MD simulations (using the same force field), and is possibly due to the larger (experimental) density of pure urea (ca. $1335\,\mathrm{kg\,m^{-3}}$ at room conditions), compared to that of pure choline chloride (ca. $1024\,\mathrm{kg\,m^{-3}}$ at room conditions). At an HBD mole fraction of 0.67 (1:2 molar ratio), the density of ChClU is overestimated from the simulations (by 2.8%) compared to the (extrapolated) experimental value by Yadav and Pandey [181], at the same temperature. This overestimation has also been observed in MD studies of ChClU with the same force field parameters [61, 128], and is not considered significant. Currently, no experimental data are available for the density of ChClU at other liquid compositions than the eutectic ratio. For ChClEg, the simulation results indicate a negligible effect of the mole fraction of ethylene glycol on the liquid density. Such insensitivity of the density of ChClEg with respect to liquid composition has also been experimentally observed by Abbott et al. [4] at 293 K, although in that study, the density of ChClEg slightly decreased as the mole fraction of ethylene glycol was increased. The small influence of the liquid composition on the density of ChClEg can be explained by the relatively close densities of pure choline

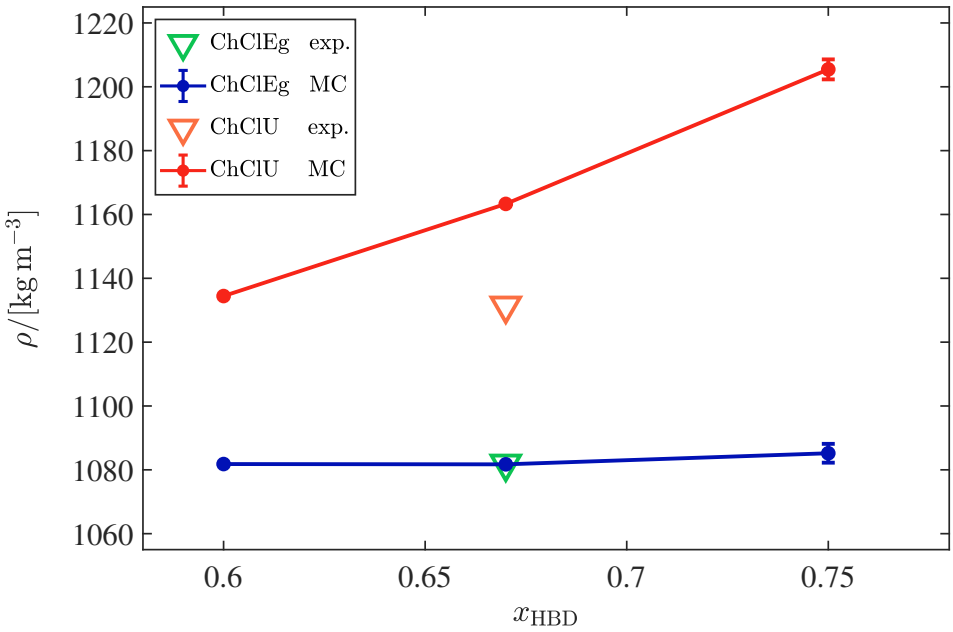

Figure 4.4: Computed liquid densities of ChClEg (at 353 K) and ChClU (at 393 K) as a function of the mole fraction of the HBD component (ethylene glycol or urea) in the liquid phase. The solid lines are drawn to guide the eye. The (extrapolated) experimental data by Yadav and Pandey [181] (for ChClU), and Yadav et al. [36] (for ChClEg) are also shown for comparison.

chloride (ca. $1024\,\mathrm{kg\,m^{-3}}$ at room conditions) and pure ethylene glycol (ca. $1113\,\mathrm{kg\,m^{-3}}$ at room conditions). As shown in Fig. 4.4, the computed density of ChClEg is in excellent agreement with the experimental value by Yadav et al. [36] at the HBD mole fraction of 0.67. Just as for ChClU, no experimental data are currently available for the density of ChClEg at other compositions, at the temperatures considered here. Similar results were obtained for the densities of ChClEg and ChClU at other temperatures, as presented in Fig. A20 of the Appendix. The difference between the computed density of ChClU and the experimental value increases with an increase in temperature, i.e., 3.9% relative deviation at 433 K compared to 2.8% at 393 K, indicating the reduced suitability of the used force field parameters at higher temperatures. For ChClEg, the excellent agreement between the computed density and the experimental measurement is maintained at the higher temperature of 393 K (Fig. A20). It is important to note that for achieving a better agreement between the computed densities of ChClU and experimental data, the force field parameters would need to be refined. This would possibly result in an increase in the computed vapor

pressures of ChClU and the partial pressures of its components (listed in Tables 4.2 and 4.3), due to the weakening of the intermolecular forces at a reduced density. Furthermore, the charge scaling factors used for the cation and anion were originally obtained based on the properties of ChClU and ChClEg, with HBA:HBD molar ratios of 1:2. This means that the accuracy of the models may be compromised at other liquid compositions. However, due to the lack or scarcity of experimental data for these DESs at other compositions, it is currently not possible to fine-tune the existing force field parameters.

The computed partial pressures of the HBD components of ChClEg (ethylene glycol) and ChClU (urea) are presented in Fig. 4.5, as a function of the liquid phase mole fraction of the HBD. As can be observed in Fig. 4.5, with an increase in x_{HBD} from 0.6 to 0.75, the partial pressure of ethylene glycol increases significantly: from 523 Pa to 1757 Pa, at 353 K, and from 4133 Pa to 10837 Pa, at 393 K. In sharp contrast, the partial pressures of urea only slightly increase with an increase in x_{HBD} from 0.6 to 0.75. These variations in the partial pressure of urea, however, fall within the uncertainty limits (shown with error bars in Fig. 4.5). Considering the small differences in the values of x_{HBD}, such small changes in the partial pressure of urea imply the insensitivity of its activity coefficient, and thus non-ideality, towards the liquid phase composition (based on Eq. 4.13), within the studied range of x_{HBD}. Celebi et al. [77] quantified the non-ideality of ChClU from MD simulations by computing the so-called thermodynamic factor, defined (for a binary mixture) as [319–321]:

$$\Gamma = 1 + \left(\frac{\partial \ln \gamma_1}{\partial \ln x_1} \right)_{T,P} \tag{4.14}$$

where γ_1 is the activity coefficient of component 1 (e.g., urea) of the binary mixture, and x_1 is the liquid phase mole fraction of component 1. Celebi et al. [77] found a non-ideal behavior for ChClU (values of Γ larger than 1), which was only slightly affected by the liquid phase mole fraction of urea (consistent with the results of Fig. 4.5b). It is possible that increasing the concentration of ethylene glycol largely disrupts the hydrogen bond network of ChClEg, resulting in an increase in the vapor pressure, whereas the hydrogen bonding network of ChClU is retained or restructured (and the vapor pressure not considerably changed) when the urea content is increased. A detailed comparison of the two systems using hydrogen bond analysis is required to corroborate this [61, 77, 118, 121]. The influence of the liquid phase composition on the partial pressures of choline chloride

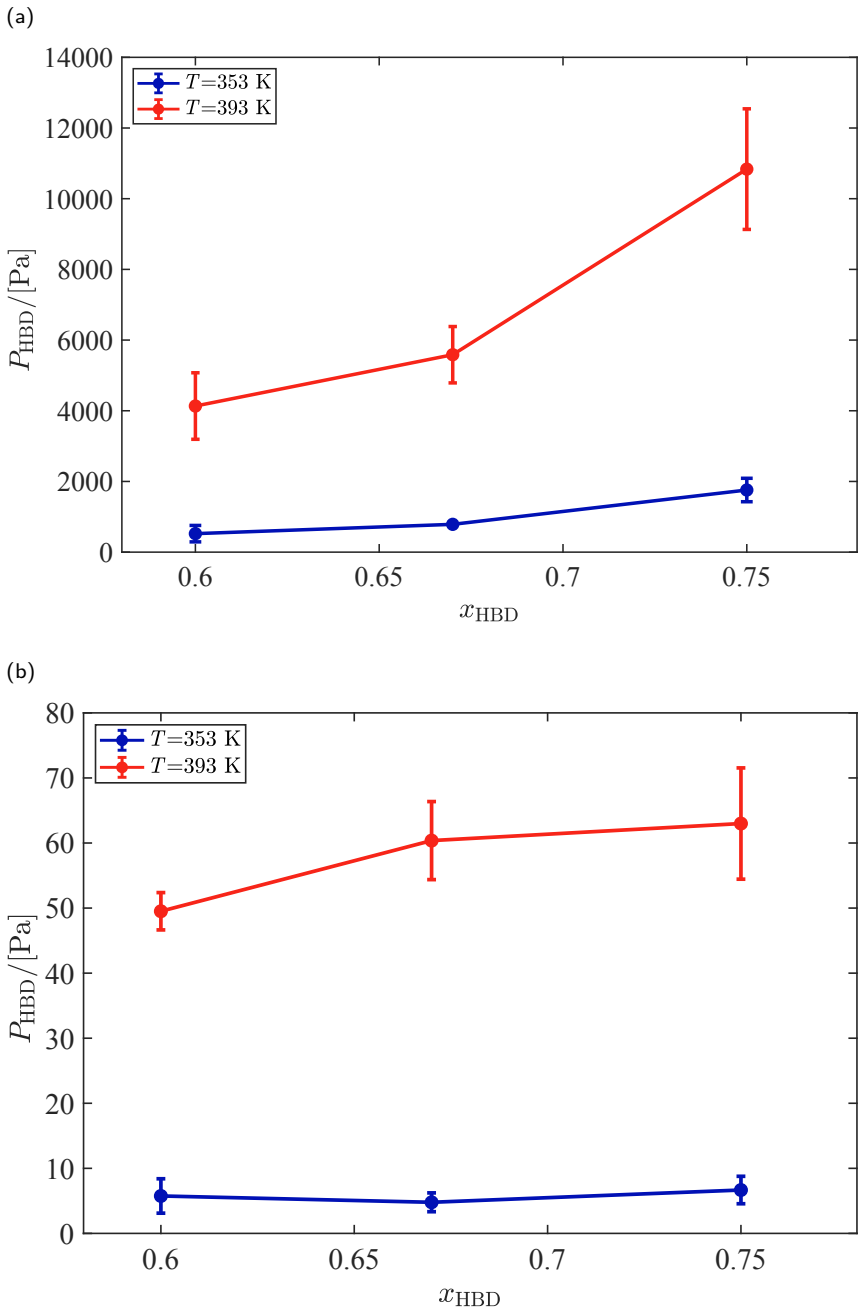

Figure 4.5: Computed partial pressures of (a) ethylene glycol in ChClEg, and (b) urea in ChClU, at various temperatures, as a function of the liquid phase mole fraction of the HBD component (ethylene glycol or urea). The solid lines are drawn to guide the eye.

in both DESs is presented in Fig. 4.6. Despite the slight decrease in the average partial pressure of choline chloride with an increase in the mole fraction of the HBD (except in ChClEg at 353 K), the differences generally fall within the uncertainty limits, implying a negligible influence of the liquid composition on the partial pressure of choline chloride. For future research, it is recommended to compute the partial pressures over a wider range of HBD mole fractions, where the differences in the partial pressures may become more conspicuous. One should, however, be cautious when considering larger deviations from the eutectic molar ratio, as transition to solid phase may occur for either of the components. Therefore, it may be necessary to consider higher temperatures for such computations. Additionally, as explained earlier, the accuracy of the force field may be reduced at larger deviations from the molar ratio for which the optimal force field parameters were obtained (most often the eutectic ratio).

The y-x phase diagram, i.e., the vapor phase mole fraction as a function of the liquid phase mole fraction, is presented in Fig. 4.7 for the ChClU components, at 393 K. It can be observed that at all the liquid compositions, a considerable amount of choline chloride (7%-12%, mole fraction-based) is present in the vapor phase. As expected, by increasing the urea content in the liquid phase, the average vapor phase mole fraction of choline chloride decreases, while that of urea increases, with slopes of less than unity for both components. Similar values and trends were observed for the vapor phase composition of ChClU at 433 K, as provided in Fig. A21 of the Appendix. At both temperatures, the variations in the vapor phase composition with the liquid phase mole fraction of urea fall within the uncertainty limits. From the computed vapor phase and liquid phase mole fractions, the relative volatilities of urea with respect to choline chloride were calculated according to [322]:

$$\alpha_{ij} = \frac{y_i/x_i}{y_j/x_j} \tag{4.15}$$

where i and j represent urea and choline chloride, respectively. The relative volatitilies of urea with respect to choline chloride were computed at 393 K as 4.7, 4.9, and 4.6 at urea mole fractions of 0.6, 0.67, and 0.75, respectively. These values were computed at 433 K as 5.4, 5.6, and 7.6, respectively, indicating an increase in the relative volatility with an increase in temperature, particularly at $x_{\mathrm{HBD}} = 0.75$. Although Fig. 4.7 provides useful information on the phase equilibrium of ChClU, it does not quantify the non-ideality of the mixture. Measurements of the solid-liquid phase

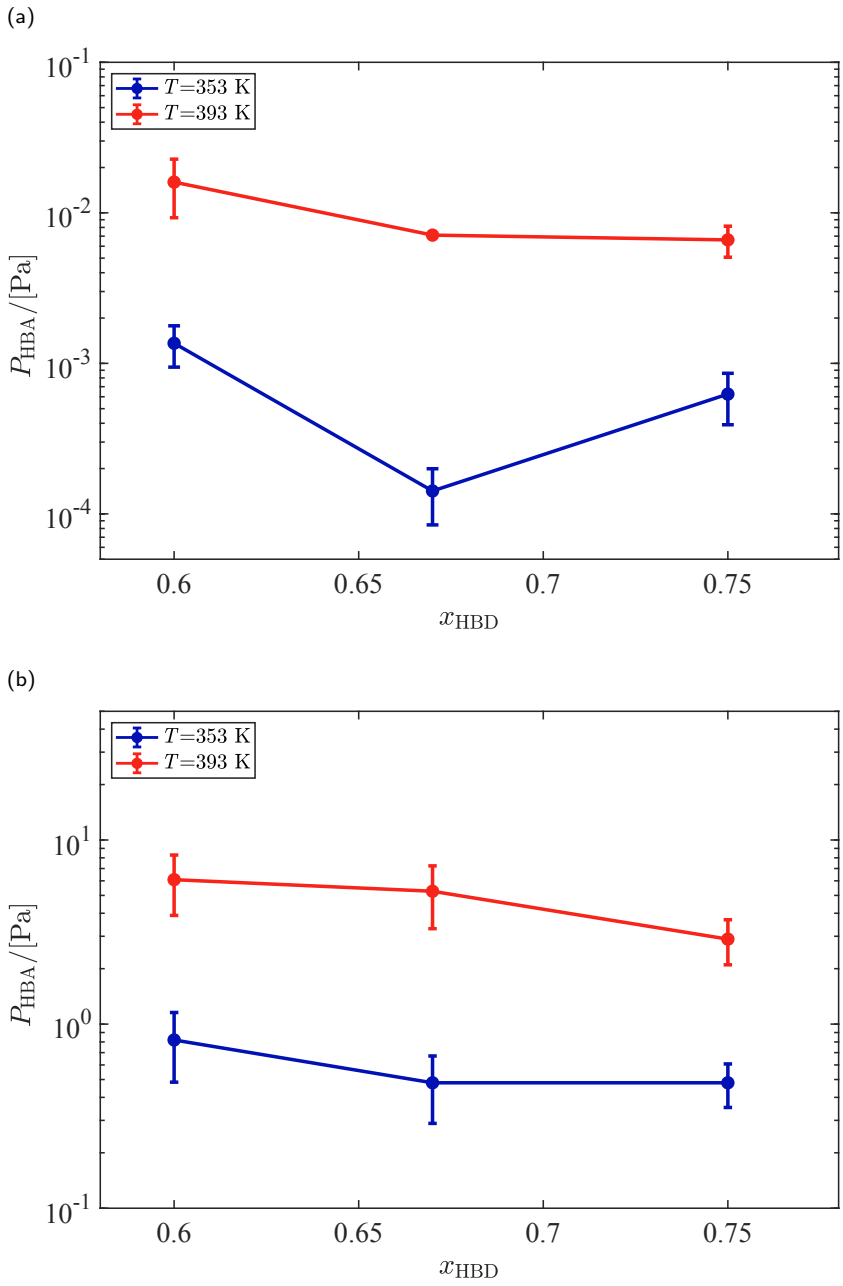

Figure 4.6: Computed partial pressures of choline chloride (the HBA component) in (a) ChClEg, and (b) ChClU, at various temperatures, as a function of the liquid phase mole fraction of the HBD component (ethylene glycol or urea). The solid lines are drawn to guide the eye.

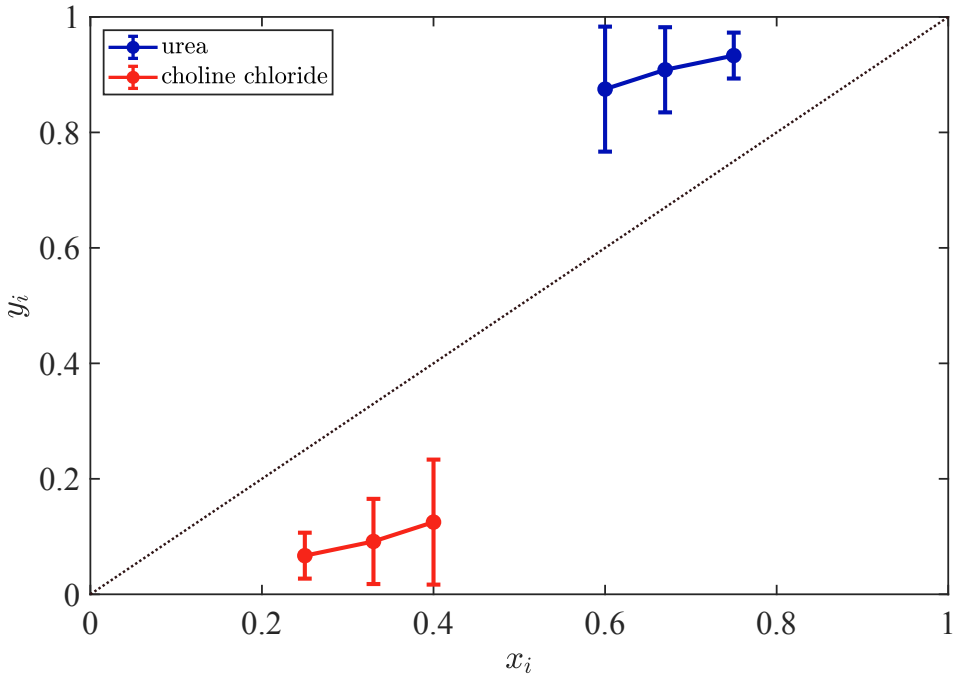

Figure 4.7: Computed vapor phase mole fraction of each component i (urea or choline chloride) of ChClU as a function of its mole fraction in the liquid phase, at 393 K. The solid lines connecting the data points, are drawn to guide the eye. The black dotted line denotes $y_i = x_i$.

equilibrium of ChClU have shown a high non-ideality (with a negative deviation from Raoult's law) for urea, and an almost ideal behavior for choline chloride [14, 32]. Using the vapor-liquid equilibrium, the non-ideality of real mixtures can be evaluated by computing the activity coefficients of the mixture components from the modified Raoult's law (Eq. 4.13). However, as explained in Section 4.2, pure urea and pure choline chloride are solids at the temperatures considered here. As a result, the pure component vapor pressures (P^{sat}), and thus the activity coefficients could not be calculated from the simulations.

To study the non-ideality of ChClEg, the vapor pressure of pure (liquid) ethylene glycol was computed at 353 K, using the same force field parameters as in ChClEg. The vapor pressure of pure ethylene glycol was computed as ca. 2575 Pa, a value considerably larger than the experimental value of 676 Pa, as reported by Verevkin [323]. The volatility of pure ethylene glycol is therefore overestimated with the GAFF force field parameters used here. The computed density of pure ethylene glycol (ca. 1070 kg m^{-3}) is nonethe-

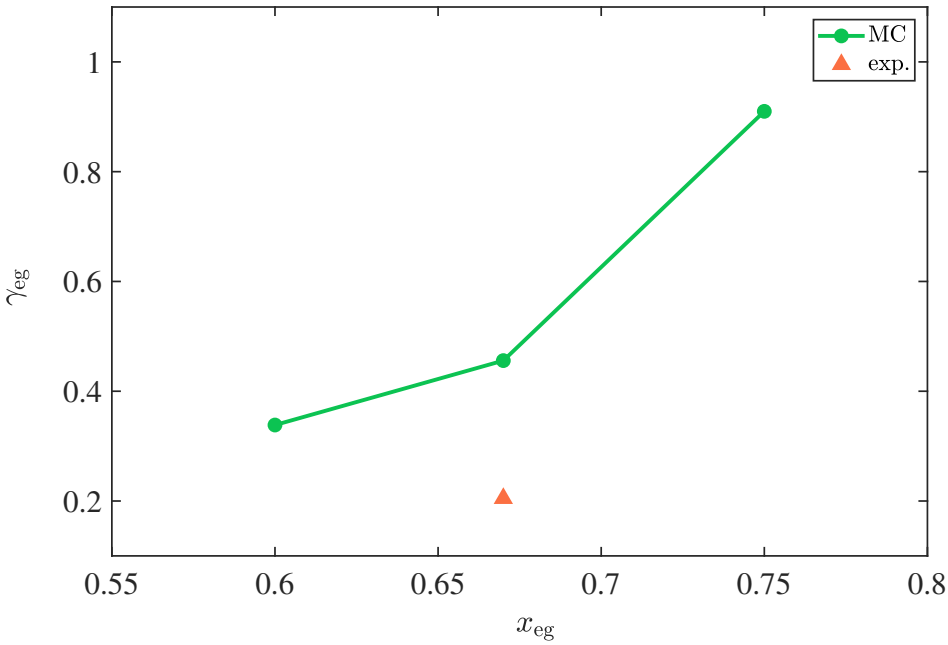

Figure 4.8: Computed activity coefficients of ethylene glycol (denoted by 'eg') in ChClEg at 353 K, as a function of the mole fraction of ethylene glycol in the liquid phase of the DES, compared with the value obtained from experimental data [50, 323]. The solid line is drawn to guide the eye.

less in close agreement (1.5% relative deviation) with the experimental value by Skylogianni et al. [324] (1087 $\mathrm{kg\,m^{-3}}$). The activity coefficient of ethylene glycol in ChClEg was computed using Eq. 4.13, from the obtained vapor pressures in pure form and in the DES mixture. For comparison, the experimental activity coefficient of ethylene glycol in ChClEg was computed based on the vapor pressure data by Verevkin [323] (for pure ethylene glycol), and Ravula et al. [50] (for ChClEg), assuming the vapor phase of ChClEg to be entirely composed of ethylene glycol (as supported by the results in Table 4.2). The activity coefficient results are presented in Fig. 4.8 for various liquid phase mole fractions of ethylene glycol in ChClEg. While the computed vapor pressures of both pure ethylene glycol and ChClEg are overestimated compared to the experimental measurements, the calculated activity coefficient (proportional to the ratio of these vapor pressures, assuming $y_{eg} = 1$ in ChClEg) at the HBD mole fraction of 0.67 is in reasonable agreement with the experimental value. The obtained activity coefficient of ethylene glycol in ChClEg from the simulations sharply increases with an increase in the liquid phase mole fraction of ethylene glycol, since at the

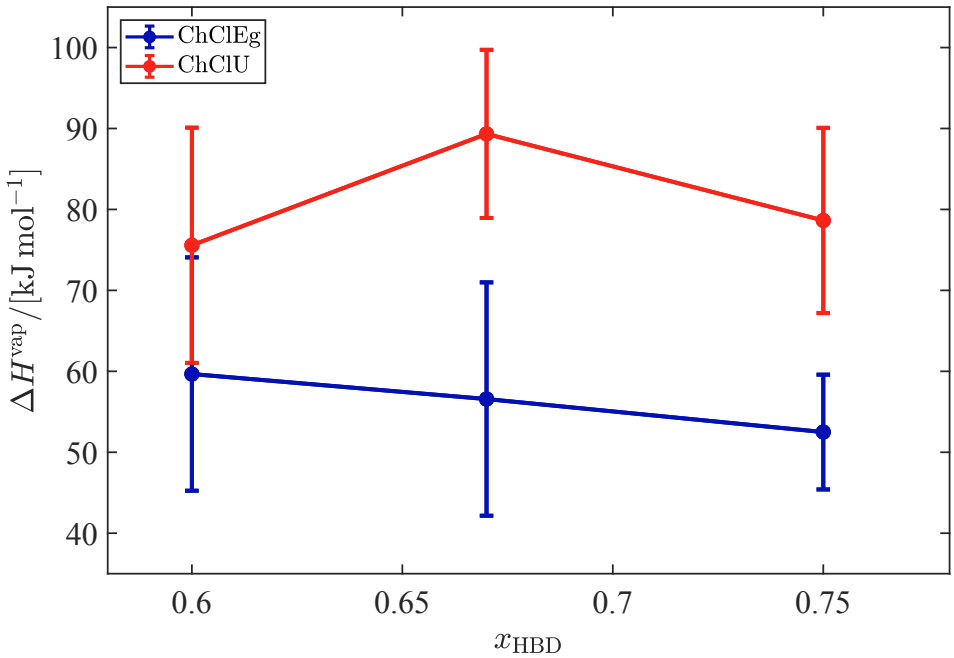

Figure 4.9: Computed enthalpies of vaporization of ChClEg and ChClU as a function of the liquid phase mole fraction of the HBD component (ethylene glycol or urea). The enthalpies of vaporization were obtained by fitting the Clausius-Clapeyron relation (Eq. 2.2) to the computed vapor pressures in temperature ranges of 353 K to 393 K for ChClEg, and 393 K to 433 K for ChClU. The solid lines are drawn to guide the eye.

higher ethylene glycol mole fractions, the liquid composition of the DES approaches that of pure ethylene glycol. Therefore, at the liquid phase mole fractions of 0.6 and 0.67, ethylene glycol shows a non-ideal behavior with large negative deviations from Raoult's law, while at the mole fraction of 0.75, it exhibits an almost ideal behavior. This increase in the activity coefficient of ethylene glycol in ChClEg is the main contributor to the drastic increase in its partial pressure at higher liquid phase mole fractions (Fig. 4.5).

The enthalpies of vaporization were also computed at different liquid phase compositions. The results are presented in Fig. 4.9 for both DESs. It can be observed that the differences in the enthalpies of vaporization at the various mole fractions of the HBD lie within the error bars (standard deviations). The error bars were calculated based on the propagation of errors of the corresponding partial pressures. The computed enthalpies of vaporization are thus insensitive to composition changes within the considered range. The computation of the enthalpies of vaporization can be improved

by lowering the uncertainty of data at each vapor pressure point (e.g., by longer simulations), as well as increasing the number of temperature points to be used in Eq. 2.2.

Overall, the GAFF force field performs reasonably well regarding the computation of the vapor pressures and enthalpies of vaporization of the DESs, although a larger number of experimental data is required for a more precise comparison. It would be interesting in the future to study the influence of the force field parameters and, in particular, the charge scaling value on the accuracy of the computed properties. Based on the small values of the standard deviations reported here, i.e., average standard deviations of 1.5 kJ mol^{-1} for the liquid phase excess Gibbs energies, and 174 Pa for partial pressures, thermodynamic integration is a reliable method for the study of the vapor-liquid phase equilibrium of DESs. This method is therefore recommended for the computation of the vapor pressures, vapor phase compositions, and enthalpies of vaporization of other DESs, for which the values of these properties are unavailable or scarce in literature. It is important to note that the computations in this chapter were carried out at high temperatures, where the viscosities of the DESs are relatively low, i.e., below 9 cP for ChClU [181], and below 5 cP for ChClEg [185]. Therefore, the equilibration of the system is relatively fast, and sufficient sampling can be performed for the computation of the excess Gibbs energy. These computations would become much more challenging at lower temperatures, where the viscosities of the DESs are exponentially larger, and the equilibration and sampling efficiencies are deteriorated. An alternative approach for the low temperature computations would therefore be to obtain the vapor pressures at high temperatures, and use the Clausius-Clapeyron relation (Eq. 2.2) or other correlations [51] to extrapolate the vapor pressures to lower temperatures.

4.4 Conclusions

The excess Gibbs energies, vapor pressures, and vapor phase compositions of ChClEg and ChClU were computed at various temperatures from MC simulations, using thermodynamic integration. Based on the obtained vapor pressures, the enthalpies of vaporization were calculated, and compared with the scarce experimental data available in literature. The influence of the liquid composition of the DESs on the computed properties was studied by considering different HBA:HBD molar ratios (or HBD mole fractions) of 1:1.5, 1:2, and 1:3. For ChClU, the computed vapor pressure and enthalpy of vaporization were in reasonable agreement with experi-

mental data. For ChClEg, the computed enthalpy of vaporization was in excellent agreement with the experimental value, while the vapor pressure was considerably overestimated in the simulations. The computed vapor pressures of both DESs were larger than those of common ILs as reported in literature. Based on the computations of the vapor pressures and enthalpies of vaporization, the GAFF force field performed reasonably well. The inconsistencies of the experimental data, however, hindered a precise comparison with the simulation results. The computed partial pressures indicated a much larger volatility of ethylene glycol in ChClEg, compared to that of choline chloride, causing the vapor phase of ChClEg to consist entirely of ethylene glycol. For ChClU, small amounts of choline chloride (7%-12% mole fraction-based) were present in the vapor phase. The density of ChClU was found to significantly increase as the mole fraction of urea in the liquid phase was increased, whereas the density of ChClEg was not considerably influenced by the mole fraction of ethylene glycol in the liquid phase. The computed partial pressure of ethylene glycol in ChClEg increased with an increase in its liquid phase mole fraction, while the partial pressure of urea in ChClU, and the partial pressures of choline chloride in both DESs were relatively insensitive to the liquid phase composition. As expected, the average vapor phase mole fractions of both components of ChClU slightly increased with an increase in the corresponding liquid phase mole fractions. The computed vaporization enthalpies of both DESs were not considerably affected by the liquid phase compositions. The non-ideal behavior of ethylene glycol in ChClEg was evaluated by computing activity coefficients. It was observed that consistent with experimental data, ethylene glycol exhibited a non-ideal behavior, with negative deviations from Raoult's law, particularly at the lower liquid phase mole fractions. The combination of force field-based MC simulations and thermodynamic integration was shown to be suitable for the computation of the vapor-liquid phase equilibrium of DESs.

Chapter 5

Thermodynamic, transport, and structural properties of hydrophobic deep eutectic solvents

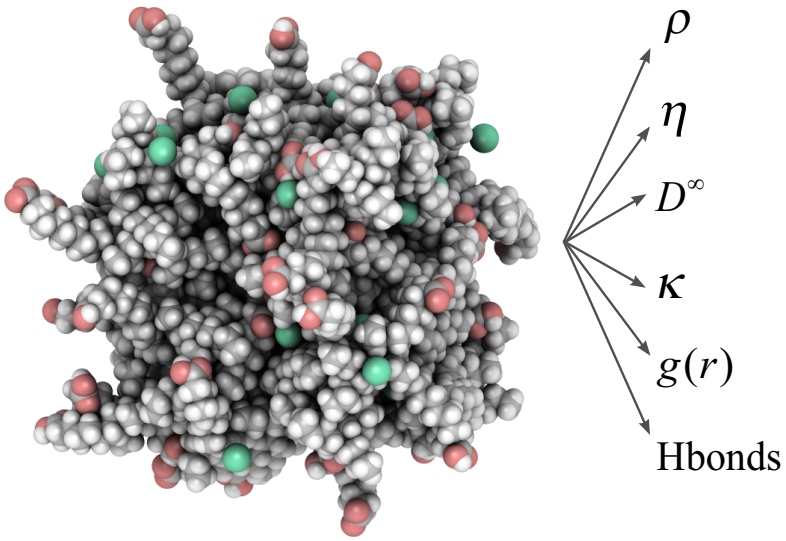

This chapter is based on the following paper: H.S. Salehi, A.T. Celebi, T.J.H. Vlugt, O.A. Moultos, Thermodynamic, transport, and structural properties of hydrophobic deep eutectic solvents composed of tetraalkylammonium chloride and decanoic acid, *Journal of Chemical Physics*, **2021**, 154, 144502.

5.1 Introduction

As discussed in chapter 1, since the recent introduction of hydrophobic DESs, these solvents have been considered in a wide range of applications, such as carbon capture [5, 22, 23], extraction of various solutes from aqueous solutions [20, 25, 27, 28, 30, 325], and catalysis [326]. So far, most of the studies on hydrophobic DESs have concentrated on the application of these solvents, rather than a fundamental investigation of molecular/atomic-scale interactions and the effect of these interactions on the macroscopic properties of the DESs [21]. Therefore, systematic knowledge on the liquid structure, the dominant intermolecular interactions, is largely lacking for hydrophobic DESs. Furthermore, structure-property relationships, for instance the influence of the alkyl chain lengths (i.e., the hydrophobicity) on the thermodynamic and thermodynamic properties, of hydrophobic DESs are not well-established. Limited literature is available on theoretical modeling of hydrophobic DESs, where mainly COSMO-based [327–330] and PC-SAFT equation of state [5, 22, 25, 26] modeling techniques are used. Despite the widespread use of MD simulations for computing the properties of hydrophilic DESs [59, 61, 68, 118, 119, 121–124, 126–130], very few MD studies are available for hydrophobic DESs [132, 139, 158]. In a few recent publications, MD simulations were used to model the phase behavior and thermodynamic properties of hydrophobic DESs, based on DL-menthol, tetraalkylammonium chloride, and (long-chain) carboxylic acids, in the presence of water [132, 139, 158]. However, in these works, mostly the properties of aqueous solutions of DESs or DES/water biphasic systems were computed, rather than the properties of neat DESs (except for a few density data [132, 158]). Furthermore, in the studies by Verma et al. [158], and Paul et al. [132], the force field validation for the DESs was performed solely based on experimental densities, which may therefore reduce the suitability of the developed force fields for the calculation of other thermo-physical properties, such as the viscosity.

In this chapter, MD simulations were performed to study the liquid structure, and thermodynamic and transport properties of hydrophobic DESs based on tetraalkylammonium chloride (TRAC) salts as the HBA component, and decanoic acid (a long-chain fatty acid) as the HBD component, with HBA:HBD molar ratios of 1:2. To examine the influence of the alkyl chain length of the cation (i.e., the number of alkyl chain carbon atoms), and thus the hydrophobicity of the DESs, on the liquid structure and thermo-physical properties, various cation chain lengths were used in the simulations: 4 (butyl), 7 (heptyl), and 8 (octyl). The respective

DESs, listed in Table 1.1, are designated as TBAC-dec, THAC-dec, and TOAC-dec. These DESs were considered here due to their many potential applications, particularly in liquid-liquid extraction of solutes [20, 27, 29, 31]. It is important to note that TRAC + fatty acid DESs exhibit significant negative deviations from ideality, which increase with the cation chain length [331]. Therefore, a eutectic temperature much lower than the ideal solution eutectic temperature is observed for these mixtures, rendering them as 'deep' eutectic mixtures [32]. In Section 5.2, the simulation details, the force field parameters of the DESs, and the methods used to compute the thermodynamic, transport, and structural properties, are described. In Section 5.3, the force field validation and simulation results are presented, and the results are compared with available experimental data from literature. Finally, in Section 5.4, conclusions are provided regarding the MD simulation of TRAC-dec DESs.

5.2 Computational details

The all-atom GAFF force field [155] was used to model the inter- and intramolecular interactions of the DESs. Non-bonded terms, consisting of LJ and electrostatic energies, and bonded terms, i.e., bond-stretching, bond-bending, and torsion, were taken into account. The LJ parameters by Fox and Kollman [332] were used for chloride anion. The electrostatic potential was computed for the optimized geometry of each isolated individual molecule or ion at the HF/6-31G* level of theory, and the partial atomic charges were obtained using the RESP method [292]. The geometry optimization and charge derivation were performed using the Gaussian 09 Rev.B.01 software [333] and the R.E.D-III.52 tools [305]. As discussed in the previous chapters, to obtain a better agreement between the simulation results (particularly for transport properties) and experimental data, often the ionic (partial) charges are scaled [56, 59, 61, 68, 118, 121, 128, 130, 145, 334, 335]. Adjustment and scaling of LJ interactions have been reported as alternative methods to enhance the simulation results [318, 336, 337]. Here, combinations of ionic charge scaling factors (f_{q}) in the range of 0.6 to 1.0 and LJ well-depth (ϵ) scaling factors (f_{ϵ}) in the range of 0.9 to 1.0 were examined. The ionic charge scaling factors were only applied to the (partial) charges of the cations and anions. The scaling of the σ parameter of the LJ potential was not considered due to the drastic adverse effect on the density, observed in preliminary test simulations. Following the approach of Jamali et al. [337] for carbohydrates, the LJ scaling factors were used for all atoms in the DES mixtures. This is in contrast to the approach of Chaumont et

al. [336], where only the LJ parameters of specific atoms (hydroxyl hydrogen and oxygen) were modified in ChClEg and ChClG DESs. The latter approach was not employed here, as it may introduce extra complication to the optimization procedure [337]. The 1-4 intramolecular electrostatic and LJ interactions were scaled by 0.833 and 0.5, respectively [155, 204]. The force field parameters of all the molecules are provided in Tables A37 to A43 and A53 to A56 of the Appendix. The molecular structures of the components (except for the chloride anion) of all DESs are shown in Figs. A7 to A9 and A12 of the Appendix. The PPPM method [69] with a relative error of 10^{-6} was used to computed the long-range electrostatic energies. A cutoff radius of 12 Å was used for both the short-range LJ and electrostatic energies. Analytic tail corrections [70] were used for LJ energies and pressure. The Lorentz-Berthelot mixing rules [70] were applied to obtain the LJ interactions between non-identical atom types. The Nosé-Hoover thermostat and barostat [69] were used to impose the temperature and pressure, respectively. The velocity Verlet algorithm [69, 210, 211] was used to integrate the equations of motion with a timestep of 1 fs. Initial low-density configurations were constructed using the PACKMOL package [212], and the simulations were carried out with the LAMMPS software [110] (version 16 March 2018). The VMD visualization software [338] was used to view snapshots of the systems, and perform hydrogen bond analysis (using the HBonds plugin).

In all simulations, the energy of the system was initially minimized using the conjugate gradient method to remove atomic overlaps. After equilibration of the system over 40 ns, the average densities of the DESs were computed at 1 atm and various temperatures in the NPT ensemble over 20 ns. It is important to note that such long equilibration times were necessary, particularly at lower temperatures, for a complete convergence of the density and total energy. This is possibly due to the high viscosity of the DESs and the entanglement of the long alkyl chains. After performing the NPT simulations, transport and structural properties were computed at various temperatures in the NVT ensemble, where the simulation box size was set according to the average densities obtained from the NPT simulations. The NVT simulations consisted of 10 ns equilibration and 440 ns to 650 ns (depending on the DES and temperature) production runs. For each data point, 5 independent simulations were run, over which averages and standard deviations were calculated. For enhanced equilibration and the circumvention of local energy minima, each system was annealed at elevated temperatures (600 K and 400 K) for 8 ns before both the NPT and NVT equilibration runs. All simulations consisted of 50 HBA (50 tetraalky-

lammonium cations and 50 chloride anions) and 100 HBD (decanoic acid) molecules, corresponding to an HBA:HBD molar ratio of 1:2. The OCTP plugin [339] in LAMMPS was used for the computation of transport properties and finite size-corrected RDFs [340, 341]. The computations by the OCTP package are performed on-the-fly, and thus atomic trajectories were not printed from the simulations for post-processing and obtaining the transport properties.

The OCTP plugin computes transport properties with the order-n algorithm [69, 342] using Einstein relations. The shear viscosity of each DES was obtained from the production runs using [70]:

$$\eta = \lim_{t\to\infty} \frac{1}{2t} \frac{V}{k_{\mathrm{B}}T} \left\langle \Big(\int_0^t P_{\alpha\beta}(t')\mathrm{d}t' \Big)^2 \right\rangle \tag{5.1}$$

where the brackets $\langle ... \rangle$ denote an ensemble average, $P_{\alpha\beta}$ ($\alpha, \beta = x, y, z$ and $\alpha \neq \beta$) is any of the off-diagonal components of the pressure tensor for an isotropic system, V is the volume of the simulation box, t is time, T is the absolute temperature, and k_{B} is the Boltzmann constant.

The self-diffusion coefficient of species i, $D^{\mathrm{MD}}_{\mathrm{self},i}$, in the DES mixture was computed from the last 100 ns to 200 ns of the production runs according to [70, 343]:

$$D^{\mathrm{MD}}_{\mathrm{self},i} = \lim_{t\to\infty} \frac{1}{6N_i t} \left\langle \sum_j^{N_i} |\mathbf{r}_{ji}(t) - \mathbf{r}_{ji}(0)|^2 \right\rangle \tag{5.2}$$

where $\mathbf{r}_{ji}$ is the position vector of molecule j of type i, and N_i is the total number of molecules of type i. In sharp contrast to the shear viscosity, the self-diffusion coefficient significantly depends on the system size [343–345]. The Yeh-Hummer correction was used to obtain the self-diffusion coefficient of each molecule type i in the thermodynamic limit, $D^{\infty}_{\mathrm{self},i}$, as [343, 346, 347]:

$$D^{\infty}_{\mathrm{self},i} = D^{\mathrm{MD}}_{\mathrm{self},i} + \frac{k_{\mathrm{B}}T\xi}{6\pi\eta L} \tag{5.3}$$

where L is the length of the simulation box, η is the shear viscosity (which does not depend on the system size [344]) computed from MD simulations using Eq. 5.1, and ξ is a constant with a value of 2.837298 for a 3D periodic lattice.

The ionic conductivity of each DES was estimated using the Nernst-Einstein equation as [348]:

$$\kappa = \frac{e^2}{k_B T V} \sum_i N_i q_i^2 D_{\text{self},i}^{\infty} \tag{5.4}$$

where q_i is the net charge of each ion type i, N_i is the total number of ions of type i in the system, V is the volume of the simulation box, e is the elementary charge, and the summation runs over all ion types i. Since only the computed diffusion coefficients (and indirectly the viscosities, via Equation 5.3) from the simulations are used in Eq. 5.4, no additional computations are required to obtain the ionic conductivities using the Nernst-Einstein relation. The ionic conductivity can also be computed using the Green-Kubo or Einstein relations which take into account the cross-correlation of charge fluxes/displacements [348–350]. To be able to use the Green-Kubo or Einstein relations, the output data of atomic trajectories would be required at a sufficient sampling frequency, and extensive subsequent post-processing must be performed. Therefore, for simplicity, the Nernst-Einstein relation was used here. Furthermore, Celebi et al. [128] have shown that the Nernst-Einstein equation yields a reasonable accuracy for the ionic conductivity of the aqueous solution of ChClU in a wide range of temperatures and water mass fractions.

The liquid structure of the DESs was analyzed using finite size-corrected RDFs for various atom-type pairs [340, 341]. The first solvation shell coordination numbers were computed by integrating the RDFs up to the first minimum. The populations of various types of hydrogen bonds were calculated from snapshots of atomic trajectories over the last 100 ns to 150 ns (depending on the DES) of the production runs. The criteria for the detection of hydrogen bonds were set to a donor-hydrogen-acceptor angle of 30° and a (heavy-to-heavy atom) cutoff distance of 3.5 Å [61, 128, 351–353].

5.3 Results and discussion

5.3.1 Thermodynamic and transport properties

Fine-tuning of the force field parameters was performed for TBAC-dec with different charge and LJ scaling factors, and the obtained parameters were evaluated for the other DESs. The force field development was hindered by inconsistencies observed between the experimental data reported in literature. For instance, van Osch et al. [20] reported the viscosities of

TBAC-dec, THAC-dec, and TOAC-dec at 298 K as 265 cP, 173 cP, and 473 cP, respectively, showing no clear trend with respect to the cation chain length. The authors noted water contents of 8140 ppm, 7740 ppm, and 4640 ppm for TBAC-dec, THAC-dec, and TOAC-dec, respectively. The amount of water content has been shown to have a significant effect on the viscosity of TBAC-dec [29], as well as other (hydrophilic) DESs [45, 181, 230]. Assuming that the reported values are on a mass fraction basis, the mole fraction-based water content of THAC-dec (10.2%) in the study by van Osch et al. [20] was larger than that of TBAC-dec (8.6%), which may have resulted in the lower viscosity of THAC-dec. Furthermore, the experimental viscosity of TBAC-dec at 298 K is reported as 265 cP [20], 429 cP [29], and 489 cP [354] in different studies. This disparity between the viscosities may also be attributed to variations in the water content of the DES, or may be due to the inaccuracy of the experimental measurements. As discussed in chapter 3, such inconsistencies are also observed for the properties of hydrophilic DESs. Here, the simulation results are compared with the experimental data by van Osch et al. [20], except for the viscosity of THAC-dec.

The density and viscosity of TBAC-dec based on different charge and LJ scaling factors are presented in Fig. 5.1. Due to the slow dynamics of the DESs, the computation of the transport properties, including the viscosity, was restricted to relatively elevated temperatures ($T \geq 323\,\mathrm{K}$). The experimental viscosity data by van Osch et al. [20] show an Arrhenius-type temperature dependence (Eq. 2.6) with a correlation coefficient of $R^2 = 0.9994$, and were therefore extrapolated to higher temperatures for the purpose of comparison with the MD results. It can be observed in Fig. 5.1 that the density and viscosity of TBAC-dec decrease by reducing the LJ and ionic charge scaling factors (farther from 1), due to the weakening of intermolecular interactions. As shown in Fig. 5.1, the combination of $f_\mathrm{q} = 0.6$ and $f_\epsilon = 1.0$ (no LJ scaling) yields a reasonable agreement between the simulation results and the experimental data, with average relative deviations of 1.72% and 15% for the density and viscosity, respectively. It should be noted that $f_\mathrm{q} = 0.6$ is smaller than the ionic charge scaling factors commonly used in the simulations of DESs and ILs (0.7-0.9) [59, 61, 68, 118, 121, 128, 129, 147, 288, 334, 355, 356], although occasionally the use of scaling factors in the range of 0.6 to 0.7 has also been reported [357, 358]. As far as hydrophobic DESs are concerned, Paul et al. [132] reported no use of charge scaling for TBAC-octanoic acid (nor for the more hydrophilic TBAC-acetic acid DES). However, the authors only validated the force field parameters based on the density, which, in contrast to the viscosity, is not

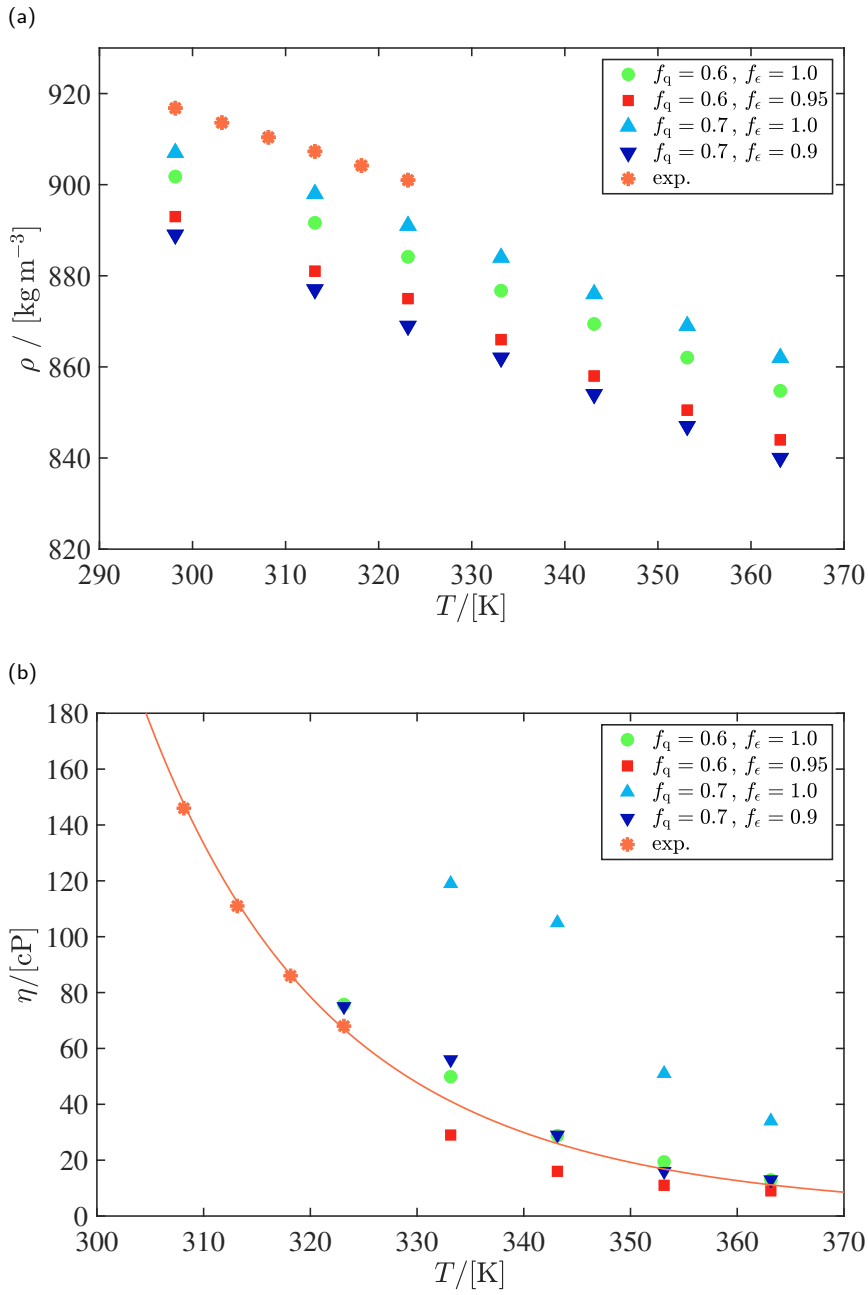

Figure 5.1: (a) Density and (b) viscosity of TBAC-dec as a function of temperature with various ionic charge scaling (f_q) and LJ scaling (f_ϵ) factors, compared with the experimental data by van Osch et al. [20]. The solid line in (b) depicts an Arrhenius fit (Eq. 2.6) to the experimental data.

significantly influenced by charge scaling, as can be clearly seen in Fig. 5.1. Details on the use/non-use of charge scaling are not mentioned in the MD studies by Shah et al. [359], and Verma et al. [158].

It has been suggested that for ILs, the ionic charge scaling factor is correlated with the dielectric constant (as $1/\sqrt{\epsilon_{\mathrm{el}}}$) and the refractive index (as $1/n_{\mathrm{D}}$) [360, 361]. Although such correlations are not established for DESs, the relatively small values of f_{q} for TBAC-dec may suggest a large polarizability. Dielectric constant and refractive index data are not available in literature for TBAC-dec to corroborate this. The Kamlet-Taft dipolarity/polarizability parameter (π^*) of TBAC-dec has been reported as 0.73 [226], along with other TRAC-carboxylic acid DESs having π^* values ranging from 0.69 to 1.06 [39, 226]. These values are typically lower than those of choline chloride-based DESs (1.00-1.23) [225], for which mostly charge scaling values of 0.8 and 0.9 are used in simulation studies [61, 121, 128, 129, 334]. This suggests a lower dipolarity/polarizability of TRAC-carboxylic acid DESs (incl. TBAC-dec), compared to choline chloride-based DESs. Chaumont et al. [336] have suggested that the success of the charge scaling approach is, however, not due to the inclusion of the polarizability effects and charge transfer processes. The authors have argued that since the gas phase polarities obtained from the commonly used charge derivation methods (including RESP [292]) are exaggerated, implicitly accounting for polarizability in aqueous solutions, the derived charges may lead to overestimation of the interactions in DESs/ILs, which can be alleviated using charge scaling. Schröder [355] has also argued that charge-scaled models do not represent the average polarizability, although the scaling factors may be seen as useful additional force field parameters that improve the accuracy of the computation of transport properties.

As shown in Fig. 5.1b, using a larger f_{q} (i.e., 0.7 instead of 0.6) for TBAC-dec results in significantly slower dynamics of the system and thus larger viscosities that are far from the experimental data. This issue may be overcome by using $f_\epsilon < 1.0$. A combination of $f_{\mathrm{q}} = 0.7$ and $f_\epsilon = 0.9$ results in viscosities that are similar to those obtained with $f_{\mathrm{q}} = 0.6$ and $f_\epsilon = 1.0$ (Fig. 5.1b). Nonetheless, due to the adverse effect of LJ scaling on the density (Fig. 5.1a), $f_{\mathrm{q}} = 0.6$ and $f_\epsilon = 1.0$ were chosen as the optimal scaling factors. Therefore, the values $f_{\mathrm{q}} = 0.6$ and $f_\epsilon = 1.0$ were used for all the DESs in all production runs. As mentioned in Section 5.2, the LJ parameters by Fox and Kollman [332] ($\epsilon = 0.265\,\mathrm{kcal\,mol^{-1}}$ and $\sigma = 3.471\,\text{Å}$) were used for the chloride anion, as the standard GAFF parameters ($\epsilon = 0.100\,\mathrm{kcal\,mol^{-1}}$ and $\sigma = 4.401\,\text{Å}$) considerably underestimate the densities of all DESs (for all values of f_{q}). For instance, the density of TBAC-dec (with $f_{\mathrm{q}} = 0.6$)

Table 5.1: Computed average densities of TBAC-dec, THAC-dec, and TOAC-dec at various temperatures and 1 atm. The values in parentheses are the standard deviations to the precision of the last significant digit.

T/[K]	ρ/[kg m^{-3}]		
	TBAC-dec	THAC-dec	TOAC-dec
298	901.8(1)	885.7(3)	883.0(10)
313	891.6(3)	875.6(6)	872.4(4)
323	884.2(3)	868.0(8)	865.1(7)
333	876.7(4)	861.1(3)	858.4(5)
343	869.4(3)	853.7(4)	850.8(8)
353	862.0(2)	846.7(5)	843.7(2)
363	854.8(2)	839.6(2)	836.9(2)

at 298 K, using the standard GAFF parameters for chloride, was computed as 867 kg m^{-3}. With the chloride LJ parameters by Fox and Kollman [332], however, a density of 902 kg m^{-3} was computed which is in a closer agreement (by 3.8%) with the experimental measurement (917 kg m^{-3}) [20]. It is interesting that the standard GAFF LJ parameters for chloride can accurately reproduce the experimental densities of choline chloride-based hydrophilic DESs [61, 121, 129] (as also shown in chapter 3), in contrast to the DESs considered here. This clearly indicates the crucial role of chloride anion in molecular packing within TRAC-dec hydrophobic DESs, and the necessity for LJ parameters with larger well-depths and less repulsive cores.

The computed densities of all the DESs (with the optimal force field parameters) are presented as a function of temperature in Fig. 5.2a, and as a function of the cation alkyl chain length at 323 K in Fig. 5.2b. The computed densities of all the DESs are also listed in Table 5.1. It can be observed in Fig. 5.2 that for all the DESs, the MD results are in close agreement with the experimental data by van Osch et al. [20]. The average relative deviations of the computed densities from the experimental data are 1.72%, 0.65%, and 0.79% for TBAC-dec, THAC-dec, and TOAC-dec, respectively. Furthermore, the linear reduction of density with the increase in temperature is well captured from the MD simulations. From the slopes of the computed densities as a function of temperature, the volumetric thermal expansion coefficients (at constant pressure) were computed according to [118, 234, 362, 363]:

$$\alpha_{\mathrm{P}} = \frac{1}{\rho}\left(\frac{\partial \rho}{\partial T}\right)_{P} \tag{5.5}$$

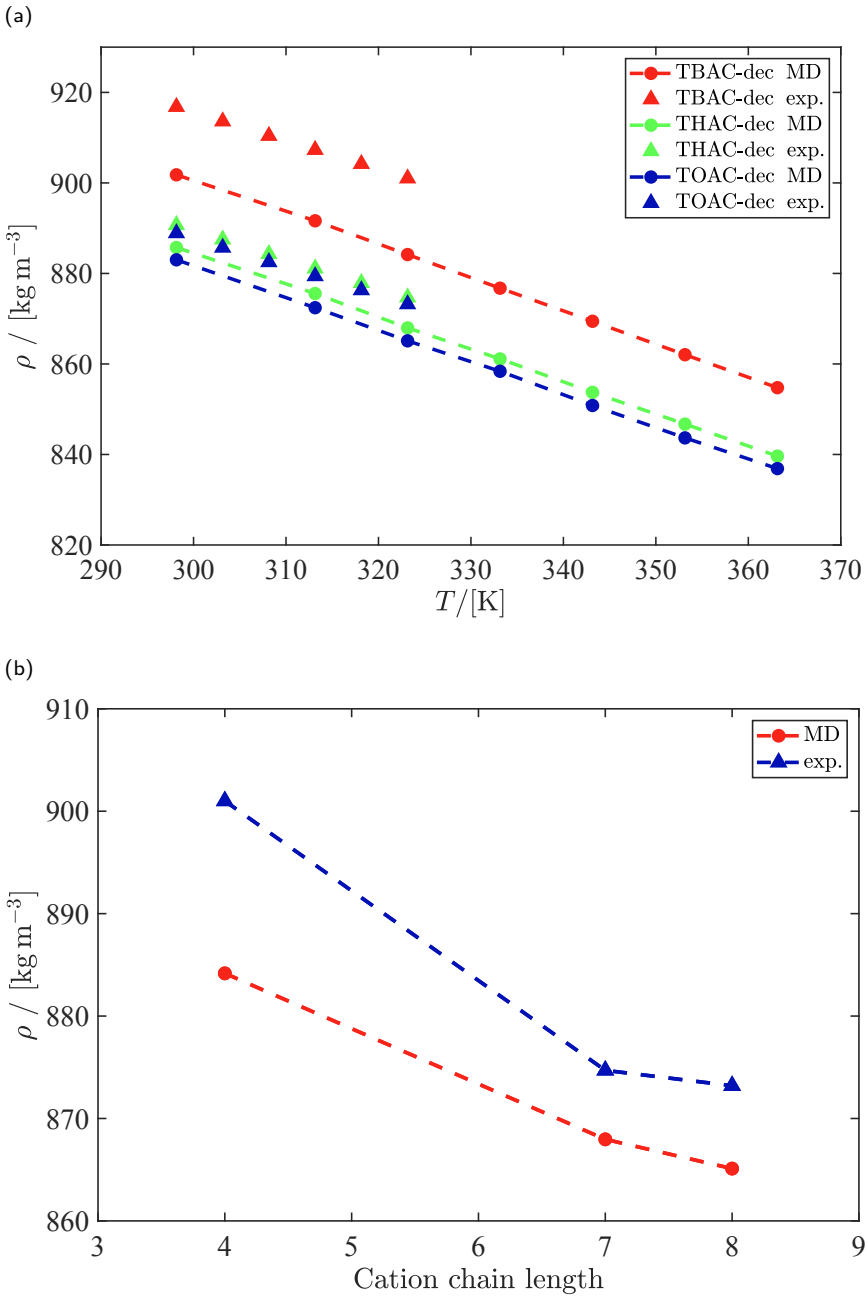

Figure 5.2: Densities of TBAC-dec, THAC-dec, and TOAC-dec (a) as a function of temperature, and (b) as a function of the cation alkyl chain length at 323 K, compared with the experimental data by van Osch et al. [20]. The dashed lines are added to guide the eye.

Table 5.2: Computed average viscosities of TBAC-dec, THAC-dec, and TOAC-dec at various temperatures and 1 atm. The values in parentheses are the standard deviations to the precision of the last significant digit.

T/[K]	η/[cP]		
	TBAC-dec	THAC-dec	TOAC-dec
323	75.8(68)	122.9(109)	188.2(551)
333	49.9(74)	91.0(130)	100.0(108)
343	28.8(42)	63.3(88)	69.3(38)
353	19.4(8)	38.8(28)	41.8(62)
363	13.0(15)	26.1(7)	31.1(40)

where ρ is the density, T is the absolute temperature, and P is the pressure. For all DESs, the thermal expansion coefficient was calculated as ca. $8.3 \times 10^{-4}\,\mathrm{K}^{-1}$. This value is in agreement with the thermal expansion coefficients computed from the experimental densities reported by van Osch et al. [20], i.e., ca. $7.0 \times 10^{-4}\,\mathrm{K}^{-1}$ for TBAC-dec, and ca. $7.3 \times 10^{-4}\,\mathrm{K}^{-1}$ for THAC-dec and TOAC-dec. As shown in Fig. 5.2b, the computed density decreases as the cation chain length is increased from 4 to 8, which is consistent with the experimental data (although the slopes of this decrease are somewhat different). The reduction of density with an increase in the cation chain length is also reported for ILs [364–367] and other DESs [41, 60, 368, 369] in literature, and is the opposite of the trend found for alkanes [370]. This effect may be attributed to the steric hindrance of the cation chains which hampers the packing of the molecules [364, 366, 369].

The computed viscosities of the DESs are presented as a function of temperature in Fig. 5.3a (THAC-dec data are not shown for clarity), and as a function of the cation alkyl chain length at 343 K in Fig. 5.3b. The computed viscosities of all the DESs are listed in Table 5.2. As expected, an increase in the temperature results in enhanced molecular motions and thus lower viscosities of all the DESs. The viscosities of the DESs increase with an increase in the cation chain length (observed at all temperatures), possibly due the additional dispersion forces of the chains, promoting friction with other molecules. Similarly, the experimental data by van Osch et al. [20] show an increase in the viscosity from TBAC-dec with a cation chain length of 4 to TOAC-dec with a cation chain length of 8. However, as mentioned earlier, the experimental viscosity of THAC-dec (with a chain length of 7) is reported lower than those of both TBAC-dec and TOAC-dec, which may be due to a larger mole fraction-based water content of THAC-dec used in those experiments. The increase in viscosity with the cation chain length

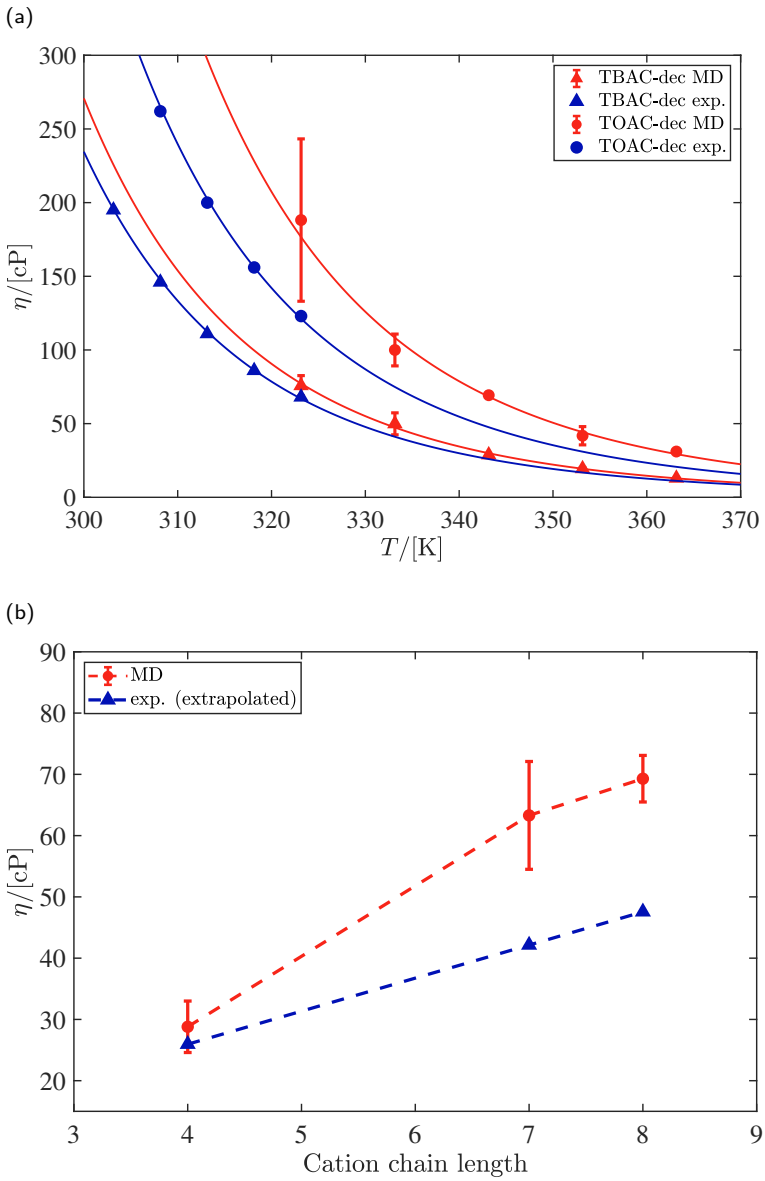

Figure 5.3: Viscosities of the TRAC-dec DESs (a) as a function of temperature (THAC-dec data are not shown for clarity), and (b) as a function of the cation alkyl chain length at 343 K, compared with the experimental data by van Osch et al. [20], extrapolated to 343 K. The experimental viscosity data point of THAC-dec in (b) was obtained by interpolating the experimental viscosities of TBAC-dec and TOAC-dec with respect to the cation chain length, and is therefore not equal to the value reported by van Osch et al. [20]. The solid lines in (a) denote the fits to the Arrhenius equation (Eq. 2.6). The dashed lines in (b) are added to guide the eye. For clarity, error bars that are smaller than the symbol size are not shown.

has also been observed for other DESs based on (tetra)alkylammonium halide HBAs [140, 368, 369, 371]. Thus, to compare the computed viscosities of THAC-dec with experimental data, a 'revised' set of experimental data (presented in Fig. 5.3b and Table 5.2) was obtained for THAC-dec by interpolation from the experimental viscosities of TBAC-dec and TOAC-dec with respect to the cation chain length. As mentioned previously, due to computational limitations, the viscosities were computed at $T \geq 323\,\mathrm{K}$. Therefore, the viscosities from the MD simulations and experiments overlap in only one temperature point, i.e., at $T = 323\,\mathrm{K}$. However, the experimental viscosity data exhibit an Arrhenius-type temperature correlation (Eq. 2.6), with $R^2 = 0.9994$ for all the DESs, that allowed for extrapolation to higher temperatures. It was observed that the computed viscosities from MD could also be fitted to an Arrhenius functional form (Eq. 2.6), with R^2 values of 0.9978, 0.9871, and 0.9916 for TBAC-dec, THAC-dec, and TOAC-dec, respectively, allowing for the prediction of viscosities at lower temperatures. The Arrhenius fitting curves for both the simulation and experimental data are denoted by the solid lines in Fig. 5.3a. As can be observed in Fig. 5.3, the computed viscosities agree reasonably well with the (extrapolated) experimental data by van Osch et al. [20] over a wide range of temperatures and cation chain lengths. The average relative deviations of the computed viscosities from the extrapolated experimental data are 15%, 37%, and 44% for TBAC-dec, THAC-dec, and TOAC-dec, respectively. This finding indicates a systematic increase in the relative deviations from the experimental data as the cation chain length increases, which is reasonable since the optimal force field parameters were chosen based on the density and viscosity of TBAC-dec. As mentioned previously, the DESs used in the experiments of van Osch et al. [20] contained some amounts of water (4640-8140 ppm), which may have lowered the measured viscosities. Moreover, the experimental viscosities reported by Ruggeri et al. [29] (429 cP), and Saydan et al. [354] (489 cP) for TBAC-dec at 298 K are larger than the one reported by van Osch et al. [20] (265 cP), possibly due to differences in the hydration level of the DES. Therefore, the viscosities of the anhydrous DESs are likely larger that those reported by van Osch et al. [20].

The relatively larger deviations of the computed viscosities from the experimental data at larger cation chain lengths may be improved by further fine-tuning of the force field parameters for each DES, e.g., using smaller charge and/or LJ scaling factors for DESs with longer cation chains. This would, however, compromise the transferability of the obtained force field parameters. Nevertheless, more experimental measurements are required for

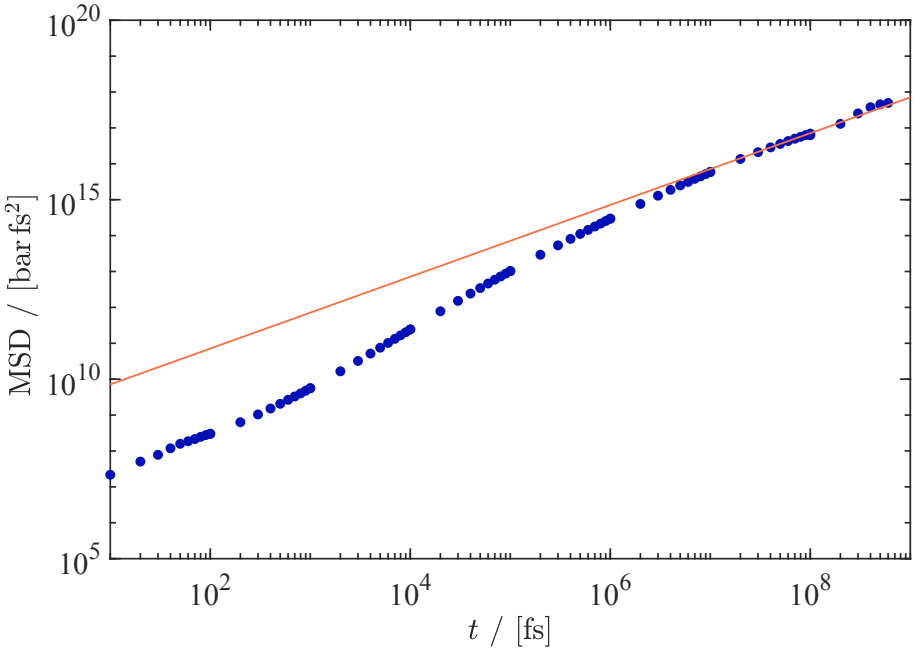

Figure 5.4: Log-log plot of the MSD of the off-diagonal pressure tensor elements in TOAC-dec at 343 K as a function of correlation time (blue circles). The orange solid line corresponds to the linear fit with a slope of 1 (indicating the diffusive regime). From Eq. 5.1, a viscosity of 69.3 cP is obtained.

the viscosities of the DESs studied here (and hydrophobic DESs in general), without which it is difficult to provide accurate force field parameters. It should be noted that at larger cation chain lengths and lower temperatures (thus higher viscosities), the linear regime could not be readily achieved for the mean squared displacements (MSDs). This impeded the accurate calculation of the viscosities, and resulted in large uncertainties (as shown with error bars in Fig. 5.3). Instead of averaging the viscosities from the various independent runs, first, the MSDs of the independent runs were averaged, and subsequently, linear regression was performed on the averaged MSDs to obtain the average value of the viscosity. This method enhanced the quality of the linear regression of the MSDs, and is therefore recommended for the calculation of the transport properties of viscous fluids, such as DESs, using the Einstein formulation. As an example, the averaged MSDs (of the off-diagonal pressure tensor elements) are presented for TOAC-dec at 343 K in Fig. 5.4, as a function of correlation time in a log-log plot. As mentioned in chapter 2, often more complicated correlations such as the VFT function (Eq. 2.7) are used to model the temperature dependence of

Table 5.3: Computed average finite size-corrected self-diffusion coefficients of the HBD, anion, and cation components in TBAC-dec, THAC-dec, and TOAC-dec at various temperatures and 1 atm.

	T/[K]	$D^{\infty}_{\text{self}}/[10^{-11}\text{m}^2\,\text{s}^{-1}]$		
		anion	cation	HBD
TBAC-dec	323	1.22	0.93	1.44
	333	2.20	1.67	2.53
	343	3.53	2.77	3.89
	353	5.59	4.20	6.37
	363	8.58	6.47	9.24
THAC-dec	323	0.55	0.39	0.90
	333	0.93	0.69	1.55
	343	1.42	1.03	2.44
	353	2.33	1.72	3.73
	363	3.46	2.51	5.67
TOAC-dec	323	0.48	0.31	0.80
	333	0.74	0.51	1.32
	343	1.19	0.87	2.21
	353	1.83	1.32	3.35
	363	2.70	2.10	4.91

the viscosities of DESs [13, 45, 181, 185, 230]. The viscosities computed here could also be modeled well with the VFT function ($R^2 > 0.9989$ for all the DESs). Nevertheless, the simple Arrhenius model showed sufficient capability for capturing the temperature dependence of the viscosities of the studied DESs. It is important to note that the VFT model should be used with caution when extrapolating the viscosity data to lower temperatures, as it is known to overestimate viscosities at low temperatures [372]. Therefore, in case of extrapolation to lower temperatures, other functional forms, e.g., the Mauro-Yue-Ellison-Gupta-Allan (MYEGA) equation may be preferable [372, 373].

Self-diffusion coefficients were computed for the HBD, cation, and anion components of the DESs at different temperatures, based on the center-of-mass motion of the molecules. The resulting finite size-corrected diffusivities are presented in Fig. 5.5 as a function of temperature, and as a function of the cation chain length at 343 K. For clarity, the diffusivities of the THAC-dec components are not shown in Fig. 5.5a. The computed self-diffusion coefficients are listed in Table 5.3 for the components of all the DESs. The Yeh-Hummer finite size corrections account for 10%-32% (on

average 20%) of the final diffusion coefficients presented in Fig. 5.5 and Table 5.3. Unfortunately, no experimental data are available for the diffusion coefficients of the DESs studied here, so a direct validation of the computed diffusivities is not possible. It can be observed that for all the DESs, the self-diffusion coefficients of all the components increase by increasing the temperature. All the computed finite size-corrected diffusivities obey an Arrhenius-type temperature dependence (denoted by the solid lines in Fig. 5.5a) with $R^2 > 0.998$, according to:

$$D^{\infty}_{\text{self}} = A \exp\left[\frac{E^{\text{diff}}_{\text{a}}}{RT}\right] \tag{5.6}$$

where A is a constant, R is the universal gas constant, T is the absolute temperature, and $E^{\text{diff}}_{\text{a}}$ is the activation energy of diffusion.

As shown in Fig. 5.5 and Table 5.3, for all the DESs and at all temperatures, the largest diffusion coefficient belongs to the HBD, while the cation exhibits the smallest diffusivity. A similar order for the diffusivities of DES components has been reported in literature for several choline chloride-based DESs [37, 61, 128, 336]. As can be observed in Fig. 5.5b, the diffusion coefficients of all the components decrease as the cation chain length is increased. This may be due to stronger intermolecular interactions (which also result in higher viscosities) in the DESs with longer cation chains. Furthermore, with an increase in the cation chain length, the hydrodynamic radius and molecular weight of the cation are increased. This may contribute to a further decrease in the mobility and self-diffusion coefficient of the cation. Fig. 5.5b shows that as the cation alkyl chain length is increased from 4 to 8, the difference between the diffusion coefficients of the HBD and anion becomes larger, while the difference between the diffusion coefficients of the anion and cation decreases. This effect was observed at all temperatures, and may imply that at larger cation chain lengths, the motions of the cation and anion are coupled, while at smaller cation chain lengths, the motions of the HBD and anion are coupled. This is counter-intuitive, as one would expect the increase in the cation chain length to reduce the anion-cation electrostatic interactions, due to the steric hindrance of the chains.

The ionic conductivities of the DESs were calculated at various temperatures, based on the computed finite size-corrected diffusivities, and the results are presented in Fig. 5.6. The computed data for the ionic conductivities of all the DESs are also listed in Table 5.4. For all the DESs, the ionic conductivity becomes larger when the temperature is increased, due to the enhanced diffusion of ions. Similar to the viscosities and diffusivities, this

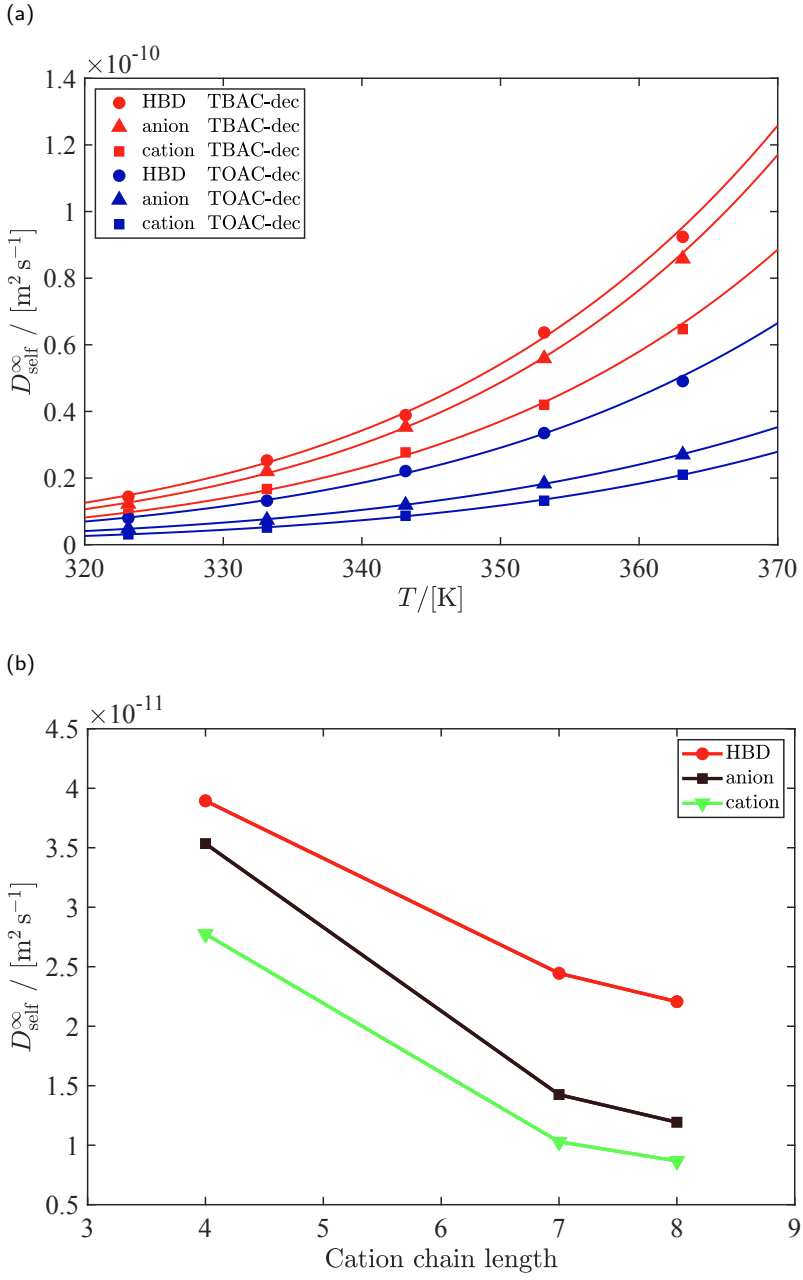

Figure 5.5: Finite size-corrected self-diffusion coefficients of the HBD, cation, and anion components (a) as a function of temperature for TBAC-dec and TOAC-dec, with the corresponding Arrhenius fits (Eq. 5.6) indicated by the solid lines, and (b) as a function of the cation alkyl chain length at 343 K. The lines in (b) are drawn to guide the eye.

Table 5.4: Computed average ionic conductivities of TBAC-dec, THAC-dec, and TOAC-dec at various temperatures and 1 atm.

T/[K]	$\kappa/[\mu\mathrm{S\,cm^{-1}}]$		
	TBAC-dec	THAC-dec	TOAC-dec
323	380.5	129.3	101.0
333	658.4	212.8	153.6
343	1035.1	311.2	243.2
353	1546.6	496.0	358.0
363	2295.0	703.0	527.5

temperature dependence can be described by an Arrhenius-type relationship (depicted by the solid lines in Fig. 5.6), with $R^2 > 0.9985$, according to:

$$\kappa = A \exp\left[\frac{E_\mathrm{a}^\mathrm{cond}}{RT}\right] \tag{5.7}$$

where A is a constant, R is the universal gas constant, T is the absolute temperature, and $E_\mathrm{a}^\mathrm{cond}$ is the activation energy of ionic conductivity. As shown in Fig. 5.6, at all temperatures, the ionic conductivity decreases with an increase in the cation chain length, which is attributed to the slower diffusion of ions in the DESs with longer cation chains. Comparable effects of the cation chain length on the ionic conductivity have been observed for other DESs based on (tetraalkyl)ammonium halides [368, 374]. Ruggeri et al. [29] reported an experimental ionic conductivity of ca. $40\,\mu\mathrm{S\,cm^{-1}}$ at 298 K for TBAC-dec with a water content of 0.11% (mass fraction-based). It is expected for the ionic conductivity of TBAC-dec with no water content to be even lower than $40\,\mu\mathrm{S\,cm^{-1}}$, as the presence of water has been shown to increase the ionic conductivity of other DESs due to an increased mobility of ions [128, 375]. When extrapolated to 298 K, the MD simulation results for TBAC-dec yield an ionic conductivity of $102\,\mu\mathrm{S\,cm^{-1}}$. It is important to note that the Nernst-Einstein relation (Eq. 5.4) neglects any cross-correlation between the motions of different ions in the mixture [349]. Dong et al. [376] showed for aqueous solutions of tetraalkylammonium bromide IL, with various IL concentrations, that ionic conductivities calculated from the Nernst-Einstein equation may be several times larger than the ones computed from the Einstein relation (using the cross-correlation of charge displacements), due to the strongly correlated motions of the ions. Similarly, it is possible that here, the ionic conductivity of TBAC-dec (and possibly the other DESs) is overestimated from Eq. 5.4 because of a strong

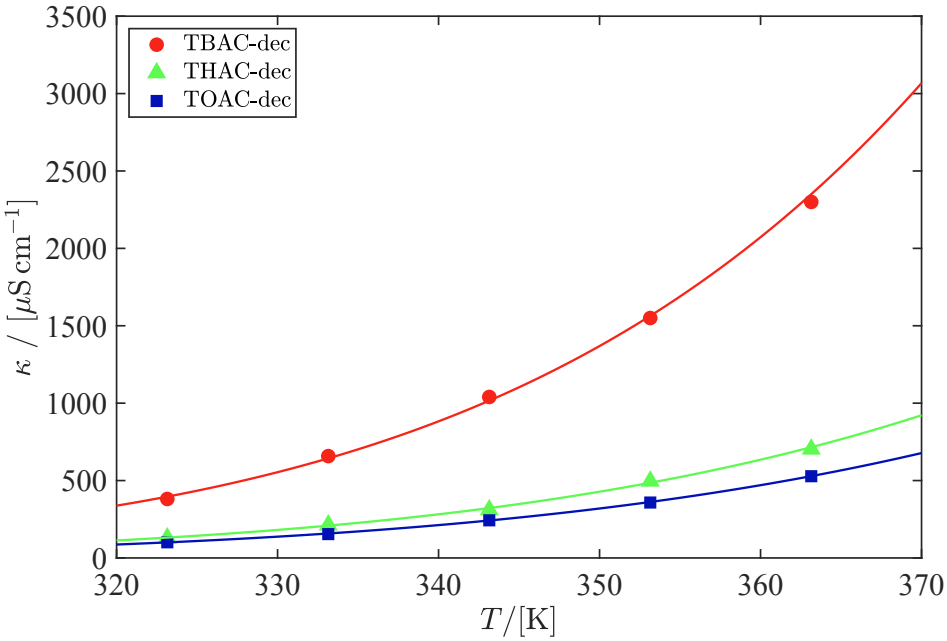

Figure 5.6: Ionic conductivities of TBAC-dec, THAC-dec, and TOAC-dec as a function of temperature. The solid lines indicate the corresponding Arrhenius fits (Eq. 5.7).

correlation between the motions of the cation and anion. It is also possible, however, that this difference is simply caused by an overestimation of the diffusivities from the MD simulations. More experimental data are required for the transport properties of TRAC-dec DESs to provide more accurate conclusions in this regard.

5.3.2 Liquid structure

To study the liquid structure of the DESs, RDFs were computed for different atom-type pairs. The RDFs for the most dominant interactions (largest peaks) are presented in Fig. 5.7 for TBAC-dec, THAC-dec, and TOAC-dec at 343 K. As shown in Fig. 5.7a, for all the DESs, a large RDF peak is observed at ca. 1.9 Å for the interaction between chloride (Cl) and the hydroxyl hydrogen of decanoic acid (HO), implying a hydrogen bond between these atoms. Strong hydrogen bonds between the chloride anion and the hydroxyl groups of the HBD or cation have also been reported for other (hydrophilic) DESs in literature [61, 118, 280, 334]. The RDFs for the interaction of the nitrogen atom of cation (N) with chloride show a peak (although smaller than that of the Cl-HO RDFs) at an average distance of

ca. 4.3 Å, likely due to the cation-anion electrostatic interactions. As shown in Fig. 5.7b, the RDFs for the interaction of the carbonyl oxygen (O) with the hydroxyl hydrogen of decanoic acid exhibit one large peak with a left shoulder, centered around 2.0 Å (the shoulder is at ca. 1.7 Å), and a smaller peak at 3.0 Å. By post-processing snapshots of atomic coordinates from the simulations, it was found that the left shoulder of the first peak corresponds to the intermolecular O-HO (hydrogen bond) interaction between different decanoic acid molecules, while the peaks at 2.0 Å and 3.0 Å correspond to O-HO intramolecular interactions within each decanoic acid molecule. The decomposed O-HO RDF into the intermolecular and intramolecular contributions is presented in Fig. A22 of the Appendix for TBAC-dec at 343 K. By calculating the dihedral angle between the carbonyl oxygen and hydroxyl hydrogen ($\phi_{\mathrm{O-C-OH-HO}}$) of decanoic acid molecules, it was found that the peaks of the O-HO intramolecular RDF represent two distinct dihedral angle ranges: The peak at 2.0 Å corresponds to $\phi_{\mathrm{O-C-OH-HO}}$ values in the range of ca. 0° to 40° and thus a cis configuration between O and HO (on the same side of the molecule), whereas the peak at 3.0 Å corresponds to $\phi_{\mathrm{O-C-OH-HO}}$ values in the range of ca. 140° to 180° and therefore a trans configuration (on opposite sides). The correlation between the dihedral angle and the intramolecular O-HO distance is shown Fig. 5.8. Based on the RDFs in Fig. 5.7b, it may be concluded that the probability of finding the cis configuration between O and HO is larger than that of the trans configuration. The large intermolecular O-HO and Cl-HO peaks shown in Fig. 5.7 indicate that strong HBD-HBD and HBD-anion (hydrogen bond) interactions are present in all the DESs. This is in contrast to the relatively weak HBD-cation interactions, as represented by the RDFs for the interaction of the carbonyl oxygen of decanoic acid with the nitrogen of cation (O-N), in Fig. 5.7b. This may be due to the lack of hydrogen bond accepting/donating moieties on the cation, which prevents any considerable interaction with the HBD.

In the preliminary testing of force field parameters for TBAC-dec (at 298 K), it was found that by increasing the ionic charge scaling factor (approaching 1), the Cl-HO RDF peak intensity is significantly increased: from 33 at $f_{\mathrm{q}} = 0.6$ to 49 at $f_{\mathrm{q}} = 0.7$, and 64 at $f_{\mathrm{q}} = 0.8$ (presented in Fig. 5.9a). Considering the negligible effect of charge scaling on the density (less than 0.5% at 298 K), such differences in the peak heights indicate a major contribution of electrostatics to the Cl-HO interactions. As can be observed in Fig. 5.9, with an increase in the charge scaling factor, the Cl-HO peak position is slightly shifted to smaller distances, implying stronger electrostatic interactions. Perkins et al. [61] have reported a comparable

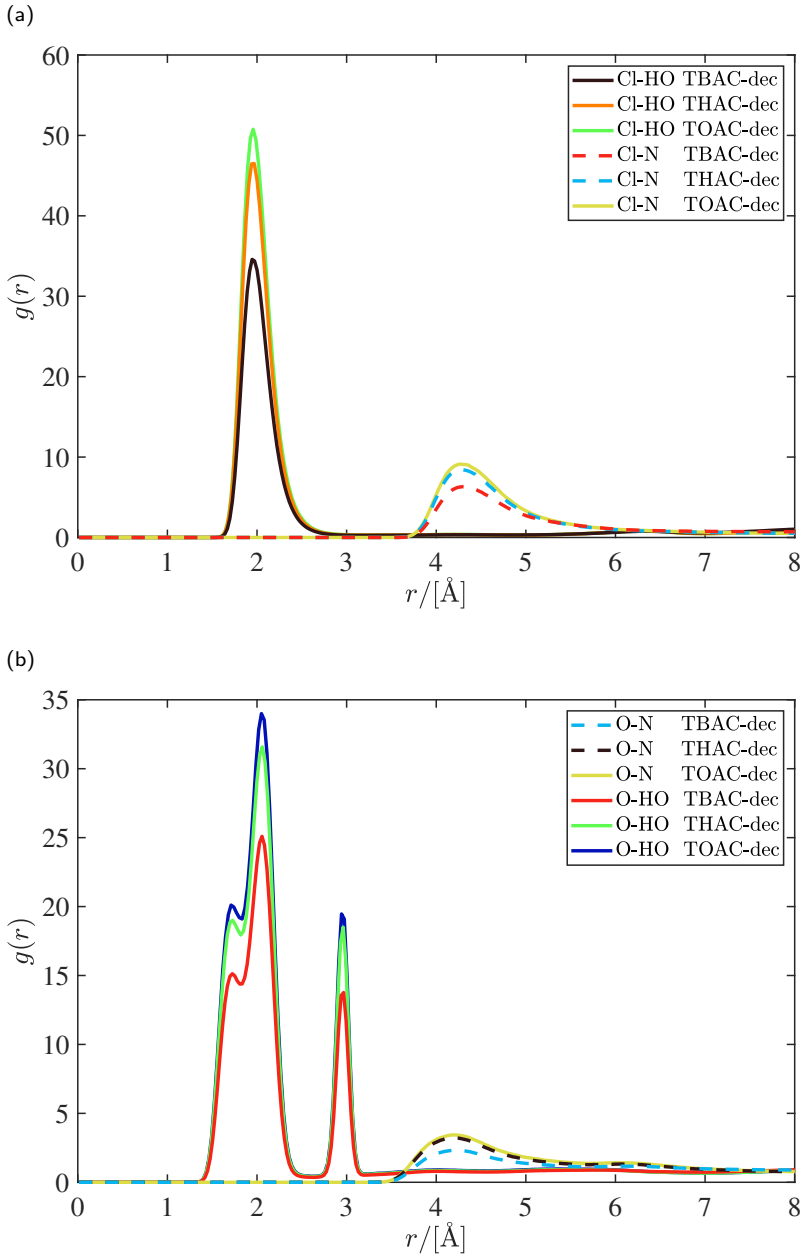

Figure 5.7: RDFs for the interactions between (a) chloride and the hydroxyl hydrogen of decanoic acid (Cl-HO), chloride and the nitrogen of cation (Cl-N), (b) the carbonyl oxygen of decanoic acid and the nitrogen of cation (O-N), and the carbonyl oxygen and hydroxyl hydrogen of decanoic acid (O-HO), from MD simulations of TBAC-dec, THAC-dec, and TOAC-dec at 343 K.

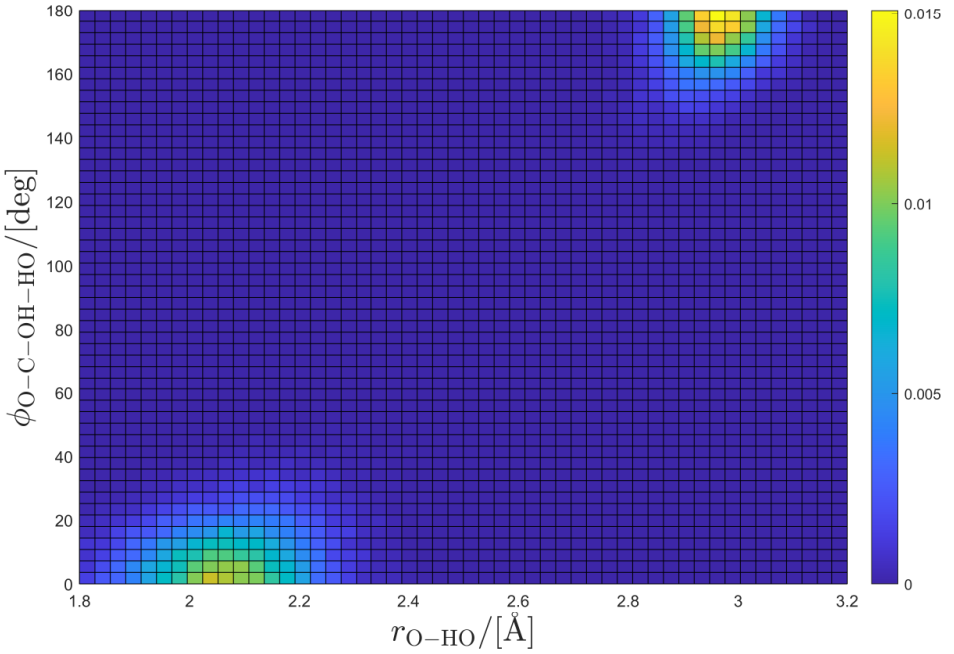

Figure 5.8: The O-C-OH-HO dihedral angle of decanoic acid at various intramolecular O-HO distances in TBAC-dec at 343 K and 1 atm. The various colors describe the probabilities for the combination of the dihedral angle and O-HO distance within each grid cell, according to the color bar on the right-hand side. The data were obtained from snapshots of atomic coordinates from all 5 independent *NVT* runs (for the last 100 ns to 150 ns).

influence of charge scaling on the interaction between the chloride anion and the hydroxyl group of choline cation in ChClU. A similar, albeit less drastic, effect of the charge scaling is observed on the N-Cl RDF (Fig. A23 of the Appendix). For the O-HO interaction, it was found that with an increase in the charge scaling factor, the height of the intermolecular RDF peak decreases (Fig. 5.9b). This is possibly due to a competition between the O-HO and Cl-HO (hydrogen bond) interactions, where larger ionic charge scaling factors and thus stronger Cl-HO (anion-HBD) interactions result in the weakening of O-HO interactions. As shown in Fig. 5.9b, by increasing the charge scaling factor, the height of the intramolecular O-HO peak at 2.0 Å decreases, while that of the intramolecular peak at 3.0 Å increases. This implies that by using larger charge scaling factors, the probability of the O-HO trans configuration increases, while the probability of the cis configuration decreases. This may be caused by the stronger Cl-HO interactions at larger charge scaling factors: The HO atom is moved to the opposite side of the carbonyl oxygen to reduce the repulsive electrostatic

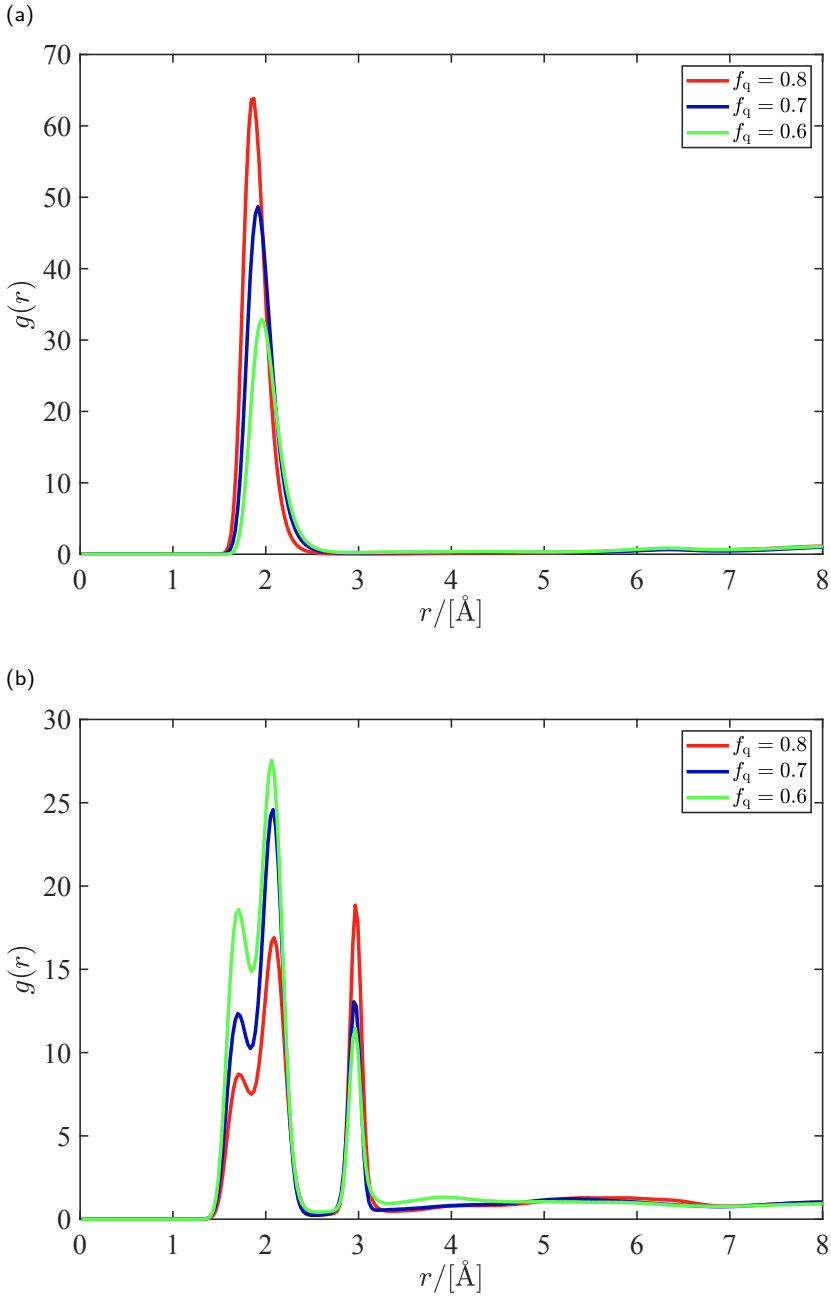

Figure 5.9: RDFs for the interactions between (a) chloride and the hydroxyl hydrogen of decanoic acid (Cl-HO), and (b) the carbonyl oxygen and hydroxyl hydrogen of decanoic acid (O-HO), from MD simulations of TBAC-dec at 298 K and 1 atm, for various ionic charge scaling factors (f_q).

Table 5.5: Coordination numbers, CN_{ij} (of atom type j around atom type i), in TBAC-dec, THAC-dec, and TOAC-dec at 343 K and 1 atm. O, HO, N, and Cl denote the carbonyl oxygen and hydroxyl hydrogen of decanoic acid, the nitrogen of cation, and the chloride anion, respectively. If the numbers of atoms of types i and j are the same in the mixture, then $CN_{ij} = CN_{ji}$. For the calculation of the O-HO coordination number, only the intermolecular contribution to the RDF was considered.

		TBAC-dec		THAC-dec		TOAC-dec	
atom type i	atom type j	CN_{ij}	CN_{ji}	CN_{ij}	CN_{ji}	CN_{ij}	CN_{ji}
N	Cl	2.43	2.43	2.03	2.03	2.02	2.02
O	HO	0.39	0.39	0.37	0.37	0.37	0.37
O	N	0.75	1.49	0.74	1.49	0.70	1.40
Cl	HO	1.20	0.60	1.24	0.62	1.18	0.59

interaction between chloride and the carbonyl oxygen, both with relatively large negative (partial) charges.

As shown in Fig. 5.7a, the heights of the RDF peaks increase with an increase in the cation chain length. For instance, the Cl-HO RDFs show peak intensities of 35, 47, and 51 for TBAC-dec, THAC-dec, and TOAC-dec, respectively. This is mainly due to the differences in the simulation box volumes (and thus the densities) of the DESs, with respect to which the RDFs are normalized, rather than profound differences in the interactions and heterogeneity of the DESs. Furthermore, the RDF peak positions are not influenced by the cation chain length. As can be observed in Fig. 5.7, the RDFs for the interactions of nitrogen (representing the center-of-mass of the cation) with other atoms exhibit the first peak at comparatively larger distances, which is consistent with RDFs reported for ChClU [128]. This is likely due to the large size of the cation and the steric hindrance of its alkyl chains. It was found that all of the RDFs show negligible sensitivity towards temperature, with only a slight decrease in the peak intensities with increasing the temperature (Fig. A24 of the Appendix). This is consistent with other findings in literature for DESs [118, 128]. First solvation shell coordination numbers, calculated at 343 K by integrating the RDFs up to the first minimum, are listed in Table 5.5. It is important to note that unlike RDFs, coordination numbers do not depend on the system volume [348], and may therefore better reflect structural differences between systems of different densities. As shown in Table 5.5, the calculated coordination numbers are not significantly affected by the cation chain length, confirming the negligible effect of the chain length on the liquid structure of the studied DESs. Only a slight decrease in the N-Cl coordination number is observed

with an increase in the cation chain length, which is possibly due to the steric hindrance effect.

The results of the hydrogen bond analysis for the DESs are shown in Fig. 5.10, as a function of temperature for TBAC-dec, and as a function of the cation chain length at 343 K. The plots in Fig. 5.10 are presented in terms of the number of hydrogen bonds per number of hydroxyl hydrogen atoms in the system (H-bond/HO). For all the DESs, 100 HO atoms (due to 100 decanoic acid molecules) were present in the mixture. Three types of hydrogen bonds were considered in the analysis: (1) between the carbonyl oxygen and hydroxyl hydrogen (O-HO) of decanoic acid, (2) between the hydroxyl oxygen and hydroxyl hydrogen (OH-HO) of decanoic acid, and (3) between chloride and the hydroxyl hydrogen (Cl-HO) of decanoic acid. As shown in Fig. 5.10, the Cl-HO hydrogen bond is found to be the most prominent type of hydrogen bond in TBAC-dec with a population of ca. 0.40 H-bond/HO. To a lesser extent, O-HO hydrogen bonds are formed with an average population of ca. 0.27 H-bond/HO, although this number includes both intermolecular and intramolecular interactions (as discussed for the RDFs). Only a small number of OH-HO hydrogen bonds (0.02 H-bond/HO) are found in the mixture, implying the preference of the hydroxyl hydrogen of decanoic acid to form hydrogen bonds with the carbonyl oxygen, rather than the hydroxyl oxygen, of other decanoic acid molecules. It is important to note that the strong HBD-HBD and HBD-anion hydrogen bonds may ultimately lead to proton transfers, which may affect the macroscopic properties of the DESs. However, commonly used non-reactive atomic force fields, such as the GAFF force field used here, are not capable of modeling proton transfers. As shown in Fig. 5.10a, the populations of the hydrogen bonds do not change significantly with temperature. This temperature independence of the number of hydrogen bonds has also been reported by Celebi et al. [128] in MD simulations of ChClU and ChClEg. As can be observed in Fig. 5.10b, increasing the cation chain length does not have a considerable influence on the populations of the various hydrogen bonds (only a slight increase in the number of Cl-HO hydrogen bonds). This is in agreement with the findings from the RDFs (Fig. 5.7) regarding the effect of the cation chain length on the peak heights and positions, and the liquid structure of the DESs. The insensitivity of the number of hydrogen bonds to the cation chain length was noticed at all temperatures (Fig. A25 of the Appendix). Overall, based on the results from the RDFs and the hydrogen bond analysis, the liquid structures of the DESs with various cation chain lengths are almost identical, and the same intermolecular interactions dominate all the mixtures. This is in sharp contrast to the transport properties

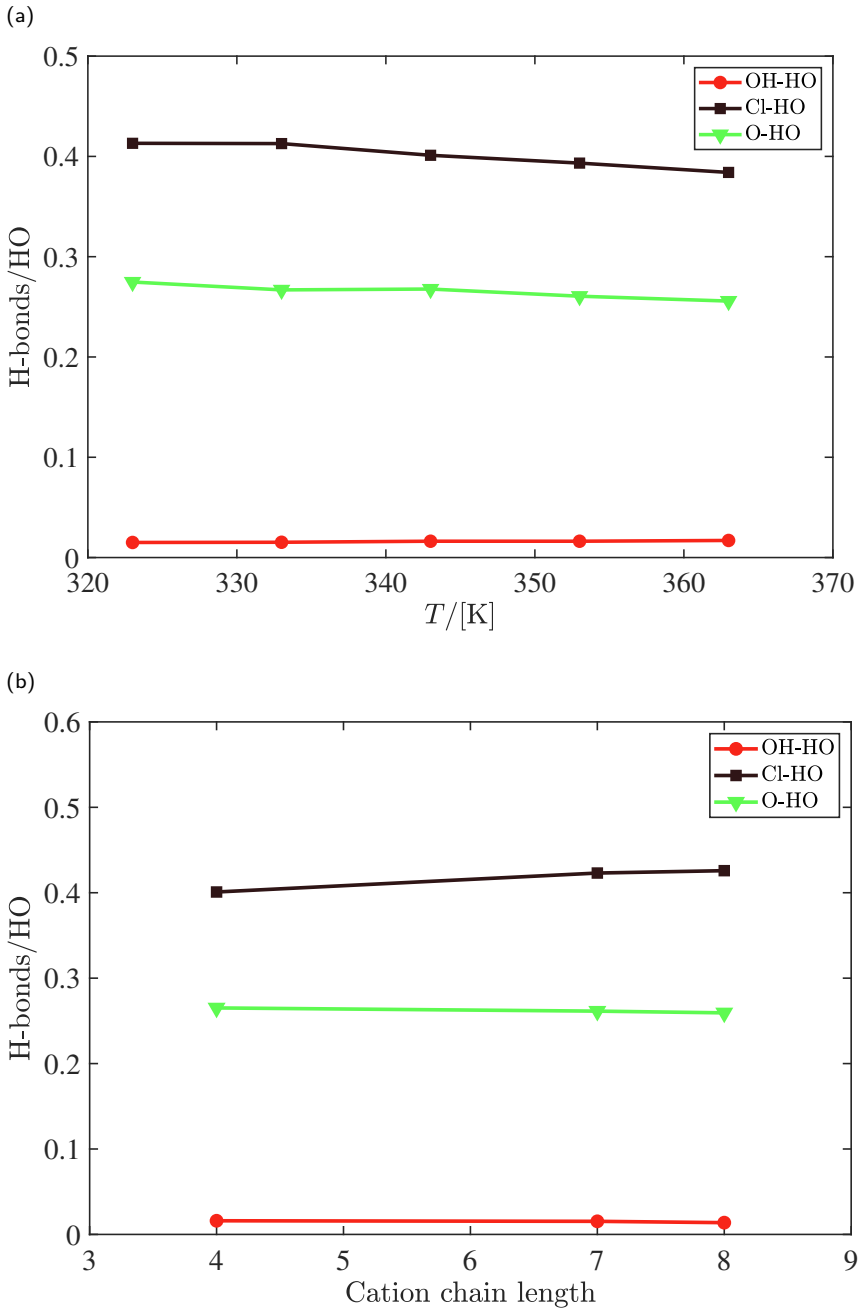

Figure 5.10: Populations of various types of hydrogen bonds per number of hydroxyl hydrogen atoms in the mixture, as a function of (a) temperature for TBAC-dec, and (b) the cation chain length at 343 K. The solid lines are drawn to guide the eye.

(and to a lesser degree the densities) of the DESs, which are considerably affected by the cation chain length. It is postulated that such differences in the density and transport properties of these DESs are observed mainly because an increase in the size of the cation hinders the packing of the molecules, and results in stronger frictional forces (due to the dispersion forces of the chains), rather than causing extensive changes to the liquid nanostructure. As future work, it would be interesting to systematically examine, at a molecular level, how the transport and structural properties of these DESs alter with the chain length of the HBD component.

5.4 Conclusions

MD simulations were performed to compute densities, transport, and structural properties of tetraalkylammonium chloride-decanoic acid DESs with cation chain lengths of 4, 7, and 8. A modified GAFF force field with an ionic charge scaling factor of 0.6 was used to model all the DESs. The computed densities and viscosities of the DESs were in reasonable agreement with experimental data from literature. An increase in the cation chain length was found to decrease the density of the DESs, possibly due to a hindered packing of molecules. The viscosity of the DESs increased with increasing the cation chain length, suggesting larger molecular friction. Consistently, the self-diffusion coefficients and ionic conductivity decreased when the cation chain length was increased, due to a lower mobility of molecules/ions. The self-diffusion coefficients of the various components exhibited the following order in all the DES systems: HBD > anion > cation. The computed RDFs showed strong interactions between the hydroxyl and carbonyl groups of decanoic acid molecules, as well as between the hydroxyl group of decanoic acid and the chloride anion. The hydrogen bond analysis indicated large populations of hydrogen bonds between the hydroxyl and carbonyl groups of decanoic acid, and the hydroxyl of decanoic acid and chloride (corroborating the RDF results), while also showing a negligible number of hydroxyl-hydroxyl hydrogen bonds between decanoic acid molecules. The effect of the cation chain length on the RDFs and the hydrogen bond populations was found to be insignificant, in sharp contrast to its pronounced influence on the transport properties.

Chapter 6

Interfacial properties of hydrophobic deep eutectic solvents with water

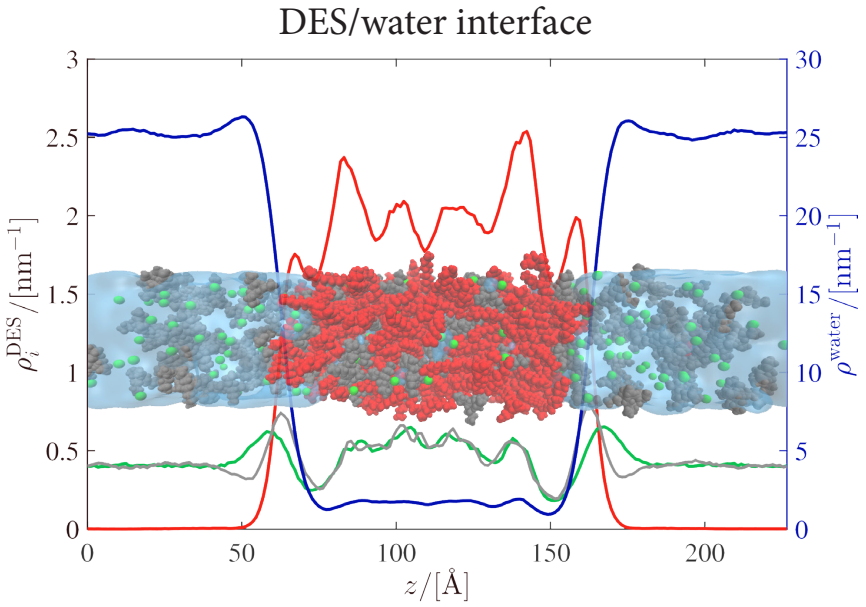

This chapter is based on the following paper: H.S. Salehi, O.A. Moultos, T.J.H. Vlugt, Interfacial properties of hydrophobic deep eutectic solvents with water, *Journal of Physical Chemistry B*, **2021**, 125, 12303–12314.

6.1 Introduction

Most DESs reported in the literature so far are of hydrophilic nature [21]. This hydrophilicity has advantages in applications where DESs are mixed with water or other hydrophilic compounds, such as alcohols, for improved thermo-physical properties. However, it limits the use of DESs for applications where miscibility with water is undesirable, for instance, in liquid-liquid extraction of solutes from water. To tackle this problem, a growing number of hydrophobic DESs have been recently synthesized, and proposed for a variety of applications, including the extraction of compounds (e.g., metals [27–29], pesticides [325], and antibiotics [24]) from aqueous phases.

Despite the high potential as water-immisible solvents, hydrophobic DESs have been mostly studied from an application standpoint. For efficient design and optimization of hydrophobic DESs (and hydrophobic extractants in general) for liquid-liquid extraction from water, theoretical studies of DES/water interfaces at the nanoscale, and the quantification of the hydrophobicity are of utmost importance. MD simulations have been widely used to study the thermodynamic and structural properties of aqueous solutions of hydrophilic DESs [119, 124, 128, 129, 133, 137, 377–379]. Several MD studies investigating the interfacial properties of biphasic systems of hydrophobic ILs and water are also available [380–387]. In sharp contrast to this, very limited studies are available exploring the interfacial properties of hydrophobic DESs with water using MD simulations [132, 139, 158]. Verma et al. [158] studied the extraction efficiency of alcohols from aqueous solutions using menthol-based DESs. These authors computed a variety of properties, such as RDFs, diffusion coefficients, and interaction energies of the DES-alcohol-water ternary systems. Paul et al. [132] investigated the stability of several hydrophobic DESs in the presence of water, and computed structural properties, such as hydrogen bond populations and RDFs, as well as self-diffusivities in the water-DES mixtures. The authors further investigated the efficiency of extraction of the pesticide nitenpyram from water using menthol-octanoic acid DES, and concluded that this DES is a suitable extractant for this process. In a recent study, Paul et al. [139] computed structural properties of biphasic systems of water and lidocaine-oleic acid DES, as well as dynamical properties (e.g., dipole autocorrelation function) of water in these system, at various temperatures, in order to understand the phase segregation mechanism above the lower critical solution temperature (LCST).

In this chapter, interfacial properties of several hydrophobic DESs with water were studied using MD simulations. The DESs were composed of decanoic acid as the HBD component, and tetrabutylammonium chloride, thymol, or DL-menthol (racemic mixture of enantiomers D-menthol and L-menthol) as the HBA component. The DESs, denoted as 'TBAC-dec', 'Thy-dec', and 'Men-dec', respectively, are listed in Table 1.1. The HBA:HBD molar ratios of 1:2, 1:2, and 2:1 were used in the simulations of the TBAC-dec/water, Thy-dec/water, and Men-dec/water systems, respectively. The density profiles of various species in the direction perpendicular to the interface were computed from MD trajectories. To quantify the hydrophobicity of the DESs, the mutual solubilities of DES and water (from the obtained density profiles) and the interfacial tensions were computed for each DES/water system. The effect of the charge scaling factors of DESs on the computed properties of TBAC-dec/water and Thy-dec/water mixtures was studied. A hydrogen bond analysis was performed to investigate the interactions of the various mixture components, which result in the computed interfacial tensions and density profiles. In Section 6.2, the force field parameters and computational methods are described. In Section 6.3, the simulation results are discussed, and compared with the available data from literature. Finally, in Section 6.4, conclusions are provided regarding the computation of the interfacial properties of hydrophobic DESs with water.

6.2 Computational details

The GAFF force field [155] was used to model intramolecular and intermolecular interactions of the DESs. The bonded terms of the force field consisted of bond-stretching, bond-bending, torsions, and improper torsions, and the non-bonded terms consisted of the Lennard-Jones (LJ) and electrostatic energies. The LJ parameters of Fox and Kollman [332] were used for the chloride ion. The electrostatic potential was computed for optimized geometries of isolated molecules/ions at the HF/6-31G* level of theory. The partial charges were obtained from the electrostatic potential using the RESP method [292]. The Gaussian 09 Rev.B.01 software [333] and the R.E.D-III.52 tools [305] were used to optimize molecular geometries, and obtain the electrostatic potential and charges. In chapter 5, the force field parameters were validated for neat TBAC-dec, where a charge scaling factor, f_{q}, of 0.6 for the cation and anion (the HBA component) resulted in more accurate densities and shear viscosities compared to experimental data by van Osch et al. [20]. To investigate the effect of charge scaling on the DES/water interfacial properties, different charge scaling

values (0.6-0.9) were used for the HBA component of TBAC-dec, i.e., the tetrabutylammonium chloride salt. For Men-dec and Thy-dec, the force fields parameters were validated by computing the densities and shear viscosities of the pure DESs, and comparing the results with experimental data available in literature [299, 388]. Based on these results, the optimal charge scaling factors were chosen for Men-dec and Thy-dec DESs. For all DESs, the 1-4 intramolecular LJ and electrostatic energies were scaled by 0.5 and 0.833, respectively [155, 204]. The SPC/E model [389] was used for water. To prevent atomic overlaps, the LJ parameters $\epsilon = 0.001\,\mathrm{kcal\,mol^{-1}}$ and $\sigma = 0.1\,\text{Å}$ were used for unprotected hydroxyl hydrogen atoms in DES and water molecules. The force field parameters of all the molecules are provided in Tables A37 and A40 to A57 of the Appendix. The molecular structures of the SPC/E water and the components (except for the chloride anion) of all DESs are shown in Figs. A7, A10 to A12, and A18 of the Appendix. To compute the LJ interactions between non-identical atom types, the Lorentz-Berthelot mixing rules [70] were used. The SHAKE algorithm [70, 390] was used to keep the bond lengths and angles of the water molecules fixed. The velocity Verlet algorithm [69, 210, 211] was used to integrate the equations of motion with a timestep of 1 fs. The Nosé-Hoover thermostat and barostat [69] were used to impose the temperature and pressure. The barostat was only applied in the direction perpendicular to the interface, thus, only changing the simulation box length in that direction, respectively. Periodic boundary conditions were used in all three dimensions. All simulations were performed with the LAMMPS software (version 16 March 2018), [110] and the initial configurations were generated using the PACKMOL package. [212] The VMD software [338] was used to visualize the snapshots of the systems.

In all simulations, a cutoff radius of 12 Å was used for both short-range LJ and short-range electrostatic energies. Due to the inhomogeneity of the system, analytic corrections [70] were not used for the long-range contributions of the LJ interactions. Instead, the long-range LJ interactions, as well as the long-range electrostatic interactions, were computed using the PPPM method [69, 391, 392]. The desired accuracies for the real-space and reciprocal parts of the long-range LJ interactions were set to 0.0001 and 0.002, respectively, while an accuracy of 10^{-6} was used for the long-range electrostatic energies. To test the adequacy of the PPPM accuracies for the LJ interactions, test simulations were performed for water and for each of the DESs in pure form. Densities and RDFs were computed from these simulations, and compared with those obtained from simulations in which analytic tail corrections (and no PPPM calculations for LJ interactions)

were used. Negligible differences were observed between the computed densities and RDFs of these simulations, thereby verifying the suitability of the selected PPPM accuracies.

To validate the force field parameters of Men-dec and Thy-dec, MD simulations were carried out for the computation of densities and shear viscosities of the neat DESs. For Men-dec, 100 menthol (50 L-menthol and 50 D-menthol) and 50 decanoic acid molecules, and for Thy-dec, 75 thymol and 75 decanoic acid molecules were used. The molar ratio of Thy-dec, at which the force field validation was performed (1:1), is different than the one used for Thy-dec/water simulations (1:2). Nevertheless, as observed from experiments [388], the densities and shear viscosities of Thy-dec are not considerably affected by the liquid composition, i.e., densities and viscosities of Thy-dec are ca. $906\,\mathrm{kg\,m^{-3}}$ and 4.2 cP at a molar ratio of 1:1, and ca. $895\,\mathrm{kg\,m^{-3}}$ and 4.3 cP at a molar ratio of 1:2, respectively. The force field validation simulations consisted of an initial energy minimization (using the conjugate gradient method), followed by 50 ns of equilibration in the NPT ensemble, and 50 ns and 140 ns of equilibration and production in the NVT ensemble at the equilibrium densities. A pressure of 1 atm and temperatures of 343 K and 328 K for Men-dec and Thy-dec, respectively, were used in the simulations. The average equilibrium box lengths were ca. 36 Å and 35.5 Å for Men-dec and Thy-dec, respectively. During the NVT production runs, the shear viscosities of the DESs were computed with the OCTP package [339], using the methodology described in chapter 5.

For the DES/water simulations, each phase (DES or water) was equilibrated separately. During the equilibration, the changes in the box dimensions were limited to only one direction, z (which is perpendicular to the interface), while the box lengths in the other two dimensions were kept fixed at 42 Å for all systems. The simulation of each phase consisted of energy minimization, and 20 ns (for water) or 30 ns (for DESs) of equilibration runs at 1 atm and 343 K in the NPT ensemble. For the DESs, before the NPT runs, the systems were annealed at 600 K and 450 K (each for 5 ns) in the NVT ensemble to facilitate the equilibration. Two replicas of the equilibrated water phase were placed adjacent to the equilibrated DES phase, on the two opposite sides. Before this, the minimum image convention [70] was used to re-attach the fragments of molecules that were broken due the periodic boundary conditions in the z-direction (perpendicular to the interface) in the simulations of the pure phases [380]. The energy of each DES/water system was minimized to remove possible atomic overlaps at the interfaces. The DES/water mixture was subsequently equilibrated at various temperatures (323 K to 363 K) and 1 atm for 55 ns to 95 ns (depending

Table 6.1: The numbers of molecules and the HBA:HBD molar ratios used in the MD simulations of DES/water systems. Each molecule of the HBA component of TBAC-dec is composed of 1 cation (tetrabutylammonium) and 1 anion (chloride). For Men-dec, equal amounts of D-menthol and L-menthol were used as the HBA component (racemic mixture), i.e., 180 D-menthol and 180 L-menthol molecules. For all mixtures, the total numbers of atoms ($N^{\text{tot}}_{\text{atoms}}$) and the approximate box dimensions, $L_x \times L_y \times L_z$ (where each box length is in units of Å, and the z-direction is perpendicular to the interface), after equilibration at 363 K and 1 atm, are also listed.

DES	molar ratio	N_{HBA}	N_{HBD}	N_{water}	$N^{\text{tot}}_{\text{atoms}}$	$L_x \times L_y \times L_z$
TBAC-dec	1:2	180	360	6000	39240	42×42×228
Thy-dec	1:2	180	360	6000	34020	42×42×203
Men-dec	2:1	360	180	6000	34920	42×42×203

on the DES and temperature), in the NPT ensemble. For all DES/water mixtures, the numbers of molecules of the components, the HBA:HBD molar ratios, the total numbers of atoms, and the approximate box dimensions after equilibration at 363 K and 1 atm are listed in Table 6.1.

Histograms of atomic positions in the z-direction were obtained during the simulations using $N_{\text{bins}} = 200$ bins. The thickness of each bin was therefore $\delta z = L_z/N_{\text{bins}}$ (L_z is the simulation box length in the z-direction for each system). The number density profile of each molecule of type i in the z-direction was calculated as:

$$\rho_i(z) = \frac{N_i(z)}{A_{xy}\delta z} \tag{6.1}$$

where $N_i(z)$ denotes the number of molecules of type i at position z, and A_{xy} is the area of the xy side of the simulation box (parallel to the interface). For each molecule, the coordinates of a single representative atom were considered for the density profile calculations: the central nitrogen for the tetrabutylammonium cation, and the hydroxyl oxygen atom for decanoic acid, thymol, and menthol.

The equilibration of each system was verified by monitoring the changes in the total energy, pressure, and the density profiles. After equilibration, NVT runs of 20 ns to 40 ns (depending on the DES and temperature) were carried at temperatures of 323 K to 363 K, during which the DES/water interfacial tensions and the water-in-DES solubilities (as well as the salt-in-water solubilities for TBAC-dec/water) were computed. To improve the statistics for the computed interfacial tensions, 5 independent runs were used for the NVT simulation of each system (all runs starting from the same equilibrated configurations obtained from the NPT simulations),

from which the averages and standard deviations were calculated. The DES/water interfacial tensions were computed according to [70, 294]:

$$\gamma = \frac{1}{2} L_z \left\langle P_{zz} - \frac{P_{xx} + P_{yy}}{2} \right\rangle \tag{6.2}$$

where the brackets $\langle ... \rangle$ denote an ensemble average, L_z is the box length in the z-direction (perpendicular to the interface), and P_{xx}, P_{yy}, and P_{zz} are the diagonal elements of the pressure tensor in the x, y, and z directions, respectively. The factor 1/2 accounts for the presence of two interfaces.

The mass fraction-based solubility of water in each DES (in units of wt%) was calculated using:

$$s = \frac{m_{\text{water}}}{m_{\text{water}} + m_{\text{DES}}} \times 100\% \tag{6.3}$$

where m_{water} and m_{DES} are the total masses of water and DES present in the DES bulk phase, respectively, and the mass of the DES equals the sum of the masses of the HBA and HBD components. The total mass of each molecule type i (DES component or water) in the DES bulk phase, was calculated by integrating its number density profile according to:

$$m_i = \frac{M_i \, A_{xy}}{N_{\text{A}}} \int_{z_{\text{min}}}^{z_{\text{max}}} \rho_i(z) \mathrm{d}z \tag{6.4}$$

where M_i is the molar mass of molecule type i, z is the position in the direction perpendicular to the interface, A_{xy} is the cross-section area of the simulation box parallel to the interface, N_{A} is the Avogadro's number, and z_{min} and z_{max} are the minimum and maximum z-coordinates of the interface edges on the DES bulk phase side, respectively. Similar calculations were performed to obtain the solubility of the HBA (salt) component of TBACdec in the aqueous phase.

The number densities of different types of hydrogen bonds, i.e., the number of each hydrogen bond type divided by $A_{xy}\delta z$ (similar to Eq. 6.1), were calculated based on MD trajectories (100-200 snapshots from the last 20 ns of the production runs) as a function of the z-coordinate, using an in-house code. 200 bins were used to compute the histograms for the number densities of the hydrogen bonds. A donor-hydrogen-acceptor angle of 30° and a cutoff distance of 3.5 Å [61, 128, 351–353] were used as the criteria for the detection of hydrogen bonds.

6.3 Results and discussion

6.3.1 Force field validation

Different charge scaling values (0.6-0.9) were used in the computations of the interfacial properties of TBAC-dec with water. In chapter 5, a charge scaling factor of 0.6 yielded the best agreement of the computed transport properties and density of neat TBAC-dec with experimental data. Consistently, from test simulations in the present chapter, it was found that the shear viscosities of neat Thy-dec (molar ratio of 1:1) and Men-dec (molar ratio of 1:2) are significantly overestimated (by a factor of ca. 3.6 for both DESs) without the use of charge scaling, compared to experimental data [299, 388]. Two sets of charge scaling factors were found to yield reasonably accurate densities and shear viscosities for Thy-dec: 0.7 for thymol and 1 for decanoic acid (denoted by 'f_{q} =0.7/1'), and 0.8 for both thymol and decanoic acid (denoted by 'f_{q} =0.8/0.8'). To investigate the effect of charge scaling on the computed interfacial properties, both charge scaling sets were used for Thy-dec in the production runs of the Thy-dec/water simulations. For Men-dec, a charge scaling of 0.8 for menthol and a charge scaling of 1 for decanoic acid (denoted by 'f_{q} =0.8/1') resulted in accurate density and shear viscosity calculations. The results of the force field validation are presented in Table 6.2 for all the DESs and charge scaling sets, and compared with available experimental data [20, 299, 388].

6.3.2 Density profiles and interfacial tensions

The number density profiles were computed for different components (i.e., molecule types) of the DESs using Eq. 6.1. The density profile results for TBAC-dec/water mixtures, at 363 K, with charge scaling factors of 0.6 and 0.8, are presented in Figs. 6.1 and 6.2, respectively, accompanied by typical snapshots of the systems. The DES/water interfaces (indicated by blue shaded areas in Figs. 6.1 and 6.2) were identified as regions where the densities of the mixture components change from the constant densities in the water phase to the constant densities in the DES phase. Based on this definition, the thickness of each interface was estimated from the difference in the z-coordinates of the two interface edges. It can be observed from Fig. 6.1 that with $f_{\mathrm{q}} = 0.6$, the structure of the TBAC-dec (at the center) remains mostly intact, with very small amounts of cation and anion transferred to the aqueous phase (on the two opposite sides of the DES). This is in sharp contrast to experimental observations where it has been shown that considerable amounts of the HBA (i.e., the salt composed of

Table 6.2: Computed densities and shear viscosities of Thy-dec (molar ratio of 1:1), using different charge scaling factors, and Men-dec (molar ratio of 1:2), compared with experimental data [299, 388]. The density and shear viscosity of TBAC-dec (molar ratio of 1:2), as computed in chapter 5, using a charge scaling factor of 0.6, have also been listed, and compared with the experimental data by van Osch et al. [20].

DES	T/[K]	f_q	ρ^{sim}/[kg m^{-3}]	ρ^{exp}/[kg m^{-3}]	η^{sim}/[cP]	η^{exp}/[cP]
TBAC-dec [a]	323	0.6	884.2	901.0	75.8	68.3
Thy-dec	328	0.7/1	899.4	906.6	5.3	4.2
		0.8/0.8	894.7		4.5	
Men-dec	343	0.8/1	859.3	862.5	3.7	3.4

[a] Simulation results from chapter 5

the cation and anion) of TBAC-dec leach to the water phase [20, 29, 325]. For instance, van Osch et al. [20] found a 34.8% leaching of the salt (i.e., the mass of the leached salt divided by the total mass of the salt in the DES) into water at 298 K, indicating a salt-in-water solubility of ca. 13.5 wt%. As can be observed in Fig. 6.1, the cation density profile shows a peak at the intersection of the water and decanoic acid profiles, indicating a favorable position for the cation that allows for interactions with both the water and decanoic acid. Fig. 6.2 shows the density profiles of the TBAC-dec/water system, using a charge scaling factor of 0.8 for the salt. It can be observed that with $f_q = 0.8$, a significant leaching of the salt into water occurs, which changes the structure and composition of the neat DES, and results in similar densities of the cation and anion in water, compared to those in the DES bulk phase. This is due to the stronger electrostatic interactions of the cation and anion with water at $f_q = 0.8$, compared to $f_q = 0.6$. Consistently, Paul et al. [132] showed, using MD simulations of TBAC-dec/water with a charge scaling factor $f_q = 1$ (no scaling), a complete leaching of the salt into water. As shown in Fig. 6.2, both the cation and anion show peaks at the intersections of the water and decanoic acid density profiles, possibly due to the simultaneously maximized HBD-HBA and HBA-water interactions. Although comparable interface thicknesses are obtained using charge scaling factors of 0.6 and 0.8 (ca. 45 Å), at $f_q = 0.8$, due to the leaching of the HBA, the thickness of the DES bulk phase is smaller, while the thickness of the aqueous phase is larger. Using both charge scaling factors, decanoic acid and water are immiscible, in agreement with experimental observations [20, 29, 325].

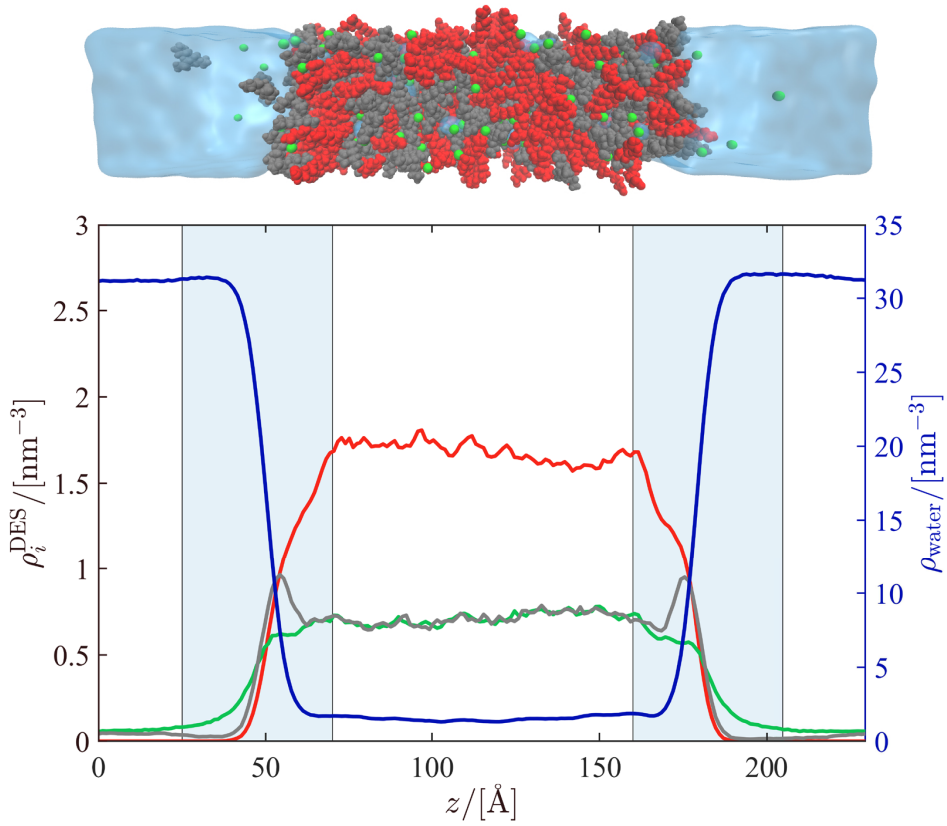

Figure 6.1: Computed number density profiles (number of molecules per nm^3) of DES components i (left vertical axis) and water (right vertical axis) in the TBAC-dec/water system at 363 K and 1 atm, using a charge scaling factor of $f_{\mathrm{q}} = 0.6$ for the HBA. A typical snapshot of the same system is shown above the plot. The red, green, gray, and blue colors correspond to decanoic acid (HBD), chloride (anion), choline (cation), and water (shown in the snapshot using the blue surfaces), respectively. For the density profiles of decanoic acid and choline, the coordinates of the hydroxyl oxygen and the nitrogen atoms were used, respectively. The DES/water interfaces are indicated in the plot using blue shaded areas.

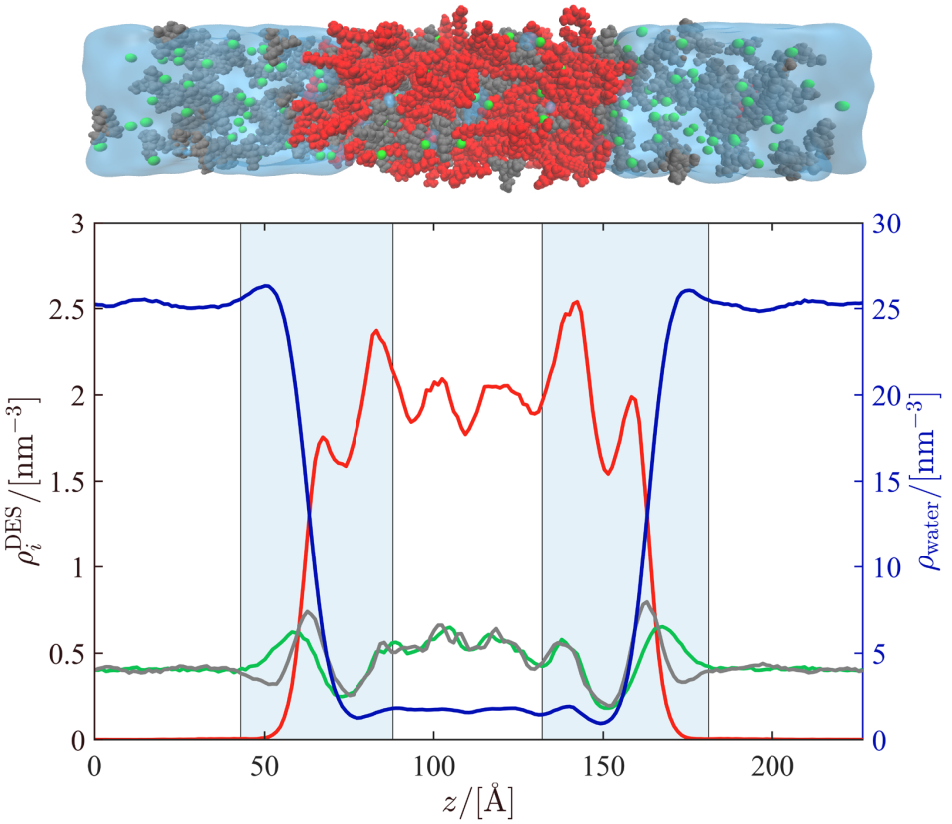

Figure 6.2: Computed number density profiles (number of molecules per nm^3) of DES components i (left vertical axis) and water (right vertical axis) in the TBAC-dec/water system at 363 K and 1 atm, using a charge scaling factor of $f_{\mathrm{q}} = 0.8$ for the HBA. A typical snapshot of the same system is shown above the plot. The red, green, gray, and blue colors correspond to decanoic acid (HBD), chloride (anion), choline (cation), and water (shown in the snapshot using the blue surfaces), respectively. For the density profiles of decanoic acid and choline, the coordinates of the hydroxyl oxygen and the nitrogen atoms were used, respectively. The DES/water interfaces are indicated in the plot using blue shaded areas.

The density profiles of the TBAC-dec/water system at 343 K, with charge scaling factors of 0.6 and 0.8, are presented in Fig. A26 of the Appendix. Similar to the results shown in Figs. 6.1 and 6.2, an increase in the charge scaling factor increases the leaching of the salt into water at 343 K (Fig. A26). By comparing Fig. A26 with Figs. 6.1 and 6.2, it can be concluded that the density profiles, and thus the hydrophobicity of TBAC-dec, are not considerably affected by temperature. Using Eqs. 6.3 and 6.4, the solubility of the salt (HBA) component of TBAC-dec in water at 363 K (the average solubilities of the cation and anion), with the charge scaling factor of 0.6, is computed as 2.4 wt%, which is significantly underestimated compared to the experimental value of 13.5 wt% at 298 K. Therefore, whereas the properties of neat TBAC-dec are accurately reproduced with $f_q = 0.6$ (chapter 5), the computed salt-in-water solubility is much lower than the experimental value (assuming a negligible effect of temperature on the solubility). Using $f_q = 0.8$, the salt-in-water solubility of TBAC-dec at 363 K is computed as 19.9 wt%, which is in a better agreement with the experimental value. The water-in-DES solubilities for TBAC-dec at 363 K, using charge scaling factors of 0.6 and 0.8, are computed as 5.0 wt% and 4.8 wt%, respectively, which are both in reasonable agreement with the experimental value of 6.9 wt% at 298 K [20].

From the results of Figs. 6.1 and 6.2 (and Fig. A26), it is indicated that the charge scaling factor of 0.8 for TBAC-dec is better suited for the computation of the properties of the DES/water biphasic system, compared to the charge scaling factor of 0.6. In chapter 5, it was shown that using charge scaling factors larger than 0.6 while not considerably affecting the density, led to highly overestimated shear viscosities of TBAC-dec (unless the LJ interactions from the GAFF force field were also scaled). For instance, the shear viscosities of TBAC-dec at 353 K using charge scaling factors of 0.6 and 0.7 were computed as 51.0 cP and 19.4 cP, respectively, whereas the (extrapolated) experimental viscosity at this temperature is 16.8 cP. The shear viscosity of TBAC-dec with $f_q = 0.8$ could not be computed from those simulations, due to non-converging mean squared displacements, which is indicative of very high viscosities. Such a high viscosity is also reflected in the relatively large fluctuations of the densities of the DES components (particularly the HBD) in Fig. 6.2, suggesting a hindered motion of the molecules, and thus a more difficult sampling. This increase in the density fluctuations with an increase in the charge scaling factor is more accentuated at 343 K (Fig. A26 in the Appendix) due to higher viscosities. Therefore, large charge scaling values, while may be appropriate for DES/water interface computations, are not suitable for computing the

properties of neat DESs. It is important to note that in the study by Paul et al. [132], where $f_q = 1$ was used, the authors did not compute the properties of neat DESs (only DES/water properties were computed), except for a few densities, which may reduce the transferability of their force fields for such computations.

The computed density profiles for the components of the Thy-dec/water mixture at 363 K, using $f_q = 0.7/1$, and a typical snapshot of the system are presented in Fig. 6.3. It can be observed that Thy-dec is almost completely immiscible with water, with a computed water-in-DES solubility of 0.71 wt%, consistent with experiments for Thy-dec with a molar ratio of 1:1 at 298 K [393]. The density profiles for Thy-dec/water with charge scaling factors $f_q = 0.8/0.8$ are shown in Fig. 6.4. By comparing Figs. 6.3 and 6.4, it is found that the density profiles of the various components are nearly identical between the two charge scaling sets. For both charge scaling sets, the thickness of each DES/water interface is ca. 35 Å. Using the charge scaling factors $f_q = 0.8/0.8$, the water-in-DES solubility for the Thy-dec/water system is computed as 0.92 wt%, which is comparable to that obtained with $f_q = 0.7/1$. In Figs. 6.3 and 6.4, two large peaks can be observed for the (hydroxyl oxygen of) decanoic acid at each interface, followed by minimums. As shown in Fig. 6.5a, these minimums correspond to density profile peaks for the terminal carbon of decanoic acid (on the opposite side of the molecule with respect to the oxygen atom). Therefore, the density profile peaks of decanoic acid in Figs. 6.3 and 6.4 are possibly caused by the fact that the decanoic acid molecules are aligned such that their hydroxyl or carbonyl oxygen atoms can form hydrogen bonds with the water molecules at the interface (i.e., with the oxygen and terminal carbon atoms of decanoic acid towards the water and DES phases, respectively). This hypothesis is supported by a close-up snapshot of the Thy-dec/water system, presented in Fig. 6.5b, which shows the orientation of decanoic acid molecules at the interface. The density profiles of the Thy-dec/water components at 343 K are presented in Fig. A27 of the Appendix, for both charge scaling sets. It can be observed that similar to TBAC-dec/water, the effect of temperature on the density profiles of Thy-dec/water and the hydrophobicity of Thy-dec is very small.

The computed density profiles of the Men-dec/water components at 363 K and a typical system snapshot are shown in Fig. 6.6. Similar to the Thy-dec/water density profiles (Figs. 6.3 and 6.4), the density profiles of Men-dec/water indicate a nearly complete immiscibility of the DES with water. The water-in-DES solubility was computed as 0.4 wt%, which compared to the experimental value of 2.1 wt% at 295 K [46], indicates an

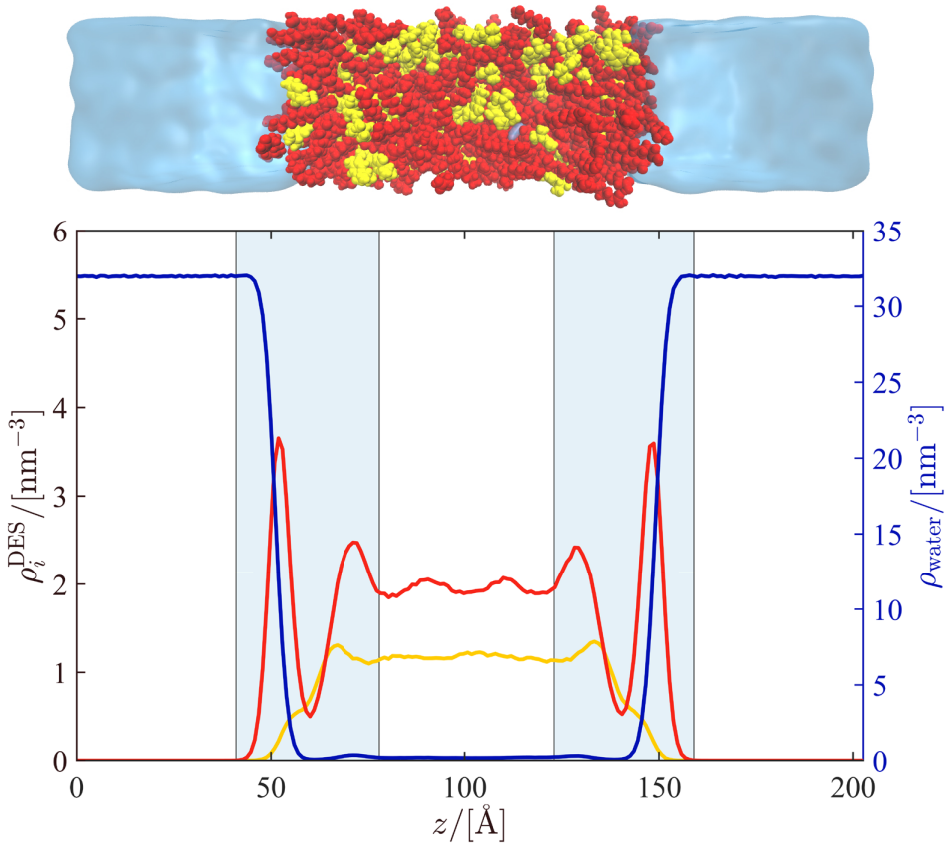

Figure 6.3: Computed number density profiles (number of molecules per nm^3) of DES components i (left vertical axis) and water (right vertical axis) in the Thy-dec/water mixture at 363 K and 1 atm, using the charge scaling factors $f_{\mathrm{q}} = 0.7/1$. A typical snapshot of the same system is shown above the plot. The red, yellow, and blue colors correspond to decanoic acid (HBD), thymol (HBA), and water (shown in the snapshot using the blue surfaces), respectively. For the density profiles of decanoic acid and thymol, the coordinates of the hydroxyl oxygen atoms were used. The DES/water interfaces are indicated in the plot using blue shaded areas.

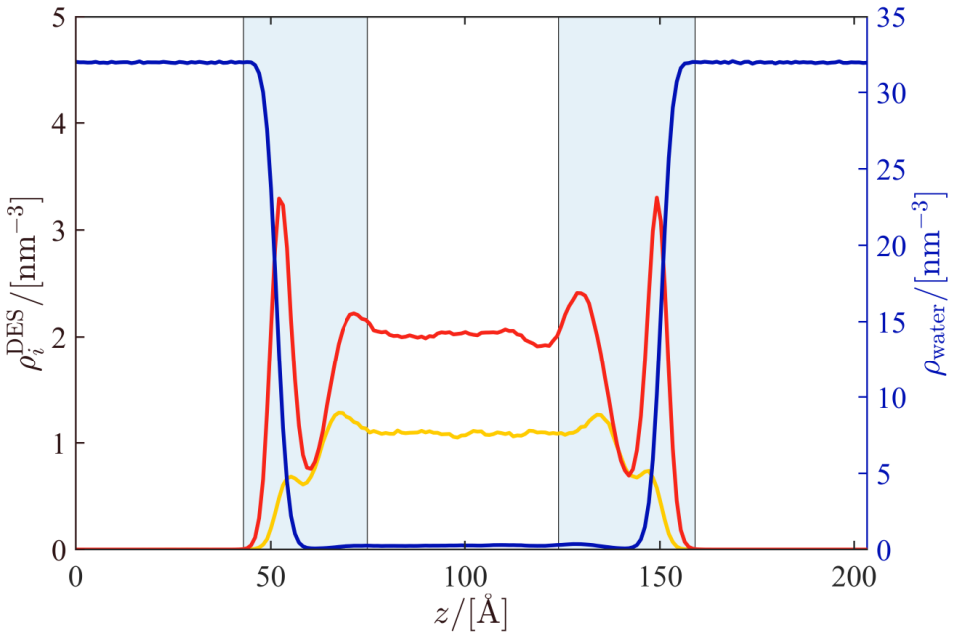

Figure 6.4: Computed number density profiles (number of molecules per nm^3) of DES components i (left vertical axis) and water (right vertical axis) in the Thy-dec/water mixture at 363 K and 1 atm, using the charge scaling factors $f_{\mathrm{q}} = 0.8/0.8$. The red, yellow, and blue profiles correspond to decanoic acid (HBD), thymol (HBA), and water, respectively. For the density profiles of decanoic acid and thymol, the coordinates of the hydroxyl oxygen atoms were used. The DES/water interfaces are designated using blue shaded areas.

underestimation of the solubility of water in Men-dec from the simulations (assuming a negligible effect of temperature on the solubility). The interface thickness of the simulated Men-dec/water system is roughly 30 Å. The density profiles for Men-dec/water show very similar features to the ones observed for Thy-dec/water, namely the large peaks of the decanoic acid profile (due to the alignment of decanoic acid molecules to form hydrogen bonds with water), and a two-step increase in the density of the HBA (menthol or thymol) from the aqueous phase to the DES phase. The relative values of the HBD and HBA densities in the DES phase of Men-dec/water are nevertheless different from those in Thy-dec/water, due to the different HBA:HBD molar ratios of the two DESs. The density profiles of the Men-dec/water components at 343 K are presented in Fig. A28 of the Appendix, which in comparison to the density profiles in Fig. 6.6, indicate a negligible influence of temperature on the DES/water interface and the hydrophobicity of Men-dec. It is important to note that in the simulations of Men-dec/water, the HBA component of Men-dec consisted of equal amounts of D-menthol

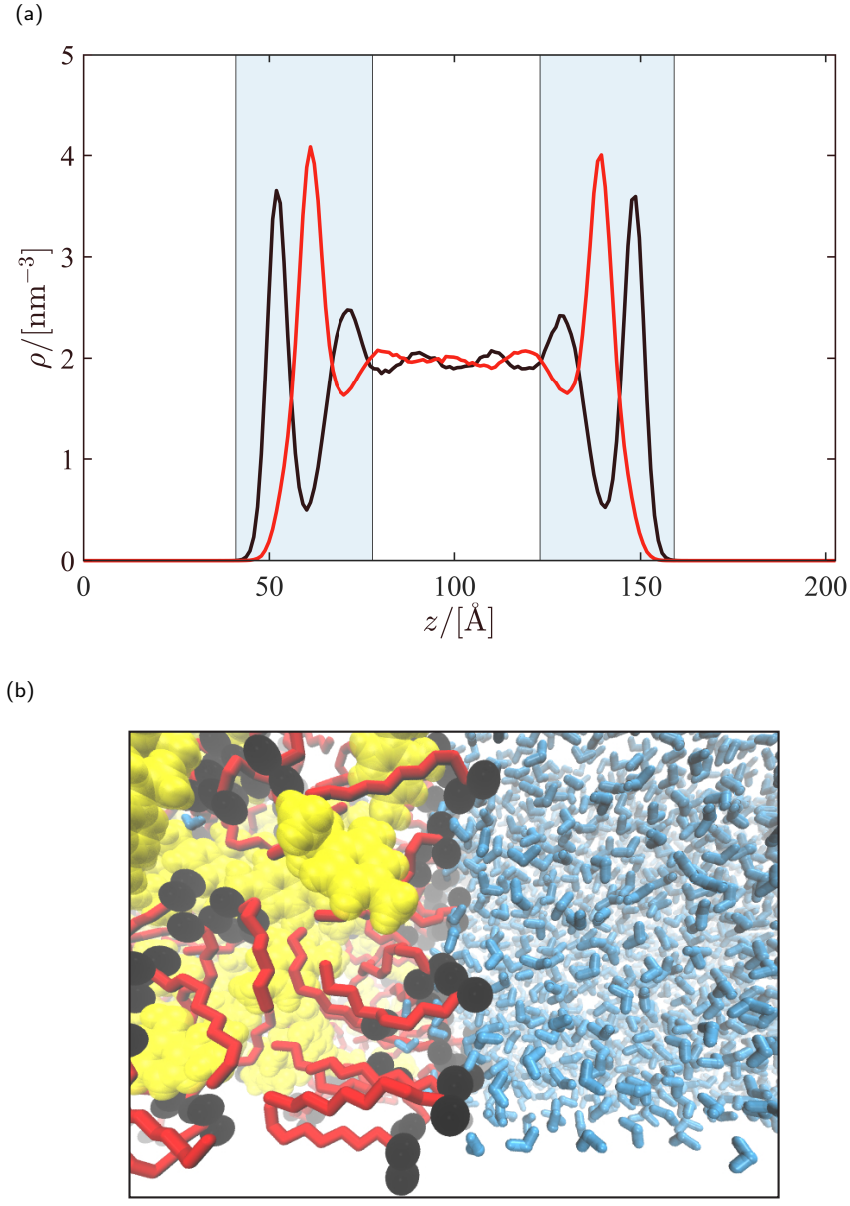

Figure 6.5: (a) Computed number density profiles (number of molecules per nm^3) for the hydroxyl oxygen, in red, and the terminal carbon, in black, of decanoic acid in the Thydec/water mixture at 363 K and 1 atm, using the charge scaling factors $f_{\mathrm{q}} = 0.7/1$. (b) A close-up snapshot of the interface of the same system, showing the alignment of the oxygen atoms (black van der Waals surfaces) of decanoic acid towards the aqueous phase. The carbon atoms of decanoic acid are colored red (the hydrogen atoms are omitted in the snapshot for clarity). The yellow and blue molecules are thymol and water, respectively.

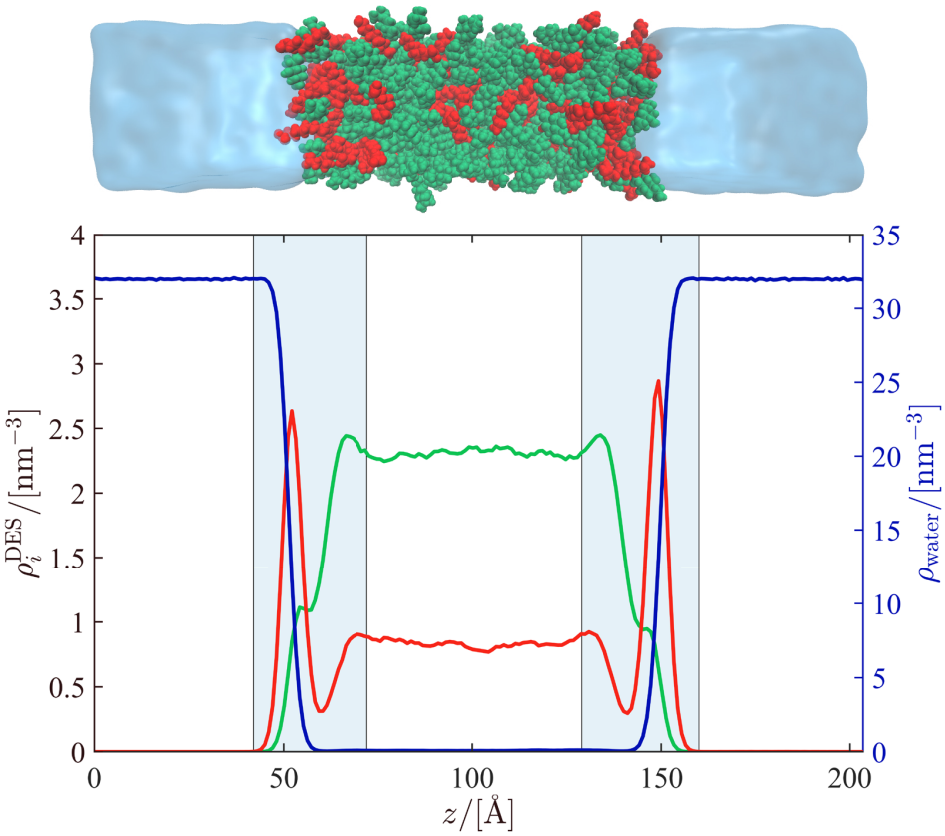

Figure 6.6: Computed number density profiles (number of molecules per nm^3) of DES components i (left vertical axis) and water (right vertical axis) in the Men-dec/water mixture at 363 K and 1 atm, using the charge scaling factors $f_{\mathrm{q}} = 0.8/1$. A typical snapshot of the same system is shown above the plot. The red, green, and blue colors correspond to decanoic acid (HBD), menthol (HBA), and water (shown in the snapshot using the blue surfaces), respectively. For the density profiles of decanoic acid and menthol, the coordinates of the hydroxyl oxygen atoms were used. The density profile of menthol in the plot and its representation in the snapshot, include both D-menthol and L-menthol molecules. The DES/water interfaces are indicated in the plot using blue shaded areas.

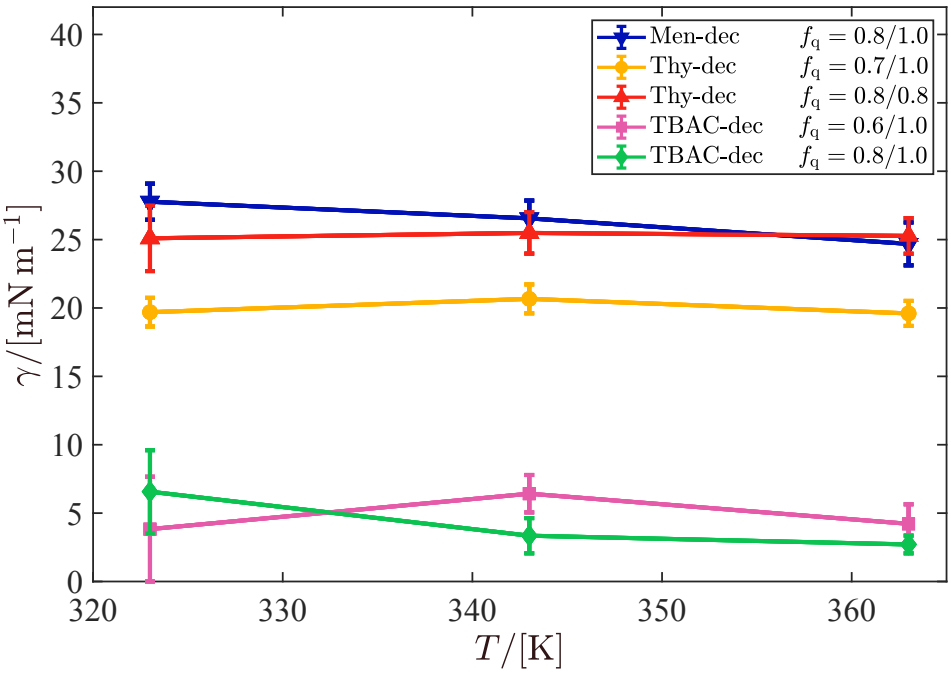

Figure 6.7: Computed DES/water interfacial tensions for the various DESs and charge scaling sets, as a function of temperature (at 1 atm). The lines are drawn to guide the eye.

and L-menthol (racemic mixture). However, negligible differences were observed for the density profiles and hydrogen bonds (the following section) between D-menthol and L-menthol. Therefore, the density profiles and hydrogen bonds of D-menthol and L-menthol were lumped together as a single 'menthol' component, which is used throughout this chapter.

The interfacial tensions of the DESs with water were computed from *NVT* simulations at different temperatures, using Eq. 6.2. The results, presented in Fig. 6.7, indicate that the DES/water interfacial tensions of all the DESs, at all charge scaling factors, are independent of temperature (within the error bars). This further verifies that the hydrophobicity of the studied DESs is insensitive to temperature. As shown in Fig. 6.7, TBAC-dec has the smallest interfacial tension with water, and thus the lowest hydrophobicity. The differences between the TBAC-dec/water interfacial tensions at $f_q = 0.6$ and $f_q = 0.8$ generally fall within the error bars (i.e., the standard deviation of the interfacial tensions from the 5 independent runs) shown in Fig. 6.7, although from the density profiles and simulation snapshots (Figs. 6.1 and 6.2), it can be concluded that $f_q = 0.6$ leads to a higher hydrophobicity for TBAC-dec. The high DES/water interfacial tensions of

Thy-dec and Men-dec corroborate the large extent of the hydrophobicity of these DESs, deduced from the density profiles and simulation snapshots (Figs. 6.3, 6.4, and 6.6). Unlike for TBAC-dec, the DES/water interfacial tension of Thy-dec highly depends on the charge scaling set used in the simulations, i.e., the scaling factors $f_q = 0.8/0.8$ result in a larger interfacial tension, compared to $f_q = 0.7/1$. This implies the pivotal role of decanoic acid in lowering the interfacial energy of Thy-dec with water, through electrostatic forces (possibly hydrogen bonds). Considering the charge scaling factors $f_q = 0.7/1$ for Thy-dec, the relative magnitudes of the computed interfacial tensions with water (and thus the hydrophobicity) of the DESs are in the following order: TBAC-dec < Thy-dec < Men-dec. Consistently, this is the reverse of the order of water-in-DES solubilities, calculated from the density profiles, which is in agreement with the order of water-in-DES solubilities described by Florindo et al. [21], based on the DES constituents (menthol < thymol < quaternary ammonium salts).

6.3.3 Hydrogen bond analysis

The number densities of various types of hydrogen bonds (ρ_{Hb}) were calculated as a function of the z-coordinate (perpendicular to the interface) for all the DESs and charge scaling sets. The hydrogen bond analysis results are presented in Figs. 6.8 to 6.11. The DES/water interfaces, as deduced from the density profiles in Figs. 6.1 to 6.4 and 6.6, are also shown in Figs. 6.8 to 6.11, using blue shaded areas. As can be observed in Fig. 6.8, for TBAC-dec/water (at 363 K), using both charge scaling factors, the chloride anion forms hydrogen bonds with water in the aqueous phase, with $f_q = 0.8$ resulting in a larger number of chloride-water hydrogen bonds, compared to $f_q = 0.6$. Using the scaling factor $f_q = 0.6$, the total number of hydrogen bonds of chloride (i.e., the sum of the number of chloride-decanoic acid and chloride-water hydrogen bonds) in the DES phase is larger than that in the aqueous phase (Fig. 6.8a). This is in sharp contrast to the results for $f_q = 0.8$ (Fig. 6.8b), where the total number of hydrogen bonds of chloride in the DES phase is comparable to the number of chloride-water hydrogen bonds in the aqueous phase, which may explain the leaching of chloride into water and the more or less constant number density of chloride throughout the whole simulation box (Fig. 6.2). The leaching of the cation into water, particularly at $f_q = 0.8$, likely occurs as a result of the electrostatic interactions of the cation with water and with the leached chloride. These findings are consistent with the MD simulation results by Paul et al. [132], where a large number of hydrogen bonds were formed between the chloride anion of tetrabutylammonium chloride-octanoic acid

(molar ratio of 1:1, and $f_q = 1$) and water, substantially contributing to the leaching of the salt into the aqueous phase.

It can be observed in Fig. 6.8 that for $f_q = 0.6$, the number of decanoic acid-decanoic acid hydrogen bonds in the DES phase is similar to that of chloride-decanoic acid hydrogen bonds, whereas with a larger anion charge ($f_q = 0.8$), the number of chloride-decanoic acid hydrogen bonds is larger than that of the decanoic acid-decanoic acid hydrogen bonds. The water molecules form a considerable number of hydrogen bonds with both the anion and decanoic acid in the DES phase, driving the dissolution of water into the DES. Large peaks are observed at each interface for decanoic acid-water hydrogen bonds. The presence of these peaks supports the hypothesis that decanoic acid molecules align their acidic ends towards the water phase (as shown in Fig. 6.5 for Thy-dec/water) to maximize the hydrogen bonding with the water molecule. Whereas decanoic acid-decanoic acid, decanoic acid-chloride, and decanoic acid-water hydrogen bond interactions compete more equally in the DES bulk phase, at the interface, the hydrogen bond interactions of decanoic acid are dominated by those with the water molecules. With an increase in the charge scaling factor from 0.6 to 0.8, the intensities of the decanoic acid-water hydrogen bond peaks increase, possibly due to a stronger alignment of decanoic acid oxygen atoms towards the aqueous phase, which may be caused by the leaching of the anion into water. The number densities of decanoic acid-decanoic acid and decanoic acid/water hydrogen bonds at $f_q = 0.8$ were decomposed based on the functional group of decanoic acid participating in the hydrogen bonds, i.e., carbonyl or hydroxyl, and the results are presented in Fig. 6.9. It can be observed in Fig. 6.9 that decanoic acid-decanoic acid hydrogen bonds mainly form between the carbonyl and hydroxyl groups, whereas negligible hydroxyl-hydroxyl hydrogen bonds are formed between decanoic acid molecules (consistent with the MD results for neat TBAC-dec in chapter 5). For decanoic acid-water hydrogen bonds, significant contributions are observed from both the hydroxyl and carbonyl groups of decanoic acid (a larger contribution by the hydroxyl groups). The hydrogen bond number densities of TBAC-dec/water at 343 K are presented in Fig. A29 of the Appendix. No significant difference is found in the hydrogen bond networks of TBAC-dec/water between the two temperatures (for both charge scaling factors), which is consistent with the observations from the computed density profiles.

The hydrogen bond number densities of Thy-dec/water at 363 K are presented in Fig. 6.10 for the charge scaling sets $f_q = 0.7/1$ and $f_q = 0.8/0.8$. It can be observed that using both charge scaling sets, large peaks occur for

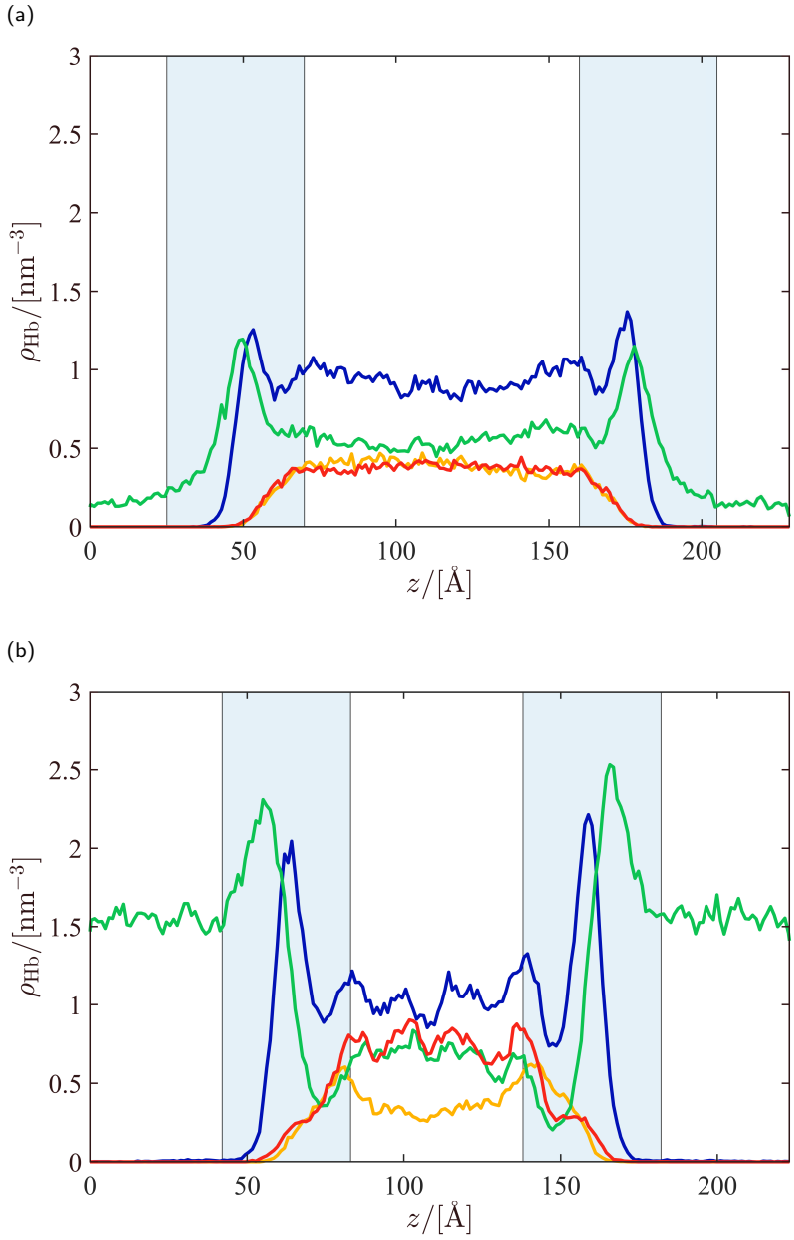

Figure 6.8: Computed hydrogen bond number densities (number of hydrogen bonds per nm^3) for the TBAC-dec/water system at 363 K and 1 atm, with charge scaling factors of (a) f_{q}=0.6, and (b) f_{q}=0.8. The blue, green, yellow, and red colors correspond to water-decanoic acid, water-chloride, decanoic acid-decanoic acid, and chloride-decanoic acid hydrogen bonds, respectively. The blue shaded areas indicate the interfaces, as deduced from the density profiles in Figs. 6.1 and 6.2.

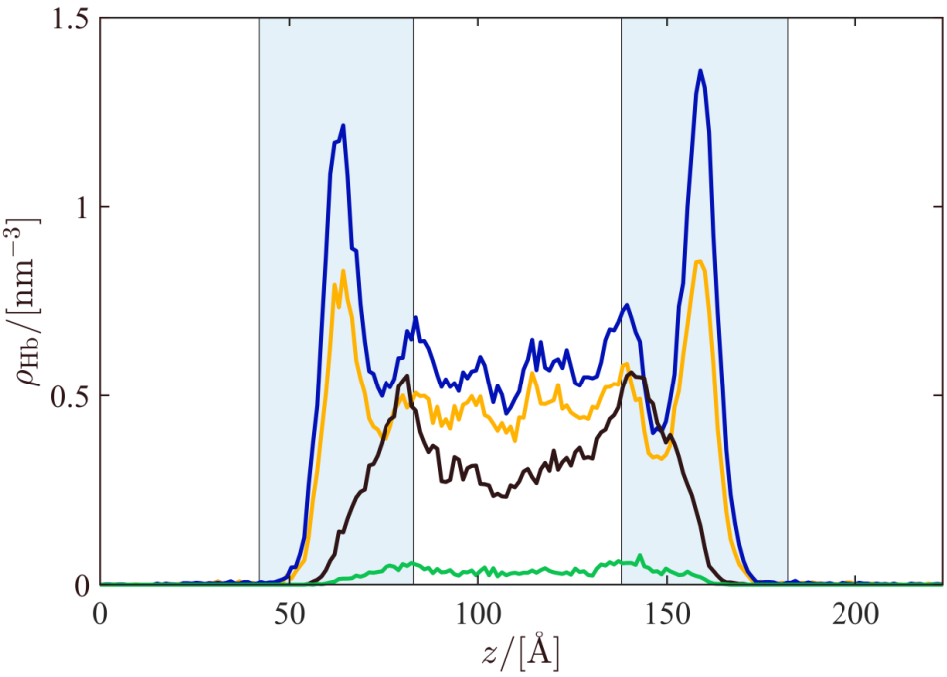

Figure 6.9: Computed hydrogen bond number densities (number of hydrogen bonds per nm^3) for the TBAC-dec/water system at 363 K and 1 atm, using the charge scaling factor of f_{q}=0.8. The colors correspond to the different types of hydrogen bonds according to: Blue, between water and the hydroxyl group of decanoic acid; orange, between water and the carbonyl group of decanoic acid; black, between the hydroxyl and carbonyl groups of decanoic acid molecules; and green, between the hydroxyl groups of decanoic acid molecules. The blue shaded areas indicate the interfaces, as deduced from the density profiles in Fig. 6.2.

water-decanoic acid hydrogen bonds at the interface, which may be caused by the larger number of water molecules present at the interface compared to the DES bulk phase, and possibly also the alignment of the oxygen atoms of decanoic acid towards the aqueous phase (Fig. 6.5). This explains the large peaks of the density profile of decanoic acid in Figs. 6.3 and 6.4. It can be observed that the numbers of decanoic acid-water and decanoic acid-decanoic acid hydrogen bonds are significantly larger for $f_{\mathrm{q}} = 0.7/1$ (with peak heights of ca. $6.1\,\mathrm{nm}^{-3}$ and $1.5\,\mathrm{nm}^{-3}$, respectively), compared to $f_{\mathrm{q}} = 0.8/0.8$ (with peak heights of $3.8\,\mathrm{nm}^{-3}$ and $0.7\,\mathrm{nm}^{-3}$, respectively), due the larger partial atomic charges of decanoic acid at $f_{\mathrm{q}} = 0.7/1$. The larger number of decanoic acid-water hydrogen bonds for $f_{\mathrm{q}} = 0.7/1$ is likely responsible for the lower Thy-dec/water interfacial tensions at $f_{\mathrm{q}} = 0.7/1$, compared to $f_{\mathrm{q}} = 0.8/0.8$ (Fig. 6.7). The thymol-water hydrogen bond densities show small peaks at the interfaces due to the interactions of the

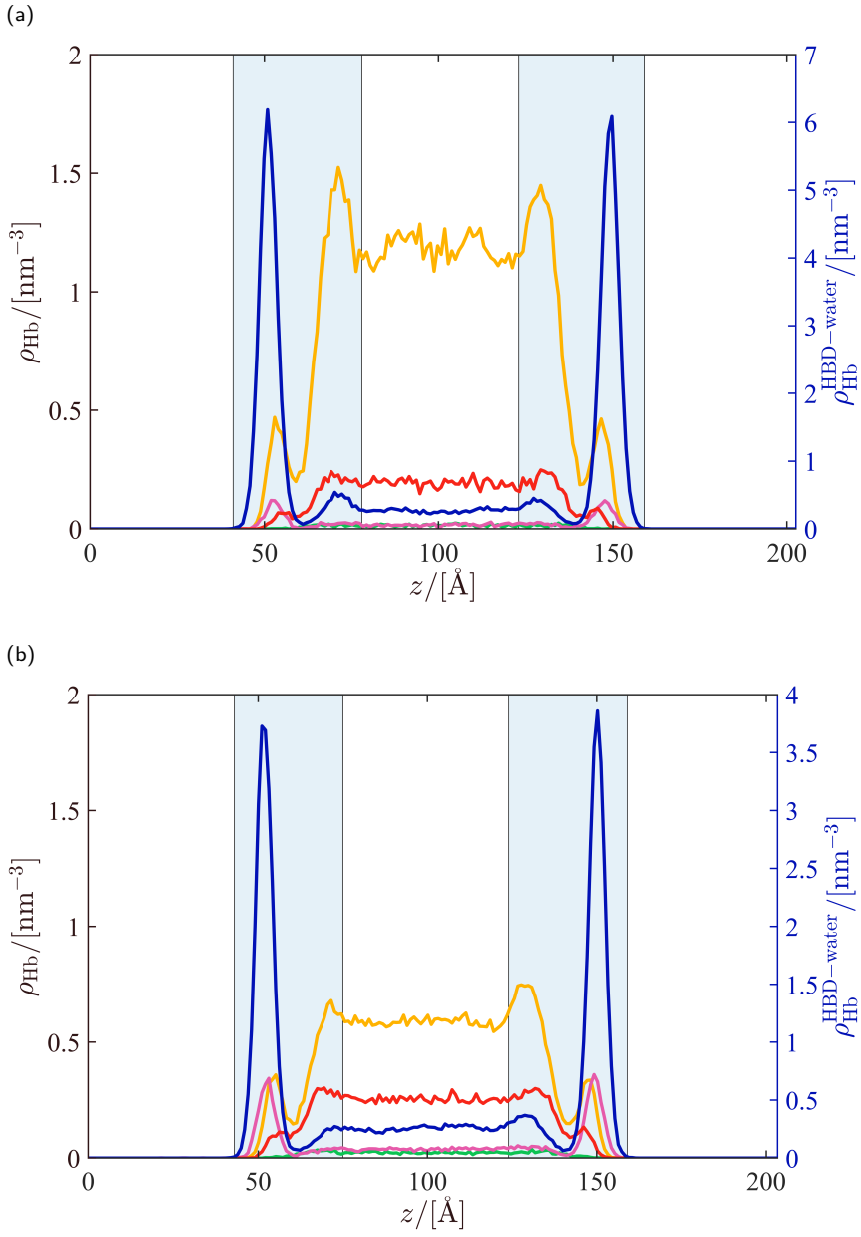

Figure 6.10: Computed hydrogen bond number densities (number of hydrogen bonds per nm^3) for the Thy-dec/water system at 363 K and 1 atm, with charge scaling factors of (a) f_{q}=0.7/1, and (b) f_{q}=0.8/0.8. The blue, green, yellow, red, and pink colors correspond to water-decanoic acid (right vertical axis), thymol-thymol, decanoic acid-decanoic acid, thymol-decanoic acid, and water-thymol hydrogen bonds, respectively. The blue shaded areas indicate the interfaces, as deduced from the density profiles in Figs. 6.3 and 6.4.

hydroxyl group of thymol with water, whereas a negligible number of thymol-water hydrogen bonds occur within the DES phase. A very small number of thymol-thymol hydrogen bonds is formed in the DES bulk phase, while a more considerable number of thymol molecules participate in hydrogen bonding with decanoic acid. The hydrogen bond number densities for Thy-dec/water at 343 K are provided in Fig. A30 of the Appendix, showing an insignificant effect of temperature on the hydrogen bond network of the system (compared to Fig. 6.10).

For Men-dec/water, the hydrogen bond number densities of the various components are shown in Fig. 6.11, for temperatures of 343 K and 363 K. It can be observed that similar to TBAC-dec/water and Thy-dec/water mixtures, the effect of temperature on all hydrogen bond densities in Men-dec/water is negligible. As shown in Fig. 6.11, large peaks are observed at the interfaces for the water-decanoic acid hydrogen bond densities, while comparatively smaller peaks are found for the densities of menthol-water, menthol-decanoic acid, and decanoic acid-decanoic acid hydrogen bonds. The menthol-decanoic acid and decanoic acid-decanoic acid hydrogen bonds mostly occur in the DES bulk phase. Similar to TBAC-dec/water and Thy-dec/water, the large number density peaks for the water-decanoic acid hydrogen bonds at the interfaces of Men-dec/water may be due to the higher concentration of water at the interfaces compared to the DES bulk phase, and the alignment of decanoic acid oxygen atoms towards the aqueous phase. The total numbers of water-menthol and water-decanoic acid hydrogen bonds in the Men-dec/water mixture at 363 K were calculated as ca. 16 and 113, respectively. This is in agreement with the MD simulation results of Paul et al. [132], where for a mixture of Men-dec (with a molar ratio of 1:1, and no charge scaling) and water, a significantly larger number of water-decanoic acid hydrogen bonds were found, compared to that of water-menthol hydrogen bonds. The large number of water-decanoic acid hydrogen bonds at the interfaces, observed in Fig. 6.11, justifies the large density profile peaks for (the hydroxyl oxygen of) decanoic acid, in Fig. 6.6. In contrast to the Thy-dec/water system, in Men-dec/water, the number of HBA-HBA (menthol-menthol) hydrogen bonds in the DES bulk phase is comparable to the numbers of other hydrogen bonds (i.e., menthol-decanoic acid and decanoic acid-decanoic acid hydrogen bonds), which may mostly be due the larger mole fraction of menthol in Men-dec, compared to that of thymol in Thy-dec.

From the study of the density profiles and the hydrogen bond analysis, it was found that the hydrogen bonding between the various components, particularly the decanoic acid-water and the anion-water (in TBAC-dec)

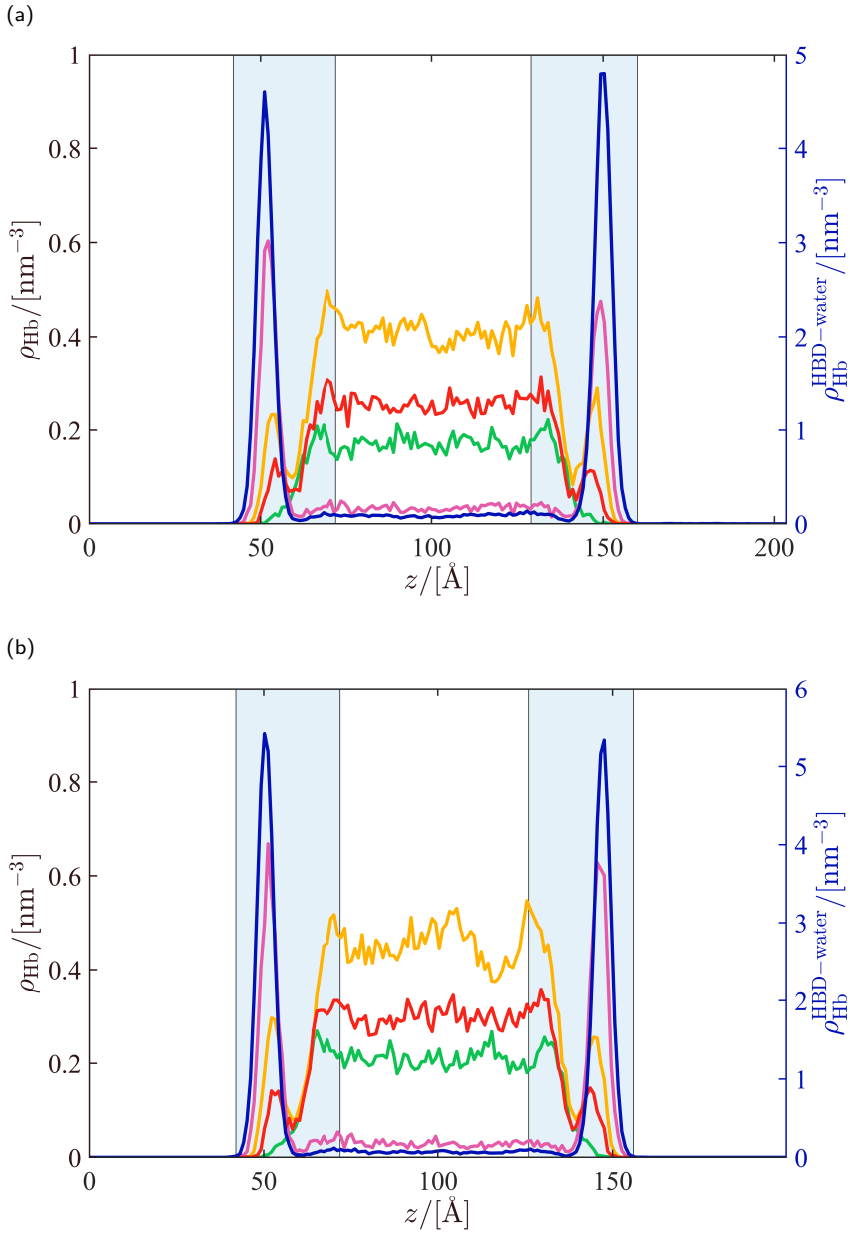

Figure 6.11: Computed hydrogen bond number densities (number of hydrogen bonds per nm^3) for the Men-dec/water system, with charge scaling factors of f_{q}=0.8/1, at 1 atm and (a) 343 K, and (b) 363 K. The blue, green, yellow, red, and pink colors correspond to water-decanoic acid (right vertical axis), menthol-menthol, decanoic acid-decanoic acid, menthol-decanoic acid, and water-menthol hydrogen bonds, respectively. The blue shaded areas indicate the interfaces, as deduced from the density profiles in Figs. A28 and 6.6.

hydrogen bonds, play a crucial role in the phase behavior of the DESs in the presence of water. The effect of charge scaling was found to be significant on the DES/water interface of TBAC-dec, and the leaching of the salt into the aqueous phase. For Thy-dec, using a charge scaling set with larger partial charges for decanoic acid ($f_q = 0.7/1$), resulted in a larger number of decanoic acid-water hydrogen bonds. Although this did not have a considerable effect on the density profiles, it led to lower Thy-dec/water interfacial tensions. This means that for an accurate prediction of the DES/water interface, a complete set of relevant parameters must be computed. For future research, it would be beneficial to consider a wider range of HBA and HBD components, and HBA:HBD mixing ratios for the computation of the DES/water interfacial properties, to achieve a more systematic understanding of the effect of the chemical structures of the DES constituents and the DES liquid composition on these properties.

6.4 Conclusions

The interfacial properties of binary mixtures of hydrophobic DESs and water were computed for TBAC-dec (1:2), Thy-dec (1:2), and Men-dec (2:1) DESs. The GAFF force field was used for all DESs, and the SPC/E model was used for water. Different charge scaling factors were considered for TBAC-dec ($f_q = 0.6 - 0.9$) and Thy-dec ($f_q = 0.7/1$ and $f_q = 0.8/0.8$). The density profiles of the various components of the mixtures were computed from MD trajectories as a function of the z-direction (perpendicular to the interface). The water-in-DES solubilities (and salt-in-water solubilities for TBAC-dec) were computed from the density profiles. Based on snapshots of atomic coordinates, the number densities of various types of hydrogen bonds were calculated. The interfacial tensions of the DES/water systems were computed at various temperatures. It was observed that the interfacial tensions of the DES/water mixtures and thus the hydrophobicity of the DESs were not considerably influenced by temperature. Using the charge scaling factors $f_q = 0.7/1$ for Thy-dec, the hydrophobicity of the DESs was computed as: TBAC-dec < Thy-dec < Men-dec, consistent with experimental observations. The density profiles of all DES/water mixtures showed significant peaks for (the hydroxyl oxygen atom of) decanoic acid, partly associated with an alignment of the oxygen atoms of decanoic acid molecules towards the aqueous phase for maximized hydrogen bonding interactions with water. This was corroborated by the computed hydrogen bond number densities and a close-up visualization of the Thy-dec/water interface. Whereas using $f_q = 0.6$ for TBAC-dec resulted in a small amount

of leaching of the salt into water, and thus an underestimated salt-in-water solubility, the charge scaling factor $f_q = 0.8$ resulted in a considerable leaching of the salt, and a salt-in-water solubility that was in better agreement with the experimental value. The number of hydrogen bonds between chloride and water in the TBAC-dec/water mixture was found to significantly increase with an increase in the charge scaling factor, thereby contributing to the leaching of the anion (and thus the salt as a whole) into water. For Thy-dec and Men-dec, no leaching of the DES components into water was observed, and these DES showed strongly hydrophobic behaviors and negligible water-in-DES solubilities. For the Thy-dec/water system, the use of different charge scaling sets for Thy-dec showed a negligible effect on the density profiles, while resulting in different interfacial tensions, due to different numbers of decanoic acid-water hydrogen bonds formed at the interfaces. The numbers of thymol-thymol and water-thymol interactions in the Thy-dec bulk phase were much smaller than those of other hydrogen bond types (e.g., thymol-decanoic acid hydrogen bonds). Small numbers of menthol-menthol, decanoic acid-decanoic acid, and menthol-decanoic acid hydrogen bonds were formed in the DES bulk phase of Men-dec/water. At the interfaces of Men-dec/water, a much larger number of decanoic acid-water hydrogen bonds was found, compared to the numbers of other hydrogen bond types (e.g., menthol-water hydrogen bonds).

Conclusions

Deep eutectic solvents (DESs) are a novel class of designer solvent mixtures that possess very low vapor pressures, low melting points, and tunable physico-chemical properties. DESs are largely biodegradable, non-toxic, inexpensive and easy to prepare, and non-flammable. Due to these properties, DESs have attracted much attention as potential solvents for a wide range of applications. Despite this, experimental data for several properties of DESs (e.g., gas solubilities and vapor pressures) are scarce or contradictory, which may be due to measurement difficulties. Due to the large number of DESs that can be synthesized, it is not possible to conduct experiments for measuring properties of all DESs. For the computation of the physico-chemical properties of DESs, force field-based molecular simulations can be used as an alternative to costly, difficult, dangerous, or time-consuming experiments. An important advantage of molecular simulation is that it can provide valuable information about the intermolecular interactions and the nanostructure of DESs, and it can be used to establish structure-property relationships. Molecular simulations of DESs are, however, faced by major challenges, some of which were addressed in this thesis. For instance, due to high viscosities (caused by strong intermolecular interactions) of many DESs, Molecular Dynamics (MD) simulations are seriously hindered by very slow equilibration and a poor convergence of transport properties. As shown in chapter 5, very long simulation times (up to 650 ns) at elevated temperatures ($T \geq 323\,\mathrm{K}$), as well as annealing of the systems during equilibration were used to overcome these issues. The strong intermolecular interactions of DESs (and thus high viscosities) are even more troublesome in Monte Carlo (MC) simulations, in which often molecules are moved sequentially (as opposed to the collective molecular motion in MD simulations), and no massive parallelization can be performed easily (other than embarrassingly parallelization). Additionally, as a result of such strong interactions, the insertion and deletion of solute molecules are performed inefficiently (low acceptance probabilities) in MC simulations of open ensembles. These

problems were tackled in chapters 3 and 4, by using the state-of-the-art continuous fractional component Monte Carlo (CFCMC) method [91]. The gradual insertion/deletion of 'fractional' molecules, and the additional trial moves of this method (i.e., reinsertions and identity changes) made it possible to compute, with high precision, the solubilities of different gases in choline chloride-based DESs, as well as the vapor pressures and vapor phase compositions of these DESs. Further improvements of the equilibration and sampling in MC simulations can be achieved by applying advanced methods such as smart Monte Carlo (SMC) [394] or hybrid MC/MD [395]. Additionally, methods that rely on collective trial moves (i.e., trial moves that attempt to move all atoms/molecules), such as collective SMC [80] and collective hybrid MC/MD [81], have been very successful in increasing the efficiency of MC simulations [81].

Although DESs are mixtures of various components, it is often more convenient and computationally cheaper to consider them as pseud-pure compounds. This approach as been extensively used in PC-SAFT modeling of DESs [22, 26, 60, 129, 208, 209]. As discussed in chapter 2, by considering DESs as mixtures, the computation of solubility parameters (for which no experimental data are yet available) from the thermodynamic definition is not straightforward. Therefore, the pseudo-pure compound approach was used to compute the solubility parameters of DESs, and estimate the polarity of these solvents, considering 'DES clusters' (HBA-HBD complexes with molar ratios as in the liquid phase) as the vaporizing entities. The proposed methodology can be applied to other non-volatile mixtures, for which the values of the enthalpies of vaporization and solubility parameters (i.e., the extent of polarity) are not known.

As shown in this thesis, it is a major challenge to accurately compute thermodynamic and transport properties of DESs, even when using two of the best available force fields, i.e., the OPLS force field [154] and the General Amber Force Field (GAFF) [155]. This is due to the complex intermolecular interactions (e.g., dispersion, dipole-dipole, and hydrogen bonding), the structural heterogeneity, and the wide range of possible molecular structures and liquid phase compositions of DESs, which limit the accuracy and transferability of such force fields. Furthermore, many physico-chemical phenomena are not captured by these force fields, such as proton and charge transfers, polarization, and chemical reactions.

The partial charges computed from conventional quantum mechanical methods (from gas phase calculations), such as the restraint electrostatic potential (RESP) method [292], often lead to highly overestimated viscosities and underestimated diffusivities. A simple and computationally cheap

method to address this problem is to scale the charges (mostly ionic charges) by a specific factor. This methods has been extensively used in literature to enhance the agreement between the simulation results and experimental data. Currently, there are contrary opinions in literature as to why the charge scaling method is successful [61, 130, 145, 291, 308, 335, 336, 355, 360, 396, 397]. It is still unclear whether the success of charge scaling is due to accounting for the effective polarization and charge transfer processes in the liquid phase, or whether it is due to the mitigation of overpolarization caused by charge derivation methods (gas phase calculations). In this thesis, it was shown that the choice of the charge scaling factor significantly influences the computed properties, such densities, transport properties, Henry coefficients of gases, DES/water interfacial tensions, liquid structures, and hydrogen bonds. A particularly interesting observation from chapters 3 and 5 was that while choosing a specific charge scaling factor (e.g., 0.8 for choline chloride, or 0.6 for tetrabutylammonium chloride) may lead to accurate computed properties for the neat DES (e.g., density and transport properties), it may not result in accurate mixture properties, such as the Henry coefficients of gases or salt-in-water solubilities (the amount of leaching of the cation and anion into water). To improve the accuracy of force fields, charge derivation methods based on a combination of gas phase and aqueous phase calculations (e.g., RESP2 [291]) have been proposed as a replacement for the standard gas phase charge derivation methods. Polarizable force fields, which are more complicated and computationally intensive, have been considered as an alternative to the conventional force fields for DESs and ionic liquids (ILs) [398, 399]. With the drastic rise in computational power in recent years, a growing number of articles have been published on simulating ILs and DESs using polarizable force fields [355, 376, 398–400]. However, polarizable force fields are not yet extensively implemented in commonly used molecular simulation software packages such as LAMMPS [110] and GROMACS [108, 109]. Very recently, the use of machine learning algorithms for obtaining optimal force field parameters [401] has been extended to ILs [402] and DESs [403]. These algorithms rely on a large number of experimental and computational data to predict the properties of materials. Considering the complex nature of DESs and the large number of possible chemical structures, it is very likely that machine learning algorithms will be more extensively used in the future to predict physico-chemical properties of DESs. Therefore, these algorithms may play an important role in screening and designing DESs for specific applications.

Appendix

A.1 Molecular structures

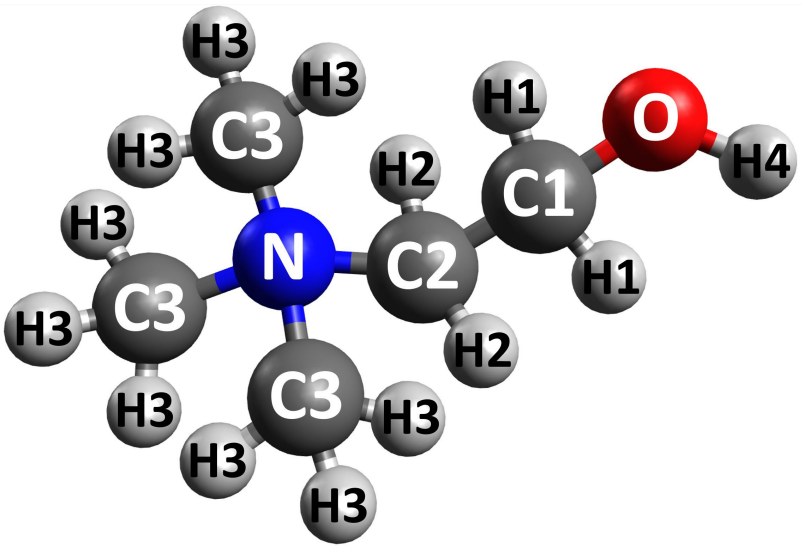

Figure A1: Structure and atom labels of choline.

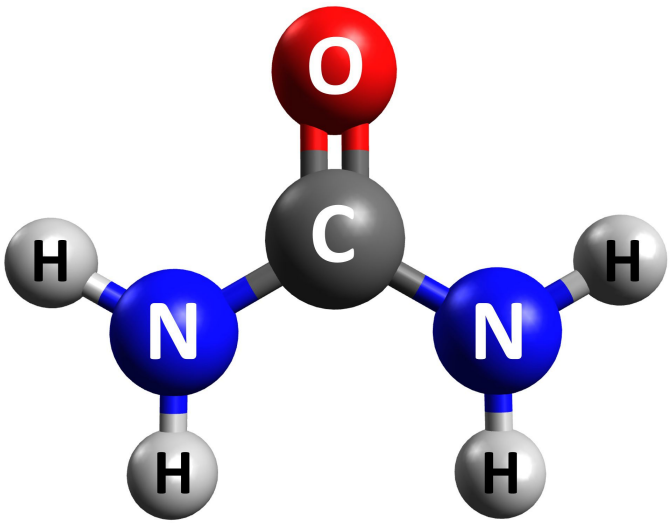

Figure A2: Structure and atom labels of urea.

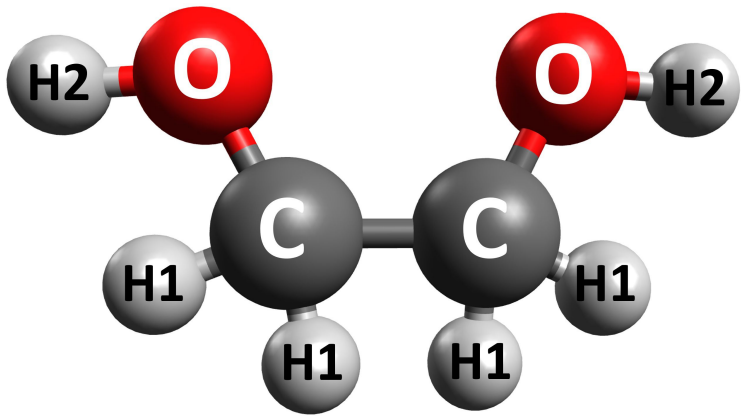

Figure A3: Structure and atom labels of ethylene glycol.

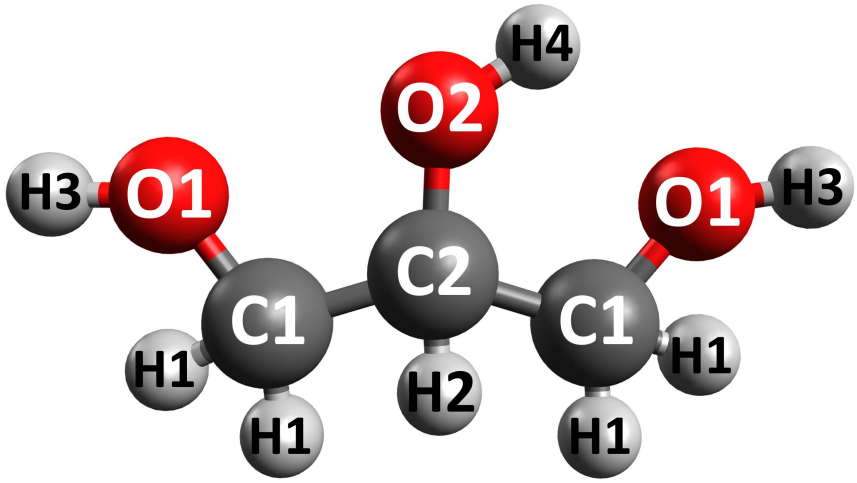

Figure A4: Structure and atom labels of glycerol.

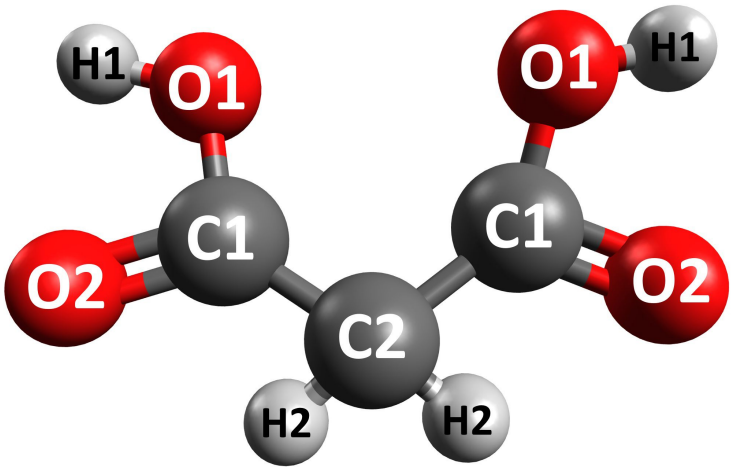

Figure A5: Structure and atom labels of malonic acid.

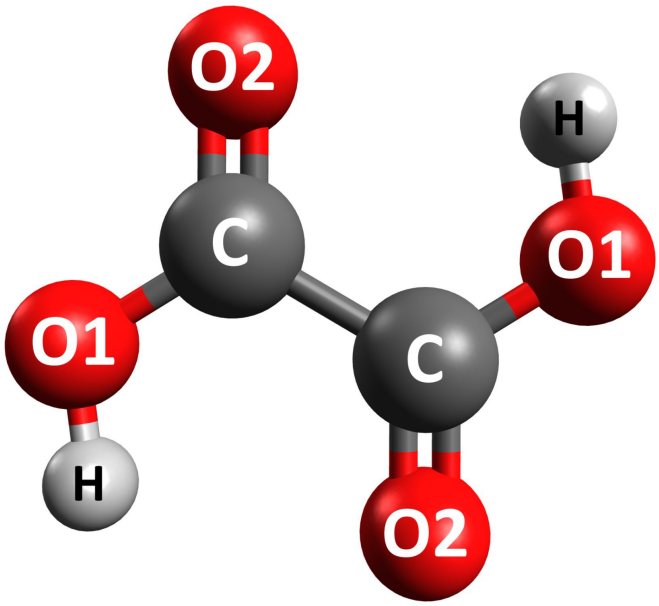

Figure A6: Structure and atom labels of oxalic acid.

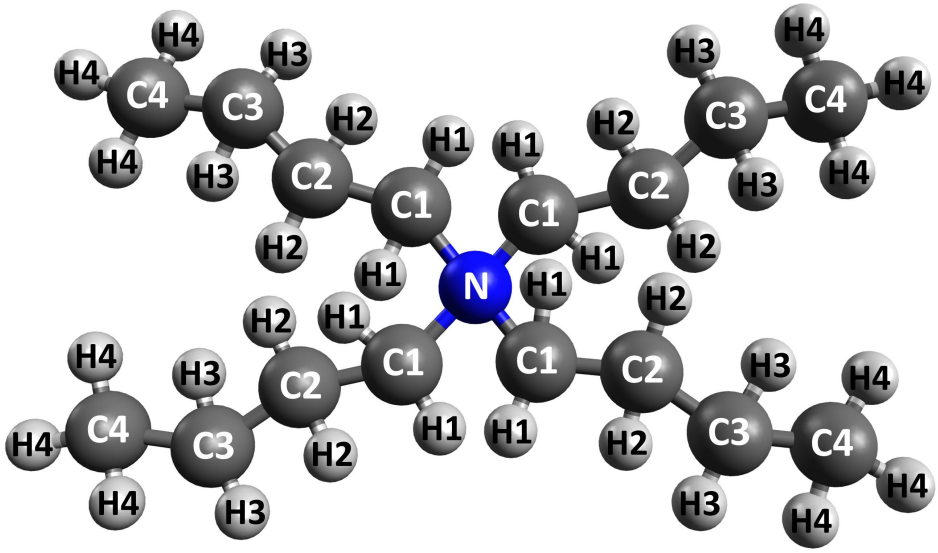

Figure A7: Structure and atom labels of tetrabutylammonium.

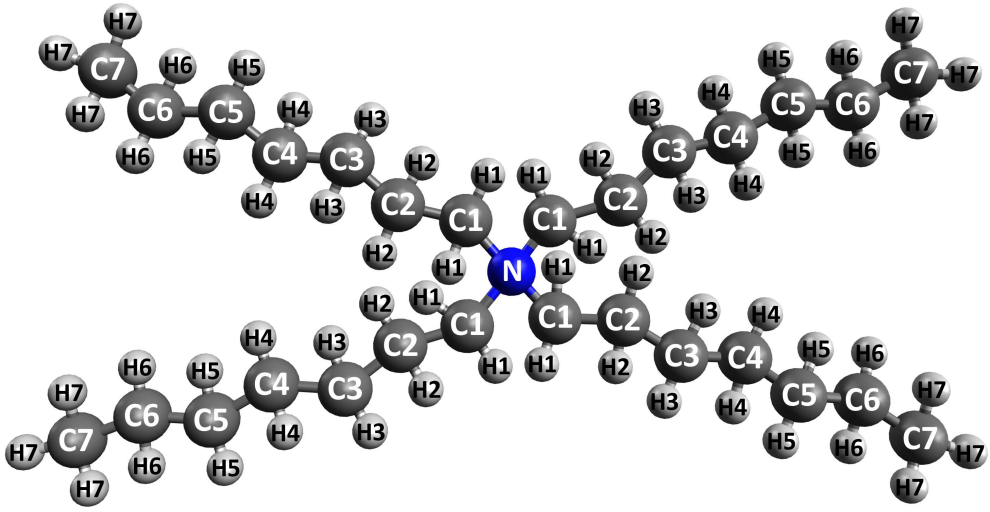

Figure A8: Structure and atom labels of tetraheptylammonium.

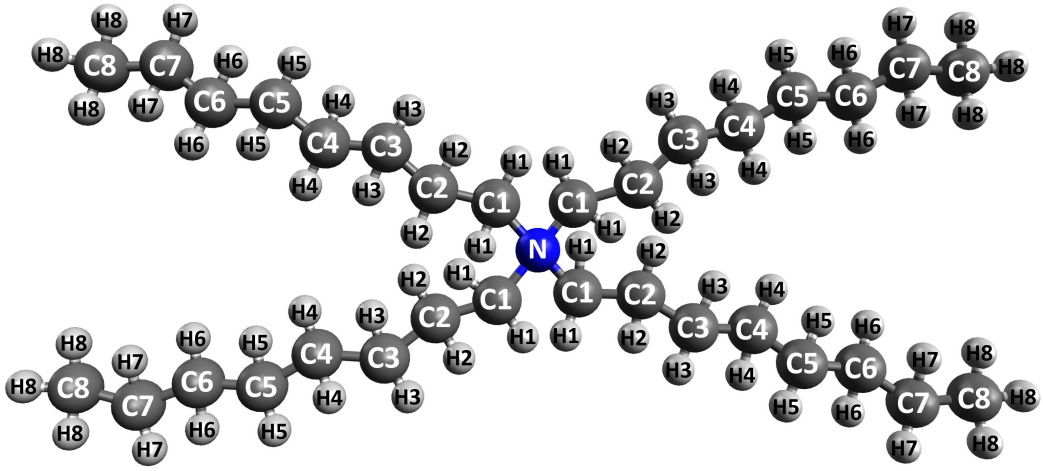

Figure A9: Structure and atom labels of tetraoctylammonium.

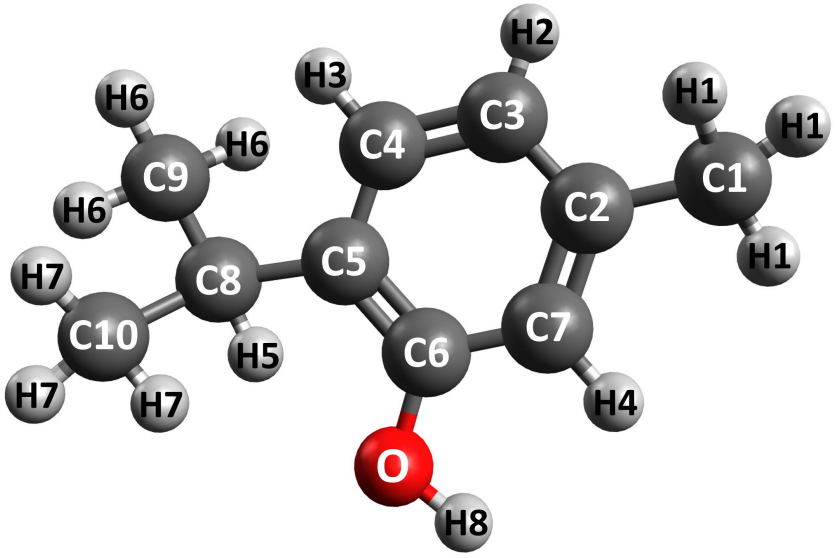

Figure A10: Structure and atom labels of thymol.

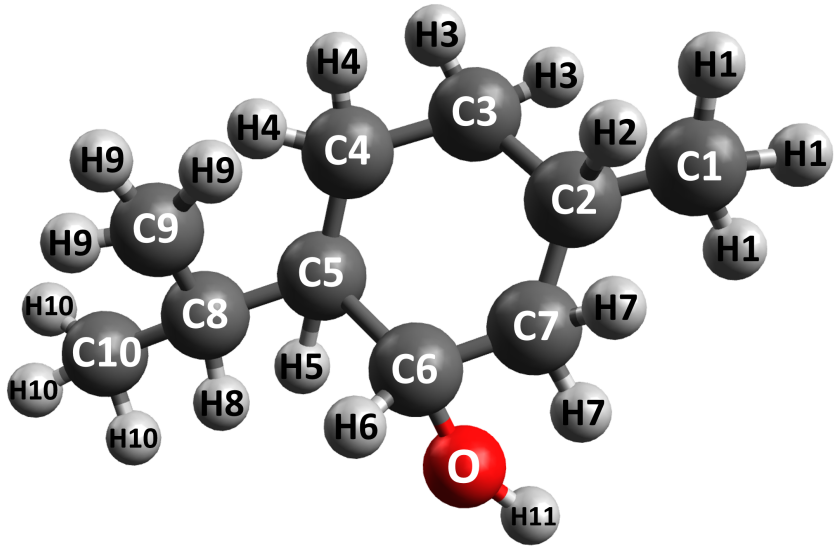

Figure A11: Structure and atom labels of menthol.

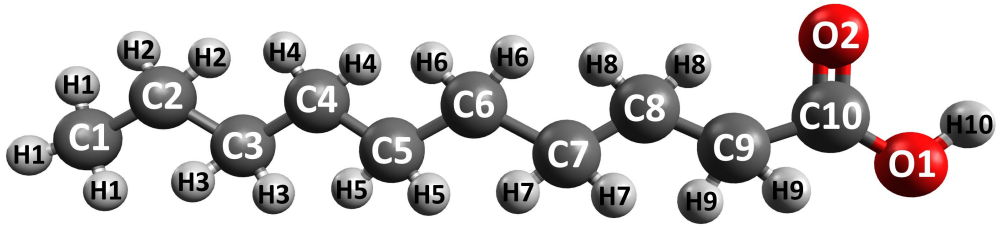

Figure A12: Structure and atom labels of decanoic acid.

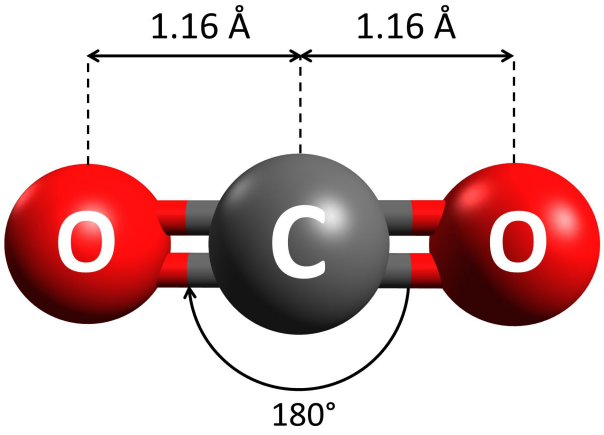

Figure A13: Structure and atom labels of carbon dioxide [259].

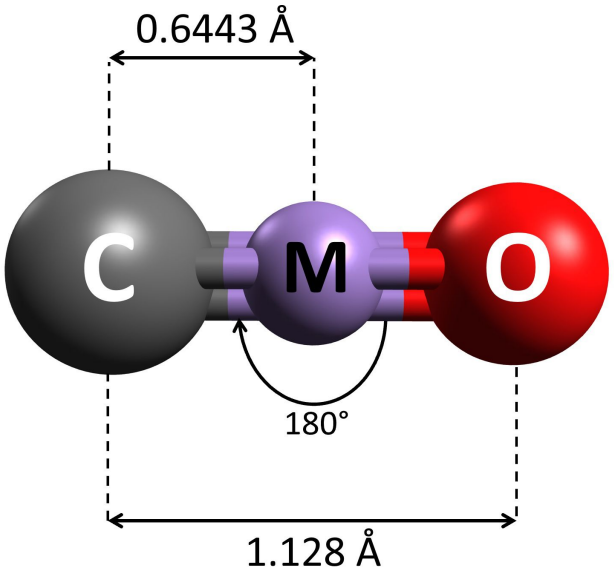

Figure A14: Structure and atom labels of carbon monoxide [263].

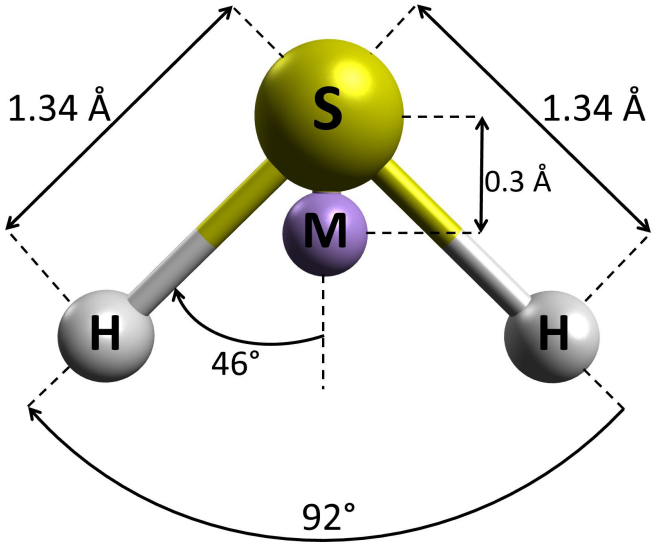

Figure A15: Structure and atom labels of hydrogen sulfide [261].

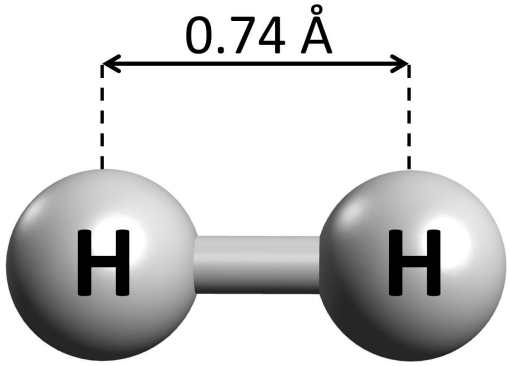

Figure A16: Structure and atom labels of hydrogen [262].

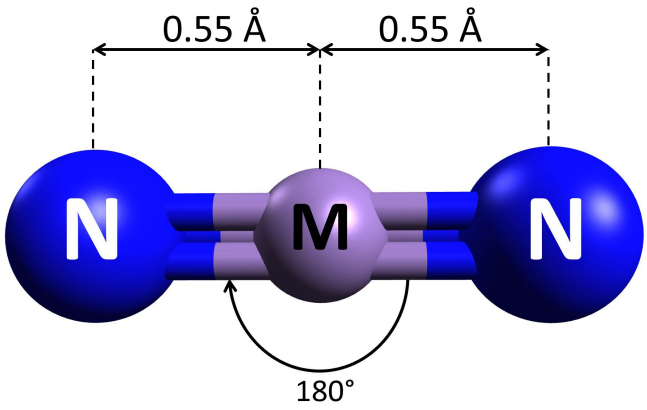

Figure A17: Structure and atom labels of nitrogen [259].

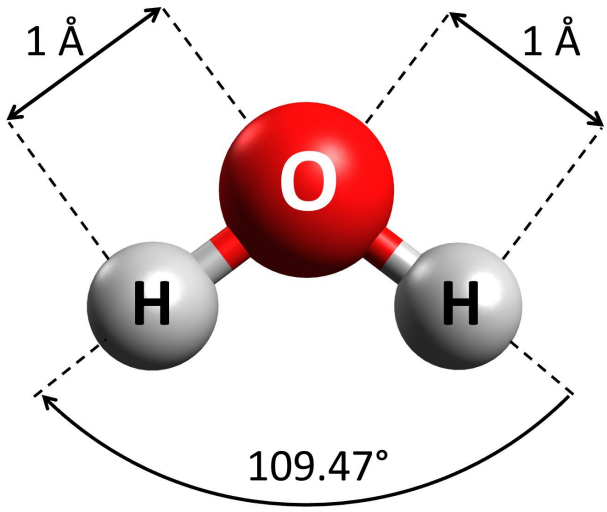

Figure A18: Structure and atom labels of water (SPC/E model [389]).

A.2 Force field parameters

A.2.1 GAFF force field parameters for choline chloride

Table A1: Atom types and non-bonded parameters for choline chloride [61, 155]. The LJ energy is calculated according to: $E_{\mathrm{LJ}}(r) = 4\epsilon[(\sigma/r)^{12} - (\sigma/r)^{6}]$, where r is the site-site distance. The listed charges are the unscaled values, and should therefore be multiplied by the proper scaling factors when used in simulations. The atom labels of choline are defined in Fig. A1.

atom label	atom type	$q/[\mathrm{e}^{-}]$	$\epsilon/[\mathrm{kcal\,mol}^{-1}]$	$\sigma/[\mathrm{\AA}]$
C1	cw	0.1501	0.1094	3.3997
C2	cs	-0.0322	0.1094	3.3997
C3	c3	-0.1342	0.1094	3.3997
H1	h1	0.0510	0.0157	2.4714
H2	hx	0.1116	0.0157	1.9600
H3	hx	0.1193	0.0157	1.9600
H4	ho	0.4545	0.0010	0.1000
N	n4	0.0502	0.1700	3.2500
O	oh	-0.6189	0.2104	3.0665
Cl	c1	-1.0000	0.1000	4.4010

Table A2: Bond-stretching interaction parameters for the choline ion [61, 155]. The bond-stretching energy is calculated according to: $E_{\mathrm{stretching}}(r) = k_{\mathrm{r}}(r - r_0)^2$. The atom types and atom labels can be found in Table A1 and Fig. A1.

bond type	$k_{\mathrm{r}}/[\mathrm{kcal\,mol}^{-1}\,\mathrm{\AA}^{-2}]$	$r_0/[\mathrm{\AA}]$
c3-hx	338.7	1.091
c3-n4	293.6	1.499
n4-cs	293.6	1.499
cs-hx	338.7	1.091
cs-c3	303.1	1.535
cw-h1	335.9	1.093
cw-oh	314.1	1.426
oh-ho	369.6	0.974

Table A3: Bond-bending interaction parameters for the choline ion [61, 155]. The bond-bending energy is calculated according to: $E_{\mathrm{bending}}(\theta) = k_\theta(\theta - \theta_0)^2$. The atom types and atom labels can be found in Table A1 and Fig. A1.

angle type	$k_\theta/[\mathrm{kcal\,mol^{-1}\,rad^{-2}}]$	θ_0
hx-c3-hx	39.0	110.74
hx-c3-n4	49.0	107.91
c3-n4-cs	62.8	110.64
n4-cs-hx	49.0	107.91
n4-cs-cw	64.5	114.3
cs-cw-h1	46.4	110.07
cs-cw-oh	67.7	109.43
hx-cs-cw	46.0	111.74
h1-cw-oh	51.0	109.88
cw-oh-ho	47.1	108.16
c3-n4-c3	62.8	110.64
hx-c3-hx	39.0	110.74
h1-cw-h1	39.2	109.55

Table A4: Dihedral parameters for the choline ion [61, 155]. The dihedral energy is calculated according to: $E_{\mathrm{dihedral}}(\phi) = \frac{V_n}{2}[1 + \cos(n\phi - \gamma)]$. For each dihedral a-b-c-d, ϕ is the angle between the planes a-b-c and b-c-d. The atom types and atom labels can be found in Table A1 and Fig. A1.

dihedral type	$\frac{V_n}{2}/[\mathrm{kcal\,mol^{-1}}]$	n	γ
h1-cw-oh-ho	0.167	3	0
cs-cw-oh-ho	0.160	-3	0
cs-cw-oh-ho	0.250	1	0
h1-cw-cs-hx	0.156	3	0
h1-cw-cs-n4	0.156	3	0
oh-cw-cs-hx	0.156	3	0
oh-cw-cs-n4	0.156	3	0
cw-cs-n4-c3	0.156	3	0
hx-cs-n4-c3	0.156	3	0
cs-n4-c3-hx	0.156	3	0
c3-n4-c3-hx	0.156	3	0

A.2.2 OPLS force field parameters for choline chloride

Table A5: Atom types and non-bonded parameters for choline chloride [59, 154]. The LJ energy is calculated according to: $E_{\mathrm{LJ}}(r) = 4\epsilon[(\sigma/r)^{12} - (\sigma/r)^{6}]$, where r is the site-site distance. The listed charges are scaled by 0.8, as used in simulations. The atom labels of choline are defined in Fig. A1.

atom label	atom type	$q/[\mathrm{e}^{-}]$	$\epsilon/[\mathrm{kcal\,mol}^{-1}]$	$\sigma/[\mathrm{\AA}]$
C1	cw	0.132	0.066	3.50
C2	cs	-0.131	0.066	3.50
C3	ca	-0.100	0.066	3.50
H1	hw	0.034	0.030	2.20
H2	hs	0.068	0.030	2.60
H3	ha	0.033	0.030	2.50
H4	hy	0.275	0.001	0.10
N	na	0.791	0.170	3.25
O	oy	-0.468	0.170	3.07
Cl	cl	-0.800	0.148	3.77

Table A6: Bond-stretching interaction parameters for the choline ion [59, 154]. The bond-stretching energy is calculated according to: $E_{\mathrm{stretching}}(r) = k_{\mathrm{r}}(r - r_0)^2$. The atom types and atom labels can be found in Table A5 and Fig. A1.

bond type	$k_{\mathrm{r}}/[\mathrm{kcal\,mol}^{-1}\,\mathrm{\AA}^{-2}]$	$r_0/[\mathrm{\AA}]$
ha-ca	340	1.0990
ca-na	490	1.4980
na-cs	490	1.5160
cs-hs	340	1.0805
cs-cw	317	1.5210
cw-hw	340	1.0850
cw-oy	450	1.3950
oy-hy	553	0.9490

Table A7: Bond-bending interaction parameters for the choline ion [59, 154]. The bond-bending energy is calculated according to: $E_{\mathrm{bending}}(\theta) = k_\theta(\theta - \theta_0)^2$. The atom types and atom labels can be found in Table A5 and Fig. A1.

angle type	$k_\theta/[\mathrm{kcal\,mol^{-1}\,rad^{-2}}]$	θ_0
ha-ca-ha	35.0	110.01
ha-ca-na	35.0	108.90
ca-na-cs	51.8	110.20
na-cs-hs	35.0	106.40
na-cs-cw	70.0	116.60
cs-cw-hw	35.0	108.30
cs-cw-oy	80.0	109.60
hs-cs-cw	35.0	109.30
hw-cw-oy	35.0	111.60
cw-oy-hy	35.0	110.90
ca-na-ca	55.0	108.73
hs-cs-hs	35.0	108.60
hw-cw-hw	35.0	107.40

Table A8: Dihedral parameters for the choline ion [59, 154]. The dihedral energy is calculated according to: $E_{\mathrm{dihedral}}(\phi) = \frac{1}{2}V_1[1 + \cos(\phi)] + \frac{1}{2}V_2[1 - \cos(2\phi)] + \frac{1}{2}V_3[1 + \cos(3\phi)]$. For each dihedral a-b-c-d, ϕ is the angle between the planes a-b-c and b-c-d. The atom types and atom labels can be found in Table A5 and Fig. A1.

dihedral types	$V_1/[\mathrm{kcal\,mol^{-1}}]$	$V_2/[\mathrm{kcal\,mol^{-1}}]$	$V_3/[\mathrm{kcal\,mol^{-1}}]$
cw-cs-na-ca	0.100	0.550	0.650
ca-na-ca-ha	0.000	0.000	0.825
cs-na-ca-ha	0.000	0.000	0.940
hs-cs-na-ca	0.000	1.000	0.700
oy-cw-cs-na	-6.000	-5.000	3.200
oy-cw-cs-hs	-0.500	-2.500	0.250
hw-cw-cs-na	-6.000	-7.000	0.750
hw-cw-cs-hs	6.000	-3.000	2.000
hy-oy-cw-cs	-0.356	-0.174	0.350
hy-oy-cw-hw	-3.000	1.000	-2.000
cs-na-ca-ca [a]	0.000	2.000	0.000
ca-na-ca-ca [a]	0.000	2.000	0.000

[a] These are improper dihedrals. The energy functional form for improper dihedrals is the same as for the (proper) dihedrals. However, for each improper dihedral a-b-c-d, the angle ϕ is defined as the angle between the planes a-b-c and a-c-d.

A.2.3 GAFF force field parameters for urea

Table A9: Atom types and non-bonded parameters for urea [61, 155]. The LJ energy is calculated according to: $E_{\mathrm{LJ}}(r) = 4\epsilon[(\sigma/r)^{12} - (\sigma/r)^{6}]$, where r is the site-site distance. The atom labels are defined in Fig. A2.

atom label	atom type	$q/[\mathrm{e}^-]$	$\epsilon/[\mathrm{kcal\,mol}^{-1}]$	$\sigma/[\mathrm{\AA}]$
C	c	1.0401	0.0860	3.3997
H	hn	0.4167	0.0157	1.0691
N	n	-1.0246	0.1700	3.2500
O	o	-0.6577	0.2100	2.9599

Table A10: Bond-stretching interaction parameters for urea [61, 155]. The bond-stretching energy is calculated according to: $E_{\mathrm{stretching}}(r) = k_{\mathrm{r}}(r - r_0)^2$. The atom types and atom labels can be found in Table A9 and Fig. A2.

bond type	$k_{\mathrm{r}}/[\mathrm{kcal\,mol}^{-1}\,\mathrm{\AA}^{-2}]$	$r_0/[\mathrm{\AA}]$
c-o	648.0	1.214
c-n	478.2	1.345
n-hn	410.2	1.009

Table A11: Bond-bending interaction parameters for urea [61, 155]. The bond-bending energy is calculated according to: $E_{\mathrm{bending}}(\theta) = k_{\theta}(\theta - \theta_0)^2$. The atom types and atom labels can be found in Table A9 and Fig. A2.

angle type	$k_{\theta}/[\mathrm{kcal\,mol}^{-1}\,\mathrm{rad}^{-2}]$	θ_0
n-c-o	75.8	122.03
c-n-hn	49.2	118.46
hn-n-hn	39.7	117.85
n-c-n	74.8	113.40

Table A12: Dihedral parameters for urea [61, 155]. The dihedral energy is calculated according to: $E_{\mathrm{dihedral}}(\phi) = \frac{V_{\mathrm{n}}}{2}[1 + \cos(n\phi - \gamma)]$. For each dihedral a-b-c-d, ϕ is the angle between the planes a-b-c and b-c-d. The atom types and atom labels can be found in Table A9 and Fig. A2.

dihedral types	$\frac{V_{\mathrm{n}}}{2}/[\mathrm{kcal\,mol^{-1}}]$	n	γ
hn-n-c-o	2.5	-2	180
hn-n-c-o	2.0	1	0
n-c-n-hn	2.5	2	180
o-c-n-n [a]	10.5	2	180
hn-n-c-hn [a]	1.1	2	180

[a] These are improper dihedrals. The energy functional form for improper dihedrals is the same as for the (proper) dihedrals. However, for each improper dihedral a-b-c-d, the angle ϕ is defined as the angle between the planes a-b-c and a-c-d.

A.2.4 OPLS force field parameters for urea

Table A13: Atom types and non-bonded parameters for urea [59, 154]. The LJ energy is calculated according to: $E_{\mathrm{LJ}}(r) = 4\epsilon[(\sigma/r)^{12} - (\sigma/r)^{6}]$, where r is the site-site distance. The atom labels are defined in Fig. A2.

atom label	atom type	$q/[\mathrm{e^-}]$	$\epsilon/[\mathrm{kcal\,mol^{-1}}]$	$\sigma/[\mathrm{\AA}]$
C	c	0.124	0.1575	3.75
H	hc	0.276	0.0010	0.10
N	n	-0.453	0.2550	3.55
O	o	-0.322	0.3150	2.96

Table A14: Bond-stretching interaction parameters for urea [59, 154]. The bond-stretching energy is calculated according to: $E_{\mathrm{stretching}}(r) = k_{\mathrm{r}}(r - r_0)^2$. The atom types and atom labels can be found in Table A13 and Fig. A2.

bond type	$k_{\mathrm{r}}/[\mathrm{kcal\,mol^{-1}\,\AA^{-2}}]$	$r_0/[\mathrm{\AA}]$
o-c	570	1.229
n-c	490	1.335
hc-n	434	1.010

Table A15: Bond-bending interaction parameters for urea [59, 154]. The bond-bending energy is calculated according to: $E_{\mathrm{bending}}(\theta) = k_\theta(\theta - \theta_0)^2$. The atom types and atom labels can be found in Table A13 and Fig. A2.

angle type	$k_\theta/[\mathrm{kcal\,mol^{-1}\,rad^{-2}}]$	θ_0
o-c-n	80	122.9
c-n-hc	35	119.8
n-c-n	70	114.2
hc-n-hc	35	120.0

Table A16: Dihedral parameters for urea [59, 154]. The dihedral energy is calculated according to: $E_{\mathrm{dihedral}}(\phi) = \frac{1}{2}V_1[1+\cos(\phi)] + \frac{1}{2}V_2[1-\cos(2\phi)] + \frac{1}{2}V_3[1+\cos(3\phi)]$. For each dihedral a-b-c-d, ϕ is the angle between the planes a-b-c and b-c-d. The atom types and atom labels can be found in Table A13 and Fig. A2.

dihedral types	$V_1/[\mathrm{kcal\,mol^{-1}}]$	$V_2/[\mathrm{kcal\,mol^{-1}}]$	$V_3/[\mathrm{kcal\,mol^{-1}}]$
hc-n-c-o	0.000	4.900	0.000
hc-n-c-n	0.000	4.900	0.000
hc-n-c-hc [a]	0.000	21.000	0.000
o-c-n-n [a]	0.000	5.000	0.000

[a] These are improper dihedrals. The energy functional form for improper dihedrals is the same as for the (proper) dihedrals. However, for each improper dihedral a-b-c-d, the angle ϕ is defined as the angle between the planes a-b-c and a-c-d.

A.2.5 GAFF force field parameters for ethylene glycol

Table A17: Atom types and non-bonded parameters for ethylene glycol [155]. The LJ energy is calculated according to: $E_{\mathrm{LJ}}(r) = 4\epsilon[(\sigma/r)^{12} - (\sigma/r)^6]$, where r is the site-site distance. The atom labels are defined in Fig. A3.

atom label	atom type	$q/[\mathrm{e^-}]$	$\epsilon/[\mathrm{kcal\,mol^{-1}}]$	$\sigma/[\mathrm{Å}]$
C	c3	0.1615	0.1094	3.3997
H1	h1	0.0328	0.0157	2.4714
H2	ho	0.4069	0.0010	0.1000
O	oh	-0.6340	0.2104	3.0665

Table A18: Bond-stretching interaction parameters for ethylene glycol [155]. The bond-stretching energy is calculated according to: $E_{\mathrm{stretching}}(r) = k_{\mathrm{r}}(r - r_0)^2$. The atom types and atom labels can be found in Table A17 and Fig. A3.

bond type	$k_{\mathrm{r}}/[\mathrm{kcal\,mol^{-1}\,\AA^{-2}}]$	$r_0/[\mathrm{\AA}]$
oh-ho	369.6	0.974
c3-oh	314.1	1.426
c3-c3	303.1	1.535
h1-c3	335.9	1.093

Table A19: Bond-bending interaction parameters for ethylene glycol [155]. The bond-bending energy is calculated according to: $E_{\mathrm{bending}}(\theta) = k_{\theta}(\theta - \theta_0)^2$. The atom types and atom labels can be found in Table A17 and Fig. A3.

angle type	$k_{\theta}/[\mathrm{kcal\,mol^{-1}\,rad^{-2}}]$	θ_0
ho-oh-c3	47.1	108.16
oh-c3-c3	67.7	109.43
oh-c3-h1	51.0	109.88
c3-c3-h1	46.4	110.07
h1-c3-h1	39.2	109.55

Table A20: Dihedral parameters for ethylene glycol [155]. The dihedral energy is calculated according to: $E_{\mathrm{dihedral}}(\phi) = \frac{V_{\mathrm{n}}}{2}[1 + \cos(n\phi - \gamma)]$. For each dihedral a-b-c-d, ϕ is the angle between the planes a-b-c and b-c-d. The atom types and atom labels can be found in Table A17 and Fig. A3.

dihedral type	$\frac{V_{\mathrm{n}}}{2}/[\mathrm{kcal\,mol^{-1}}]$	n	γ
ho-oh-c3-h1	0.167	3	0
c3-c3-oh-ho	0.160	-3	0
c3-c3-oh-ho	0.250	1	0
h1-c3-c3-h1	0.156	3	0
oh-c3-c3-h1	0.250	1	0
oh-c3-c3-oh	0.144	-3	0
oh-c3-c3-oh	1.175	2	0

A.2.6 OPLS force field parameters for ethylene glycol

Table A21: Atom types and non-bonded parameters for ethylene glycol [59, 154]. The LJ energy is calculated according to: $E_{\mathrm{LJ}}(r) = 4\epsilon[(\sigma/r)^{12} - (\sigma/r)^{6}]$, where r is the site-site distance. The atom labels are defined in Fig. A3.

atom label	atom type	$q/[\mathrm{e}^-]$	$\epsilon/[\mathrm{kcal\,mol}^{-1}]$	$\sigma/[\mathrm{\AA}]$
C	cg	0.116	0.1155	3.50
H1	hg	0.048	0.0525	2.50
H2	ho	0.348	0.0010	0.10
O	oh	-0.560	0.2975	3.00

Table A22: Bond-stretching interaction parameters for ethylene glycol [59, 154]. The bond-stretching energy is calculated according to: $E_{\mathrm{stretching}}(r) = k_{\mathrm{r}}(r - r_0)^2$. The atom types and atom labels can be found in Table A21 and Fig. A3.

bond type	$k_{\mathrm{r}}/[\mathrm{kcal\,mol}^{-1}\,\mathrm{\AA}^{-2}]$	$r_0/[\mathrm{\AA}]$
oh-ho	553	0.945
cg-oh	320	1.410
cg-cg	268	1.529
hg-cg	340	1.090

Table A23: Bond-bending interaction parameters for ethylene glycol [59, 154]. The bond-bending energy is calculated according to: $E_{\mathrm{bending}}(\theta) = k_{\theta}(\theta - \theta_0)^2$. The atom types and atom labels can be found in Table A21 and Fig. A3.

angle type	$k_{\theta}/[\mathrm{kcal\,mol}^{-1}\,\mathrm{rad}^{-2}]$	θ_0
ho-oh-cg	55.0	108.5
oh-cg-cg	50.0	108.0
oh-cg-hg	35.0	109.5
cg-cg-hg	37.5	110.7
hg-cg-hg	33.0	107.8

Table A24: Dihedral parameters for ethylene glycol [59, 154]. The dihedral energy is calculated according to: $E_{\mathrm{dihedral}}(\phi) = \frac{1}{2}V_1[1 + \cos(\phi)] + \frac{1}{2}V_2[1 - \cos(2\phi)] + \frac{1}{2}V_3[1 + \cos(3\phi)]$. For each dihedral a-b-c-d, ϕ is the angle between the planes a-b-c and b-c-d. The atom types and atom labels can be found in Table A21 and Fig. A3.

dihedral types	$V_1/[\mathrm{kcal\,mol}^{-1}]$	$V_2/[\mathrm{kcal\,mol}^{-1}]$	$V_3/[\mathrm{kcal\,mol}^{-1}]$
oh-cg-cg-oh	3.887	-1.192	3.206
cg-cg-oh-ho	0.413	-0.754	1.028

A.2.7 OPLS force field parameters for glycerol

Table A25: Atom types and non-bonded parameters for glycerol [59, 154]. The LJ energy is calculated according to: $E_{\mathrm{LJ}}(r) = 4\epsilon[(\sigma/r)^{12} - (\sigma/r)^{6}]$, where r is the site-site distance. The atom labels are defined in Fig. A4.

atom label	atom type	$q/[\mathrm{e}^{-}]$	$\epsilon/[\mathrm{kcal\,mol}^{-1}]$	$\sigma/[\mathrm{\AA}]$
C1	cb	0.16000	0.1452	3.50
C2	cm	0.14200	0.1452	3.50
H1	hc	0.06370	0.0660	2.50
H2	hz	0.02210	0.0660	2.50
H3	ho	0.03043	0.0010	0.10
H4	hm	0.29120	0.0010	0.10
O1	oh	-0.54700	0.3740	3.07
O2	om	-0.54470	0.3740	3.07

Table A26: Bond-stretching interaction parameters for glycerol [59, 154]. The bond-stretching energy is calculated according to: $E_{\mathrm{stretching}}(r) = k_{\mathrm{r}}(r - r_0)^2$. The atom types and atom labels can be found in Table A25 and Fig. A4.

bond type	$k_{\mathrm{r}}/[\mathrm{kcal\,mol}^{-1}\,\mathrm{\AA}^{-2}]$	$r_0/[\mathrm{\AA}]$
om-cm	320	1.410
cb-cm	268	1.529
hm-om	553	0.945
hz-cm	340	1.090
hc-cb	340	1.090
oh-cb	320	1.410
ho-oh	553	0.945

Table A27: Bond-bending interaction parameters for glycerol [59, 154]. The bond-bending energy is calculated according to: $E_{\mathrm{bending}}(\theta) = k_\theta(\theta - \theta_0)^2$. The atom types and atom labels can be found in Table A25 and Fig. A4.

angle type	$k_\theta/[\mathrm{kcal\,mol^{-1}\,rad^{-2}}]$	θ_0
om-cm-cb	50.00	108.5
cm-om-hm	55.00	108.5
om-cm-hz	35.00	109.5
cm-cb-hc	37.50	110.7
cm-cb-oh	50.00	109.5
cb-oh-ho	55.00	108.5
cb-cm-cb	58.35	112.7
cb-cm-hz	37.50	110.7
hc-cb-hc	33.00	107.8
hc-cb-oh	35.00	109.5

Table A28: Dihedral parameters for glycerol [59, 154]. The dihedral energy is calculated according to: $E_{\mathrm{dihedral}}(\phi) = \frac{1}{2}V_1[1 + \cos(\phi)] + \frac{1}{2}V_2[1 - \cos(2\phi)] + \frac{1}{2}V_3[1 + \cos(3\phi)]$. For each dihedral a-b-c-d, ϕ is the angle between the planes a-b-c and b-c-d. The atom types and atom labels can be found in Table A25 and Fig. A4.

dihedral types	$V_1/[\mathrm{kcal\,mol^{-1}}]$	$V_2/[\mathrm{kcal\,mol^{-1}}]$	$V_3/[\mathrm{kcal\,mol^{-1}}]$
hm-om-cm-cb	-0.356	-0.174	0.492
hz-cm-om-hm	0.000	0.000	0.352
hc-cb-cm-om	0.000	0.000	0.468
oh-cb-cm-om	12.234	0.000	0.000
ho-oh-cb-cm	-0.356	-0.174	0.492
hc-cb-cm-cb	0.000	0.000	0.300
oh-cb-cm-cb	-1.552	0.000	0.000
hc-cb-cm-hz	0.000	0.000	0.300
oh-cb-cm-hz	0.000	0.000	0.468
ho-oh-cb-hc	0.000	0.000	0.352

A.2.8 OPLS force field parameters for malonic acid

Table A29: Atom types and non-bonded parameters for malonic acid [59, 154]. The LJ energy is calculated according to: $E_{\mathrm{LJ}}(r) = 4\epsilon[(\sigma/r)^{12} - (\sigma/r)^{6}]$, where r is the site-site distance. The atom labels are defined in Fig. A5.

atom label	atom type	$q/[\mathrm{e}^{-}]$	$\epsilon/[\mathrm{kcal\,mol^{-1}}]$	$\sigma/[\mathrm{\AA}]$
C1	cd	0.416	0.2625	3.75
C2	ct	-0.096	0.1650	3.50
H1	ho	0.360	0.0010	0.10
H2	hc	0.048	0.0750	2.50
O1	oh	-0.424	0.4250	3.00
O2	od	-0.352	0.5250	2.96

Table A30: Bond-stretching interaction parameters for malonic acid [59, 154]. The bond-stretching energy is calculated according to: $E_{\mathrm{stretching}}(r) = k_{\mathrm{r}}(r - r_0)^2$. The atom types and atom labels can be found in Table A29 and Fig. A5.

bond type	$k_{\mathrm{r}}/[\mathrm{kcal\,mol^{-1}\,\mathring{A}^{-2}}]$	$r_0/[\mathrm{\AA}]$
od-cd	570	1.229
oh-cd	450	1.364
ct-cd	317	1.522
ho-oh	553	0.945
hc-ct	340	1.090

Table A31: Bond-bending interaction parameters for malonic acid [59, 154]. The bond-bending energy is calculated according to: $E_{\mathrm{bending}}(\theta) = k_{\theta}(\theta - \theta_0)^2$. The atom types and atom labels can be found in Table A29 and Fig. A5.

angle type	$k_{\theta}/[\mathrm{kcal\,mol^{-1}\,rad^{-2}}]$	θ_0
od-cd-oh	80	121.0
od-cd-ct	80	120.4
cd-oh-ho	35	113.0
cd-ct-cd	63	111.1
cd-ct-hc	35	109.5
ct-cd-oh	70	108.0
hc-ct-hc	33	107.8

Table A32: Dihedral parameters for malonic acid [59, 154]. The dihedral energy is calculated according to: $E_{\mathrm{dihedral}}(\phi) = \frac{1}{2}V_1[1+\cos(\phi)] + \frac{1}{2}V_2[1-\cos(2\phi)] + \frac{1}{2}V_3[1+\cos(3\phi)]$. For each dihedral a-b-c-d, ϕ is the angle between the planes a-b-c and b-c-d. The atom types and atom labels can be found in Table A29 and Fig. A5.

dihedral types	$V_1/[\mathrm{kcal\,mol^{-1}}]$	$V_2/[\mathrm{kcal\,mol^{-1}}]$	$V_3/[\mathrm{kcal\,mol^{-1}}]$
ho-oh-cd-ct	1.500	5.500	0.000
hc-ct-cd-od	0.000	0.000	0.000
cd-ct-cd-oh	1.000	0.546	0.450
hc-ct-cd-oh	0.000	0.000	0.000
od-cd-oh-ho	0.000	5.500	0.000
od-cd-ct-cd	0.000	0.000	0.000
oh-cd-od-ct [a]	0.000	21.000	0.000

[a] This is an improper dihedral. The energy functional form for improper dihedrals is the same as for the (proper) dihedrals. However, for each improper dihedral a-b-c-d, the angle ϕ is defined as the angle between the planes a-b-c and a-c-d.

A.2.9 OPLS force field parameters for oxalic acid

Table A33: Atom types and non-bonded parameters for oxalic acid [59, 154]. The LJ energy is calculated according to: $E_{\mathrm{LJ}}(r) = 4\epsilon[(\sigma/r)^{12} - (\sigma/r)^6]$, where r is the site-site distance. The atom labels are defined in Fig. A6.

atom	atom type	$q/[\mathrm{e^-}]$	$\epsilon/[\mathrm{kcal\,mol^{-1}}]$	$\sigma/[\mathrm{\AA}]$
C	cd	0.416	0.1575	3.75
H	ho	0.330	0.0010	0.10
O1	oh	-0.394	0.2550	2.92
O2	od	-0.352	0.3150	2.96

Table A34: Bond-stretching interaction parameters for oxalic acid [59, 154]. The bond-stretching energy is calculated according to: $E_{\mathrm{stretching}}(r) = k_{\mathrm{r}}(r-r_0)^2$. The atom types and atom labels can be found in Table A33 and Fig. A6.

bond type	$k_{\mathrm{r}}/[\mathrm{kcal\,mol^{-1}\,\AA^{-2}}]$	$r_0/[\mathrm{\AA}]$
od-cd	570	1.229
oh-cd	450	1.364
cd-cd	350	1.510
ho-oh	553	0.945

Table A35: Bond-bending interaction parameters for oxalic acid [59, 154]. The bond-bending energy is calculated according to: $E_{\mathrm{bending}}(\theta) = k_\theta(\theta - \theta_0)^2$. The atom types and atom labels can be found in Table A33 and Fig. A6.

angle type	$k_\theta/[\mathrm{kcal\,mol^{-1}\,rad^{-2}}]$	θ_0
oh-cd-od	80.00	121.00
cd-oh-ho	35.00	113.00
cd-cd-oh	70.96	118.03
cd-cd-od	80.00	121.40

Table A36: Dihedral parameters for oxalic acid [59, 154]. The dihedral energy is calculated according to: $E_{\mathrm{dihedral}}(\phi) = \frac{1}{2}V_1[1 + \cos(\phi)] + \frac{1}{2}V_2[1 - \cos(2\phi)] + \frac{1}{2}V_3[1 + \cos(3\phi)]$. For each dihedral a-b-c-d, ϕ is the angle between the planes a-b-c and b-c-d. The atom types and atom labels can be found in Table A33 and Fig. A6.

dihedral types	$V_1/[\mathrm{kcal\,mol^{-1}}]$	$V_2/[\mathrm{kcal\,mol^{-1}}]$	$V_3/[\mathrm{kcal\,mol^{-1}}]$
ho-oh-cd-cd	3.000	5.500	0.000
oh-cd-cd-oh	1.600	3.200	0.000
ho-oh-cd-od	0.000	5.500	0.000
od-cd-cd-oh	1.600	3.200	0.000
od-cd-cd-od	1.600	3.200	0.000
oh-cd-od-cd [a]	0.000	21.000	0.000

[a] This is an improper dihedral. The energy functional form for improper dihedrals is the same as for the (proper) dihedrals. However, for each improper dihedral a-b-c-d, the angle ϕ is defined as the angle between the planes a-b-c and a-c-d.

A.2.10 GAFF force field parameters for TRAC salts

Table A37: Atom types and non-bonded parameters for the TBA cation [155]. The LJ energy is calculated according to: $E_{\mathrm{LJ}}(r) = 4\epsilon[(\sigma/r)^{12} - (\sigma/r)^{6}]$, where r is the site-site distance. The listed charges are the unscaled values, and should therefore be multiplied by the proper scaling factors when used in simulations. The atom labels are defined in Fig. A7.

atom label	atom type	$q/[\mathrm{e}^{-}]$	$\epsilon/[\mathrm{kcal\,mol}^{-1}]$	$\sigma/[\mathrm{\AA}]$
C1	c3	-0.0048	0.1094	3.3997
C2	c3	-0.0178	0.1094	3.3997
C3	c3	-0.0096	0.1094	3.3997
C4	c3	-0.1069	0.1094	3.3997
H1	hx	0.0663	0.0157	1.9600
H2	hc	0.0368	0.0157	2.6495
H3	hc	0.0284	0.0157	2.6495
H4	hc	0.0419	0.0157	2.6495
N	n4	0.0016	0.1700	3.2500

Table A38: Atom types and non-bonded parameters for the THA cation [155]. The LJ energy is calculated according to: $E_{\mathrm{LJ}}(r) = 4\epsilon[(\sigma/r)^{12} - (\sigma/r)^{6}]$, where r is the site-site distance. The listed charges are the unscaled values, and should therefore be multiplied by the proper scaling factors when used in simulations. The atom labels are defined in Fig. A8.

atom label	atom type	$q/[\mathrm{e}^{-}]$	$\epsilon/[\mathrm{kcal\,mol}^{-1}]$	$\sigma/[\mathrm{\AA}]$
C1	c3	-0.0018	0.1094	3.3997
C2	c3	0.0095	0.1094	3.3997
C3	c3	-0.0205	0.1094	3.3997
C4	c3	-0.0118	0.1094	3.3997
C5	c3	-0.0055	0.1094	3.3997
C6	c3	0.0225	0.1094	3.3997
C7	c3	-0.0989	0.1094	3.3997
H1	hx	0.0654	0.0157	1.9600
H2	hc	0.0292	0.0157	2.6495
H3	hc	0.0148	0.0157	2.6495
H4	hc	0.0050	0.0157	2.6495
H5	hc	0.0114	0.0157	2.6495
H6	hc	0.0106	0.0157	2.6495
H7	hc	0.0288	0.0157	2.6495
N	n4	-0.0108	0.1700	3.2500

Table A39: Atom types and non-bonded parameters for the TOA cation [155]. The LJ energy is calculated according to: $E_{\mathrm{LJ}}(r) = 4\epsilon[(\sigma/r)^{12} - (\sigma/r)^{6}]$, where r is the site-site distance. The listed charges are the unscaled values, and should therefore be multiplied by the proper scaling factors when used in simulations. The atom labels are defined in Fig. A9.

atom label	atom type	$q/[\mathrm{e}^{-}]$	$\epsilon/[\mathrm{kcal\,mol}^{-1}]$	$\sigma/[\mathrm{\AA}]$
C1	c3	-0.0028	0.1094	3.3997
C2	c3	0.0071	0.1094	3.3997
C3	c3	-0.0226	0.1094	3.3997
C4	c3	-0.0007	0.1094	3.3997
C5	c3	0.0001	0.1094	3.3997
C6	c3	-0.0088	0.1094	3.3997
C7	c3	0.0212	0.1094	3.3997
C8	c3	-0.0891	0.1094	3.3997
H1	hx	0.0646	0.0157	1.9600
H2	hc	0.0287	0.0157	2.6495
H3	hc	0.0165	0.0157	2.6495
H4	hc	0.0040	0.0157	2.6495
H5	hc	0.0040	0.0157	2.6495
H6	hc	0.0101	0.0157	2.6495
H7	hc	0.0070	0.0157	2.6495
H8	hc	0.0252	0.0157	2.6495
N	n4	0.0008	0.1700	3.2500

Table A40: Atom type and non-bonded parameters for the chloride anion in TRAC salts [332]. The LJ energy is calculated according to: $E_{\mathrm{LJ}}(r) = 4\epsilon[(\sigma/r)^{12} - (\sigma/r)^{6}]$, where r is the site-site distance. The listed charge is the unscaled value, and should therefore be multiplied by the proper scaling factor when used in simulations.

atom label	atom type	$q/[\mathrm{e}^{-}]$	$\epsilon/[\mathrm{kcal\,mol}^{-1}]$	$\sigma/[\mathrm{\AA}]$
Cl	cl	-1.0	0.2650	3.4709

Table A41: Bond-stretching interaction parameters for the TBA, THA, and TOA cations [155]. The bond-stretching energy is calculated according to: $E_{\mathrm{stretching}}(r) = k_{\mathrm{r}}(r - r_0)^2$. The atom types and atom labels can be found in Tables A37 to A39 and Figs. A7 to A9.

bond type	$k_{\mathrm{r}}/[\mathrm{kcal\,mol}^{-1}\,\mathrm{\AA}^{-2}]$	$r_0/[\mathrm{\AA}]$
c3-c3	303.1	1.535
c3-hc	337.3	1.092
c3-hx	338.7	1.091
c3-n4	293.6	1.499

Table A42: Bond-bending interaction parameters for the TBA, THA, and TOA cations [155]. The bond-bending energy is calculated according to: $E_{\mathrm{bending}}(\theta) = k_\theta(\theta - \theta_0)^2$. The atom types and atom labels can be found in Tables A37 to A39 and Figs. A7 to A9.

angle type	$k_\theta/[\mathrm{kcal\,mol^{-1}\,rad^{-2}}]$	θ_0
c3-c3-c3	63.2	110.63
c3-c3-hc	46.4	110.05
c3-c3-hx	46.0	111.74
c3-c3-n4	66.0	108.93
c3-n4-c3	62.8	110.64
hc-c3-hc	39.4	108.35
hx-c3-hx	39.0	110.74
hx-c3-n4	49.0	107.91

Table A43: Dihedral parameters for the TBA, THA, and TOA cations [155]. The dihedral energy is calculated according to: $E_{\mathrm{dihedral}}(\phi) = A_0 + A_1\cos(\phi) + A_2\cos^2(\phi) + A_3\cos^3(\phi)$. For each dihedral a-b-c-d, ϕ is the angle between the planes a-b-c and b-c-d. The atom types and atom labels can be found in Tables A37 to A39 and Figs. A7 to A9.

dihedral type	$A_0/[\mathrm{kcal\,mol^{-1}}]$	$A_1/[\mathrm{kcal\,mol^{-1}}]$	$A_2/[\mathrm{kcal\,mol^{-1}}]$	$A_3/[\mathrm{kcal\,mol^{-1}}]$
c3-c3-c3-c3	0.8800	-0.7400	-0.5000	0.7200
c3-c3-c3-hc	0.1600	-0.4800	0.0000	0.6400
c3-c3-c3-hx	0.1556	-0.4667	0.0000	0.6222
c3-c3-c3-n4	0.1556	-0.4667	0.0000	0.6222
c3-c3-n4-c3	0.1556	-0.4667	0.0000	0.6222
hc-c3-c3-hc	0.1500	-0.4500	0.0000	0.6000
hc-c3-c3-hx	0.1556	-0.4667	0.0000	0.6222
hc-c3-c3-n4	0.1556	-0.4667	0.0000	0.6222
hx-c3-n4-c3	0.1556	-0.4667	0.0000	0.6222

A.2.11 GAFF force Field Parameters for Thymol

Table A44: Atom types and non-bonded parameters for thymol [155]. The LJ energy is calculated according to: $E_{\mathrm{LJ}}(r) = 4\epsilon[(\sigma/r)^{12} - (\sigma/r)^{6}]$, where r is the site-site distance. The listed charges are the unscaled values, and should therefore be multiplied by the proper scaling factors when used in simulations. The atom labels are defined in Fig. A10.

atom label	atom type	$q/[\mathrm{e}^{-}]$	$\epsilon/[\mathrm{kcal\,mol}^{-1}]$	$\sigma/[\mathrm{\AA}]$
C1	c3	-0.1835	0.1094	3.3997
C2	ca	0.0799	0.0860	3.3997
C3	ca	-0.2007	0.0860	3.3997
C4	ca	-0.3135	0.0860	3.3997
C5	ca	0.0679	0.0860	3.3997
C6	ca	0.1919	0.0860	3.3997
C7	ca	-0.2712	0.0860	3.3997
C8	c3	0.2411	0.1094	3.3997
C9	c3	-0.2008	0.1094	3.3997
C10	c3	-0.2008	0.1094	3.3997
H1	hc	0.0678	0.0157	2.6495
H2	ha	0.1507	0.0150	2.5996
H3	ha	0.1999	0.0150	2.5996
H4	ha	0.1442	0.0150	2.5996
H5	hc	0.0211	0.0157	2.6495
H6	hc	0.0385	0.0157	2.6495
H7	hc	0.0385	0.0157	2.6495
H8	ho	0.4403	0.0010	0.1000
O	oh	-0.6009	0.2104	3.0665

Table A45: Bond-stretching interaction parameters for thymol [155]. The bond-stretching energy is calculated according to: $E_{\mathrm{stretching}}(r) = k_{\mathrm{r}}(r - r_0)^2$. The atom types and atom labels can be found in Table A44 and Fig. A10.

bond type	$k_{\mathrm{r}}/[\mathrm{kcal\,mol}^{-1}\,\mathrm{\AA}^{-2}]$	$r_0/[\mathrm{\AA}]$
c3-c3	303.1	1.535
c3-hc	337.3	1.092
ho-oh	369.6	0.974
ca-c3	323.5	1.513
ca-ca	478.4	1.387
ca-oh	386.1	1.362
ca-ha	344.3	1.087

Table A46: Bond-bending interaction parameters for thymol [155]. The bond-bending energy is calculated according to: $E_{\mathrm{bending}}(\theta) = k_\theta(\theta - \theta_0)^2$. The atom types and atom labels can be found in Table A44 and Fig. A10.

angle type	$k_\theta/[\mathrm{kcal\,mol^{-1}\,rad^{-2}}]$	θ_0
c3-c3-c3	63.2	110.63
c3-c3-hc	46.4	110.05
hc-c3-hc	39.4	108.35
ca-c3-hc	47.0	110.15
ca-ca-ca	67.2	119.97
ca-ca-c3	63.8	120.63
ca-ca-ha	48.5	120.01
ca-oh-ho	48.9	109.47
ca-ca-oh	69.8	119.94
ca-c3-c3	62.5	114.61

Table A47: Dihedral parameters for thymol [155]. The dihedral energy is calculated according to: $E_{\mathrm{dihedral}}(\phi) = A_0 + A_1\cos(\phi) + A_2\cos^2(\phi) + A_3\cos^3(\phi)$. For each dihedral a-b-c-d, ϕ is the angle between the planes a-b-c and b-c-d. The atom types and atom labels can be found in Table A44 and Fig. A10.

dihedral type	$A_0/[\mathrm{kcal\,mol^{-1}}]$	$A_1/[\mathrm{kcal\,mol^{-1}}]$	$A_2/[\mathrm{kcal\,mol^{-1}}]$	$A_3/[\mathrm{kcal\,mol^{-1}}]$
c3-c3-c3-hc	0.1600	-0.4800	0.0000	0.6400
hc-c3-c3-hc	0.1500	-0.4500	0.0000	0.6000
c3-c3-ca-ca	0.0000	0.0000	0.0000	0.0000
c3-ca-ca-ca	7.2500	0.0000	-7.2500	0.0000
c3-ca-ca-ha	7.2500	0.0000	-7.2500	0.0000
c3-ca-ca-oh	7.2500	0.0000	-7.2500	0.0000
ca-c3-c3-hc	0.1556	-0.4667	0.0000	0.6222
ca-ca-ca-ca	7.2500	0.0000	-7.2500	0.0000
ca-ca-ca-oh	7.2500	0.0000	-7.2500	0.0000
ca-ca-oh-ho	1.8000	0.0000	-1.8000	0.0000
ha-ca-ca-ha	7.2500	0.0000	-7.2500	0.0000
ha-ca-ca-oh	7.2500	0.0000	-7.2500	0.0000
hc-c3-ca-ca	0.0000	0.0000	0.0000	0.0000
ca-ca-ca-ha	7.2500	0.0000	-7.2500	0.0000
c3-ca-ca-ca [a]	2.2000	0.0000	-2.2000	0.0000
ha-ca-ca-ca [a]	2.2000	0.0000	-2.2000	0.0000
oh-ca-ca-ca [a]	2.2000	0.0000	-2.2000	0.0000

[a] These are improper dihedrals. The energy functional form for improper dihedrals is the same as for the (proper) dihedrals. However, for each improper dihedral a-b-c-d, the angle ϕ is defined as the angle between the planes a-b-c and a-c-d.

A.2.12 GAFF force Field Parameters for DL-Menthol

Table A48: Atom types and non-bonded parameters for D-menthol [155]. The LJ energy is calculated according to: $E_{\mathrm{LJ}}(r) = 4\epsilon[(\sigma/r)^{12} - (\sigma/r)^{6}]$, where r is the site-site distance. The listed charges are the unscaled values, and should therefore be multiplied by the proper scaling factors when used in simulations. The atom labels are defined in Fig. A11.

atom label	atom type	$q/[\mathrm{e}^{-}]$	$\epsilon/[\mathrm{kcal\,mol}^{-1}]$	$\sigma/[\mathrm{\AA}]$
C1	c3	-0.1819	0.1094	3.3997
C2	c3	0.1651	0.1094	3.3997
C3	c3	-0.0985	0.1094	3.3997
C4	c3	-0.1855	0.1094	3.3997
C5	c3	-0.0084	0.1094	3.3997
C6	c3	0.1368	0.1094	3.3997
C7	c3	-0.1807	0.1094	3.3997
C8	c3	0.1673	0.1094	3.3997
C9	c3	-0.1985	0.1094	3.3997
C10	c3	-0.1985	0.1094	3.3997
H1	hc	0.0394	0.0157	2.6495
H2	hc	-0.0076	0.0157	2.6495
H3	hc	0.0361	0.0157	2.6495
H4	hc	0.0639	0.0157	2.6495
H5	hc	0.0370	0.0157	2.6495
H6	h1	0.1171	0.0157	2.4714
H7	hc	0.0571	0.0157	2.6495
H8	hc	0.0082	0.0157	2.6495
H9	hc	0.0417	0.0157	2.6495
H10	hc	0.0417	0.0157	2.6495
H11	ho	0.3972	0.0010	0.1000
O	oh	-0.6517	0.2104	3.0665

Table A49: Atom types and non-bonded parameters for L-menthol [155]. The LJ energy is calculated according to: $E_{\mathrm{LJ}}(r) = 4\epsilon[(\sigma/r)^{12} - (\sigma/r)^{6}]$, where r is the site-site distance. The listed charges are the unscaled values, and should therefore be multiplied by the proper scaling factors when used in simulations. The atom labels are defined in Fig. A11.

atom label	atom type	$q/[\mathrm{e}^{-}]$	$\epsilon/[\mathrm{kcal\,mol}^{-1}]$	$\sigma/[\mathrm{\AA}]$
C1	c3	-0.1783	0.1094	3.3997
C2	c3	0.1580	0.1094	3.3997
C3	c3	-0.0982	0.1094	3.3997
C4	c3	-0.1892	0.1094	3.3997
C5	c3	-0.0082	0.1094	3.3997
C6	c3	0.1331	0.1094	3.3997
C7	c3	-0.1716	0.1094	3.3997
C8	c3	0.1690	0.1094	3.3997
C9	c3	-0.1997	0.1094	3.3997
C10	c3	-0.1997	0.1094	3.3997
H1	hc	0.0387	0.0157	2.6495
H2	hc	-0.0059	0.0157	2.6495
H3	hc	0.0366	0.0157	2.6495
H4	hc	0.0651	0.0157	2.6495
H5	hc	0.0374	0.0157	2.6495
H6	h1	0.1171	0.0157	2.4714
H7	hc	0.0555	0.0157	2.6495
H8	hc	0.0081	0.0157	2.6495
H9	hc	0.0420	0.0157	2.6495
H10	hc	0.0420	0.0157	2.6495
H11	ho	0.3965	0.0010	0.1000
O	oh	-0.6509	0.2104	3.0665

Table A50: Bond-stretching interaction parameters for DL-menthol [155]. The bond-stretching energy is calculated according to: $E_{\mathrm{stretching}}(r) = k_{\mathrm{r}}(r - r_0)^2$. The atom types and atom labels can be found in Tables A48 and A49 and Fig. A11.

bond type	$k_{\mathrm{r}}/[\mathrm{kcal\,mol}^{-1}\,\mathrm{\AA}^{-2}]$	$r_0/[\mathrm{\AA}]$
c3-c3	303.1	1.535
c3-hc	337.3	1.092
ho-oh	369.6	0.974
c3-h1	335.9	1.093
c3-oh	314.1	1.426

Table A51: Bond-bending interaction parameters for DL-menthol [155]. The bond-bending energy is calculated according to: $E_{\mathrm{bending}}(\theta) = k_\theta(\theta - \theta_0)^2$. The atom types and atom labels can be found in Tables A48 and A49 and Fig. A11.

angle type	$k_\theta/[\mathrm{kcal\,mol^{-1}\,rad^{-2}}]$	θ_0
c3-c3-c3	63.2	110.63
c3-c3-hc	46.4	110.05
hc-c3-hc	39.4	108.35
c3-c3-h1	46.4	110.07
c3-c3-oh	67.7	109.43
c3-oh-ho	47.1	108.16
h1-c3-oh	51.0	109.88

Table A52: Dihedral parameters for DL-menthol [155]. The dihedral energy is calculated according to: $E_{\mathrm{dihedral}}(\phi) = A_0 + A_1\cos(\phi) + A_2\cos^2(\phi) + A_3\cos^3(\phi)$. For each dihedral a-b-c-d, ϕ is the angle between the planes a-b-c and b-c-d. The atom types and atom labels can be found in Tables A48 and A49 and Fig. A11.

dihedral type	$A_0/[\mathrm{kcal\,mol^{-1}}]$	$A_1/[\mathrm{kcal\,mol^{-1}}]$	$A_2/[\mathrm{kcal\,mol^{-1}}]$	$A_3/[\mathrm{kcal\,mol^{-1}}]$
c3-c3-c3-hc	0.1600	-0.4800	0.0000	0.6400
c3-c3-c3-c3	0.8800	-0.7400	0.5000	0.7200
hc-c3-c3-hc	0.1500	-0.4500	0.0000	0.6000
c3-c3-c3-h1	0.1556	-0.4667	0.0000	0.6222
c3-c3-c3-oh	0.1556	-0.4667	0.0000	0.6222
h1-c3-c3-hc	0.1556	-0.4667	0.0000	0.6222
h1-c3-oh-ho	0.1667	-0.5000	0.0000	0.6667
hc-c3-c3-oh	0.2500	0.2500	0.0000	0.0000
c3-c3-oh-ho	0.4100	-0.2300	0.0000	0.6400

A.2.13 GAFF force field parameters for decanoic acid

Table A53: Atom types and non-bonded parameters for decanoic acid [155]. The LJ energy is calculated according to: $E_{\mathrm{LJ}}(r) = 4\epsilon[(\sigma/r)^{12} - (\sigma/r)^{6}]$, where r is the site-site distance. The atom labels are defined in Fig. A12.

atom label	atom type	$q/[\mathrm{e}^-]$	$\epsilon/[\mathrm{kcal\,mol}^{-1}]$	$\sigma/[\mathrm{Å}]$
C1	c3	-0.0977	0.1094	3.3997
C2	c3	0.0308	0.1094	3.3997
C3	c3	0.0032	0.1094	3.3997
C4	c3	-0.0033	0.1094	3.3997
C5	c3	0.0023	0.1094	3.3997
C6	c3	0.0138	0.1094	3.3997
C7	c3	-0.0092	0.1094	3.3997
C8	c3	-0.0189	0.1094	3.3997
C9	c3	-0.0228	0.1094	3.3997
C10	c	0.7355	0.0860	3.3997
H1	hc	0.0216	0.0157	2.6495
H2	hc	0.0012	0.0157	2.6495
H3	hc	0.0028	0.0157	2.6495
H4	hc	-0.0025	0.0157	2.6495
H5	hc	-0.0023	0.0157	2.6495
H6	hc	0.0037	0.0157	2.6495
H7	hc	-0.0005	0.0157	2.6495
H8	hc	0.0145	0.0157	2.6495
H9	hc	0.0400	0.0157	2.6495
H10	ho	0.4595	0.0010	0.1000
O1	oh	-0.6752	0.2104	3.0665
O2	o	-0.5966	0.2100	2.9599

Table A54: Bond-stretching interaction parameters for decanoic acid [155]. The bond-stretching energy is calculated according to: $E_{\mathrm{stretching}}(r) = k_{\mathrm{r}}(r - r_0)^2$. The atom types and atom labels can be found in Table A53 and Fig. A12.

bond type	$k_{\mathrm{r}}/[\mathrm{kcal\,mol}^{-1}\,\mathrm{Å}^{-2}]$	$r_0/[\mathrm{Å}]$
c-c3	328.3	1.508
c-o	648.0	1.214
c-oh	466.4	1.306
c3-c3	303.1	1.535
c3-hc	337.3	1.092
ho-oh	369.6	0.974

Table A55: Bond-bending interaction parameters for decanoic acid [155]. The bond-bending energy is calculated according to: $E_{\mathrm{bending}}(\theta) = k_\theta(\theta - \theta_0)^2$. The atom types and atom labels can be found in Table A53 and Fig. A12.

angle type	$k_\theta/[\mathrm{kcal\,mol^{-1}\,rad^{-2}}]$	θ_0
c-c3-c3	63.8	110.53
c3-c3-c3	63.2	110.63
c-oh-ho	51.2	107.37
c3-c-o	68.0	123.11
c3-c-oh	69.8	112.20
c3-c3-hc	46.4	110.05
c-c3-hc	47.2	109.68
hc-c3-hc	39.4	108.35
o-c-oh	77.4	122.88

Table A56: Dihedral parameters for decanoic acid [155]. The dihedral energy is calculated according to: $E_{\mathrm{dihedral}}(\phi) = A_0 + A_1\cos(\phi) + A_2\cos^2(\phi) + A_3\cos^3(\phi)$. For each dihedral a-b-c-d, ϕ is the angle between the planes a-b-c and b-c-d. The atom types and atom labels can be found in Table A53 and Fig. A12.

dihedral type	$A_0/[\mathrm{kcal\,mol^{-1}}]$	$A_1/[\mathrm{kcal\,mol^{-1}}]$	$A_2/[\mathrm{kcal\,mol^{-1}}]$	$A_3/[\mathrm{kcal\,mol^{-1}}]$
c3-c3-c3-hc	0.1600	-0.4800	0.0000	0.6400
c3-c3-c3-c3	0.8800	-0.7400	0.5000	0.7200
c-c3-c3-c3	0.1556	-0.4667	0.0000	0.6222
c-c3-c3-hc	0.1556	-0.4667	0.0000	0.6222
hc-c3-c3-hc	0.1500	-0.4500	0.0000	0.6000
c3-c-oh-ho	4.6000	0.0000	-4.6000	0.0000
o-c-c3-c3	0.0000	0.0000	0.0000	0.0000
o-c-c3-hc	0.8800	1.0400	0.0000	-0.3200
o-c-oh-ho	6.5000	1.9000	-4.6000	0.0000
oh-c-c3-c3	0.0000	0.0000	0.0000	0.0000
oh-c-c3-hc	0.0000	0.0000	0.0000	0.0000
oh-c-o-c3 [a]	2.2000	0.0000	-2.2000	0.0000

[a] This is an improper dihedral. The energy functional form for improper dihedrals is the same as for the (proper) dihedrals. However, for each improper dihedral a-b-c-d, the angle ϕ is defined as the angle between the planes a-b-c and a-c-d.

A.2.14 Force field parameters for solute molecules and water

Table A57: Atom types and non-bonded parameters for CO_2 [259], CO [263], CH_4 (united atom) [260], H_2S [261], H_2 [262], N_2 [259], and H_2O (SPC/E model) [389]. The LJ energy is calculated according to: $E_{LJ}(r) = 4\epsilon[(\sigma/r)^{12} - (\sigma/r)^6]$, where r is the site-site distance. For the unprotected hydrogen of H_2O and the dummy sites (denoted as 'M') of CO, H_2S, and N_2, the LJ parameters $\epsilon = 0.001\,\mathrm{kcal\,mol^{-1}}$ and $\sigma = 0.1$ Å are listed, which prevent atomic overlaps in simulations. The molecular structures and atom labels can be found in Figs. A13 to A18.

molecules	atom type	$q/[e^-]$	$\epsilon/[\mathrm{kcal\,mol^{-1}}]$	$\sigma/[\text{Å}]$
CO_2	C	0.7000	0.0536	2.800
	O	-0.3500	0.1569	3.050
CO	C	-0.2424	0.0321	3.636
	O	-0.2744	0.1946	2.979
	M	0.5168	0.0010	0.100
CH_4	CH4	0.0000	0.2939	3.730
H_2S	S	0.0000	0.2423	3.600
	H	0.2100	0.0993	2.500
	M	-0.4200	0.0010	0.100
H_2	H	0.0000	0.0248	2.590
N_2	N	-0.4820	0.0715	3.310
	M	0.9640	0.0010	0.100
H_2O	O	-0.8476	0.1553	3.166
	H	0.4238	0.0010	0.100

A.3 Additional simulation results

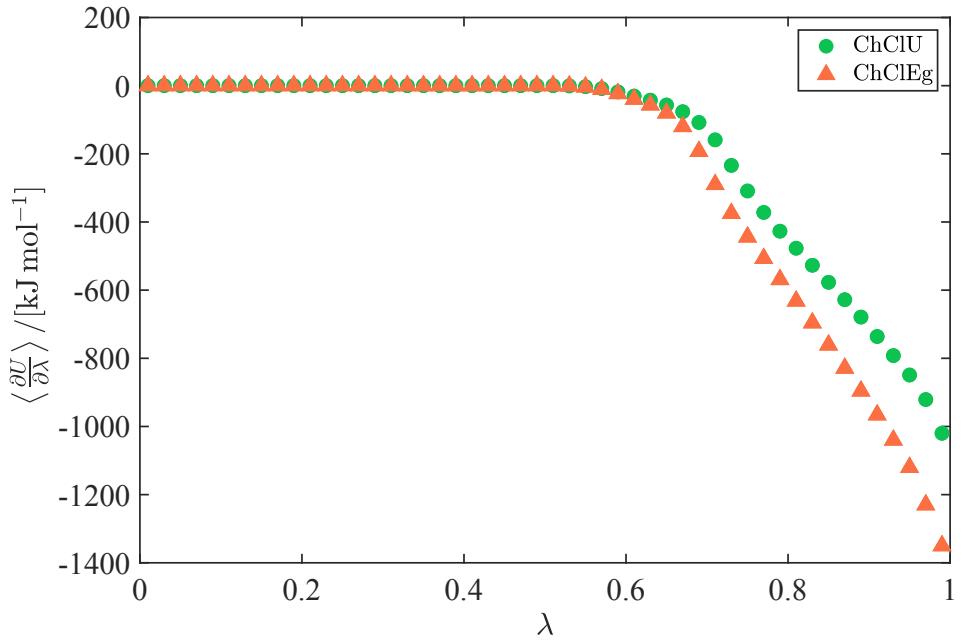

Figure A19: Average values of the derivative of the total energy with respect to λ, as a function of λ, for choline chloride in ChClU (at 393 K) and ChClEg (at 353 K), from gas phase MC simulations (additional results from chapter 4). The differences between the values of $\left\langle \frac{\partial U}{\partial \lambda} \right\rangle$ for choline chloride in ChClEg and ChClU result from the different charge scaling factors used for choline chloride: 0.8 in ChClU, and 0.9 in ChClEg.

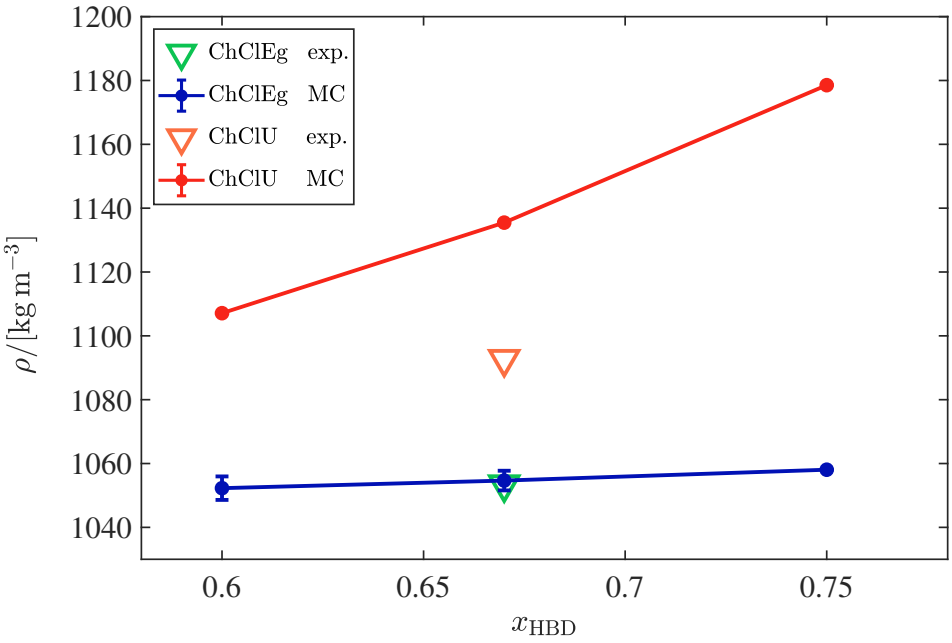

Figure A20: Computed liquid densities of ChClEg (at 393 K) and ChClU (at 433 K) as a function of the liquid phase mole fraction of the HBD component, i.e., ethylene glycol or urea (additional results from chapter 4). The solid lines are drawn to guide the eye. The (extrapolated) experimental values by Yadav and Pandey [181] (for ChClU), and Yadav et al. [36] (for ChClEg) are also shown for comparison.

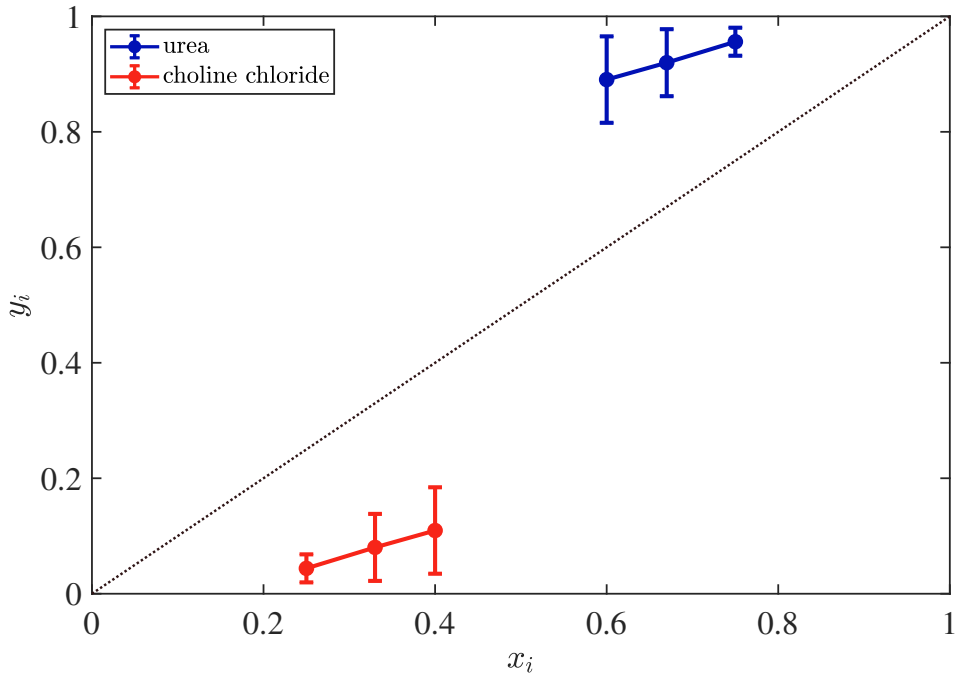

Figure A21: Computed vapor phase mole fraction of each component i (urea or choline chloride) of ChClU at 433 K as a function of its mole fraction in the liquid phase (additional results from chapter 4). The solid lines are drawn to guide the eye. The black dotted line denotes $y_i = x_i$.

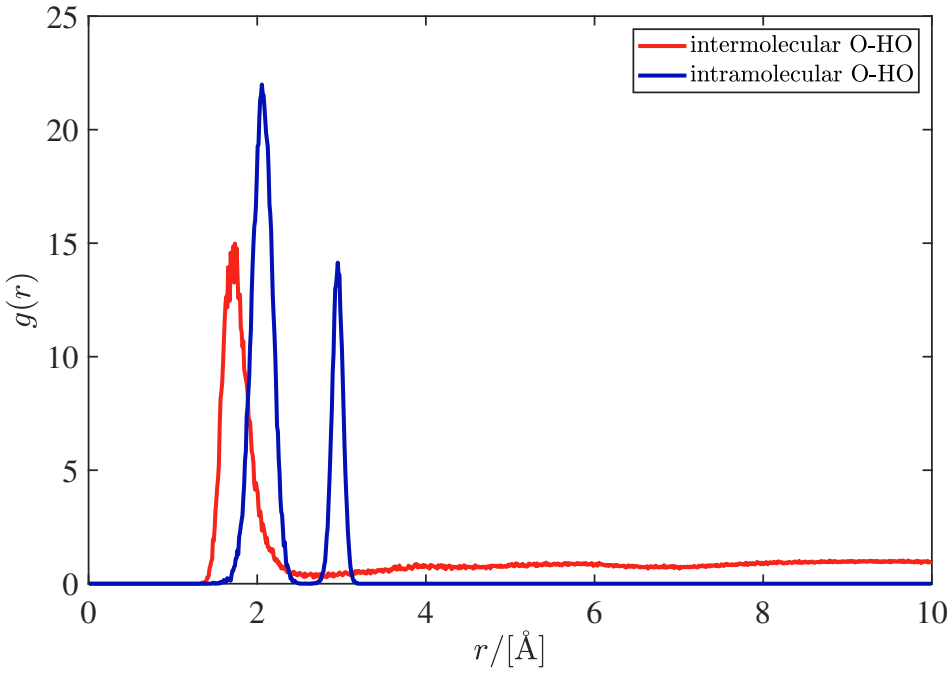

Figure A22: Inter- and intramolecular radial distribution functions for the interaction between the hydroxyl hydrogen and carbonyl oxygen of decanoic acid in TBAC-dec at 343 K and 1 atm (additional results from chapter 5).

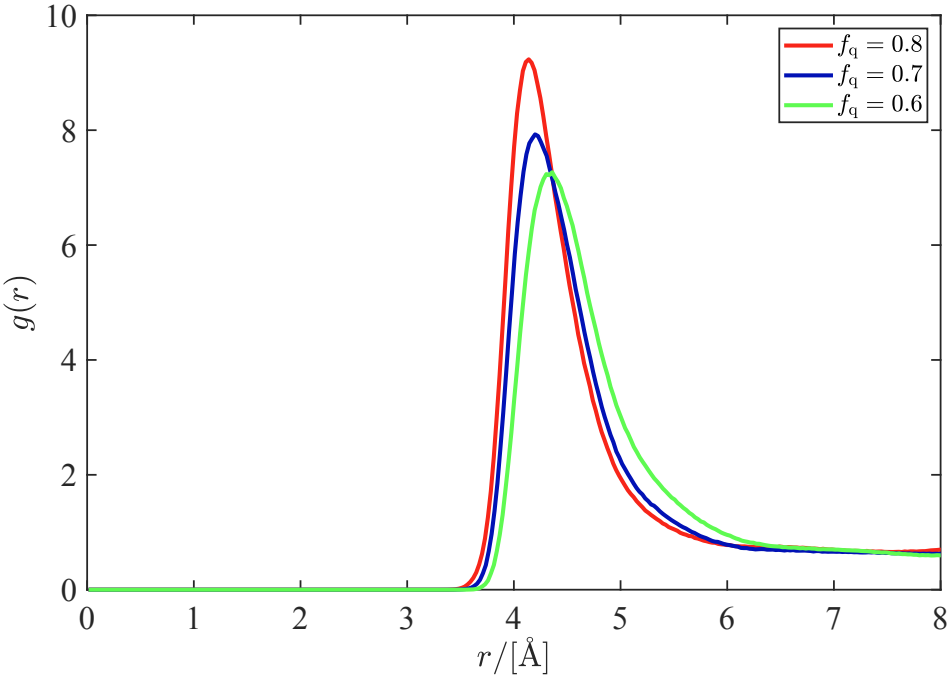

Figure A23: Radial distribution functions for the interaction between the nitrogen atom of cation and the chloride anion (N-Cl) in TBAC-dec at 298 K and 1 atm, for various ionic charge scaling factors (f_q) of choline chloride (additional results from chapter 5).

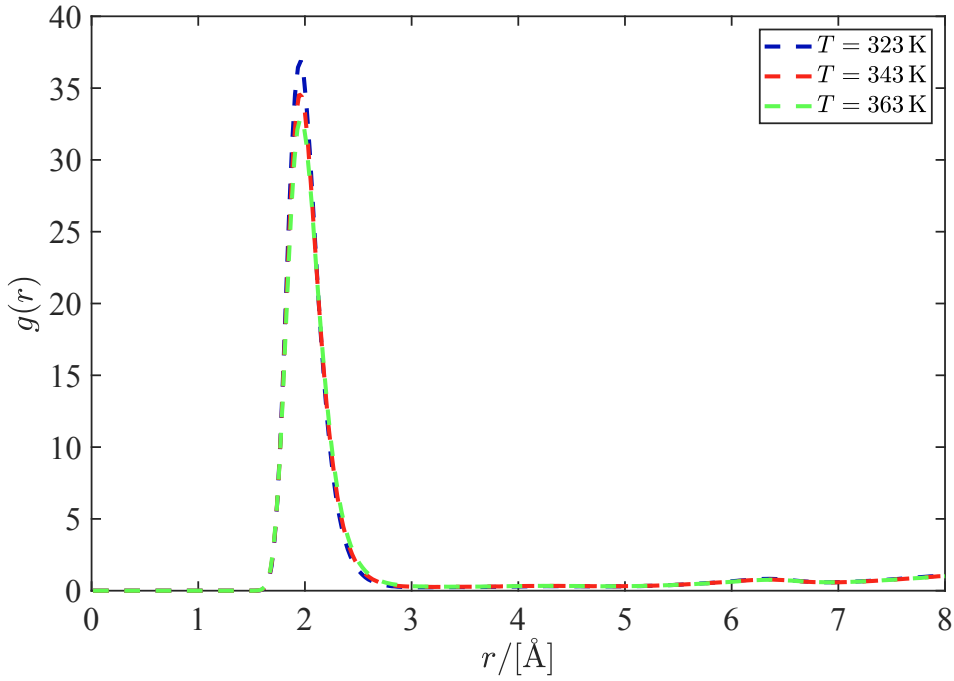

Figure A24: Radial distribution functions for the interaction between the chloride anion and the hydroxyl hydrogen of decanoic acid (Cl-HO) in TBAC-dec, at various temperatures and 1 atm (additional results from chapter 5).

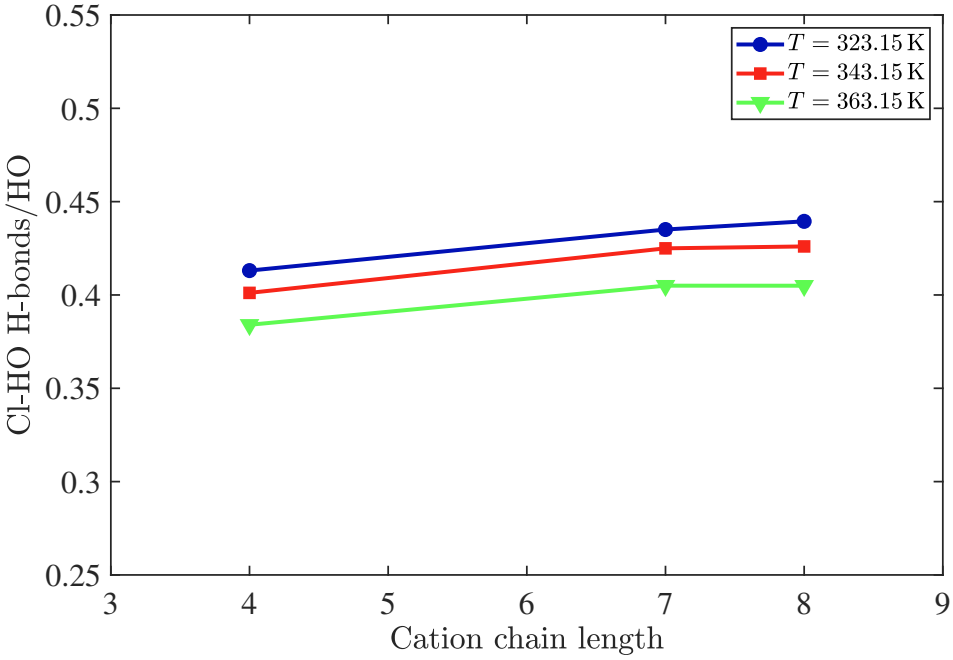

Figure A25: Populations of the Cl-HO hydrogen bond (per number of HO atoms) at various temperatures and 1 atm, as a function of the cation chain length for TRAC-dec DESs (additional results from chapter 5).

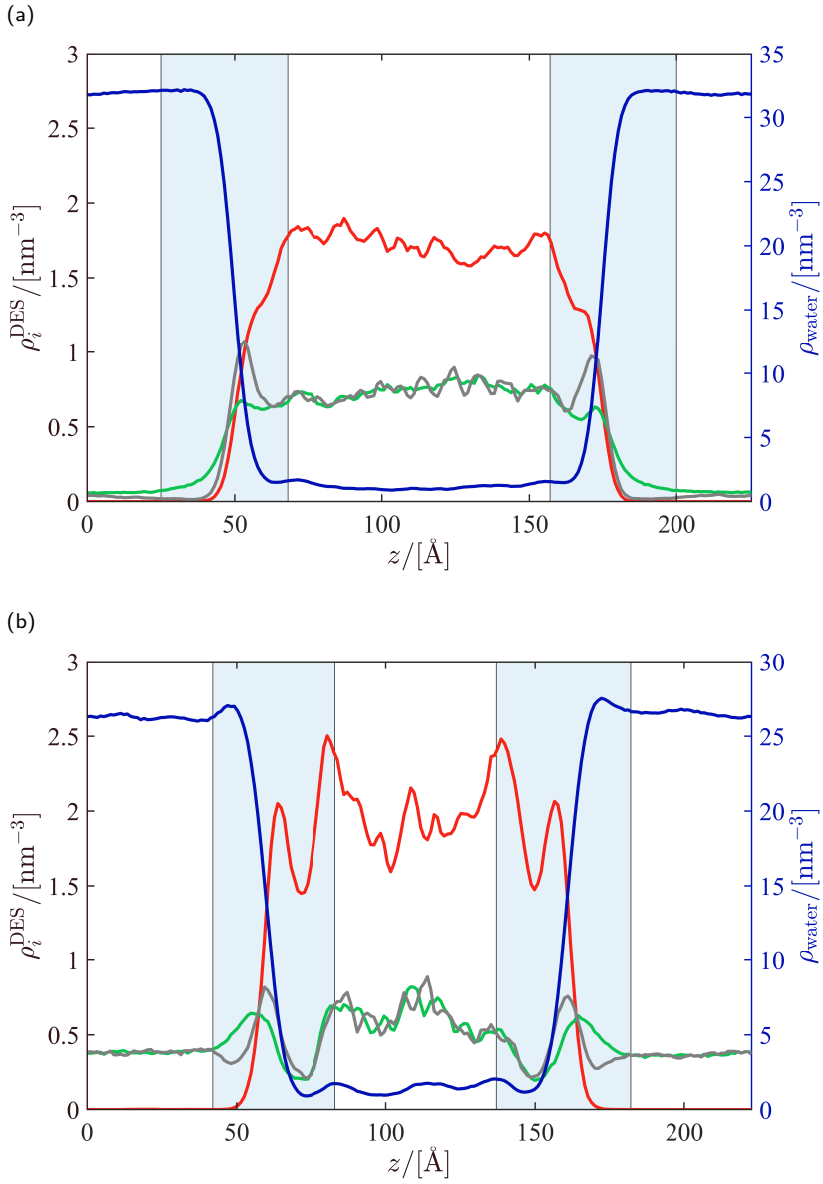

Figure A26: Computed number density profiles (number of molecules per nm^3) of DES components i (left vertical axis) and water (right vertical axis) in the TBAC-dec/water mixture at 343 K and 1 atm, using charge scaling factors of (a) $f_{\mathrm{q}} = 0.6$, and (b) $f_{\mathrm{q}} = 0.8$ for the HBA (additional results from chapter 6). The red, green, gray, and blue colors correspond to decanoic acid (HBD), chloride (anion), choline (cation), and water, respectively. For the density profiles of decanoic acid and choline, the coordinates of the hydroxyl oxygen and the nitrogen atoms were used, respectively. The DES/water interfaces are indicated using blue shaded areas.

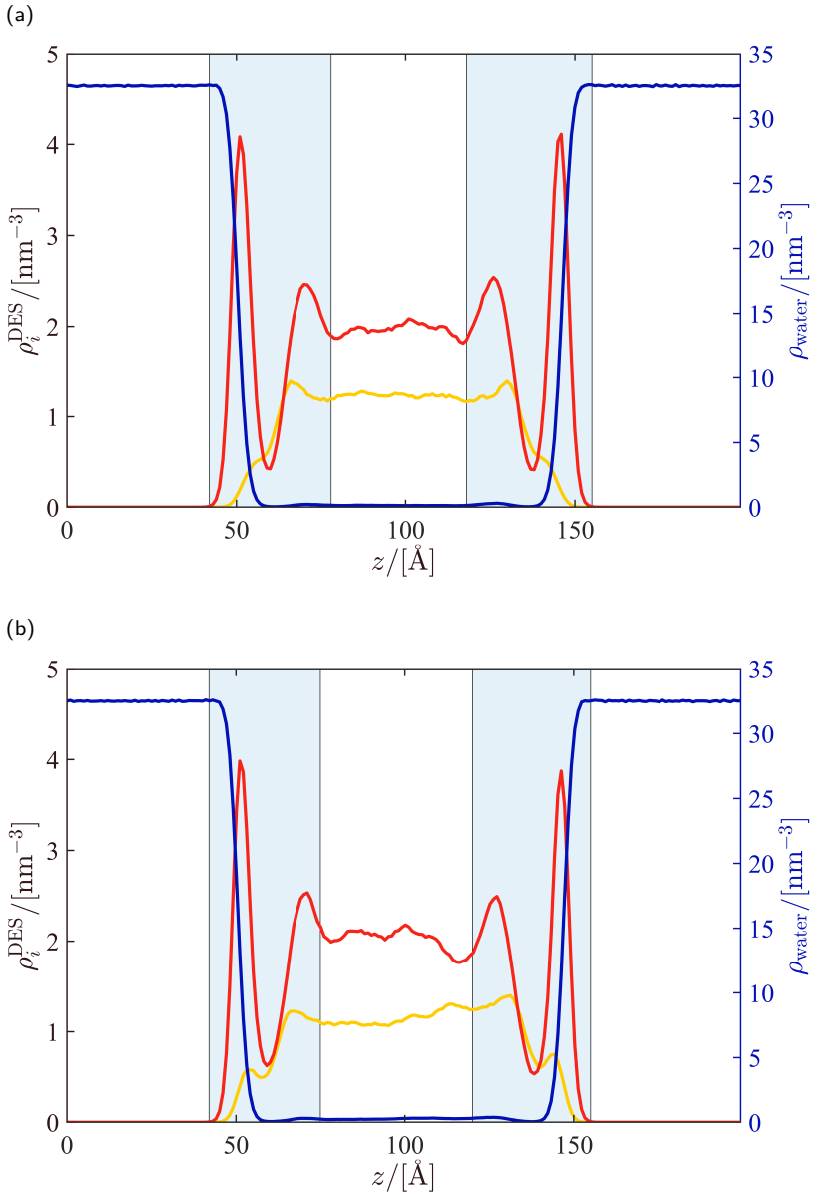

Figure A27: Computed number density profiles (number of molecules per nm^3) of DES components i (left vertical axis) and water (right vertical axis) in the Thy-dec/water mixture at 343 K and 1 atm, using the charge scaling factors (a) $f_{\mathrm{q}} = 0.7/1$, and (b) $f_{\mathrm{q}} = 0.8/0.8$ (additional results from chapter 6). The red, yellow, and blue profiles correspond to decanoic acid (HBD), thymol (HBA), and water, respectively. For the density profiles of decanoic acid and thymol, the coordinates of the hydroxyl oxygen atoms were used. The DES/water interfaces are designated using blue shaded areas.

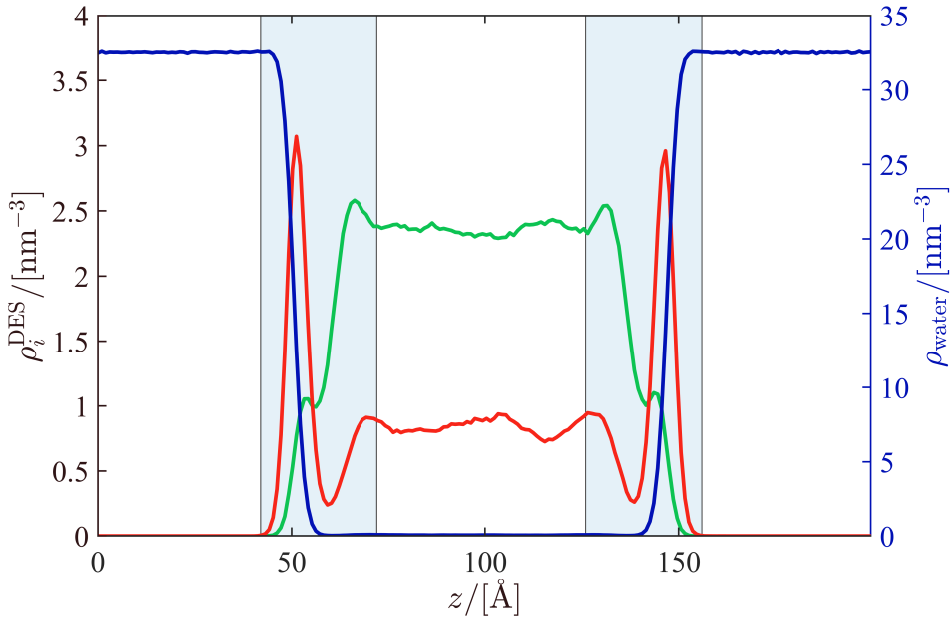

Figure A28: Computed number density profiles (number of molecules per nm^3) of DES components i (left vertical axis) and water (right vertical axis) in the Men-dec/water mixture at 343 K and 1 atm, using the charge scaling factors $f_{\mathrm{q}} = 0.8/1$ (additional results from chapter 6). The red, green, and blue profiles correspond to decanoic acid (HBD), menthol (HBA), and water, respectively. For the density profiles of decanoic acid and menthol, the coordinates of the hydroxyl oxygen atoms were used. The density profile of menthol includes both D-menthol and L-menthol molecules. The DES/water interfaces are indicated using blue shaded areas.

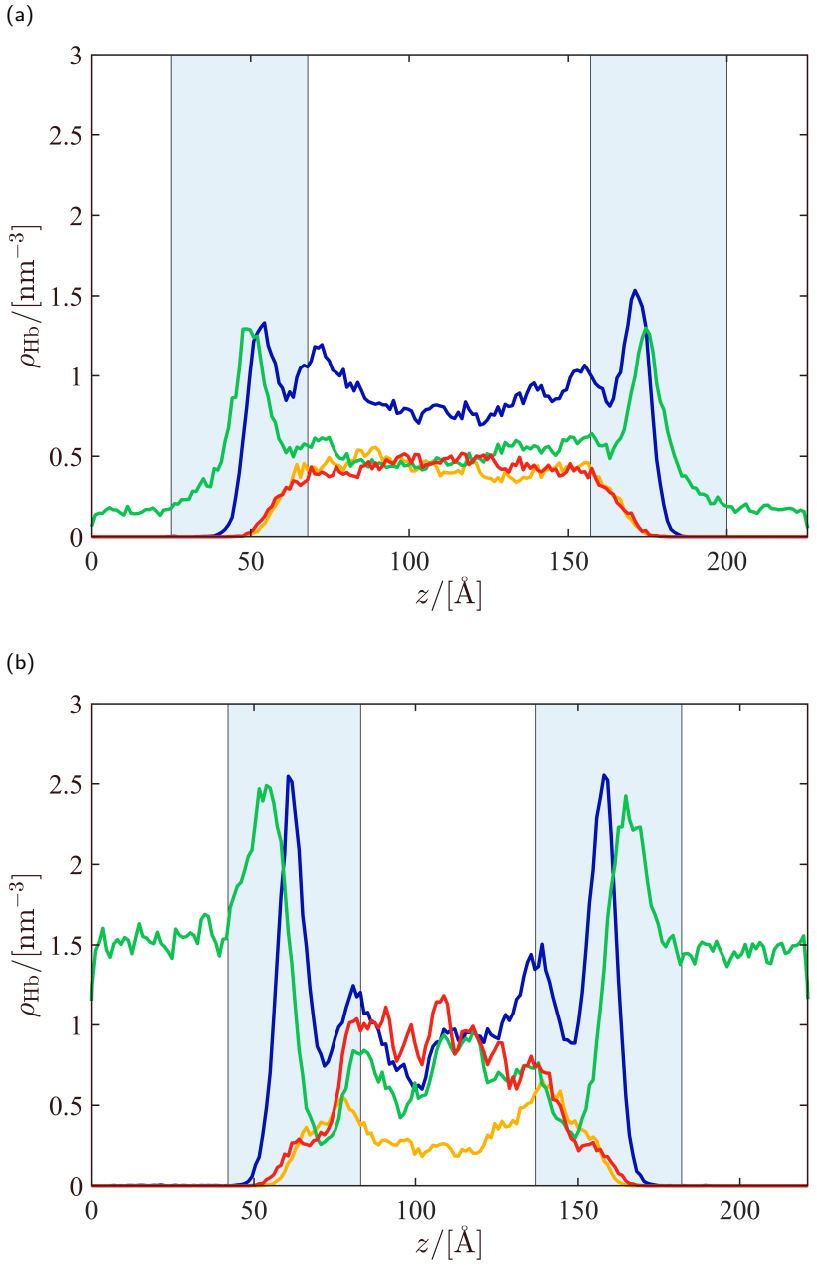

Figure A29: Computed hydrogen bond number densities (number of hydrogen bonds per nm^3) for the TBAC-dec/water system at 343 K and 1 atm, with charge scaling factors of (a) f_{q}=0.6, and (b) f_{q}=0.8 (additional results from chapter 6). The blue, green, yellow, and red colors correspond to water-decanoic acid, water-chloride, decanoic acid-decanoic acid, and chloride-decanoic acid hydrogen bonds, respectively. The blue shaded areas indicate the interfaces.

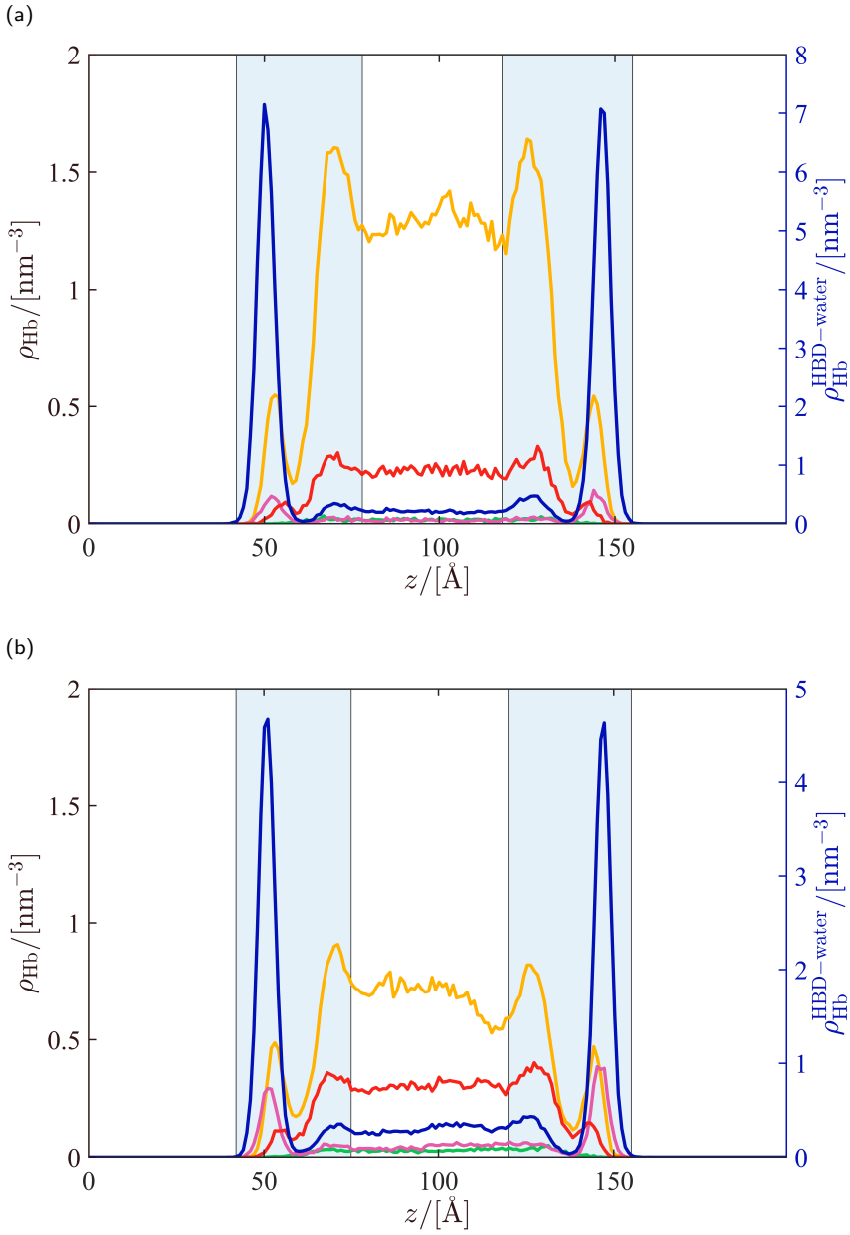

Figure A30: Computed hydrogen bond number densities (number of hydrogen bonds per nm^3) for the Thy-dec/water system at 343 K and 1 atm, with charge scaling factors of (a) f_{q}=0.7/1, and (b) f_{q}=0.8/0.8 (additional results from chapter 6). The blue, green, yellow, red, and pink colors correspond to water-decanoic acid (right vertical axis), thymol-thymol, decanoic acid-decanoic acid, thymol-decanoic acid, and water-thymol hydrogen bonds, respectively. The blue shaded areas indicate the interfaces.

References

(1) Ramdin, M.; de Loos, T. W.; Vlugt, T. J. H. State-of-the-art of CO_2 capture with ionic liquids. *Ind. Eng. Chem. Res.* **2012**, *51*, 8149–8177.

(2) Marsh, K. N; Boxall, J. A; Lichtenthaler, R. Room temperature ionic liquids and their mixtures—a review. *Fluid Phase Equilib.* **2004**, *219*, 93–98.

(3) Singh, S. K.; Savoy, A. W. Ionic liquids synthesis and applications: An overview. *J. Mol. Liq.* **2020**, *297*, 112038.

(4) Abbott, A. P.; Capper, G.; Davies, D. L.; Rasheed, R. K.; Tambyrajah, V. Novel solvent properties of choline chloride/urea mixtures. *Chem. Commun.* **2003**, 70–71.

(5) Zubeir, L. F.; van Osch, D. J. G. P.; Rocha, M. A. A.; Banat, F.; Kroon, M. C. Carbon dioxide solubilities in decanoic acid-based hydrophobic deep eutectic solvents. *J. Chem. Eng. Data* **2018**, *63*, 913–919.

(6) Smith, E. L.; Abbott, A. P.; Ryder, K. S. Deep eutectic solvents (DESs) and their applications. *Chem. Rev.* **2014**, *114*, 11060–11082.

(7) Francisco, M.; van den Bruinhorst, A.; Kroon, M. C. Low-transition-temperature mixtures (LTTMs): A new generation of designer solvents. *Angew. Chemie - Int. Ed.* **2013**, *52*, 3074–3085.

(8) Marcus, Y., *Deep eutectic solvents*; Springer International Publishing: Cham, Switzerland, 2019; Vol. 1.

(9) Sarmad, S.; Xie, Y.; Mikkola, J. P.; Ji, X. Screening of deep eutectic solvents (DESs) as green CO_2 sorbents: from solubility to viscosity. *New J. Chem.* **2016**, *41*, 290–301.

(10) Zhang, Q.; De Oliveira Vigier, K.; Royer, S.; Jérôme, F. Deep eutectic solvents: Syntheses, properties and applications. *Chem. Soc. Rev.* **2012**, *41*, 7108–7146.

(11) van Osch, D. J. G. P.; Dietz, C. H. J. T.; Warrag, S. E. E.; Kroon, M. C. The curious case of hydrophobic deep eutectic solvents: A story on the discovery, design, and applications. *ACS Sustain. Chem. Eng.* **2020**, *8*, 10591–10612.

(12) Paiva, A.; Craveiro, R.; Aroso, I.; Martins, M.; Reis, R. L.; Duarte, A. R. C. Natural deep eutectic solvents - Solvents for the 21st century. *ACS Sustain. Chem. Eng.* **2014**, *2*, 1063–1071.

(13) Hansen, B. B.; Spittle, S.; Chen, B.; Poe, D.; Zhang, Y.; Klein, J. M.; Horton, A.; Adhikari, L.; Zelovich, T.; Doherty, B. W.; Gurkan, B.; Maginn, E. J.; Ragauskas, A.; Dadmun, M.; Zawodzinski, T. A.; Baker, G. A.; Tuckerman, M. E.; Savinell, R. F.; Sangoro, J. R. Deep eutectic solvents: A review of fundamentals and applications. *Chem. Rev.* **2021**, *121*, 1232–1285.

(14) Kollau, L. J. B. M.; Vis, M.; van den Bruinhorst, A.; Esteves, A. C. C.; Tuinier, R. Quantification of the liquid window of deep eutectic solvents. *Chem. Commun.* **2018**, *54*, 13351–13354.

(15) Haerens, K.; Matthijs, E.; Chmielarz, A.; Van der Bruggen, B. The use of ionic liquids based on choline chloride for metal deposition: A green alternative? *J. Environ. Manage.* **2009**, *90*, 3245–3252.

(16) Wen, Q.; Chen, J. X.; Tang, Y. L.; Wang, J.; Yang, Z. Assessing the toxicity and biodegradability of deep eutectic solvents. *Chemosphere* **2015**, *132*, 63–69.

(17) Liu, Y.; Friesen, J. B.; McAlpine, J. B.; Lankin, D. C.; Chen, S. N.; Pauli, G. F. Natural deep eutectic solvents: Properties, applications, and perspectives. *J. Nat. Prod.* **2018**, *81*, 679–690.

(18) Abbott, A. P.; Edler, K. J.; Page, A. J. Deep eutectic solvents - The vital link between ionic liquids and ionic solutions. *J. Chem. Phys.* **2021**, *155*, 150401.

(19) Abranches, D. O.; Martins, M. A. R.; Silva, L. P.; Schaeffer, N.; Pinho, S. P.; Coutinho, J. A. P. Phenolic hydrogen bond donors in the formation of non-ionic deep eutectic solvents: the quest for type V DES. *Chem. Commun.* **2019**, *55*, 10253–10256.

(20) van Osch, D. J. G. P.; Zubeir, L. F.; van den Bruinhorst, A.; Rocha, M. A. A.; Kroon, M. C. Hydrophobic deep eutectic solvents as water-immiscible extractants. *Green Chem.* **2015**, *17*, 4518–4521.

(21) Florindo, C.; Branco, L. C.; Marrucho, I. M. Quest for green-solvent design: from hydrophilic to hydrophobic (deep) eutectic solvents. *ChemSusChem* **2019**, *12*, 1549–1559.

(22) Dietz, C. H. J. T.; van Osch, D. J. G. P.; Kroon, M. C.; Sadowski, G.; van Sint Annaland, M.; Gallucci, F.; Zubeir, L. F.; Held, C. PC-SAFT modeling of CO_2 solubilities in hydrophobic deep eutectic solvents. *Fluid Phase Equilib.* **2017**, *448*, 94–98.

(23) Haider, M. B.; Jha, D.; Kumar, R.; Marriyappan Sivagnanam, B. Ternary hydrophobic deep eutectic solvents for carbon dioxide absorption. *Int. J. Greenh. Gas Control* **2020**, *92*, 102839.

(24) Tang, W.; Dai, Y.; Row, K. H. Evaluation of fatty acid/alcohol-based hydrophobic deep eutectic solvents as media for extracting antibiotics from environmental water. *Anal. Bioanal. Chem.* **2018**, *410*, 7325–7336.

(25) Dietz, C. H. J. T.; Kroon, M. C.; van Sint Annaland, M.; Gallucci, F. Thermophysical properties and solubility of different sugar-derived molecules in deep eutectic solvents. *J. Chem. Eng. Data* **2017**, *62*, 3633–3641.

(26) Dietz, C. H. J. T.; Erve, A.; Kroon, M. C.; van Sint Annaland, M.; Gallucci, F.; Held, C. Thermodynamic properties of hydrophobic deep eutectic solvents and solubility of water and HMF in them: Measurements and PC-SAFT modeling. *Fluid Phase Equilib.* **2019**, *489*, 75–82.

(27) Tereshatov, E. E.; Boltoeva, M. Y.; Folden, C. M. First evidence of metal transfer into hydrophobic deep eutectic and low-transition-temperature mixtures: Indium extraction from hydrochloric and oxalic acids. *Green Chem.* **2016**, *18*, 4616–4622.

(28) Phelps, T. E.; Bhawawet, N.; Jurisson, S. S.; Baker, G. A. Efficient and selective extraction of $^{99m}TcO_4^-$ from aqueous media using hydrophobic deep eutectic solvents. *ACS Sustain. Chem. Eng.* **2018**, *6*, 13656–13661.

(29) Ruggeri, S.; Poletti, F.; Zanardi, C.; Pigani, L.; Zanfrognini, B.; Corsi, E.; Dossi, N.; Salomäki, M.; Kivelä, H.; Lukkari, J.; Terzi, F. Chemical and electrochemical properties of a hydrophobic deep eutectic solvent. *Electrochim. Acta* **2019**, *295*, 124–129.

(30) van Osch, D. J. G. P.; Parmentier, D.; Dietz, C. H. J. T.; van den Bruinhorst, A.; Tuinier, R.; Kroon, M. C. Removal of alkali and transition metal ions from water with hydrophobic deep eutectic solvents. *Chem. Commun.* **2016**, *52*, 11987–11990.

(31) Zhu, S.; Zhou, J.; Jia, H.; Zhang, H. Liquid–liquid microextraction of synthetic pigments in beverages using a hydrophobic deep eutectic solvent. *Food Chem.* **2018**, *243*, 351–356.

(32) Martins, M. A. R.; Pinho, S. P.; Coutinho, J. A. P. Insights into the nature of eutectic and deep eutectic mixtures. *J. Solution Chem.* **2019**, *48*, 962–982.

(33) Alomar, M. K.; Hayyan, M.; Alsaadi, M. A.; Akib, S.; Hayyan, A.; Hashim, M. A. Glycerol-based deep eutectic solvents: Physical properties. *J. Mol. Liq.* **2016**, *215*, 98–103.

(34) Pandey, A.; Rai, R.; Pal, M.; Pandey, S. How polar are choline chloride-based deep eutectic solvents? *Phys. Chem. Chem. Phys.* **2014**, *16*, 1559–1568.

(35) Florindo, C.; Oliveira, F. S.; Rebelo, L. P. N.; Fernandes, A. M.; Marrucho, I. M. Insights into the synthesis and properties of deep eutectic solvents based on cholinium chloride and carboxylic acids. *ACS Sustain. Chem. Eng.* **2014**, *2*, 2416–2425.

(36) Yadav, A.; Kar, J. R.; Verma, M.; Naqvi, S.; Pandey, S. Densities of aqueous mixtures of (choline chloride + ethylene glycol) and (choline chloride + malonic acid) deep eutectic solvents in temperature range 283.15–363.15 K. *Thermochim. Acta* **2015**, *600*, 95–101.

(37) D'Agostino, C.; Harris, R. C.; Abbott, A. P.; Gladden, L. F.; Mantle, M. D. Molecular motion and ion diffusion in choline chloride based deep eutectic solvents studied by ^{1}H pulsed field gradient NMR spectroscopy. *Phys. Chem. Chem. Phys.* **2011**, *13*, 21383–21391.

(38) Faraone, A.; Wagle, D. V.; Baker, G. A.; Novak, E. C.; Ohl, M.; Reuter, D.; Lunkenheimer, P.; Loidl, A.; Mamontov, E. Glycerol hydrogen-bonding network dominates structure and collective dynamics in a deep eutectic solvent. *J. Phys. Chem. B* **2018**, *122*, 1261–1267.

(39) Teles, A. R. R.; Capela, E. V.; Carmo, R. S.; Coutinho, J. A. P.; Silvestre, A. J. D.; Freire, M. G. Solvatochromic parameters of deep eutectic solvents formed by ammonium-based salts and carboxylic acids. *Fluid Phase Equilib.* **2017**, *448*, 15–21.

(40) Leron, R. B.; Caparanga, A.; Li, M. H. Carbon dioxide solubility in a deep eutectic solvent based on choline chloride and urea at T = 303.15-343.15 K and moderate pressures. *J. Taiwan Inst. Chem. Eng.* **2013**, *44*, 879–885.

(41) Deng, D.; Jiang, Y.; Liu, X.; Zhang, Z.; Ai, N. Investigation of solubilities of carbon dioxide in five levulinic acid-based deep eutectic solvents and their thermodynamic properties. *J. Chem. Thermodyn.* **2016**, *103*, 212–217.

(42) Dietz, C. H. J. T.; Creemers, J. T.; Meuleman, M. A.; Held, C.; Sadowski, G.; van Sint Annaland, M.; Gallucci, F.; Kroon, M. C. Determination of the total vapor pressure of hydrophobic deep eutectic solvents: Experiments and perturbed-chain statistical associating fluid theory modeling. *ACS Sustain. Chem. Eng.* **2019**, *7*, 4047–4057.

(43) Ahmadi, R.; Hemmateenejad, B.; Safavi, A.; Shojaeifard, Z.; Shahsavar, A.; Mohajeri, A.; Heydari Dokoohaki, M.; Zolghadr, A. R. Deep eutectic-water binary solvent associations investigated by vibrational spectroscopy and chemometrics. *Phys. Chem. Chem. Phys.* **2018**, *20*, 18463–18473.

(44) Meng, X.; Ballerat-Busserolles, K.; Husson, P.; Andanson, J. M. Impact of water on the melting temperature of urea + choline chloride deep eutectic solvent. *New J. Chem.* **2016**, *40*, 4492–4499.

(45) Siongco, K. R.; Leron, R. B.; Li, M. H. Densities, refractive indices, and viscosities of N,N-diethylethanol ammonium chloride-glycerol or -ethylene glycol deep eutectic solvents and their aqueous solutions. *J. Chem. Thermodyn.* **2013**, *65*, 65–72.

(46) van Osch, D. J. G. P.; Dietz, C. H. J. T.; van Spronsen, J.; Kroon, M. C.; Gallucci, F.; van Sint Annaland, M.; Tuinier, R. A search for natural hydrophobic deep eutectic solvents based on natural components. *ACS Sustain. Chem. Eng.* **2019**, *7*, 2933–2942.

(47) Basaiahgari, A.; Panda, S.; Gardas, R. L. Acoustic, volumetric, transport, optical and rheological properties of benzyltripropylammonium based deep eutectic solvents. *Fluid Phase Equilib.* **2017**, *448*, 41–49.

(48) Ma, C.; Laaksonen, A.; Liu, C.; Lu, X.; Ji, X. The peculiar effect of water on ionic liquids and deep eutectic solvents. *Chem. Soc. Rev.* **2018**, *47*, 8685–8720.

(49) Chen, Y.; Yu, D.; Chen, W.; Fu, L.; Mu, T. Water absorption by deep eutectic solvents. *Phys. Chem. Chem. Phys.* **2019**, *21*, 2601–2610.

(50) Ravula, S.; Larm, N. E.; Mottaleb, M. A.; Heitz, M. P.; Baker, G. A. Vapor pressure mapping of ionic liquids and low-volatility fluids using graded isothermal thermogravimetric analysis. *ChemEngineering* **2019**, *3*, 42.

(51) Shahbaz, K.; Mjalli, F. S.; Vakili-Nezhaad, G.; AlNashef, I. M.; Asadov, A.; Farid, M. M. Thermogravimetric measurement of deep eutectic solvents vapor pressure. *J. Mol. Liq.* **2016**, *222*, 61–66.

(52) Liu, F.; Chen, W.; Mi, J.; Zhang, J. Y.; Kan, X.; Zhong, F. Y.; Huang, K.; Zheng, A. M.; Jiang, L. Thermodynamic and molecular insights into the absorption of H_2S, CO_2, and CH_4 in choline chloride plus urea mixtures. *AIChE J.* **2019**, *65*, 1–10.

(53) Mirza, N. R.; Nicholas, N. J.; Wu, Y.; Mumford, K. A.; Kentish, S. E.; Stevens, G. W. Experiments and thermodynamic modeling of the solubility of carbon dioxide in three different deep eutectic solvents (DESs). *J. Chem. Eng. Data* **2015**, *60*, 3246–3252.

(54) Chapman, W. G.; Gubbins, K. E.; Jackson, G.; Radosz, M. SAFT: Equation-of-state solution model for associating fluids. *Fluid Phase Equilib.* **1989**, *52*, 31–38.

(55) Gross, J.; Sadowski, G. Perturbed-chain SAFT: An equation of state based on a perturbation theory for chain molecules. *Ind. Eng. Chem. Res.* **2001**, *40*, 1244–1260.

(56) González de Castilla, A.; Bittner, J. P.; Müller, S.; Jakobtorweihen, S.; Smirnova, I. Thermodynamic and transport properties modeling of deep eutectic solvents: A review on g^E-models, equations of state, and Molecular Dynamics. *J. Chem. Eng. Data* **2020**, *65*, 943–967.

(57) Cea-Klapp, E.; Polishuk, I.; Canales, R. I.; Quinteros-Lama, H.; Garrido, J. M. Estimation of thermodynamic properties and phase equilibria in systems of deep eutectic solvents by PC-SAFT EoS. *Ind. Eng. Chem. Res.* **2020**, *59*, 22292–22300.

(58) Alkhatib, I. I. I.; Bahamon, D.; Llovell, F.; Abu-Zahra, M. R. M.; Vega, L. F. Perspectives and guidelines on thermodynamic modelling of deep eutectic solvents. *J. Mol. Liq.* **2020**, *298*, 112183.

(59) Doherty, B. W.; Acevedo, O. OPLS force field for choline chloride-based deep eutectic solvents. *J. Phys. Chem. B* **2018**, *122*, 9982–9993.

(60) Zubeir, L. F.; Held, C.; Sadowski, G.; Kroon, M. C. PC-SAFT modeling of CO_2 solubilities in deep eutectic solvents. *J. Phys. Chem. B* **2016**, *120*, 2300–2310.

(61) Perkins, S. L.; Painter, P.; Colina, C. M. Molecular dynamic simulations and vibrational analysis of an ionic liquid analogue. *J. Phys. Chem. B* **2013**, *117*, 10250–10260.

(62) Wagle, D. V.; Adhikari, L.; Baker, G. A. Computational perspectives on structure, dynamics, gas sorption, and bio-interactions in deep eutectic solvents. *Fluid Phase Equilib.* **2017**, *448*, 50–58.

(63) Kamgar, A.; Mohsenpour, S.; Esmaeilzadeh, F. Solubility prediction of CO_2, CH_4, H_2, CO and N_2 in choline chloride/urea as a eutectic solvent using NRTL and COSMO-RS models. *J. Mol. Liq.* **2017**, *247*, 70–74.

(64) Haghbakhsh, R.; Raeissi, S. Modeling the phase behavior of carbon dioxide solubility in deep eutectic solvents with the cubic plus association equation of state. *J. Chem. Eng. Data* **2018**, *63*, 897–906.

(65) Haghbakhsh, R.; Raeissi, S. Modeling vapor-liquid equilibria of mixtures of SO_2 and deep eutectic solvents using the CPA-NRTL and CPA-UNIQUAC models. *J. Mol. Liq.* **2018**, *250*, 259–268.

(66) Ma, C.; Guo, Y.; Li, D.; Zong, J.; Ji, X.; Liu, C.; Lu, X. Molar enthalpy of mixing for choline chloride/urea deep eutectic solvent + water system. *J. Chem. Eng. Data* **2016**, *61*, 4172–4177.

(67) Schaeffer, N.; Abranches, D. O.; Silva, L. P.; Martins, M. A. R.; Carvalho, P. J.; Russina, O.; Triolo, A.; Paccou, L.; Guinet, Y.; Hedoux, A.; Coutinho, J. A. P. Non-ideality in thymol + menthol type V deep eutectic solvents. *ACS Sustain. Chem. Eng.* **2021**, *9*, 2203–2211.

(68) Mainberger, S.; Kindlein, M.; Bezold, F.; Elts, E.; Minceva, M.; Briesen, H. Deep eutectic solvent formation: a structural view using Molecular Dynamics simulations with classical force fields. *Mol. Phys.* **2017**, *115*, 1309–1321.

(69) Frenkel, D.; Smit, B., *Understanding molecular simulation: from algorithms to applications*, 2nd ed.; Academic Press: San Diego, CA, USA, 2002; Vol. 1.

(70) Allen, M. P.; Tildesley, D. J., *Computer simulation of liquids*, 2nd; Oxford University Press, Inc.: New York, NY, USA, 2017.

(71) Zhou, T.; McBride, K.; Linke, S.; Song, Z.; Sundmacher, K. Computer-aided solvent selection and design for efficient chemical processes. *Curr. Opin. Chem. Eng.* **2020**, *27*, 35–44.

(72) Shudo, Y.; Izumi, A.; Hagita, K.; Nakao, T.; Shibayama, M. Structure-mechanical property relationships in crosslinked phenolic resin investigated by Molecular Dynamics simulation. *Polymer* **2017**, *116*, 506–514.

(73) Zhang, M.; Zhang, X.; Liu, Y.; Wu, K.; Zhu, Y.; Lu, H.; Liang, B. Insights into the relationships between physicochemical properties, solvent performance, and applications of deep eutectic solvents. *Environ. Sci. Pollut. Res.* **2021**, *28*, 35537–35563.

(74) Mauri, A.; Consonni, V.; Todeschini, R, *Molecular descriptors.* 2nd ed.; Handbook of computational chemistry, Vol. 1; Springer International Publishing: Cham, Switzerland, 2017.

(75) Kaur, S.; Kumari, M.; Kashyap, H. K. Microstructure of deep eutectic solvents: Current understanding and challenges. *J. Phys. Chem. B* **2020**, *124*, 10601–10616.

(76) Urukova, I.; Vorholz, J.; Maurer, G. Solubility of CO_2, CO, and H_2 in the ionic liquid [bmim][PF_6] from Monte Carlo simulations. *J. Phys. Chem. B* **2005**, *109*, 12154–12159.

(77) Celebi, A. T.; Dawass, N.; Moultos, O. A.; Vlugt, T. J. H. How sensitive are physical properties of choline chloride–urea mixtures to composition changes: Molecular Dynamics simulations and Kirkwood–Buff theory. *J. Chem. Phys.* **2021**, *154*, 184502.

(78) Karadas, F.; Atilhan, M.; Aparicio, S. Review on the use of ionic liquids (ILs) as alternative fluids for CO_2 capture and natural gas sweetening. *Energy and Fuels* **2010**, *24*, 5817–5828.

(79) Ramdin, M.; Chen, Q.; Balaji, S. P.; Vicent-Luna, J. M.; Torres-Knoop, A.; Dubbeldam, D.; Calero, S.; de Loos, T. W.; Vlugt, T. J. H. Solubilities of CO_2, CH_4, C_2H_6, and SO_2 in ionic liquids and Selexol from Monte Carlo simulations. *J. Comput. Sci.* **2016**, *15*, 74–80.

(80) Moučka, F.; Nezbeda, I.; Smith, W. R. Computationally efficient Monte Carlo simulations for polarisable models: Multi-particle move method for water and aqueous electrolytes. *Mol. Simul.* **2013**, *39*, 1125–1134.

(81) Polat, H. M.; Salehi, H. S.; Hens, R.; Wasik, D. O.; de Meyer, F.; Houriez, C.; Coquelet, C.; Calero, S.; Dubbeldam, D.; Moultos, O. A.; Vlugt, T. J. H. New features of the open source Monte Carlo software Brick-CFCMC: Thermodynamic integration and hybrid trial moves. *J. Chem. Inf. Model.* **2021**, *61*, 3752–3757.

(82) Panagiotopoulos, A. Z. Direct determination of phase coexistence properties of fluids by Monte Carlo simulation in a new ensemble. *Mol. Phys.* **1987**, *61*, 813–826.

(83) Panagiotopoulos, A. Z.; Quirke, N.; Stapleton, M.; Tildesley, D. J. Phase equilibria by simulation in the Gibbs ensemble. *Mol. Phys.* **1988**, *63*, 527–545.

(84) Adams, D. J. Chemical potential of hard-sphere fluids by Monte Carlo methods. *Mol. Phys.* **1974**, *28*, 1241–1252.

(85) Adams, D. J. Grand canonical ensemble Monte Carlo for a Lennard-Jones fluid. *Mol. Phys.* **1975**, *29*, 307–311.

(86) Yao, J.; Greenkorn, R. A.; Chao, K. C. Monte Carlo simulation of the grand canonical ensemble. *Mol. Phys.* **1982**, *46*, 587–594.

(87) Brennan, J. K.; Madden, W. G. Phase coexistence curves for off-lattice polymer-solvent mixtures: Gibbs-Duhem integration simulations. *Mol. Simul.* **2003**, *29*, 91–100.

(88) Banaszak, B. J.; Faller, R.; de Pablo, J. J. Simulation of the effects of chain architecture on the sorption of ethylene in polyethylene. *J. Chem. Phys.* **2004**, *120*, 11304–11315.

(89) Dubbeldam, D.; Torres-Knoop, A.; Walton, K. S. On the inner workings of Monte Carlo codes. *Mol. Simul.* **2013**, *39*, 1253–1292.

(90) Theodorou, D. N. Progress and outlook in Monte Carlo simulations. *Ind. Eng. Chem. Res.* **2010**, *49*, 3047–3058.

(91) Rahbari, A.; Hens, R.; Ramdin, M.; Moultos, O. A.; Dubbeldam, D.; Vlugt, T. J. H. Recent advances in the continuous fractional component Monte Carlo methodology. *Mol. Simul.* **2021**, *47*, 804–823.

(92) Siepmann, J. I.; Frenkel, D. Configurational bias Monte Carlo: A new sampling scheme for flexible chains. *Mol. Phys.* **1992**, *75*, 59–70.

(93) Frenkel, D.; Mooij, G. C. A. M.; Smit, B. Novel scheme to study structural and thermal properties of continuously deformable molecules. *J. Phys. Condens. Matter* **1992**, *4*, 3053–3076.

(94) Laso, M.; de Pablo, J. J.; Suter, U. W. Simulation of phase equilibria for chain molecules. *J. Chem. Phys.* **1992**, *97*, 2817–2819.

(95) Vlugt, T. J. H.; Martin, M. G.; Smit, B; Siepmann, J. I.; Krishna, R Improving the efficiency of the configurational-bias Monte Carlo algorithm. *Mol. Phys.* **1998**, *94*, 727–733.

(96) Shi, W.; Maginn, E. J. Continuous fractional component Monte Carlo: An adaptive biasing method for open system atomistic simulations. *J. Chem. Theory Comput.* **2007**, *3*, 1451–1463.

(97) Shi, W.; Maginn, E. J. Improvement in molecule exchange efficiency in Gibbs ensemble Monte Carlo: Development and implementation of the continuous fractional component move. *J. Comput. Chem.* **2008**, *29*, 2520–2530.

(98) Rosch, T. W.; Maginn, E. J. Reaction ensemble Monte Carlo simulation of complex molecular systems. *J. Chem. Theory Comput.* **2011**, *7*, 269–279.

(99) Poursaeidesfahani, A.; Torres-Knoop, A.; Dubbeldam, D.; Vlugt, T. J. H. Direct free energy calculation in the continuous fractional component Gibbs ensemble. *J. Chem. Theory Comput.* **2016**, *12*, 1481–1490.

(100) Poursaeidesfahani, A.; Hens, R.; Rahbari, A.; Ramdin, M.; Dubbeldam, D.; Vlugt, T. J. H. Efficient application of continuous fractional component Monte Carlo in the reaction ensemble. *J. Chem. Theory Comput.* **2017**, *13*, 4452–4466.

(101) Consta, S.; Wilding, N. B.; Frenkel, D.; Alexandrowicz, Z. Recoil growth: An efficient simulation method for multi-polymer systems. *J. Chem. Phys.* **1999**, *110*, 3220–3228.

(102) Consta, S.; Vlugt, T. J. H.; Wichers Hoeth, J.; Smit, B.; Frenkel, D. Recoil growth algorithm for chain molecules with continuous interactions. *Mol. Phys.* **1999**, *97*, 1243–1254.

(103) Koch, W.; Holthausen, M. C., *A chemist's guide to density functional theory*, 2nd ed.; John Wiley & Sons: Hoboken, NJ, USA, 2001.

(104) Tuckerman, M., *Statistical mechanics: Theory and molecular simulation*, 1st ed.; Oxford Graduate Texts; OUP Oxford: Oxford, UK, 2010.

(105) Rapaport, D. C., *The art of Molecular Dynamics simulation*, 2nd ed.; Cambridge University Press: Cambridge, UK, 2004.

(106) Leach, A. R., *Molecular modelling: Principles and applications*, 2nd ed.; Prentice Hall: Hoboken, NJ, USA, 2001.

(107) Vlugt, T. J. H.; van der Eerden, J. P. J. M.; Dijkstra, M.; Smit, B.; Frenkel, D., *Introduction to molecular simulation and statistical thermodynamics*, URL: http://homepage.tudelft.nl/v9k6y/imsst/index.html, last accessed on 19-09-2021, 2009.

(108) Berendsen, H. J. C.; van der Spoel, D.; van Drunen, R. GROMACS: A message-passing parallel Molecular Dynamics implementation. *Comput. Phys. Commun.* **1995**, *91*, 43–56.

(109) Abraham, M. J.; Murtola, T.; Schulz, R.; Páll, S.; Smith, J. C.; Hess, B.; Lindahl, E. GROMACS: High performance molecular simulations through multi-level parallelism from laptops to supercomputers. *SoftwareX* **2015**, *1-2*, 19–25.

(110) Plimpton, S. Fast parallel algorithms for short-range molecular dynamics. *J. Comput. Phys.* **1995**, *117*, 1–19.

(111) Phillips, J. C.; Braun, R.; Wang, W.; Gumbart, J.; Tajkhorshid, E.; Villa, E.; Chipot, C.; Skeel, R. D.; Kalé, L.; Schulten, K. Scalable Molecular Dynamics with NAMD. *J. Comput. Chem.* **2005**, *26*, 1781–1802.

(112) Hens, R.; Rahbari, A.; Caro-Ortiz, S.; Dawass, N.; Erdős, M.; Poursaeidesfahani, A.; Salehi, H. S.; Celebi, A. T.; Ramdin, M.; Moultos, O. A.; Dubbeldam, D.; Vlugt, T. J. H. Brick-CFCMC: Open source software for Monte Carlo simulations of phase and reaction equilibria using the continuous fractional component method. *J. Chem. Inf. Model.* **2020**, *60*, 2678–2682.

(113) Kalé, L.; Skeel, R.; Bhandarkar, M.; Brunner, R.; Gursoy, A.; Krawetz, N.; Phillips, J.; Shinozaki, A.; Varadarajan, K.; Schulten, K. NAMD2: Greater scalability for parallel Molecular Dynamics. *J. Comput. Phys.* **1999**, *151*, 283–312.

(114) Shah, J. K.; Marin-Rimoldi, E.; Mullen, R. G.; Keene, B. P.; Khan, S.; Paluch, A. S.; Rai, N.; Romanielo, L. L.; Rosch, T. W.; Yoo, B.; Maginn, E. J. Cassandra: An open source Monte Carlo package for molecular simulation. *J. Comput. Chem.* **2017**, *38*, 1727–1739.

(115) Nejahi, Y.; Soroush Barhaghi, M.; Mick, J.; Jackman, B.; Rushaidat, K.; Li, Y.; Schwiebert, L.; Potoff, J. GOMC: GPU Optimized Monte Carlo for the simulation of phase equilibria and physical properties of complex fluids. *SoftwareX* **2019**, *9*, 20–27.

(116) Dubbeldam, D.; Calero, S.; Ellis, D. E.; Snurr, R. Q. RASPA: Molecular simulation software for adsorption and diffusion in flexible nanoporous materials. *Mol. Simul.* **2016**, *42*, 81–101.

(117) Martin, M. G. MCCCS Towhee: A tool for Monte Carlo molecular simulation. *Mol. Simul.* **2013**, *39*, 1212–1222.

(118) Ferreira, E. S. C.; Voroshylova, I. V.; Pereira, C. M.; Cordeiro, M. N. D. S. Improved force field model for the deep eutectic solvent ethaline: Reliable physicochemical properties. *J. Phys. Chem. B* **2016**, *120*, 10124–10137.

(119) Shah, D.; Mjalli, F. S. Effect of water on the thermo-physical properties of reline: An experimental and molecular simulation based approach. *Phys. Chem. Chem. Phys.* **2014**, *16*, 23900–23907.

(120) García, G.; Atilhan, M.; Aparicio, S. The impact of charges in force field parameterization for Molecular Dynamics simulations of deep eutectic solvents. *J. Mol. Liq.* **2015**, *211*, 506–514.

(121) Perkins, S. L.; Painter, P.; Colina, C. M. Experimental and computational studies of choline chloride-based deep eutectic solvents. *J. Chem. Eng. Data* **2014**, *59*, 3652–3662.

(122) Kaur, S.; Gupta, A.; Kashyap, H. K. Nanoscale spatial heterogeneity in deep eutectic solvents. *J. Phys. Chem. B* **2016**, *120*, 6712–6720.

(123) García, G.; Atilhan, M.; Aparicio, S. Interfacial properties of deep eutectic solvents regarding to CO_2 capture. *J. Phys. Chem. C* **2015**, *119*, 21413–21425.

(124) Zhekenov, T.; Toksanbayev, N.; Kazakbayeva, Z.; Shah, D.; Mjalli, F. S. Formation of type III deep eutectic solvents and effect of water on their intermolecular interactions. *Fluid Phase Equilib.* **2017**, *441*, 43–48.

(125) Ullah, R.; Atilhan, M.; Anaya, B.; Khraisheh, M.; García, G.; Elkhattat, A.; Tariq, M.; Aparicio, S. A detailed study of cholinium chloride and levulinic acid deep eutectic solvent system for CO_2 capture via experimental and molecular simulation approaches. *Phys. Chem. Chem. Phys.* **2015**, *17*, 20941–20960.

(126) Ferreira, E. S. C.; Voroshylova, I. V.; Figueiredo, N. M.; Pereira, C. M.; Cordeiro, M. N. D. S. Computational and experimental study of propeline: A choline chloride based deep eutectic solvent. *Journal of Molecular Liquids* **2020**, *298*, 111978.

(127) Ferreira, E. S. C.; Voroshylova, I. V.; Figueiredo, N. M.; Cordeiro, M. N. D. S. Molecular Dynamic study of alcohol-based deep eutectic solvents. *J. Chem. Phys.* **2021**, *155*, 064506.

(128) Celebi, A. T.; Vlugt, T. J. H.; Moultos, O. A. Structural, thermodynamic, and transport properties of aqueous reline and ethaline solutions from Molecular Dynamics simulations. *J. Phys. Chem. B* **2019**, *123*, 11014–11025.

(129) Baz, J.; Held, C.; Pleiss, J.; Hansen, N. Thermophysical properties of glyceline-water mixtures investigated by molecular modelling. *Phys. Chem. Chem. Phys.* **2019**, *21*, 6467–6476.

(130) Zhang, Y.; Poe, D.; Heroux, L.; Squire, H.; Doherty, B. W.; Long, Z.; Dadmun, M.; Gurkan, B.; Tuckerman, M. E.; Maginn, E. J. Liquid structure and transport properties of the deep eutectic solvent ethaline. *J. Phys. Chem. B* **2020**, *124*, 5251–5264.

(131) Rajbangshi, J.; Mukherjee, K.; Biswas, R. Heterogeneous orientational relaxations and translation–rotation decoupling in (choline chloride + urea) deep eutectic solvents: Investigation through Molecular Dynamics simulations and dielectric relaxation measurements. *J. Phys. Chem. B* **2021**, *125*, 5920–5936.

(132) Paul, N.; Naik, P. K.; Ribeiro, B. D.; Gooh Pattader, P. S.; Marrucho, I. M.; Banerjee, T. Molecular Dynamics insights and water stability of hydrophobic deep eutectic solvents aided extraction of nitenpyram from an aqueous environment. *J. Phys. Chem. B* **2020**, *124*, 7405–7420.

(133) Celebi, A. T.; Vlugt, T. J. H.; Moultos, O. A. Thermal conductivity of aqueous solutions of reline, ethaline, and glyceline deep eutectic solvents; a Molecular Dynamics simulation study. *Mol. Phys.* **2021**, *119*, e1876263.

(134) Stefanovic, R.; Ludwig, M.; Webber, G. B.; Atkin, R.; Page, A. J. Nanostructure, hydrogen bonding and rheology in choline chloride deep eutectic solvents as a function of the hydrogen bond donor. *Phys. Chem. Chem. Phys.* **2017**, *19*, 3297–3306.

(135) Migliorati, V.; Sessa, F.; D'Angelo, P. Deep eutectic solvents: A structural point of view on the role of the cation. *Chem. Phys. Lett. X* **2019**, *2*, 100001.

(136) Sun, H.; Li, Y.; Wu, X.; Li, G. Theoretical study on the structures and properties of mixtures of urea and choline chloride. *J. Mol. Model.* **2013**, *19*, 2433–2441.

(137) Kumari, P.; Shobhna; Kaur, S.; Kashyap, H. K. Influence of hydration on the structure of reline deep eutectic solvent: A Molecular Dynamics study. *ACS Omega* **2018**, *3*, 15246–15255.

(138) Kussainova, D.; Shah, D. Structure of monoethanolamine based type III DESs: Insights from Molecular Dynamics simulations. *Fluid Phase Equilib.* **2019**, *482*, 112–117.

(139) Paul, R.; Mitra, A.; Paul, S. Phase separation property of a hydrophobic deep eutectic solvent–water binary mixture: A Molecular Dynamics simulation study. *J. Chem. Phys.* **2021**, *154*, 244504.

(140) Hossain, S. S.; Paul, S.; Samanta, A. Liquid structure and dynamics of tetraalkylammonium bromide-based deep eutectic solvents: Effect of cation chain length. *J. Phys. Chem. B* **2019**, *123*, 6842–6850.

(141) Malik, A.; Kashyap, H. K. Heterogeneity in hydrophobic deep eutectic solvents: SAXS prepeak and local environments. *Phys. Chem. Chem. Phys.* **2021**, *23*, 3915–3924.

(142) Cui, Y.; Kuroda, D. G. Evidence of molecular heterogeneities in amide-based deep eutectic solvents. *J. Phys. Chem. A* **2018**, *122*, 1185–1193.

(143) Wang, Y.-L.; Li, B.; Sarman, S.; Mocci, F.; Lu, Z.-Y.; Yuan, J.; Laaksonen, A.; Fayer, M. D. Microstructural and dynamical heterogeneities in ionic liquids. *Chem. Rev.* **2020**, *120*, 5798–5877.

(144) Wang, Y.; Voth, G. A. Unique spatial heterogeneity in ionic liquids. *J. Am. Chem. Soc.* **2005**, *127*, 12192–12193.

(145) Liu, H.; Maginn, E. J. A Molecular Dynamics investigation of the structural and dynamic properties of the ionic liquid 1-n-butyl-3-methylimidazolium bis(trifluoromethanesulfonyl)imide. *J. Chem. Phys.* **2011**, *135*, 124507.

(146) Salehi, H. S.; Celebi, A. T.; Vlugt, T. J. H.; Moultos, O. A. Thermodynamic, transport, and structural properties of hydrophobic deep eutectic solvents composed of tetraalkylammonium chloride and decanoic acid. *J. Chem. Phys.* **2021**, *154*, 144502.

(147) Salehi, H. S.; Hens, R.; Moultos, O. A.; Vlugt, T. J. H. Computation of gas solubilities in choline chloride urea and choline chloride ethylene glycol deep eutectic solvents using Monte Carlo simulations. *J. Mol. Liq.* **2020**, *316*, 113729.

(148) Salehi, H. S.; Polat, H. M.; de Meyer, F.; Houriez, C.; Coquelet, C.; Vlugt, T. J. H.; Moultos, O. A. Vapor pressures and vapor phase compositions of choline chloride urea and choline chloride ethylene glycol deep eutectic solvents from molecular simulation. *J. Chem. Phys.* **2021**, *155*, 114504.

(149) Zhang, Y.; Maginn, E. J. A comparison of methods for melting point calculation using Molecular Dynamics simulations. *J. Chem. Phys.* **2012**, *136*, 144116.

(150) Zhang, Y.; Maginn, E. J. Molecular Dynamics study of the effect of alkyl chain length on melting points of $[C_nMIM][PF_6]$ ionic liquids. *Phys. Chem. Chem. Phys.* **2014**, *16*, 13489–13499.

(151) Bernardino, K.; Zhang, Y.; Ribeiro, M. C. C.; Maginn, E. J. Effect of alkyl-group flexibility on the melting point of imidazolium-based ionic liquids. *J. Chem. Phys.* **2020**, *153*, 044504.

(152) Hildebrand, J. H. Solubility of non-electrolytes . *J. Soc. Chem. Ind.* **1936**, *55*, 665–665.

(153) Hansen, C. M. The Three Dimensional Solubility Parameter and Solvent Diffusion Coefficient and Their Importance in Surface Coating Formulation, URL: https://hansen-solubility.com/contents/HSP1967-OCR.pdf, last accessed on 19-09-2021, Ph.D. Thesis, Copenhagen: Technical University of Denmark, 1967.

(154) Jorgensen, W. L.; Maxwell, D. S.; Tirado-Rives, J. Development and testing of the OPLS all-atom force field on conformational energetics and properties of organic liquids. *J. Am. Chem. Soc.* **1996**, *118*, 11225–11236.

(155) Wang, J.; Wolf, R. M.; Caldwell, J. W.; Kollman, P. A.; Case, D. A. Development and testing of a general Amber force field. *J. Comput. Chem.* **2004**, *25*, 1157–1174.

(156) Lovelock, K. R. J. Quantifying intermolecular interactions of ionic liquids using cohesive energy densities. *R. Soc. Open Sci.* **2017**, *4*, 171223.

(157) Xie, Y.; Dong, H.; Zhang, S.; Lu, X.; Ji, X. Solubilities of CO_2, CH_4, H_2, CO and N_2 in choline chloride/urea. *Green Energy Environ.* **2016**, *1*, 195–200.

(158) Verma, R.; Mohan, M.; Goud, V. V.; Banerjee, T. Operational strategies and comprehensive evaluation of menthol based deep eutectic solvent for the extraction of lower alcohols from aqueous media. *ACS Sustain. Chem. Eng.* **2018**, *6*, 16920–16932.

(159) Montes, I.; Lai, C.; Sanabria, D. Like dissolves like: A guided inquiry experiment for organic chemistry. *J. Chem. Educ.* **2003**, *80*, 447.

(160) Katritzky, A. R.; Fara, D. C.; Yang, H.; Tämm, K.; Tamm, T.; Karelson, M. Quantitative measures of solvent polarity. *Chem. Rev.* **2004**, *104*, 175–198.

(161) Schmid, R. Recent advances in the description of the structure of water, the hydrophobic effect, and the like-dissolves-like rule. *Monatshefte fuer Chemie/Chemical Mon.* **2001**, *132*, 1295–1326.

(162) Smith, W. L. Selective solubility: "Like dissolves like". *J. Chem. Educ.* **1977**, *54*, 228.

(163) Moran, M. J.; Shapiro, H. N.; Boettner, D. D.; Bailey, M. B., *Fundamentals of engineering thermodynamics*, 8th ed.; John Wiley & Sons: Hoboken, NJ, USA, 2014.

(164) Becher, P. The calculation of cohesive energy density from the surface tension of liquids. *J. Colloid Interface Sci.* **1972**, *38*, 291–293.

(165) Kilaru, P. K.; Condemarin, R. A.; Scovazzo, P. Correlations of low-pressure carbon dioxide and hydrocarbon solubilities in imidazolium-, phosphonium-, and ammonium-based room-temperature ionic liquids. Part 1. Using surface tension. *Ind. Eng. Chem. Res.* **2008**, *47*, 900–909.

(166) Kilaru, P. K.; Scovazzo, P. Correlations of low-pressure carbon dioxide and hydrocarbon solubilities in imidazolium-, phosphonium-, and ammonium-based room-temperature ionic liquids. Part 2. Using activation energy of viscosity. *Ind. Eng. Chem. Res.* **2008**, *47*, 910–919.

(167) Lee, S. H.; Lee, S. B. The Hildebrand solubility parameters, cohesive energy densities and internal energies of 1-alkyl-3-methylimidazolium-based room temperature ionic liquids. *Chem. Commun.* **2005**, 3469–3471.

(168) Lindvig, T.; Michelsen, M. L.; Kontogeorgis, G. M. A Flory–Huggins model based on the Hansen solubility parameters. *Fluid Phase Equilib.* **2002**, *203*, 247–260.

(169) Moganty, S. S.; Baltus, R. E. Regular solution theory for low pressure carbon dioxide solubility in room temperature ionic liquids: Ionic liquid solubility parameter from activation energy of viscosity. *Ind. Eng. Chem. Res.* **2010**, *49*, 5846–5853.

(170) Weerachanchai, P.; Chen, Z.; Leong, S. S. J.; Chang, M. W.; Lee, J. M. Hildebrand solubility parameters of ionic liquids: Effects of ionic liquid type, temperature and DMA fraction in ionic liquid. *Chem. Eng. J.* **2012**, *213*, 356–362.

(171) Weerachanchai, P.; Wong, Y.; Lim, K. H.; Tan, T. T. Y.; Lee, J. M. Determination of solubility parameters of ionic liquids and ionic liquid/solvent mixtures from intrinsic viscosity. *ChemPhysChem* **2014**, *15*, 3580–3591.

(172) Yoo, B.; Afzal, W.; Prausnitz, J. M. Solubility parameters for nine ionic liquids. *Ind. Eng. Chem. Res.* **2012**, *51*, 9913–9917.

(173) Fedors, R. F. A method for estimating both the solubility parameters and molar volumes of liquids. *Polym. Eng. Sci.* **1974**, *14*, 147–154.

(174) Koenhen, D. M.; Smolders, C. A. The determination of solubility parameters of solvents and polymers by means of correlations with other physical quantities. *J. Appl. Polym. Sci.* **1975**, *19*, 1163–1179.

(175) Marciniak, A. The solubility parameters of ionic liquids. *Int. J. Mol. Sci.* **2010**, *11*, 1973–1990.

(176) Marciniak, A. The Hildebrand solubility parameters of ionic liquids-Part 2. *Int. J. Mol. Sci.* **2011**, *12*, 3553–3575.

(177) Stefanis, E.; Panayiotou, C. Prediction of Hansen solubility parameters with a new group-contribution method. *Int. J. Thermophys.* **2008**, *29*, 568–585.

(178) Beerbower, A. Surface free energy: A new relationship to bulk energies. *J. Colloid Interface Sci.* **1971**, *35*, 126–132.

(179) Mangaraj, D.; Bhatnager, S. K.; Rath, S. B. Cohesive energy densities of high polymers. III. Estimation of C.E.D. by viscosity measurements. *Makromol. Chem.* **1963**, *67*, 75.

(180) Ewell, R. H.; Eyring, H. Theory of the viscosity of liquids as a function of temperature and pressure. *J. Chem. Phys.* **1937**, *5*, 726–736.

(181) Yadav, A.; Pandey, S. Densities and viscosities of (choline chloride + urea) deep eutectic solvent and its aqueous mixtures in the temperature range 293.15 K to 363.15 K. *J. Chem. Eng. Data* **2014**, *59*, 2221–2229.

(182) Sanders, J. R.; Ward, E. H.; Hussey, C. L. Aluminum bromide-1-methyl-3-ethylimidazolium bromide ionic liquids. *J. Electrochem. Soc.* **1986**, *133*, 325.

(183) Okoturo, O. O.; VanderNoot, T. J. Temperature dependence of viscosity for room temperature ionic liquids. *J. Electroanal. Chem.* **2004**, *568*, 167–181.

(184) Miran, M. S.; Kinoshita, H.; Yasuda, T.; Susan, M. A. B. H.; Watanabe, M. Physicochemical properties determined by $\Delta \mathrm{p}K_{\mathrm{a}}$ for protic ionic liquids based on an organic super-strong base with various Brønsted acids. *Phys. Chem. Chem. Phys.* **2012**, *14*, 5178–5186.

(185) Harifi-Mood, A. R.; Buchner, R. Density, viscosity, and conductivity of choline chloride + ethylene glycol as a deep eutectic solvent and its binary mixtures with dimethyl sulfoxide. *J. Mol. Liq.* **2017**, *225*, 689–695.

(186) Jin, H.; O'Hare, B.; Dong, J.; Arzhantsev, S.; Baker, G. A.; Wishart, J. F.; Benesi, A. J.; Maroncelli, M. Physical properties of ionic liquids consisting of the 1-butyl-3- methylimidazolium cation with various anions and the bis(trifluoromethylsulfonyl)imide anion with various cations. *J. Phys. Chem. B* **2008**, *112*, 81–92.

(187) Barton, A. F. M. Solubility parameters. *Chem. Rev.* **1975**, *75*, 731–753.

(188) Belmares, M.; Blanco, M.; Goddard, W. A.; Ross, R. B.; Caldwell, G.; Chou, S. H.; Pham, J.; Olofson, P. M.; Thomas, C. Hildebrand and Hansen solubility parameters from Molecular Dynamics with applications to electronic nose polymer sensors. *J. Comput. Chem.* **2004**, *25*, 1814–1826.

(189) Bordes, C.; Fréville, V.; Ruffin, E.; Marote, P.; Gauvrit, J. Y.; Briançon, S.; Lantéri, P. Determination of poly(ϵ-caprolactone) solubility parameters: Application to solvent substitution in a microencapsulation process. *Int. J. Pharm.* **2010**, *383*, 236–243.

(190) Buncel, E.; Rajagopal, S. Solvatochromism and solvent polarity scales. *Acc. Chem. Res.* **1990**, *23*, 226–231.

(191) Nigam, S.; Rutan, S. Principles and applications of solvatochromism. *Appl. Spectrosc.* **2001**, *55*, 362A–370A.

(192) Reichardt, C. Solvatochromic dyes as solvent polarity indicators. *Chem. Rev.* **1994**, *94*, 2319–2358.

(193) Dimroth, K.; Reichardt, C.; Siepmann, T.; Bohlmann, F. Über Pyridinium-*N*-phenol-betaine und ihre Verwendung zur Charakterisierung der Polarität von Lösungsmitteln. *Justus Liebigs Annalen der Chemie* **1963**, *661*, 1–37.

(194) Kamlet, M. J.; Taft, R. W. The solvatochromic comparison method. I. The β-scale of solvent hydrogen-bond acceptor (HBA) basicities. *J. Am. Chem. Soc.* **1976**, *98*, 377–383.

(195) Taft, R. W.; Kamlet, M. J. The solvatochromic comparison method. 2. The α-scale of solvent hydrogen-bond donor (HBD) acidities. *J. Am. Chem. Soc.* **1976**, *98*, 2886–2894.

(196) Kamlet, M. J.; Abboud, J. L. M.; Abraham, M. H.; Taft, R. W. Linear solvation energy relationships. 23. A comprehensive collection of the solvatochromic parameters, π, α, and β, and some methods for simplifying the generalized solvatochromic equation. *J. Org. Chem.* **1983**, *48*, 2877–2887.

(197) Valvi, A.; Dutta, J.; Tiwari, S. Temperature-dependent empirical parameters for polarity in choline chloride based deep eutectic solvents. *J. Phys. Chem. B* **2017**, *121*, 11356–11366.

(198) Derecskei, B.; Derecskei-Kovacs, A. Molecular modelling simulations to predict density and solubility parameters of ionic liquids. *Mol. Simul.* **2008**, *34*, 1167–1175.

(199) Sistla, Y. S.; Jain, L.; Khanna, A. Validation and prediction of solubility parameters of ionic liquids for CO_2 capture. *Sep. Purif. Technol.* **2012**, *97*, 51–64.

(200) Rai, N.; Wagner, A. J.; Ross, R. B.; Siepmann, J. I. Application of the TraPPE force field for predicting the Hildebrand solubility parameters of organic solvents and monomer units. *J. Chem. Theory Comput.* **2008**, *4*, 136–144.

(201) Luo, Y.; Wang, R.; Wang, W.; Zhang, L.; Wu, S. Molecular dynamics simulation insight into two-component solubility parameters of graphene and thermodynamic compatibility of graphene and styrene butadiene rubber. *J. Phys. Chem. C* **2017**, *121*, 10163–10173.

(202) Gupta, J.; Nunes, C.; Vyas, S.; Jonnalagadda, S. Prediction of solubility parameters and miscibility of pharmaceutical compounds by Molecular Dynamics simulations. *J. Phys. Chem. B* **2011**, *115*, 2014–2023.

(203) Wu, L.; Chen, L.; Sun, H. On accuracy of predicting densities and solubility parameters of polymers using atomistic simulations. *Mol. Simul.* **2017**, *43*, 510–518.

(204) Bayly, C. I.; Merz, K. M.; Ferguson, D. M.; Cornell, W. D.; Fox, T.; Caldwell, J. W.; Kollman, P. A.; Cieplak, P.; Gould, I. R.; Spellmeyer, D. C. A second generation force field for the simulation of proteins, nucleic acids, and organic molecules. *J. Am. Chem. Soc.* **1995**, *117*, 5179–5197.

(205) Liu, H.; Maginn, E. J.; Visser, A. E.; Bridges, N. J.; Fox, E. B. Thermal and transport properties of six ionic liquids: An experimental and Molecular Dynamics study. *Ind. Eng. Chem. Res.* **2012**, *51*, 7242–7254.

(206) Redelius, P. Bitumen solubility model using Hansen solubility parameter. *Energy and Fuels* **2004**, *18*, 1087–1092.

(207) Chertkoff, M. J.; Martin, A. N. The solubility of benzoic acid in mixed solvents. *Journal of the American Pharmaceutical Association* **1960**, *49*, 444–447.

(208) Haghbakhsh, R.; Parvaneh, K.; Raeissi, S.; Shariati, A. A general viscosity model for deep eutectic solvents: The free volume theory coupled with association equations of state. *Fluid Phase Equilib.* **2018**, *470*, 193–202.

(209) Warrag, S. E. E.; Pototzki, C.; Rodriguez, N. R.; van Sint Annaland, M.; Kroon, M. C.; Held, C.; Sadowski, G.; Peters, C. J. Oil desulfurization using deep eutectic solvents as sustainable and economical extractants via liquid-liquid extraction: Experimental and PC-SAFT predictions. *Fluid Phase Equilib.* **2018**, *467*, 33–44.

(210) Verlet, L. Computer "experiments" on classical fluids. I. Thermodynamical properties of Lennard-Jones molecules. *Phys. Rev.* **1967**, *159*, 98–103.

(211) Swope, W. C.; Andersen, H. C.; Berens, P. H.; Wilson, K. R. A computer simulation method for the calculation of equilibrium constants for the formation of physical clusters of molecules: Application to small water clusters. *J. Chem. Phys.* **1982**, *76*, 637–649.

(212) Martínez, L.; Andrade, R.; Birgin, E. G.; Martínez, J. M. PACKMOL: A package for building initial configurations for Molecular Dynamics simulations. *J. Comput. Chem.* **2009**, *30*, 2157–2164.

(213) Lee, K.; Lim, H. J.; Yang, S. J.; Kim, Y. S.; Park, C. R. Determination of solubility parameters of single-walled and double-walled carbon nanotubes using a finite-length model. *RSC Adv.* **2013**, *3*, 4814.

(214) Luo, Y.; Chen, X.; Wu, S.; Cao, S.; Luo, Z.; Shi, Y. Molecular Dynamics simulation study on two-component solubility parameters of carbon nanotubes and precisely tailoring the thermodynamic compatibility between carbon nanotubes and polymers. *Langmuir* **2020**, *36*, 9291–9305.

(215) Stresser, D.; Goulay, F.; Kelkar, M. S.; Maginn, E. J.; Leone, S. R. Photoelectron spectrum of isolated ion-pairs in ionic liquid vapor. *J. Phys. Chem. A* **2007**, *111*, 3191–3195.

(216) Leal, J. P.; Esperança, J. M. S. S.; Da Piedade, M. E. M.; Lopes, J. N. C.; Rebelo, L. P. N.; Seddon, K. R. The nature of ionic liquids in the gas phase. *J. Phys. Chem. A* **2007**, *111*, 6176–6182.

(217) Armstrong, J. P.; Hurst, C.; Jones, R. G.; Licence, P.; Lovelock, K. R. J.; Satterley, C. J.; Villar-Garcia, I. J. Vapourisation of ionic liquids. *Phys. Chem. Chem. Phys.* **2007**, *9*, 982–990.

(218) Emel'Yanenko, V. N.; Verevkin, S. P.; Heintz, A.; Corfield, J. A.; Deyko, A.; Lovelock, K. R. J.; Licence, P.; Jones, R. G. Pyrrolidinium-based ionic liquids. 1-butyl-1-methyl pyrrolidinium dicyanoamide: Thermochemical measurement, mass spectrometry, and ab initio calculations. *J. Phys. Chem. B* **2008**, *112*, 11734–11742.

(219) Chambreau, S. D.; Vaghjiani, G. L.; To, A.; Koh, C.; Strasser, D.; Kostko, O.; Leone, S. R. Heats of vaporization of room temperature ionic liquids by tunable vacuum ultraviolet photoionization. *J. Phys. Chem. B* **2010**, *114*, 1361–1367.

(220) Majer, V.; Svoboda, V.; Pick, J.; Holub, R. Relationship between heats of vaporization of binary mixtures. *Collect. Czechoslov. Chem. Commun.* **1974**, *39*, 11–19.

(221) Tamir, A. Prediction of latent heat of vaporization of multicomponent mixtures. *Fluid Phase Equilib.* **1982**, *8*, 131–147.

(222) Paulechka, Y. U.; Zaitsau, D. H.; Kabo, G. J.; Strechan, A. A. Vapor pressure and thermal stability of ionic liquid 1-butyl-3-methylimidazolium Bis(trifluoromethylsulfonyl)amide. *Thermochim. Acta* **2005**, *439*, 158–160.

(223) Wong, Y.; Chen, Z. J.; Tan, T. T. Y.; Lee, J. M. Hildebrand solubility parameters of amidium ionic liquids. *Ind. Eng. Chem. Res.* **2015**, *54*, 12150–12155.

(224) Guan, W.; Chang, N.; Yang, L.; Bu, X.; Wei, J.; Liu, Q. Determination and prediction for the polarity of ionic liquids. *J. Chem. Eng. Data* **2017**, *62*, 2610–2616.

(225) Pandey, A.; Pandey, S. Solvatochromic probe behavior within choline chloride-based deep eutectic solvents: Effect of temperature and water. *J. Phys. Chem. B* **2014**, *118*, 14652–14661.

(226) Florindo, C.; McIntosh, A. J. S.; Welton, T.; Branco, L. C.; Marrucho, I. M. A closer look into deep eutectic solvents: Exploring intermolecular interactions using solvatochromic probes. *Phys. Chem. Chem. Phys.* **2017**, *20*, 206–213.

(227) Verevkin, S. P.; Zaitsau, D. H.; Emel'yanenko, V. N.; Zhabina, A. A. Thermodynamic properties of glycerol: Experimental and theoretical study. *Fluid Phase Equilib.* **2015**, *397*, 87–94.

(228) Ambrose, D.; Hall, D. J. Thermodynamic properties of organic oxygen compounds L. The vapour pressures of 1,2-ethanediol (ethylene glycol) and bis(2-hydroxyethyl) ether (diethylene glycol). *J. Chem. Thermodyn.* **1981**, *13*, 61–66.

(229) Ciocirlan, O.; Iulian, O.; Croitoru, O. Effect of temperature on the physico-chemical properties of three ionic liquids containing choline chloride. *Rev. Chim.* **2010**, *61*, 721–723.

(230) Yadav, A.; Trivedi, S.; Rai, R.; Pandey, S. Densities and dynamic viscosities of (choline chloride + glycerol) deep eutectic solvent and its aqueous mixtures in the temperature range (283.15–363.15) K. *Fluid Phase Equilib.* **2014**, *367*, 135–142.

(231) Troter, D. Z.; Todorović, Z. B.; Đokić Stojanović, D. R.; Đordević, B. S.; Todorović, V. M.; Konstantinović, S. S.; Veljković, V. B. The physicochemical and thermodynamic properties of the choline chloride-based deep eutectic solvents. *J. Serbian Chem. Soc.* **2017**, *82*, 1039–1052.

(232) Abbott, A. P.; Boothby, D.; Capper, G.; Davies, D. L.; Rasheed, R. K. Deep eutectic solvents formed between choline chloride and carboxylic acids: Versatile alternatives to ionic liquids. *J. Am. Chem. Soc.* **2004**, *126*, 9142–9147.

(233) Xie, Y.; Dong, H.; Zhang, S.; Lu, X.; Ji, X. Effect of water on the density, viscosity, and CO_2 solubility in choline chloride/urea. *J. Chem. Eng. Data* **2014**, *59*, 3344–3352.

(234) Chemat, F.; Anjum, H.; Shariff, A. M.; Kumar, P.; Murugesan, T. Thermal and physical properties of (choline chloride + urea + l-arginine) deep eutectic solvents. *J. Mol. Liq.* **2016**, *218*, 301–308.

(235) Leron, R. B.; Li, M. H. High-pressure density measurements for choline chloride: urea deep eutectic solvent and its aqueous mixtures at $T = (298.15$ to $323.15)$ K and up to 50 MPa. *J. Chem. Thermodyn.* **2012**, *54*, 293–301.

(236) Shahbaz, K.; Ghareh Bagh, F. S.; Mjalli, F. S.; AlNashef, I. M.; Hashim, M. A. Prediction of refractive index and density of deep eutectic solvents using atomic contributions. *Fluid Phase Equilib.* **2013**, *354*, 304–311.

(237) Shahbaz, K.; Baroutian, S.; Mjalli, F. S.; Hashim, M. A.; Alnashef, I. M. Densities of ammonium and phosphonium based deep eutectic solvents: Prediction using artificial intelligence and group contribution techniques. *Thermochim. Acta* **2012**, *527*, 59–66.

(238) Shahbaz, K.; Mjalli, F. S.; Hashim, M. A.; AlNashef, I. M. Prediction of the surface tension of deep eutectic solvents. *Fluid Phase Equilib.* **2012**, *319*, 48–54.

(239) Leron, R. B.; Wong, D. S. H.; Li, M. H. Densities of a deep eutectic solvent based on choline chloride and glycerol and its aqueous mixtures at elevated pressures. *Fluid Phase Equilib.* **2012**, *335*, 32–38.

(240) Mjalli, F. S.; Vakili-Nezhaad, G.; Shahbaz, K.; Alnashef, I. M. Application of the Eötvos and Guggenheim empirical rules for predicting the density and surface tension of ionic liquids analogues. *Thermochim. Acta* **2014**, *575*, 40–44.

(241) Li, X.; Hou, M.; Han, B.; Wang, X.; Zou, L. Solubility of CO_2 in a choline chloride + urea eutectic mixture. *J. Chem. Eng. Data* **2008**, *53*, 548–550.

(242) Savi, L. K.; Carpiné, D.; Waszczynskyj, N.; Ribani, R. H.; Haminiuk, C. W. I. Influence of temperature, water content and type of organic acid on the formation, stability and properties of functional natural deep eutectic solvents. *Fluid Phase Equilibria* **2019**, *488*, 40–47.

(243) Kuddushi, M.; Nangala, G. S.; Rajput, S.; Ijardar, S. P.; Malek, N. I. Understanding the peculiar effect of water on the physicochemical properties of choline chloride based deep eutectic solvents theoretically and experimentally. *J. Mol. Liq.* **2019**, *278*, 607–615.

(244) Su, W. C.; Wong, D. S. H.; Li, M. H. Effect of water on solubility of carbon dioxide in (aminomethanamide + 2-hydroxy-*N*,*N*,*N*-trimethylethanaminium chloride). *J. Chem. Eng. Data* **2009**, *54*, 1951–1955.

(245) Ramdin, M.; Balaji, S. P.; Vicent-Luna, J. M.; Gutiérrez-Sevillano, J. J.; Calero, S.; de Loos, T. W.; Vlugt, T. J. H. Solubility of the precombustion gases CO_2, CH_4, CO, H_2, N_2, and H_2S in the ionic liquid [bmim][Tf_2N] from Monte Carlo simulations. *J. Phys. Chem. C* **2014**, *118*, 23599–23604.

(246) Jamali, S. H.; Ramdin, M.; Becker, T. M.; Torres-Knoop, A.; Dubbeldam, D.; Buijs, W.; Vlugt, T. J. H. Solubility of sulfur compounds in commercial physical solvents and an ionic liquid from Monte Carlo simulations. *Fluid Phase Equilib.* **2017**, *433*, 50–55.

(247) Singh, R. A Monte Carlo simulation study to predict the solubility of H_2S in ionic liquids with 1-butyl-3-methylimidazolium ([C_4mim^+]) cation and tetrafluoroborate ([BF_4^-]), hexaflorophosphate ([PF_6^-]) and bis(trifluoromethanesulfonyl)amide ([Tf_2N^-]) anions. *Mol. Simul.* **2017**, *43*, 291–297.

(248) Singh, R.; Marin-Rimoldi, E.; Maginn, E. J. A Monte Carlo simulation study to predict the solubility of carbon dioxide, hydrogen, and their mixture in the ionic liquids 1-alkyl-3-methylimidazolium bis(trifluoromethanesulfonyl)amide ([C_nmim^+][Tf_2N^-], $n = 4, 6$). *Ind. Eng. Chem. Res.* **2015**, *54*, 4385–4395.

(249) Shah, J. K.; Maginn, E. J. Monte Carlo simulations of gas solubility in the ionic liquid 1-*n*-butyl-3-methylimidazolium hexafluorophosphate. *J. Phys. Chem. B* **2005**, *109*, 10395–10405.

(250) Kumełan, J.; Kamps, Á. P. S.; Urukova, I.; Tuma, D.; Maurer, G. Solubility of oxygen in the ionic liquid [bmim][PF_6]: Experimental and molecular simulation results. *J. Chem. Thermodyn.* **2005**, *37*, 595–602.

(251) Wittich, B.; Deiters, U. K. Calculating thermodynamic properties of an ionic liquid with Monte Carlo simulations with an orthorhombic and a cubic simulation box. *J. Phys. Chem. B* **2010**, *114*, 8954–8960.

(252) Ali, E.; Hadj-Kali, M. K.; Mulyono, S.; Alnashef, I. M.; Fakeeha, A.; Mjalli, F. S.; Hayyan, A. Solubility of CO_2 in deep eutectic solvents: Experiments and modelling using the Peng-Robinson equation of state. *Chem. Eng. Res. Des.* **2014**, *92*, 1898–1906.

(253) Ojeda, R. M.; Llovell, F. Soft-SAFT transferable molecular models for the description of gas solubility in eutectic ammonium salt-based solvents. *J. Chem. Eng. Data* **2018**, *63*, 2599–2612.

(254) Lloret, J. O.; Vega, L. F.; Llovell, F. Accurate description of thermophysical properties of tetraalkylammonium chloride deep eutectic solvents with the soft-SAFT equation of state. *Fluid Phase Equilib.* **2017**, *448*, 81–93.

(255) Haider, M. B.; Jha, D.; Marriyappan Sivagnanam, B.; Kumar, R. Thermodynamic and kinetic studies of CO_2 capture by glycol and amine-based deep eutectic solvents. *J. Chem. Eng. Data* **2018**, *63*, 2671–2680.

(256) Ma, C.; Xie, Y.; Ji, X.; Liu, C.; Lu, X. Modeling, simulation and evaluation of biogas upgrading using aqueous choline chloride/urea. *Appl. Energy* **2018**, *229*, 1269–1283.

(257) Leron, R. B.; Li, M. H. Solubility of carbon dioxide in a choline chloride-ethylene glycol based deep eutectic solvent. *Thermochim. Acta* **2013**, *551*, 14–19.

(258) Jahanbakhsh-Bonab, P.; Esrafili, M. D.; Rastkar Ebrahimzadeh, A.; Jahanbin Sardroodi, J. Are choline chloride-based deep eutectic solvents better than methyl diethanolamine solvents for natural gas Sweetening? Theoretical insights from Molecular Dynamics simulations. *J. Mol. Liq.* **2021**, *338*, 116716.

(259) Potoff, J. J.; Siepmann, J. I. Vapor-liquid equilibria of mixtures containing alkanes, carbon dioxide, and nitrogen. *AIChE J.* **2001**, *47*, 1676–1682.

(260) Martin, M. G.; Siepmann, J. I. Transferable potentials for phase equilibria. 1. United-atom description of *n*-alkanes. *J. Phys. Chem. B* **1998**, *102*, 2569–2577.

(261) Shah, M. S.; Tsapatsis, M.; Siepmann, J. I. Development of the transferable potentials for phase equilibria model for hydrogen sulfide. *J. Phys. Chem. B* **2015**, *119*, 7041–7052.

(262) Cracknell, R. F. Molecular simulation of hydrogen adsorption in graphitic nanofibres. *Phys. Chem. Chem. Phys.* **2001**, *3*, 2091–2097.

(263) Martín-Calvo, A.; Lahoz-Martín, F. D.; Calero, S. Understanding carbon monoxide capture using metal-organic frameworks. *J. Phys. Chem. C* **2012**, *116*, 6655–6663.

(264) Ewald, P. P. Die Berechnung optischer und elektrostatischer Gitterpotentiale. *Ann. Phys.* **1921**, *369*, 253–287.

(265) Leron, R. B.; Soriano, A. N.; Li, M. H. Densities and refractive indices of the deep eutectic solvents (choline chloride + ethylene glycol or glycerol) and their aqueous mixtures at the temperature ranging from 298.15 to 333.15 K. *J. Taiwan Inst. Chem. Eng.* **2012**, *43*, 551–557.

(266) Wang, F.; Landau, D. P. Efficient, multiple-range random walk algorithm to calculate the density of states. *Phys. Rev. Lett.* **2001**, *86*, 2050–2053.

(267) Poulain, P.; Calvo, F.; Antoine, R.; Broyer, M.; Dugourd, P. Performances of Wang-Landau algorithms for continuous systems. *Phys. Rev. E - Stat. Nonlinear, Soft Matter Phys.* **2006**, *73*, 1–11.

(268) Beutler, T. C.; Mark, A. E.; van Schaik, R. C.; Gerber, P. R.; van Gunsteren, W. F. Avoiding singularities and numerical instabilities in free energy calculations based on molecular simulations. *Chem. Phys. Lett.* **1994**, *222*, 529–539.

(269) Pham, T. T.; Shirts, M. R. Identifying low variance pathways for free energy calculations of molecular transformations in solution phase. *J. Chem. Phys.* **2011**, *135*, 034114.

(270) Hens, R.; Vlugt, T. J. H. Molecular simulation of vapor-liquid equilibria using the Wolf method for electrostatic interactions. *J. Chem. Eng. Data* **2018**, *63*, 1096–1102.

(271) Rahbari, A.; Hens, R.; Dubbeldam, D.; Vlugt, T. J. H. Improving the accuracy of computing chemical potentials in CFCMC simulations. *Mol. Phys.* **2019**, *117*, 3493–3508.

(272) Dawass, N.; Wanderley, R. R.; Ramdin, M.; Moultos, O. A.; Knuutila, H. K.; Vlugt, T. J. H. Solubility of carbon dioxide, hydrogen sulfide, methane, and nitrogen in monoethylene glycol; Experiments and molecular simulation. *J. Chem. Eng. Data* **2021**, *66*, 524–534.

(273) Sandler, S. I., *Chemical, biochemical, and engineering thermodynamics*, Fifth; John Wiley & Sons: Hoboken, NJ, USA, 2017.

(274) Poling, B. E.; Prausnitz, J. M.; O'Connell, J. P., *The properties of gases and liquids*, 5th ed.; McGraw-Hill: New York, NY, USA, 2001.

(275) Boulougouris, G. C.; Voutsas, E. C.; Economou, I. G.; Theodorou, D. N.; Tassios, D. P. Henry's constant analysis for water and nonpolar solvents from experimental data, macroscopic models, and molecular simulation. *J. Phys. Chem. B* **2001**, *105*, 7792–7798.

(276) Shi, W.; Maginn, E. J. Atomistic simulation of the absorption of carbon dioxide and water in the ionic liquid 1-*n*-hexyl-3-methylimidazolium bis(trifluoromethylsulfonyl)imide [hmim][Tf_2N]. *J. Phys. Chem. B* **2008**, *112*, 2045–2055.

(277) Lemmon, E. W.; Bell, I. H.; Huber, M. L.; McLinden, M. O. NIST standard reference database 23: Reference fluid thermodynamic and transport properties-REFPROP, version 10.0, National Institute of Standards and Technology, 2018.

(278) Peng, D. Y.; Robinson, D. B. A new two-constant equation of state. *Ind. Eng. Chem. Fundam.* **1976**, *15*, 59–64.

(279) Shahbaz, K.; Mjalli, F. S.; Hashim, M. A.; Alnashef, I. M. Prediction of deep eutectic solvents densities at different temperatures. *Thermochim. Acta* **2011**, *515*, 67–72.

(280) Hammond, O. S.; Bowron, D. T.; Edler, K. J. Liquid structure of the choline chloride-urea deep eutectic solvent (reline) from neutron diffraction and atomistic modelling. *Green Chem.* **2016**, *18*, 2736–2744.

(281) Vanommeslaeghe, K.; Hatcher, E.; Acharya, C.; Kundu, S.; Zhong, S.; Shim, J.; Darian, E.; Guvench, O.; Lopes, P.; Vorobyov, I.; Mackerell, A. D. CHARMM general force field: A force field for drug-like molecules compatible with the CHARMM all-atom additive biological force fields. *J. Comput. Chem.* **2009**, *32*, NA–NA.

(282) MacKerell, A. D.; Wiorkiewicz-Kuczera, J.; Karplus, M. An all-atom empirical energy function for the simulation of nucleic acids. *J. Am. Chem. Soc.* **1995**, *117*, 11946–11975.

(283) Lopes, J. N. C.; Pádua, A. A. H. Molecular force field for ionic liquids composed of triflate or bistriflylimide anions. *J. Phys. Chem. B* **2004**, *108*, 16893–16898.

(284) Sambasivarao, S. V.; Acevedo, O. Development of OPLS-AA force field parameters for 68 unique ionic liquids. *J. Chem. Theory Comput.* **2009**, *5*, 1038–1050.

(285) Szefczyk, B.; Cordeiro, M. N. D. S. Physical properties at the base for the development of an all-atom force field for ethylene glycol. *J. Phys. Chem. B* **2011**, *115*, 3013–3019.

(286) Anthony, J. L.; Anderson, J. L.; Maginn, E. J.; Brennecke, J. F. Anion effects on gas solubility in ionic liquids. *J. Phys. Chem. B* **2005**, *109*, 6366–6374.

(287) Son, C. Y.; McDaniel, J. G.; Schmidt, J. R.; Cui, Q.; Yethiraj, A. First-principles united atom force field for the ionic liquid $BMIM^+BF_4^-$: An alternative to charge scaling. *J. Phys. Chem. B* **2016**, *120*, 3560–3568.

(288) Bhargava, B. L.; Balasubramanian, S. Refined potential model for atomistic simulations of ionic liquid [bmim][PF_6]. *J. Chem. Phys.* **2007**, *127*, 114510.

(289) Choi, E.; Yethiraj, A. Entropic mechanism for the lower critical solution temperature of poly(ethylene oxide) in a room temperature ionic liquid. *ACS Macro Lett.* **2015**, *4*, 799–803.

(290) Cui, K.; Yethiraj, A.; Schmidt, J. R. Influence of charge scaling on the solvation properties of ionic liquid solutions. *J. Phys. Chem. B* **2019**, *123*, 9222–9229.

(291) Schauperl, M.; Nerenberg, P. S.; Jang, H.; Wang, L.-P.; Bayly, C. I.; Mobley, D. L.; Gilson, M. K. Non-bonded force field model with advanced restrained electrostatic potential charges (RESP2). *Commun. Chem.* **2020**, *3*, 1–11.

(292) Bayly, C. I.; Cieplak, P.; Cornell, W. D.; Kollman, P. A. A well-behaved electrostatic potential based method using charge restraints for deriving atomic charges: The RESP model. *J. Phys. Chem.* **1993**, *97*, 10269–10280.

(293) Fyta, M.; Netz, R. R. Ionic force field optimization based on single-ion and ion-pair solvation properties: Going beyond standard mixing rules. *J. Chem. Phys.* **2012**, *136*, 124103.

(294) Papavasileiou, K. D.; Moultos, O. A.; Economou, I. G. Predictions of water/oil interfacial tension at elevated temperatures and pressures: A Molecular Dynamics simulation study with biomolecular force fields. *Fluid Phase Equilib.* **2018**, *476*, 30–38.

(295) Chen, J. L.; Xue, B.; Harwood, D. B.; Chen, Q. P.; Peters, C. J.; Siepmann, J. I. A Monte Carlo simulation study of the interfacial tension for water/oil mixtures at elevated temperatures and pressures: Water/n-dodecane, water/toluene, and water/(n-dodecane + toluene). *Fluid Phase Equilib.* **2018**, *476*, 16–24.

(296) Lima, F.; Dietz, C. H. J. T.; Silvestre, A. J. D.; Branco, L. C.; Canongia Lopes, J.; Gallucci, F.; Shimizu, K.; Held, C.; Marrucho, I. M. Vapor pressure assessment of sulfolane-based eutectic solvents: Experimental, PC-SAFT, and Molecular Dynamics. *J. Phys. Chem. B* **2020**, *124*, 10386–10397.

(297) Boisset, A.; Jacquemin, J.; Anouti, M. Physical properties of a new deep eutectic solvent based on lithium bis[(trifluoromethyl)sulfonyl]imide and N-methylacetamide as superionic suitable electrolyte for lithium ion batteries and electric double layer capacitors. *Electrochim. Acta* **2013**, *102*, 120–126.

(298) Wu, S. H.; Caparanga, A. R.; Leron, R. B.; Li, M. H. Vapor pressure of aqueous choline chloride-based deep eutectic solvents (ethaline, glyceline, maline and reline) at 30-70 °C. *Thermochim. Acta* **2012**, *544*, 1–5.

(299) Xin, K.; Roghair, I.; Gallucci, F.; van Sint Annaland, M. Total vapor pressure of hydrophobic deep eutectic solvents: Experiments and modelling. *J. Mol. Liq.* **2021**, *325*, 115227.

(300) Klamt, A. Conductor-like screening model for real solvents: A new approach to the quantitative calculation of solvation phenomena. *J. Phys. Chem.* **1995**, *99*, 2224–2235.

(301) Aissaoui, T.; AlNashef, I. M.; Benguerba, Y. Dehydration of natural gas using choline chloride based deep eutectic solvents: COSMO-RS prediction. *J. Nat. Gas Sci. Eng.* **2016**, *30*, 571–577.

(302) Salehi, H. S.; Ramdin, M.; Moultos, O. A.; Vlugt, T. J. H. Computing solubility parameters of deep eutectic solvents from Molecular Dynamics simulations. *Fluid Phase Equilib.* **2019**, *497*, 10–18.

(303) Rai, N.; Maginn, E. J. Vapor-liquid coexistence and critical behavior of ionic liquids via molecular simulations. *J. Phys. Chem. Lett.* **2011**, *2*, 1439–1443.

(304) Rai, N.; Maginn, E. J. Critical behaviour and vapour-liquid coexistence of 1-alkyl-3-methylimidazolium bis(trifluoromethylsulfonyl)amide ionic liquids via Monte Carlo simulations. *Faraday Discuss.* **2012**, *154*, 53–69.

(305) Dupradeau, F. Y.; Pigache, A.; Zaffran, T.; Savineau, C.; Lelong, R.; Grivel, N.; Lelong, D.; Rosanski, W.; Cieplak, P. The R.E.D. tools: Advances in RESP and ESP charge derivation and force field library building. *Phys. Chem. Chem. Phys.* **2010**, *12*, 7821–7839.

(306) Verevkin, S. P.; Zaitsau, D. H.; Emel'yanenko, V. N.; Yermalayeu, A. V.; Schick, C.; Liu, H.; Maginn, E. J.; Bulut, S.; Krossing, I.; Kalb, R. Making sense of enthalpy of vaporization trends for ionic liquids: New experimental and simulation data show a simple linear relationship and help reconcile previous data. *J. Phys. Chem. B* **2013**, *117*, 6473–6486.

(307) Zaitsau, D. H.; Siewert, R.; Pimerzin, A. A.; Bülow, M.; Held, C.; Loor, M.; Schulz, S.; Verevkin, S. P. From volatility to solubility: Thermodynamics of imidazolium-based ionic liquids containing chloride and bromide anions. *J. Mol. Liq.* **2021**, *323*, 114998.

(308) Morrow, T. I.; Maginn, E. J. Molecular Dynamics study of the ionic liquid 1-*n*-butyl-3-methylimidazolium hexafluorophosphate. *J. Phys. Chem. B* **2002**, *106*, 12807–12813.

(309) Kussainova, D.; Mondal, A.; Young, J. M.; Yue, S.; Panagiotopoulos, A. Z. Molecular simulation of liquid–vapor coexistence for NaCl: Full-charge vs scaled-charge interaction models. *J. Chem. Phys.* **2020**, *153*, 024501.

(310) Dawass, N.; Krüger, P.; Schnell, S. K.; Simon, J.-M.; Vlugt, T. J. H. Kirkwood-Buff integrals from molecular simulation. *Fluid Phase Equilib.* **2019**, *486*, 21–36.

(311) Panagiotopoulos, A. Z. Simulations of activities, solubilities, transport properties, and nucleation rates for aqueous electrolyte solutions. *J. Chem. Phys.* **2020**, *153*, 010903.

(312) Smith, J. M.; Van Ness, H. C.; Abbott, M., *Introduction to chemical engineering thermodynamics*, 7th ed.; McGraw-Hill: New York, NY, USA, 2005.

(313) Lide, D. R., *CRC handbook of chemistry and physics*, 85th ed.; CRC Press: Boca Raton, FL, USA, 2004.

(314) Zaitsau, D.; Kabo, G. J.; Kozyro, A. A.; Sevruk, V. M. The effect of the failure of isotropy of a gas in an effusion cell on the vapor pressure and enthalpy of sublimation for alkyl derivatives of carbamide. *Thermochim. Acta* **2003**, *406*, 17–28.

(315) Schnell, S. K.; Skorpa, R.; Bedeaux, D.; Kjelstrup, S.; Vlugt, T. J. H.; Simon, J.-M. Partial molar enthalpies and reaction enthalpies from equilibrium Molecular Dynamics simulation. *J. Chem. Phys.* **2014**, *141*, 144501.

(316) Peter, C.; Oostenbrink, C.; van Dorp, A.; van Gunsteren, W. F. Estimating entropies from Molecular Dynamics simulations. *J. Chem. Phys.* **2004**, *120*, 2652–2661.

(317) Aschenbrenner, O.; Supasitmongkol, S.; Taylor, M.; Styring, P. Measurement of vapour pressures of ionic liquids and other low vapour pressure solvents. *Green Chem.* **2009**, *11*, 1217.

(318) Köddermann, T.; Paschek, D.; Ludwig, R. Molecular dynamic simulations of ionic liquids: A reliable description of structure, thermodynamics and dynamics. *ChemPhysChem* **2007**, *8*, 2464–2470.

(319) Taylor, R.; Kooijman, H. A. Composition derivatives of activity coefficient models (for the estimation of thermodynamic factors in diffusion). *Chem. Eng. Commun.* **1991**, *102*, 87–106.

(320) Krishna, R; Wesselingh, J. A. The Maxwell-Stefan approach to mass transfer. *Chem. Eng. Sci.* **1997**, *52*, 861–911.

(321) Liu, X.; Martín-Calvo, A.; McGarrity, E.; Schnell, S. K.; Calero, S.; Simon, J.-M.; Bedeaux, D.; Kjelstrup, S.; Bardow, A.; Vlugt, T. J. H. Fick diffusion coefficients in ternary liquid systems from equilibrium Molecular Dynamics simulations. *Ind. Eng. Chem. Res.* **2012**, *51*, 10247–10258.

(322) Green, D. W.; Perry, R. H., *Perry's chemical engineers' handbook*, 8th ed.; McGraw-Hill: New York, NY, USA, 2007.

(323) Verevkin, S. P. Determination of vapor pressures and enthalpies of vaporization of 1,2-alkanediols. *Fluid Phase Equilib.* **2004**, *224*, 23–29.

(324) Skylogianni, E.; Wanderley, R. R.; Austad, S. S.; Knuutila, H. K. Density and viscosity of the nonaqueous and aqueous mixtures of methyldiethanolamine and monoethylene glycol at temperatures from 283.15 to 353.15 K. *J. Chem. Eng. Data* **2019**, *64*, 5415–5431.

(325) Florindo, C.; Branco, L. C.; Marrucho, I. M. Development of hydrophobic deep eutectic solvents for extraction of pesticides from aqueous environments. *Fluid Phase Equilib.* **2017**, *448*, 135–142.

(326) Milker, S.; Pätzold, M.; Bloh, J. Z.; Holtmann, D. Comparison of deep eutectic solvents and solvent-free reaction conditions for aldol production. *Mol. Catal.* **2019**, *466*, 70–74.

(327) Verma, R.; Banerjee, T. Liquid-liquid extraction of lower alcohols using menthol-based hydrophobic deep eutectic solvent: Experiments and COSMO-SAC predictions. *Ind. Eng. Chem. Res.* **2018**, *57*, 3371–3381.

(328) Wojeicchowski, J. P.; Ferreira, A. M.; Abranches, D. O.; Mafra, M. R.; Coutinho, J. A. P. Using COSMO-RS in the design of deep eutectic solvents for the extraction of antioxidants from rosemary. *ACS Sustain. Chem. Eng.* **2020**, *8*, 12132–12141.

(329) Adeyemi, I; Sulaiman, R; Almazroui, M; Al-Hammadi, A.; AlNashef, I. M. Removal of chlorophenols from aqueous media with hydrophobic deep eutectic solvents: Experimental study and COSMO RS evaluation. *J. Mol. Liq.* **2020**, *311*, 113180.

(330) Rodríguez-Llorente, D.; Cañada-Barcala, A.; Muñoz, C.; Pascual-Muñoz, G.; Navarro, P.; Santiago, R.; Águeda, V. I.; Álvarez-Torrellas, S.; García, J.; Larriba, M. Separation of phenols from aqueous streams using terpenoids and hydrophobic eutectic solvents. *Sep. Purif. Technol.* **2020**, *251*, 117379.

(331) Pontes, P. V. A.; Crespo, E. A.; Martins, M. A. R.; Silva, L. P.; Neves, C. M. S. S.; Maximo, G. J.; Hubinger, M. D.; Batista, E. A. C.; Pinho, S. P.; Coutinho, J. A. P.; Sadowski, G.; Held, C. Measurement and PC-SAFT modeling of solid-liquid equilibrium of deep eutectic solvents of quaternary ammonium chlorides and carboxylic acids. *Fluid Phase Equilib.* **2017**, *448*, 69–80.

(332) Fox, T.; Kollman, P. A. Application of the RESP methodology in the parametrization of organic solvents. *J. Phys. Chem. B* **1998**, *102*, 8070–8079.

(333) Frisch, M. J.; Trucks, G. W.; Schlegel, H. B.; Scuseria, G. E.; Robb, M. A.; Cheeseman, J. R.; Scalmani, G.; Barone, V.; Mennucci, B.; Petersson, G. A.; Nakatsuji, H.; Caricato, M.; Li, X.; Hratchian, H. P.; Izmaylov, A. F.; Bloino, J.; Zheng, G.; Sonnenberg, J. L.; Hada, M.; Ehara, M.; Toyota, K.; Fukuda, R.; Hasegawa, J.; Ishida, M.; Nakajima, T.; Honda, Y.; Kitao, K.; Nakai, H.; Vreven, T.; Montgomery Jr., J. A.; Peralta, J. E.; Ogliaro, F.; Bearpark, M.; Heyd, J. J.; Brothers, E.; Kudin, K. N.; Staroverov, V. N.; Keith, T.; Kobayashi, R.; Normand, J.; Raghavachari, K.; Rendell, A.; Burant, J. C.; Iyengar, S. S.; Tomasi, J.; Cossi, M.; Rega, N.; Millam, J. M.; Klene, M.; Knox, J. E.; Cross, J. B.; Bakken, V.; Adamo, C.; Jaramillo, J.; Gomperts, R.; Stratmann, R. E.; Yazyev, O.; Austin, A. J.; Cammi, R.; Pomelli, C.; Ochterski, J. W.; Martin, R. L.; Morokuma, K.; Zakrzewski, V. G.; Voth, G. A.; Salvador, P.; Dannenberg, J. J.; Dapprich, S.; Daniels, A. D.; Farkas, O.; Foresman, J. B.; Ortiz, J. V.; Cioslowski, J.; Fox, D. J., *Gaussian 09, Revision B.01*; Gaussian, Inc.: Wallingford CT, 2010.

(334) Doherty, B. W.; Zhong, X.; Gathiaka, S.; Li, B.; Acevedo, O. Revisiting OPLS force field parameters for ionic liquid simulations. *J. Chem. Theory Comput.* **2017**, *13*, 6131–6135.

(335) Zhang, Y.; Maginn, E. J. A simple AIMD approach to derive atomic charges for condensed phase simulation of ionic liquids. *J. Phys. Chem. B* **2012**, *116*, 10036–10048.

(336) Chaumont, A.; Engler, E.; Schurhammer, R. Is charge scaling really mandatory when developing fixed-charge atomistic force fields for deep eutectic solvents? *J. Phys. Chem. B* **2020**, *124*, 7239–7250.

(337) Jamali, S. H.; van Westen, T.; Moultos, O. A.; Vlugt, T. J. H. Optimizing nonbonded interactions of the OPLS force field for aqueous solutions of carbohydrates: How to capture both thermodynamics and dynamics. *J. Chem. Theory Comput.* **2018**, *14*, 6690–6700.

(338) Humphrey, W.; Dalke, A.; Schulten, K. VMD: Visual Molecular Dynamics. *J. Mol. Graph.* **1996**, *14*, 33–38.

(339) Jamali, S. H.; Wolff, L.; Becker, T. M.; de Groen, M.; Ramdin, M.; Hartkamp, R.; Bardow, A.; Vlugt, T. J. H.; Moultos, O. A. OCTP: A tool for on-the-fly calculation of transport properties of fluids with the order-n algorithm in LAMMPS. *J. Chem. Inf. Model.* **2019**, *59*, 1290–1294.

(340) Ganguly, P.; van der Vegt, N. F. A. Convergence of sampling Kirkwood-Buff integrals of aqueous solutions with Molecular Dynamics simulations. *J. Chem. Theory Comput.* **2013**, *9*, 1347–1355.

(341) Milzetti, J.; Nayar, D.; van der Vegt, N. F. A. Convergence of Kirkwood-Buff integrals of ideal and nonideal aqueous solutions using Molecular Dynamics simulations. *J. Phys. Chem. B* **2018**, *122*, 5515–5526.

(342) Dubbeldam, D.; Ford, D. C.; Ellis, D. E.; Snurr, R. Q. A new perspective on the order-n algorithm for computing correlation functions. *Mol. Simul.* **2009**, *35*, 1084–1097.

(343) Celebi, A. T.; Jamali, S. H.; Bardow, A.; Vlugt, T. J. H.; Moultos, O. A. Finite-size effects of diffusion coefficients computed from Molecular Dynamics: A review of what we have learned so far. *Mol. Simul.* **2021**, *47*, 831–845.

(344) Jamali, S. H.; Hartkamp, R.; Bardas, C.; Söhl, J.; Vlugt, T. J. H.; Moultos, O. A. Shear viscosity computed from the finite-size effects of self-diffusivity in equilibrium Molecular Dynamics. *J. Chem. Theory Comput.* **2018**, *14*, 5959–5968.

(345) Moultos, O. A.; Zhang, Y.; Tsimpanogiannis, I. N.; Economou, I. G.; Maginn, E. J. System-size corrections for self-diffusion coefficients calculated from Molecular Dynamics simulations: The case of CO_2, *n*-alkanes, and poly(ethylene glycol) dimethyl ethers. *J. Chem. Phys.* **2016**, *145*, 074109.

(346) Yeh, I.-C.; Hummer, G. System-size dependence of diffusion coefficients and viscosities from Molecular Dynamics simulations with periodic boundary conditions. *J. Phys. Chem. B* **2004**, *108*, 15873–15879.

(347) Jamali, S. H.; Bardow, A.; Vlugt, T. J. H.; Moultos, O. A. Generalized form for finite-size corrections in mutual diffusion coefficients of multicomponent mixtures obtained from equilibrium Molecular Dynamics simulation. *J. Chem. Theory Comput.* **2020**, *16*, 3799–3806.

(348) Humbert, M. T.; Zhang, Y.; Maginn, E. J. PyLAT: Python LAMMPS analysis tools. *J. Chem. Inf. Model.* **2019**, *59*, 1301–1305.

(349) Tu, K.-M.; Ishizuka, R.; Matubayasi, N. Spatial-decomposition analysis of electrical conductivity in concentrated electrolyte solution. *J. Chem. Phys.* **2014**, *141*, 044126.

(350) Müller-Plathe, F. Permeation of polymers - A computational approach. *Acta Polym.* **1994**, *45*, 259–293.

(351) Luzar, A.; Chandler, D. Effect of environment on hydrogen bond dynamics in liquid water. *Phys. Rev. Lett.* **1996**, *76*, 928–931.

(352) Zhao, W.; Leroy, F.; Heggen, B.; Zahn, S.; Kirchner, B.; Balasubramanian, S.; Müller-Plathe, F. Are there stable ion-pairs in room-temperature ionic liquids? Molecular Dynamics simulations of 1-*n*-butyl-3-methylimidazolium hexafluorophosphate. *J. Am. Chem. Soc.* **2009**, *131*, 15825–15833.

(353) Kohagen, M.; Brehm, M.; Lingscheid, Y.; Giernoth, R.; Sangoro, J.; Kremer, F.; Naumov, S.; Iacob, C.; Kärger, J.; Valiullin, R.; Kirchner, B. How hydrogen bonds influence the mobility of imidazolium-based ionic liquids. A combined theoretical and experimental study of 1-*n*-butyl-3-methylimidazolium bromide. *J. Phys. Chem. B* **2011**, *115*, 15280–15288.

(354) Saydan, G.; Yilmaz, E.; Soylak, M. Application of deep eutectic solvent in ultrasound-assisted emulsification microextraction of quercetin from some fruits and vegetables. *J. Mol. Liq.* **2019**, *279*, 571–577.

(355) Schröder, C. Comparing reduced partial charge models with polarizable simulations of ionic liquids. *Phys. Chem. Chem. Phys.* **2012**, *14*, 3089–3102.

(356) Vergadou, N.; Androulaki, E.; Hill, J. R.; Economou, I. G. Molecular simulations of imidazolium-based tricyanomethanide ionic liquids using an optimized classical force field. *Phys. Chem. Chem. Phys.* **2016**, *18*, 6850–6860.

(357) Youngs, T. G. A.; Hardacre, C. Application of static charge transfer within an ionic-liquid force field and its effect on structure and dynamics. *ChemPhysChem* **2008**, *9*, 1548–1558.

(358) Chaban, V. Polarizability versus mobility: Atomistic force field for ionic liquids. *Phys. Chem. Chem. Phys.* **2011**, *13*, 16055–16062.

(359) Shah, D.; Gapeyenko, D.; Urakpayev, A.; Torkmahalleh, M. Molecular dynamics simulations on extractive desulfurization of fuels by tetrabutylammonium chloride based deep eutectic solvents. *J. Mol. Liq.* **2019**, *274*, 254–260.

(360) Leontyev, I.; Stuchebrukhov, A. Accounting for electronic polarization in non-polarizable force fields. *Phys. Chem. Chem. Phys.* **2011**, *13*, 2613–2626.

(361) Wendler, K.; Dommert, F.; Zhao, Y. Y.; Berger, R.; Holm, C.; Delle Site, L. Ionic liquids studied across different scales: A computational perspective. *Faraday Discuss.* **2012**, *154*, 111–132.

(362) Chakraborty, M.; Barik, S.; Mahapatra, A.; Sarkar, M. Binary mixtures of ionic liquids: Ideal, non-ideal, or quasi-ideal? *J. Chem. Phys.* **2021**, *154*, 224507.

(363) Lee, S. Y.; Vicente, F. A.; Coutinho, J. A. P.; Khoiroh, I.; Show, P. L.; Ventura, S. P. M. Densities, viscosities, and refractive indexes of Good's buffer ionic liquids. *J. Chem. Eng. Data* **2016**, *61*, 2260–2268.

(364) Greaves, T. L.; Weerawardena, A.; Fong, C.; Krodkiewska, I.; Drummond, C. J. Protic ionic liquids: Solvents with tunable phase behavior and physicochemical properties. *J. Phys. Chem. B* **2006**, *110*, 22479–22487.

(365) Ghatee, M. H.; Zare, M.; Moosavi, F.; Zolghadr, A. R. Temperature-dependent density and viscosity of the ionic liquids 1-alkyl-3-methylimidazolium iodides: Experiment and Molecular Dynamics simulation. *J. Chem. Eng. Data* **2010**, *55*, 3084–3088.

(366) Bouzón Capelo, S.; Méndez-Morales, T.; Carrete, J.; López Lago, E.; Vila, J.; Cabeza, O.; Rodríguez, J. R.; Turmine, M.; Varela, L. M. Effect of temperature and cationic chain length on the physical properties of ammonium nitrate-based protic ionic liquids. *J. Phys. Chem. B* **2012**, *116*, 11302–11312.

(367) Filippov, A.; Taher, M.; Shah, F. U.; Glavatskih, S.; Antzutkin, O. N. The effect of the cation alkyl chain length on density and diffusion in dialkylpyrrolidinium bis(mandelato)borate ionic liquids. *Phys. Chem. Chem. Phys.* **2014**, *16*, 26798–26805.

(368) Chen, Z.; Ludwig, M.; Warr, G. G.; Atkin, R. Effect of cation alkyl chain length on surface forces and physical properties in deep eutectic solvents. *J. Colloid Interface Sci.* **2017**, *494*, 373–379.

(369) Nowosielski, B.; Jamrógiewicz, M.; Łuczak, J.; Śmiechowski, M.; Warmińska, D. Experimental and predicted physicochemical properties of monopropanolamine-based deep eutectic solvents. *J. Mol. Liq.* **2020**, *309*, 113110.

(370) Eremenko, L. T. Principles of the change in density in homologous series of liquid and crystalline hydrocarbons. *Bull. Acad. Sci. USSR Div. Chem. Sci.* **1968**, *17*, 1012–1016.

(371) Zubeir, L. F.; Lacroix, M. H. M.; Kroon, M. C. Low transition temperature mixtures as innovative and sustainable CO_2 capture solvents. *J. Phys. Chem. B* **2014**, *118*, 14429–14441.

(372) Zheng, Q.; Mauro, J. C. Viscosity of glass-forming systems. *J. Am. Ceram. Soc.* **2017**, *100*, 6–25.

(373) Bouarab, A. F.; Harvey, J.-P.; Robelin, C. Viscosity models for ionic liquids and their mixtures. *Phys. Chem. Chem. Phys.* **2021**, *23*, 733–752.

(374) Li, G.; Jiang, Y.; Liu, X.; Deng, D. New levulinic acid-based deep eutectic solvents: Synthesis and physicochemical property determination. *J. Mol. Liq.* **2016**, *222*, 201–207.

(375) Agieienko, V.; Buchner, R. Densities, viscosities, and electrical conductivities of pure anhydrous reline and its mixtures with water in the temperature range (293.15 to 338.15) K. *J. Chem. Eng. Data* **2019**, *64*, 4763–4774.

(376) Dong, D.; Hooper, J. B.; Bedrov, D. Structural and dynamical properties of tetraalkylammonium bromide aqueous solutions: A molecular dynamics simulation study using a polarizable force field. *J. Phys. Chem. B* **2017**, *121*, 4853–4863.

(377) Alizadeh, V.; Malberg, F.; Pádua, A. A. H.; Kirchner, B. Are there magic compositions in deep eutectic solvents? Effects of composition and water content in choline chloride/ethylene glycol from ab initio Molecular Dynamics. *J. Phys. Chem. B* **2020**, *124*, 7433–7443.

(378) Sapir, L.; Harries, D. Restructuring a deep eutectic solvent by water: The nanostructure of hydrated choline chloride/urea. *J. Chem. Theory Comput.* **2020**, *16*, 3335–3342.

(379) Aryafard, M.; Karimi, A.; Harifi-Mood, A. R.; Minofar, B. Molecular dynamics simulations, solvatochromic parameters, and preferential solvation in aqueous solutions of ethaline, ethylene glycol, and choline chloride. *J. Chem. Eng. Data* **2020**, *65*, 4556–4566.

(380) Venkatesan, S. S.; Huda, M. M.; Rai, N. Molecular insights into ionic liquid/aqueous interface of phosphonium based phase-separable ionic liquids. *AIP Adv.* **2019**, *9*, 045115.

(381) Sieffert, N.; Wipff, G. The [BMI][Tf_2N] ionic liquid/water binary system: A Molecular Dynamics study of phase separation and of the liquid-liquid interface. *J. Phys. Chem. B* **2006**, *110*, 13076–13085.

(382) Chaumont, A.; Schurhammer, R.; Wipff, G. Aqueous interfaces with hydrophobic room-temperature ionic liquids: A Molecular Dynamics study. *J. Phys. Chem. B* **2005**, *109*, 18964–18973.

(383) Chevrot, G; Schurhammer, R; Wipff, G Molecular Dynamics simulations of the aqueous interface with the [BMI][PF_6] ionic liquid: Comparison of different solvent models. *Phys. Chem. Chem. Phys.* **2006**, *8*, 4166.

(384) Ghatee, M. H.; Zolghadr, A. R. Local depolarization in hydrophobic and hydrophilic ionic liquids/water mixtures: Car–Parrinello and classical Molecular Dynamics simulation. *J. Phys. Chem. C* **2013**, *117*, 2066–2077.

(385) Konieczny, J. K.; Szefczyk, B. Structure of alkylimidazolium-based ionic liquids at the interface with vacuum and water - A Molecular Dynamics study. *J. Phys. Chem. B* **2015**, *119*, 3795–3807.

(386) Frost, D. S.; Dai, L. L. Molecular Dynamics simulations of nanoparticle self-assembly at ionic liquid–water and ionic liquid–oil interfaces. *Langmuir* **2011**, *27*, 11339–11346.

(387) Pouramini, Z.; Mohebbi, A.; Kowsari, M. H. The possibility of cadmium extraction to the ionic liquid 1-hexyl-3-methylimidazolium hexafluorophosphate in the presence of hydrochloric acid: A molecular dynamics study of the water–IL interface. *Theor. Chem. Acc.* **2019**, *138*, 99.

(388) Bergua, F.; Castro, M.; Muñoz-Embid, J.; Lafuente, C.; Artal, M. Hydrophobic eutectic solvents: Thermophysical study and application in removal of pharmaceutical products from water. *Chem. Eng. J.* **2021**, *411*, 128472.

(389) Berendsen, H. J. C.; Grigera, J. R.; Straatsma, T. P. The missing term in effective pair potentials. *J. Phys. Chem.* **1987**, *91*, 6269–6271.

(390) Ryckaert, J.-P.; Ciccotti, G.; Berendsen, H. J. C. Numerical integration of the Cartesian equations of motion of a system with constraints: Molecular Dynamics of *n*-alkanes. *J. Comput. Phys.* **1977**, *23*, 327–341.

(391) Isele-Holder, R. E.; Mitchell, W.; Ismail, A. E. Development and application of a particle-particle particle-mesh Ewald method for dispersion interactions. *J. Chem. Phys.* **2012**, *137*, 174107.

(392) Isele-Holder, R. E.; Mitchell, W.; Hammond, J. R.; Kohlmeyer, A.; Ismail, A. E. Reconsidering dispersion potentials: Reduced cutoffs in mesh-based Ewald solvers can be faster than truncation. *J. Chem. Theory Comput.* **2013**, *9*, 5412–5420.

(393) Martins, M. A. R.; Crespo, E. A.; Pontes, P. V. A.; Silva, L. P.; Bülow, M.; Maximo, G. J.; Batista, E. A. C.; Held, C.; Pinho, S. P.; Coutinho, J. A. P. Tunable hydrophobic eutectic solvents based on terpenes and monocarboxylic acids. *ACS Sustain. Chem. Eng.* **2018**, *6*, 8836–8846.

(394) Rossky, P. J.; Doll, J. D.; Friedman, H. L. Brownian dynamics as smart Monte Carlo simulation. *J. Chem. Phys.* **1978**, *69*, 4628–4633.

(395) Duane, S.; Kennedy, A. D.; Pendleton, B. J.; Roweth, D. Hybrid Monte Carlo. *Phys. Lett. B* **1987**, *195*, 216–222.

(396) Lynden-Bell, R. M.; Youngs, T. G. A. Simulations of imidazolium ionic liquids: When does the cation charge distribution matter? *J. Phys. Condens. Matter* **2009**, *21*, 424120.

(397) Rigby, J.; Izgorodina, E. I. Assessment of atomic partial charge schemes for polarisation and charge transfer effects in ionic liquids. *Phys. Chem. Chem. Phys.* **2013**, *15*, 1632–1646.

(398) Bedrov, D.; Piquemal, J. P.; Borodin, O.; MacKerell, A. D.; Roux, B.; Schröder, C. Molecular Dynamics simulations of ionic liquids and electrolytes using polarizable force fields. *Chem. Rev.* **2019**, *119*, 7940–7995.

(399) Goloviznina, K.; Gong, Z.; Costa Gomes, M. F.; Pádua, A. A. H. Extension of the CL&Pol polarizable force field to electrolytes, protic ionic liquids, and deep eutectic solvents. *J. Chem. Theory Comput.* **2021**, *17*, 1606–1617.

(400) Jeong, K.-j.; McDaniel, J. G.; Yethiraj, A. Deep eutectic solvents: Molecular simulations with a first-principles polarizable force field. *J. Phys. Chem. B* **2021**, *125*, 7177–7186.

(401) Mueller, T.; Hernandez, A.; Wang, C. Machine learning for interatomic potential models. *J. Chem. Phys.* **2020**, *152*, 050902.

(402) Islam, R.; Kabir, M. F.; Dhruba, S. R.; Afroz, K. Tuning force field parameters of ionic liquids using machine learning techniques. *Comput. Mater. Sci.* **2021**, *200*, 110759.

(403) Zhong, X.; Velez, C.; Acevedo, O. Partial charges optimized by genetic algorithms for deep eutectic solvent simulations. *J. Chem. Theory Comput.* **2021**, *17*, 3078–3087.

Summary

In this thesis, thermodynamic and structural properties of different deep eutectic solvent (DESs), and mixtures of DESs with gases or water, were computed using the state-of-the-art molecular simulations and computational methods. Discussions were presented on the influence of the intermolecular interactions and liquid structure of DESs on macroscopic properties such as densities, viscosities, diffusion coefficients, ionic conductivities, vapor pressures and vapor phase compositions, gas solubilities, solubility parameters, and interfacial tension with water.

In chapter 2, the Hildebrand and Hansen solubility parameters of DESs based on choline chloride as the hydrogen bond acceptor (HBA) and different hydrogen bond donor (HBD) components (urea, ethylene glycol, glycerol, malonic acid, or oxalic acid), were computed from Molecular Dynamics (MD) simulations. To compute these solubility parameters, energies and enthalpies of vaporization were computed from separate liquid phase and gas phase simulations. To use the thermodynamic definition of the solubility parameter, DESs were modeled as pseudo-pure compounds consisting of DES clusters, i.e., smallest units of HBA-HBD complexes with HBA:HBD molar ratios as in the liquid phase. The computed Hildebrand solubility parameters were in the range of 30 $MPa^{1/2}$ to 36 $MPa^{1/2}$. These values are larger than those of common molecular solvents and ionic liquids (ILs), suggesting a highly polar nature of DESs. For all DESs, considerable contributions to the total Hansen solubility parameter were obtained from both the dispersion and electrostatic forces, indicating the complex intermolecular interactions of the DESs and the important role of all non-bonded interactions. The computed electrostatic components of the Hansen solubility parameters of carboxylic acid-containing DESs were larger compared to other DESs, which implies stronger dipole-dipole and hydrogen bond interactions. The influence of temperature on the computed Hildebrand solubility parameters was negligible for all DESs. Using the pseudo-pure compound approach, DES clusters are assumed to be the vaporizing entities.

This assumption was tested by computing the vaporization enthalpies (and the corresponding solubility parameters) for the HBA and HBD components. The computed vaporization enthalpies of the HBD components were much smaller than those of the HBAs and DES clusters (and in better agreement with experimental data), indicating that the vapor phase of the DESs is likely dominated by HBD molecules. Two force fields were used for choline chloride-urea (ChClU), namely OPLS [154] (which was also used for the other DESs) and the General Amber Force Field (GAFF) [155]. The choice of force field did not have a significant influence on the computed enthalpies of vaporization and the solubility parameters. The energies of vaporization and cohesive energy densities were correlated with the activation energies of viscosity and the Gordon parameters. The computations of this chapter show how MD simulations can be used to compute the solubility parameters of solvent mixtures such as DESs, for a rough estimate of the solvent polarity, and provide an indication about the vapor phase composition.

In chapter 3, solubilities of CO_2, CH_4, H_2S, CO, N_2, and H_2 in ChClU and choline chloride ethylene glycol (ChClEg) were computed using Monte Carlo (MC) simulations. To tackle issues regarding the slow equilibration and inefficient molecule insertions/deletions, the continuous fractional component Monte Carlo (CFCMC) method was applied [91], which uses additional molecules with scaled interactions (indicated by the scaling parameter λ), referred to as 'fractional molecules'. Using the CFCMC method, the excess chemical potential at infinite dilution and thereby the Henry coefficient of each solute were directly computed in the NPT ensemble (at 328 K and 1 bar) from the observed probability distribution of λ of the fractional molecule. The absorption isotherm of CO_2 in ChClEg was computed from simulations in the osmotic ensemble. For ChClU, only the GAFF force field was used, while for ChClEg, both the OPLS and GAFF force fields were used. For both DESs, the computed solubilities of the gases at 328 K were in the following order: $H_2S > CO_2 > CH_4 > H_2 > CO > N_2$, which is in agreement with experimental data. Compared to experimental data, the Henry coefficients from the MC simulations were considerably overestimated (and the solubilities underestimated). The OPLS force field resulted in lower solubilities of gases in ChClEg (poorer agreement with experiments), compared to the GAFF force field (except for H_2S). It was found that decreasing the charge scaling factors of the DESs by 0.1 results in considerably smaller Henry coefficients (better agreement with experimental data), and reduced densities.

In chapter 4, MC simulations were used in combination with thermodynamic integration to compute the excess Gibbs energies and thereby,

the vapor pressures (including partial pressures of the components) and vapor phase compositions of ChClU and ChClEg at different temperatures. The vapor phases of the DESs were assumed to consist of isolated, non-interacting HBA (ion pairs) and HBD molecules. For both DESs, the computed partial pressures of the HBD component (urea or ethylene glycol) were considerably larger than those of the HBA (choline chloride). Based on the computed partial pressures, the vapor phase of ChClEg was found to be completely composed of HBD molecules, while small amounts of HBA (9% mole fraction-based) were present in the vapor phase of ChClU. This is in agreement with the results of chapter 2. The computed vapor pressures and enthalpies of vaporization were in overall agreement with available experimental data. The computed vapor pressures of ChClEg were significantly larger than those of ChClU, due to a higher volatility of ethylene glycol compared to urea. The saturated vapor pressure of pure ethylene glycol (using the GAFF force field) and, thereby, the activity coefficients of ethylene glycol in ChClEg, were computed. The computed vapor pressure of pure ethylene glycol overestimates the experimental value, while the activity coefficient of ethylene glycol at an HBA:HBD molar ratio of 1:2 was in reasonable agreement with experimental data. The computed activity coefficients indicated a highly non-ideal behavior for ethylene glycol in ChClEg (with negative deviations from Raoult's law). The partial pressures of urea and choline chloride (in both DESs), and the enthalpies of vaporization were not sensitive to the liquid phase composition (i.e., the mole fraction of the HBD in the liquid mixture), while the partial pressure of ethylene glycol significantly increased with an increase in the liquid phase mole fraction of the HBD.

In chapter 5, densities and transport properties (i.e., viscosities, finite size-corrected self-diffusivities, and ionic conductivities) for hydrophobic DESs based on decanoic acid as the HBD component and tetraalkylammonium chloride as the HBA component were computed from MD simulations at different temperatures. To investigate the influence of the cation alkyl chain lengths (i.e., hydrophobicity) on the computed properties, alkyl chain lengths of 4, 7, and 8 were used. Long simulation times (up to 650 ns) and high temperatures (323 K to 363 K) were required for the computation of the transport properties, due to the high viscosities of DESs, and difficult equilibration and sampling. To investigate the liquid structures of the DESs, radial distribution functions (RDFs) and hydrogen bond populations were computed. The influence of charge scaling on the computed viscosities was found to be significant. Based on the comparison of densities and viscosities with experimental data, a charge scaling factor of 0.6 was used in produc-

tion runs. For all DESs, the computed densities and viscosities were in agreement with experimental data from literature (particularly for smaller alkyl chain lengths). The computed densities of the DESs decreased with an increase in the alkyl chain length of the cation, possibly due to a hindered molecular packing. The viscosities of the DESs increased with an increase in the cation chain length. This may be caused by the hindered motion of the molecules due to the friction between the long cation alkyl chains. Consistently, smaller diffusion coefficient and ionic conductivities were computed for DESs with longer cation alkyl chains. The HBD component (decanoic acid) showed the highest self-diffusivity, followed by the chloride anion and the choline cation. The temperature dependence of all the computed transport properties can be well captured by the Arrhenius model. The RDFs and hydrogen bond analysis showed large numbers of decanoic acid-decanoic acid and chloride-decanoic acid hydrogen bonds. The effect of temperature on the computed RDFs and hydrogen bond populations was negligible. With an increasing charge scaling factor, chloride-decanoic acid interactions became stronger, while decanoic acid-decanoic acid interactions were weakened. Overall, the alkyl chain length of the DESs showed a significant influence on the transport properties (and to smaller extent on the densities), while did not considerably affect the liquid structure and hydrogen bonding networks.

In chapter 6, interfacial properties of mixtures of hydrophobic DESs with water were computed from MD simulations at various temperatures. The considered hydrophobic DESs were composed of decanoic acid as HBD component, and tetrabutylammonium chloride, thymol, or DL-menthol as HBA component. The density profiles of various molecules and the number densities of various hydrogen bonds were computed as a function of the z-coordinate (perpendicular to the interface). From the obtained density profiles, the water-in-DES solubilities (and salt-in-water solubilities for tetrabutylammonium chloride-decanoic acid) were computed. The interfacial tensions of the DESs with water were calculated at different temperatures at 1 atm. The influence of charge scaling on the computed interfacial properties was investigated. It was found that a charge scaling factor of 0.6 for tetrabutylammonium chloride-decanoic acid (as used in chapter 5) significantly underestimates the salt-in-water solubility for this DES (i.e., the amount of leaching of the cation and anion into water). In sharp contrast, a charge scaling factor of 0.8 resulted in a considerable leaching of the salt into water, which is in better agreement with experimental observations. No leaching of the DES components into the aqueous phase (and very little leaching of water into the DES) was observed for thymol-decanoic acid

and DL-menthol-decanoic acid, indicating the highly hydrophobic nature of these DESs. A charge scaling set of 0.7/1 for thymol-decanoic acid (i.e., scaling factors of 0.7 for thymol and 1 for decanoic acid) resulted in a larger number of decanoic acid-water hydrogen bonds at the interfaces, and thus a lower DES/water interfacial tension, compared to a charge set of 0.8/0.8. Considering the charge scaling set of 0.7/1 for thymol-decanoic acid, the computed interfacial tensions were in the following order (at all temperatures): tetrabutylammonium chloride-decanoic acid < thymol-decanoic acid < DL-menthol-decanoic acid. Larger numbers of decanoic acid-water hydrogen bonds were observed at the interfaces of thymol-decanoic acid/water and DL-menthol-decanoic acid/water mixtures, compared to the numbers of hydrogen bonds between the HBA components (thymol or DL-menthol) and water. For all DES/water mixtures, it was observed that the oxygen atoms of decanoic acid were aligned towards the aqueous phase (and the terminal carbon towards the DES phase) for maximized hydrogen bonding with water.

Samenvatting

In dit proefschrift worden thermodynamische en transport eigenschappen van verschillende deep eutectic solvents (DESs) en mengsels van DESs met verschillende gassen of water berekend met behulp van moderne moleculaire rekenmethoden en simulaties. De invloed van intermoleculaire interacties en de vloeistofstructuur van DESs op de volgende macroscopische eigenschappen werd onderzocht: dichtheden, viscositeit, diffusiecoëfficiënten (gecorrigeerd voor finite-size effecten), elektrische geleidbaarheid, dampdrukken, dampfasesamenstellingen, gasoplosbaarheden, oplosbaarheidsparameters en oppervlaktevlakspanning met water.

In hoofdstuk 2 worden met behulp van Moleculaire Dynamica (MD) simulaties de oplosbaarheidsparameters van Hildebrand en Hansen berekend voor DESs gebaseerd op choline chloride als hydrogen bond acceptor (HBA) en verschillende hydrogen bond donor (HBD) componenten (ureum, ethyleenglycol, glycerol, malonzuur of oxaalzuur). Om deze oplosbaarheidsparameters te berekenen worden verdampingsenergieën en enthalpieën berekend door middel van afzonderlijke vloeistof- en gasfase simulaties. Om de thermodynamische definitie van de oplosbaarheidsparameter te kunnen gebruiken werden de DESs gemodelleerd als pseudo-zuivere componenten bestaande uit DES-clusters, d.w.z. de kleinste eenheden van HBA-HBD-complexen met HBA:HBD-molverhoudingen zoals in de vloeibare fase. De berekende Hildebrand-oplosbaarheidsparameters varieerden van 30 $MPa^{1/2}$ tot 36 $MPa^{1/2}$. Deze waardes zijn groter dan die van gewone moleculaire oplosmiddelen en ionic liquids (ILs), hetgeen wijst op de zeer polaire aard van de DESs. Voor alle DESs resulteren zowel de dispersie- als elektrostatische interacties in aanzienlijke bijdragen tot de totale Hansen-oplosbaarheidsparameter. Dit wijst op complexe intermoleculaire interacties van DESs en de belangrijke rol van alle non-bonded interacties. De berekende elektrostatische componenten van de Hansen-oplosbaarheidsparameter zijn groter voor carbonzuurbevattende DESs in vergelijking tot andere DESs, hetgeen sterkere dipool-dipool- en water-

stofbruggen impliceert. De invloed van temperatuur op de berekende Hildebrand-oplosbaarheidsparameters is verwaarloosbaar voor alle DESs. Met behulp van de pseudo-zuivere component benadering wordt aangenomen dat DES-clusters de verdampende entiteiten zijn. Deze aanname werd getest door de verdampingsenthalpieën (en de bijbehorende oplosbaarheidsparameters) voor de HBA- en HBD-componenten van de DESs te berekenen. De berekende verdampingsenthalpieën van de HBD-componenten zijn veel kleiner dan die van de HBAs en DES-clusters (en meer in overeenstemming met experimentele gegevens). Dit duidt erop dat de dampfase van DESs waarschijnlijk wordt gedomineerd door HBD-moleculen. Voor choline chloride-ureum (ChClU) werden twee krachtvelden gebruikt, namelijk OPLS [154] (die ook voor de andere DESs werd gebruikt) en het General Amber Force Field (GAFF) [155]. De keuze van het krachtveld heeft geen significante invloed op de berekende verdampingsenthalpieën en oplosbaarheidsparameters. De verdampingsenergieën en cohesive energy densities hangen samen met de activeringsenergieën van de viscositeit en de Gordon-parameters. De berekeningen in dit hoofdstuk laten zien hoe MD simulaties kunnen worden gebruikt om de oplosbaarheidsparameters van mengsels zoals DESs te berekenen voor een ruwe schatting van de oplosmiddelpolariteit, en om een indicatie te geven voor de samenstelling van de dampfase.

In hoofdstuk 3 worden met behulp van Monte Carlo (MC) simulaties in gesloten en open ensembles de oplosbaarheden van CO_2, CH_4, H_2S, CO, N_2 en H_2 in ChClU en choline chloride-ethyleenglycol (ChClEg) berekend. Om problemen met de langzame equilibratie en inefficiënte inserties/verwijderingen van moleculen aan te pakken werd de continuous fractional component Monte Carlo (CFCMC) methode toegepast [91]. In deze methode worden extra moleculen met geschaalde interacties met de omgeving (weergegeven door de parameter λ) gebruikt. Dit type moleculen met geschaalde interacties worden 'fractionele moleculen' genoemd. Met behulp van de CFCMC methode werd de exces chemische potentiaal bij oneindige verdunning en daarmee de Henry coëfficiënt van elke opgeloste stof berekend in het *NPT* ensemble (bij 328 K en 1 bar). De exces chemische potentiaal volgt direct uit de berekende kansverdeling van λ van het fractionele molecuul. De absorptie isotherm van CO_2 in ChClEg werd berekend door middel van simulaties in het osmotische ensemble. Voor ChClU werd alleen het GAFF-krachtveld gebruikt. Voor ChClEg werden zowel de OPLS- en GAFF-krachtvelden gebruikt. Voor beide DESs kunnen de berekende oplosbaarheden van de gassen bij 328 K in de volgende volgorde worden gerangschikt: $H_2S > CO_2 > CH_4 > H_2 > CO > N_2$. Deze rangschikking is in overeenstemming met experimenten. In vergelijking met experimentele

gegevens worden de gesimuleerde Henry coëfficiënten aanzienlijk overschat (en de oplosbaarheden onderschat). Het OPLS-krachtveld resulteerde in lagere oplosbaarheden van de gassen in ChClEg (minder in lijn met experimenten) vergeleken met het GAFF-krachtveld (behalve voor H_2S). Het blijkt dat het verlagen van de schaalfactor voor ladingen van de DESs met 0.1 resulteert in aanzienlijk kleinere Henry coëfficiënten (meer in lijn met experimentele gegevens), en lagere dichtheden.

In hoofdstuk 4 worden MC simulaties gebruikt in combinatie met thermodynamische integratie om de exces Gibbsenergieën te berekenen, waarmee dampdrukken, partiële drukken van de componenten en samenstellingen van de dampfase van ChClU en ChClEg bij verschillende temperaturen kunnen worden berekend. Aangenomen werd dat de dampfase van DESs bestaat uit een ideaal gas van geïsoleerde HBA-moleculen (ionenparen) en HBD-moleculen. Voor beide DESs zijn de berekende partiële drukken van de HBD-component (ureum of ethyleenglycol) aanzienlijk groter dan die van de HBA-component (choline chloride). Op basis van de berekende partiële drukken blijkt dat de dampfase van ChClEg nagenoeg volledig bestaat uit HBD-moleculen. Kleine hoeveelheden HBA (9% op basis van molfractie) zijn aanwezig in de dampfase van ChClU. Dit is in overeenstemming met de resultaten uit hoofdstuk 2. De berekende dampdrukken en verdampingsenthalpieën zijn in het algemeen in overeenstemming met experimentele gegevens. De berekende dampdrukken van ChClEg zijn aanzienlijk groter dan die van ChClU. Dit komt door de hogere vluchtigheid van ethyleenglycol in vergelijking met ureum. De verzadigde dampdruk van zuiver ethyleenglycol werd berekend met behulp van het GAFF-krachtveld. Hiermee kunnen ook de activiteitscoëfficiënten van ethyleenglycol in ChClEg worden berekend. De dampdruk van zuiver ethyleenglycol afkomstig uit de simulaties bleek te hoog te zijn in vergelijking met experimenten, hoewel de activiteitscoëfficiënt van ethyleenglycol bij een HBA:HBD molaire verhouding van 1:2 redelijk overeenkwam met experimentele gegevens. De berekende activiteitscoëfficiënten wijzen op sterk niet-ideaal gedrag voor ethyleenglycol in ChClEg (met een negatieve afwijking van de wet van Raoult). De partiële drukken van ureum en choline chloride (in beide DESs) en de verdampingsenthalpieën hangen niet af van de samenstelling van de vloeistoffase (d.w.z. de molfractie van HBD in de vloeistof). De partiële druk van ethyleenglycol wordt significant groter bij een toename van de molfractie van de HBD in de vloeistof.

In hoofdstuk 5 worden met behulp van MD simulaties dichtheden en transporteigenschappen (viscositeit, zelf-diffusiecoëfficiënten gecorrigeerd voor finite-size effecten en elektrische geleidbaarheid) berekend

voor hydrofobe DESs op basis van decaanzuur als HBD-component en tetra-alkylammoniumchloride als HBA-component. Deze berekeningen werden uitgevoerd voor verschillende temperaturen. Om de invloed van de kation-alkylketenlengtes (hydrofobiciteit) op de berekende eigenschappen te onderzoeken werden alkylketenlengtes van 4, 7 en 8 gebruikt. Voor de berekening van de transporteigenschappen zijn lange simulaties (tot 650 ns) en hoge temperaturen (323 K to 363 K) nodig vanwege de hoge viscositeit van de DESs. Een hoge viscositeit maakt equilibratie en het samplen van de faseruimte aanzienlijk moeilijker. Om de vloeistofstructuur van de DESs te onderzoeken werden radiale distributiefuncties (RDFs) en waterstofbrugpopulaties berekend. De invloed van de schaling van atomaire ladingen op de berekende viscositeit bleek aanzienlijk te zijn. Op basis van de vergelijking van de berekende dichtheid en viscositeit met experimentele gegevens werd een schaalfactor voor atomaire ladingen van 0.6 gebruikt in productieruns. Voor alle DESs waren de berekende dichtheden en viscositeiten in overeenstemming met experimentele gegevens uit de literatuur (met name voor kleinere alkylketenlengtes). De berekende dichtheden van de DESs nemen af met een toename van de alkylketenlengte van het kation. Dit is mogelijk een gevolg van een lastigere moleculaire pakking. De viscositeiten van de DESs nemen toe met een toename van de kationketenlengte. Dit wordt mogelijk veroorzaakt door de belemmerde beweging van de moleculen als gevolg van de wrijving tussen de lange kation-alkylketens. Consequent worden kleinere diffusiecoëfficiënten en elektrische geleidbaarheden berekend voor DESs met langere kation-alkylketens. De HBD-component (decaanzuur) vertoont de grootste diffusiecoëfficiënt, gevolgd door het chloride-anion en het choline-kation. De temperatuurafhankelijkheid van alle transporteigenschappen kan worden beschreven met behulp van het Arrhenius-model. De RDFs en analyse van de waterstofbruggen laten aanzienlijke aantallen decaanzuur-decaanzuur- en chloride-decaanzuur-waterstofbruggen zien. De invloed van temperatuur op de berekende RDFs en waterstofbrugpopulaties is verwaarloosbaar. Met een toename van de schaalfactor voor atomaire ladingen worden de chloride-decaanzuur-interacties sterker, terwijl decaanzuur-decaanzuur-interacties verzwakken. In het algemeen heeft de alkylketenlengte van de DESs een belangrijke invloed op de transporteigenschappen (en in mindere mate op de dichtheden). De invloed hiervan op de vloeistofstructuur en waterstofbrugnetwerken is relatief beperkt.

In hoofdstuk 6 worden met behulp van MD simulaties oppervlakte eigenschappen van mengsels van hydrofobe DESs met water berekend bij verschillende temperaturen. Deze hydrofobe DESs zijn samengesteld

uit decaanzuur als HBD-component en tetrabutylammoniumchloride, thymol of DL-menthol als HBA-component. De dichtheidsprofielen van de verschillende moleculen en de dichtheid van verschillende waterstofbruggen werden berekend als functie van de z-coördinaat (loodrecht op het grensvlak water-DES). Uit de verkregen dichtheidsprofielen werden de water-in-DES-oplosbaarheden (en zout-in-water-oplosbaarheden voor tetrabutylammoniumchloride-decaanzuur) berekend. De oppervlaktespanningen van de DESs met water werden bij 1 atm berekend als functie van de temperatuur. De invloed van de schaling van de atomaire ladingen op de berekende oppervlakte eigenschappen werd onderzocht. Hieruit bleek dat een schaalfactor voor atomaire ladingen van 0.6 voor tetrabutylammoniumchloride-decaanzuur (zoals gebruikt in hoofdstuk 5) de zout-in-water oplosbaarheid voor deze DES (d.w.z. de hoeveelheid HBA-kation en anion in water) significant onderschat. Een schaalfactor voor atomaire ladingen van 0.8 daarentegen resulteert in een aanzienlijke oplosbaarheid van het HBA zout in water, hetgeen in betere overeenstemming is met experimenten. Er werden geen DES-componenten in de waterige fase (en zeer weinig water in de DES fase) waargenomen voor thymol-decaanzuur en DL-menthol-decaanzuur. Dit wijst op de zeer hydrofobe aard van deze DESs. Een schaalfactor van 0.7/1 voor thymol-decaanzuur (d.w.z. schaalfactoren van 0.7 voor thymol en 1 voor decaanzuur) resulteert in een groter aantal decaanzuur-waterwaterstofbruggen aan de grensvlakken, en dus een lagere oppervlakte vlakspanning vergeleken met schaalfactoren van 0.8/0.8. Rekening houdend met de schaalfactor van 0.7/1 voor thymol-decaanzuur kunnen de berekende oppervlaktespanningen als volgt worden gerangschikt (bij alle temperaturen): tetrabutylammoniumchloride-decaanzuur < thymol-decaanzuur < DL-menthol-decaanzuur zuur. Grotere aantallen decaanzuur-water-waterstofbruggen werden waargenomen nabij de grensvlakken van thymol-decaanzuur/water en DL-menthol-decaanzuur/water-mengsels, vergeleken met het aantal waterstofbruggen tussen de HBA-componenten (thymol of DL-menthol) en water. Bij alle DES/water-mengsels werd waargenomen dat de zuurstofatomen van decaanzuur uitgelijnd zijn naar de waterige fase (en het laatste koolstofatoom van de alkylketen naar de DES-fase). Dit zorgt voor maximale waterstofbindingen met water.

Curriculum vitae

Hirad S. Salehi was born on 19 December 1991 in Tehran, Iran. In 2010, he started his BSc. in mechanical engineering (specialization: thermofluidics) at Amirkabir University of Technology (Tehran Polytechnic) in Iran. After completing his BSc. studies in 2014, he move to the Netherlands to pursue an MSc. degree in mechanical engineering (specialization: sustainable processes and energy technologies) at Delft University of Technology. In his MSc. thesis, supervised by Dr. P.V. Aravind and Dr. Alessandro Cavalli, he experimentally investigated the influence of primary tars on the performance of a solid oxide fuel cell. After graduating Cum Laude from the MSc. program, Hirad joined the Engineering Thermodynamics research group at the Process and Energy department, Delft University of Technology, as a PhD candidate under the supervision of his promoter Prof. Thijs J. H. Vlugt and co-promoter Dr. Othonas Moultos. During his PhD research, Hirad studied the thermodynamic and transport properties, nanostructure, and intermolecular interactions of deep eutectic solvents (DESs) using molecular simulation techniques, i.e., Monte Carlo and Molecular Dynamics. His research aimed at gaining a fundamental understanding of the relationship between the macroscopic properties (e.g., interfacial tension, gas absorption, and self-diffusivity) of DESs and the interactions at the nanoscale, required for an optimal design of these novel solvents.

List of publications

Publications included in this thesis:

1. **H.S. Salehi**, O.A. Moultos, T.J.H. Vlugt, Interfacial properties of mixtures of hydrophobic deep eutectic solvents with water, *Journal of Physical Chemistry B*, **2021**, 125, 12303–12314.

2. **H.S. Salehi**, H.M. Polat, F. de Meyer, C. Houriez, C. Coquelet, T.J.H. Vlugt, O.A. Moultos, Vapor pressures and vapor phase compositions of choline chloride urea and choline chloride ethylene glycol deep eutectic solvents from molecular simulation, *Journal of Chemical Physics*, **2021**, 155, 114504.

3. **H.S. Salehi**, A.T. Celebi, T.J.H. Vlugt, O.A. Moultos, Thermodynamic, transport, and structural properties of hydrophobic deep eutectic solvents composed of tetraalkylammonium chloride and decanoic acid, *Journal of Chemical Physics*, **2021**, 154, 144502.

4. **H.S. Salehi**, R. Hens, O.A. Moultos, T.J.H. Vlugt, Computation of gas solubilities in choline chloride urea and choline chloride ethylene glycol deep eutectic solvents using Monte Carlo simulations, *Journal of Molecular Liquids*, **2020**, 316, 113729.

5. **H.S. Salehi**, M. Ramdin, O.A. Moultos, T.J.H. Vlugt, Computing solubility parameters of deep eutectic solvents from Molecular Dynamics simulations, *Fluid Phase Equilibria*, **2019**, 497, 10-18.

Publications not included in this thesis:

1. H.M. Polat, **H.S. Salehi**, R. Hens, D.O. Wasik, A. Rahbari, F. de Meyer, C. Houriez, C. Coquelet, S. Calero, D. Dubbeldam, O.A. Moultos, T.J.H. Vlugt, New features of the open source Monte Carlo software Brick-CFCMC: Thermodynamic integration and hybrid trial moves, *Journal of Chemical Information and Modeling*, **2021**, 61, 3752-3757.

2. R. Hens, A. Rahbari, S. Caro-Ortiz, N. Dawass, M. Erdős, A. Poursaeidesfahani, **H.S. Salehi**, A.T. Celebi, M. Ramdin, O.A. Moultos, D. Dubbeldam, T.J.H. Vlugt, Brick-CFCMC: Open source software for Monte Carlo simulations of phase and reaction equilibria using the continuous fractional component method, *Journal of Chemical Information and Modeling*, **2020**, 60, 2678-2682.

Acknowledgments

The PhD period has been a long journey with many ups and downs, during which I have grown and developed myself personally, professionally, and scientifically. I have built on my knowledge, and obtained a wide variety of skills from effective communication with my peers to programming and data analysis. My first and foremost thanks go to my promoter and supervisor, Prof. Thijs J. H. Vlugt, who has been tremendously supportive throughout my PhD, and has always been there to discuss science, to help me overcome my scientific and professional challenges, and to wisely guide me to the best solution. I feel privileged to have worked with and learned from such a distinguished scientist and such a nice, pleasant person. I am extremely grateful to my co-promoter and supervisor, Dr. Otto Moultos, who has tirelessly supported me both mentally and scientifically. I feel very lucky to have known Otto and to have him involved in my challenging PhD research, and I will be forever indebted.

I would like to thank my (ex-) colleagues in the Engineering Thermodynamics group, Reza, Remco, Noura, Alper, Mert, Ali, Seyed, Máté, Sebastian, Mahinder, and Dominika, with many of whom I have had the pleasure of fruitful discussions and co-authorship. Many thanks for the great experience, the extensive support, and for all that I have learned from you. I would like to express my gratitude to co-authors outside the university, Prof. Sofia Calero, Prof. Christophe Coquelet, Dr. Frédérick de Meyer, Dr. David Dubbeldam, and Dr. Céline Houriez, for the valuable and productive collaborations. I would also like to thank my friends, Arsha, Arya, Javad, Iman, Kourosh, Bob, Oskar, Amirhossein, Peyman, and Ali, who through mental support, enjoyable experiences, and fun travels made my PhD period a very memorable time of my life.

I am eternally grateful to my partner, Iris, who made this journey possible for me with her unconditional love and support, through tick and thin. I am extremely fortunate to have had her by my side. My deepest thanks go to my parents, Shima and Jamal, who have always believed in me,

supported me, and provided the best possible conditions for me to prosper in my life. I cannot express how grateful I am to have you as my parents.